ROYAUME DU MAROC
Université Mohammed V - RABAT -
جامعة محمد الخامس – الرباط –
Faculté des sciences
كلية العلوم
CENTRE D'ETUDES DOCTORALES - SCIENCES ET TECHNOLOGIES

N° d'ordre 3538

THESE

En vue de l'obtention du : ***DOCTORAT***

Structure de Recherche : Laboratoire de Matière Condensée et Sciences Interdisciplinaires
Discipline : Physique Informatique
Spécialité : Matière condensée et modélisation des systèmes énergétiques

Présentée et soutenue le 23/10/2021 par :

Mourad GARARA

Computational modeling of novel materials for hydrogen storage applications: Electronic structure and thermodynamics properties from first principle calculations

JURY

Hamid EZ-ZAHRAOUUY	PES, Faculté des sciences, Université Mohammed V- Rabat	Président
Abdallah El KENZ	PES, Faculté des sciences, Université Mohammed V- Rabat	Rapporteur/Examinateur
Mohamed BALLI	PES, Université Internationale de Rabat	Rapporteur/Examinateur
Rachid BENCHRIFA	PES, Faculté des sciences, Université Mohammed V- Rabat	Rapporteur/Examinateur
El Kebir HLIL	PES, Institut Néel, Université de Grenoble, France	Examinateur
Abdelilah BENYOUSSEF	PES, Académie Hassan II des sciences et techniques - Rabat	Invité
Samir RACHIDI	Dr-Ing, Directeur R\&D, Institut de Recherche en Energie Solaire et Energies Nouvelles (IRESEN), Rabat	Invité
Omar MOUNKACHI	PA, Faculté des sciences, Université Mohammed V- Rabat	Co-encadrant
Mohammed LOULIDI	PES, Faculté des sciences, Université Mohammed V- Rabat	Directeur de Thèse

Année Universitaire : 2020-2021

ROYAUME DU MAROC
Université Mohammed V - RABAT -
جامعة محمد الخامس – الرباط –
Faculté des sciences
كلية العلوم

DOCTORAL THESIS

By

Mourad Garara[1]

Supervised by

Mohammed Loulidi[2]

Computational modeling of novel materials for hydrogen storage applications: Electronic structure and thermodynamics properties from first principle calculations

President:		
Hamid EZ-ZAHRAOUY	PES	Faculté des sciences, Université Mohammed V-Rabat
Examiners:		
Abdallah El KENZ	PES	Faculté des sciences, Université Mohammed V-Rabat
Mohamed BALLI	PES	Univérsité Internationale de Rabat
Rachid BENCHRIFA	PES	Faculté des sciences, Université Mohammed V-Rabat
El Kebir HLIL	PES	Institut Néel , Université de Grenoble, France
Abdelilah BENYOUSSEF	PES	Académie Hassan II des sciences et techniques, Rabat
Samir RACHIDI	Dr-Ing	Directeur R&D, Institut de Recherche en Energie Solaire et Energies Nouvelles (IRESEN), Rabat
Omar Mounkachi	PA	Faculté des sciences, Université Mohammed V-Rabat
Mohammed LOULIDI	PES	Faculté des sciences, Université Mohammed V-Rabat

[1]E-mail:garara.mourad@gmail.com
[2]E-mail:loulidi@fsr.ac.ma
Laboratory of Condensed Matter and interdisciplinary Sciences (LaMCScI)

Acknowledgments

This thesis was carried out at the Laboratory of Condensed Matter and Interdisciplinary Sciences (LaMCScI) of Faculty of Sciences, University of Mohammed V in Rabat, Morocco under the supervision of Mr. **Mohammed LOULIDI** and the Co-supervision of Mr. **Omar MOUNKACHI**.

First of all, I would like to express my sincere gratitude to my supervisor Mr. **Mohammed LOULIDI**, Higher eduction professor at Faculty of Sciences, University of Mohammed V in Rabat, for his patience and support. His advice, constructive remarks, and scientific input have been of great help to me throughout this research project. Thank you for the trust you have placed in me and I hope this work lives up to your expectations.

I would like to thank Mr. **Omar MOUNKACHI**, Assistant professor at Faculty of Sciences, University of Mohammed V in Rabat, for his Co-supervision, guidance and assistance. Our meetings and conversations were extremely inspiring to think outside the box.

I would also thank the thesis committee for reviewing my work and giving their insightful and useful comments. It is an honor for me that they agree to judge this work.

I would like to thank Mr. **Hamid EZ-ZAHRAOUY**, Higher eduction professor at Faculty of Sciences, University of Mohammed V in Rabat, to be the president of the jury members of this thesis.

I would also like to thank Mr. **Abdallah EL KENZ**, Higher eduction professor at Faculty of Sciences, University of Mohammed V in Rabat, for reporting and examining my thesis as well as for investing time and providing interesting and valuable feedback

during the preparation of this dissertation.

I would like also to thank Mr. **Mohamed BALLI**, Higher eduction professor from the International University of Rabat, for reporting and examining my Ph.D thesis.

I extend my gratitude to Mr. **Rachid BENCHRIFA**, Higher eduction professor at Faculty of Sciences, University of Mohammed V in Rabat, for reporting and examining my research work and for his constructive comments.

My thanks are also offered to Mr. **El Kebir HLIL**, Higher eduction professor from the Institut Néel, University of Grenoble, France, for examining my thesis and for his valuable comments.

My sincere thanks go to Mr. **Abdelilah BENYOUSSEF**, Higher eduction professor and resident member at Hassan II Academy of science and technology of Rabat, for accepting my invitation to be part of this PhD thesis jury. Who was and will be invaluable source of knowledge.

I would like also to express my thanks to Mr. **Samir RACHIDI**, Doctor and engineer at Institut de Recherche en Energie Solaire et Energies Nouvelles (IRESEN) in Rabat, for accepting my invitation to be part of this PhD thesis jury.

I would like to point out that this work was done as part of the activities of the hydrogen storage group of the Laboratory of Condensed Matter and Interdisciplinary Sciences (LaMCScI) composed of professors, doctors and PhD students. The obtained results and the published works are the result of many years of hard work, long hours of effort and deep reflection of each of the founding members of the team. I thank all the members of the hydrogen storage team whom without their expertise this project could not have been accomplished. My sincere thanks to them for their efforts, their support and their encouragement.Finally, my gratitude goes to my parents, my brothers, to my friends and any person who contributes in this Ph.D studies.

Abstract

Hydrogen fuels are an attractive alternative source of energy since they are clean, non-toxic and renewable, making them suitable for use as substitutes for petroleum-derived fuels in vehicular applications. However, the greatest challenge in making hydrogen fuel-based transportation a norm in the future lies in the development of safe, compact, portable and cost-effective hydrogen storage systems with high energy densities for on-board vehicular applications. Alternative storage methods have been proposed including high pressure gas cylinders, liquid hydrogen, physisorption of hydrogen on materials with a high specific surface area, and hydrogen storage through hydrides, e.g. Magnesium-based hydrides. Perovskite hydrides with a general formula of ABH_3 such as $MgCoH_3$ possess flexible structures, low cost and lightweight, and have high hydrogen capacities. However, its high thermodynamic stability (-71.30kJ/mol.H_2) and high desorption temperature (545.52K) is still an issue that needs to be overcome and limits its large-scale industrial and technological applications. For this reason, our theoretical studies have examined many properties, in which it shows that either the biaxial strain or substitution of $MgCoH_3$ improves considerably the thermodynamic and kinetic properties, by the remarkable increase in the formation energy, and consequently the decrease in desorption temperature towards the ambient, either in kinetic point of view or the activation energies of diffusion of hydrogen atom in $MgCoH_3$ is also decreased.

Key words: Hydrogen storage; Perovskite-type hydride $MgCoH_3$; 2D materials; Phosphorene; DFT; Kinetic properties; Thermodynamic properties; activation energies.

Résumé

Récemment, l'hydrogène est considéré comme l'un des vecteurs énergétiques les plus prometteurs par rapport aux combustibles fossiles.L'hydrogène est fortement explosif et son stockage à l'état solide par rapport au stockage à l'état gazeux et liquide représente une solution à ce problème mais au détriment de la quantité d'hydrogène stockée entraîne des conditions de libération du gaz dures. Dans ce contexte, la recherche de nouveaux matériaux pour le stockage d'hydrogène avec des propriétés physico-chimiques nouvelles est souhaitable. Les hydrures perovskites de formule général ABH_3 tel que $MgCoH_3$ possèdent des structures flexibles, peu coûteuses et légères, et ont des capacités élevées en hydrogène. Cependant, son utilisation dans les applications industrielles et technologiques à grande échelle est limitée par la stabilité thermodynamique et température de désorption élevée (-71.30kJ/mol.H_2, 545.52K). Basé sur ceci, nous avons décidé de faire une étude approfondie sur l'influence des différentes stratégies utilisées pour améliorer les propriétés de $MgCoH_3$. Des études théoriques des propriétés thermodynamiques et cinétiques ont été examinées. Les résultats obtenus montrent que la contrainte bi-axiale ou la substitution améliore considérablement les propriétés de dé/hydrogénation de $MgCoH_3$ par l'augmentation remarquable des énergies de formation, et par conséquent la diminution de température déshydrogénation vers l'ambiante. En ce qui concerne la cinétique, les énergies d'activation de diffusion de l'atome d'hydrogène est également diminué.

Mots clés: Stockage de l'hydrogène; $MgCoH_3$; phosphorène; la théorie de la densité fonctionnelle; Température de désorption; Energy de formation; Energie d'activation.

Résumé détaillé

Dans notre société actuelle, l'un des défis majeurs du développement économique mondial est de satisfaire la demande en énergie tout en réduisant nos émissions de polluants et gaz à effet de serre. Le monde se tourne vers une société durable, d'une part grâce à une partie croissante de la population qui présente des considérations sur l'environnement, les dégâts de la pollution... mais surtout d'autre part par les marchés mondiaux qui y sont poussés inéluctablement par l'épuisement progressif des ressources fossiles, qui de plus sont importées de régions politiquement instables. Dans ce sens, il devient une priorité mondiale d'explorer des sources d'énergie alternatives qui sont propres, abondantes et durables. Alors que les énergies durables telles que le solaire, l'éolien et l'hydrogène peuvent répondre à la demande d'énergie, les défis actuels demeurent pour trouver des matériaux capables de stocker et/ou de convertir l'énergie efficacement et à faible coût. En tant que vecteur d'énergie très flexible, l'hydrogène peut offrir une approche énergétique globale, propre, intégrée et multi-sectorielle, qui permettra de contribuer de manière décisive à la résolution du problème environnemental et à la garantie de l'avenir énergétique de la Terre. Cependant, l'adoption massive de l'économie de l'hydrogène est lente en raison d'un manque d'incitations et de difficultés techniques dans le stockage de l'hydrogène.

Le stockage de l'hydrogène dans des composés à l'état solide semble être la solution la plus pratique étant donné qu'il s'agit d'une méthode plus sûre que la compression à haute pression ou la liquéfaction à faible température. L'objectif de notre projet est de rechercher de nouveaux matériaux pour le stockage d'hydrogène avec des propriétés physico-chimiques nouvelles et souhaitables. Afin d'étudier le stockage de l'hydrogène dans l'hydrure de pérovskite ($MgCoH_3$), de comprendre les mécanismes physiques sous-jacents et de proposer des approches qui améliorent ses propriétés de stockage de l'hydrogène tout en répondant aux critères de la US-DOE, nous avons mené une étude théorique des propriétés thermodynamiques et cinétiques en utilisant les calculs ab initio

(DFT). Les hydrures pérovskites de formule général ABH_3 tel que $MgCoH_3$ possèdent des structures flexibles, peu coûteuses et légères, et ont des capacités élevées en hydrogène. Néanmoins, Les résultats des calculs montrent que $MgCoH_3$ a une énergie de formation élevée et par conséquent une haute stabilité et une température de désorption élevée, ce qui est en accord avec les résultats théoriques trouvés dans la littérature. Par la suite, une étude détaillée de l'effet de la contrainte mécanique bi-axiale ou la substitution sur la stabilité, les propriétés thermodynamiques et la cinétique d'hydrogénation du ($MgCoH_3$) a été réalisée. Dans ces investigations numériques, lorsque la contrainte mécanique de compression a été appliquée sur la structure $MgCoH_3$, l'énergie de formation est passée de -71,30kJ/mol.H_2 pour la structure pur de $MgCoH_3$ à -37,29kJ/mol.H_2 sous la compression de -6% et la température de désorption a également diminué à 285,34K contre 545,52K pour le $MgCoH_3$ pur, ce qui est proche des valeurs optimales pour l'application pratique (289-393K et -40kJ/mol.H_2).

La deuxième stratégie utilisée pour améliorer les propriétés de de/hydrogénation est la substitution du cobalt par les atomes légers lithium (Li) ou bore (B) dans la structure stable de l'hydrure pérovskite $MgCoH_3$. Premièrement, la possibilité de fabrication de ces systèmes a été confirmée par la valeur négative des énergies de formation et les faibles modes imaginaire dans la dispersion des phonons de tous les systèmes. De plus, la température de désorption est réduite à 341.87K et 302.67K pour l'hydrogène entièrement libéré pour les systèmes $MgCo_{0.50}Li_{0.50}H_3$ et $MgCo_{0.75}B_{0.25}H_3$, respectivement. Les propriétés de stockage d'hydrogène des systèmes substitués considérablement améliorées sont attribuées à la diminution des atomes de cobalt dans le cadre du hydrure pérovskite, ce qui conduit à une hybridation plus faible entre les atomes de cobalt et d'hydrogène, et par la suite à une capacité gravimétrique élevée . De cette façon nous avons pu étudier les propriétés de stockage de l'hydrogène de $MgCoH_3$ et proposer des méthodes pour améliorer les propriétés thermodynamiques et cinétiques du composé tout en augmentant les capacités de stockage d'hydrogène du matériau. Suite à notre étude, nous remarquons que ces améliorations pourraient conduire à utiliser les hydrures pérovskites dans les applications de stockage de l'hydrogène.

La dernière étude a été consacrée à l'évaluation du potentiel du phosphorène en tant que nouveau matériau 2D pour le stockage de l'hydrogène. Les résultats obtenus montrent qu'en raison de la barrière de dissociation élevé (2.77 eV), ainsi que la forte physisorption

de H_2 sur le phosphorène (-292 à -277 meV) et la diffusion facile de H_2 (moins de 1 meV le long de la direction ”zigzag” et 14 meV le long de la direction ”armchair”), le phosphorène est un candidat prometteur pour le stockage de H_2 à température ambiante.

Contents

List of Figures

List of Tables

List of abbreviations

DoE	Department of Energy
CNTs	Carbon nanotubes
MOFs	Metal organic framework
TPES	Total primary energy supply
GHG	Greenhouse gas
PV	Photovoltaics
ICE	Internal combustion engine
PEM	proton exchange membrane
PEMFC	proton exchange membrane fuel cell
DMFC	Direct Methanol Fuel Cell
PAFC	Phosphoric Acid Fuel Cell
AFC	Alkaline Fuel Cell
SOFC	Solid Oxide Fuel Cell
MCFC	Molten Carbon Fuel Cell
COFs	Covalent organic frameworks
PIMs	Polymers of intrinsic micro-porosity
SWNT	Single wall structure
MWNT	Mmultiple wall structure
HCP	Hexagonal close-packed
DC	Direct current
RF	Radio frequency
UHV	Ultra-high vacuum
C_g	Gravimetric capacity
C_v	Volumetric capacity
wt.	Weight
T_{des}	Desorption Temperature
P	Equilibrium pressure
T	Temperature
R	The gas constant
E_a	Activation energy
K_β	Boltzmann constant
G	Free energy
ΔH	Heat of formation
ΔS	Entropy
E_{tot}	Energy total
DOS	Density of states
PDOS	Partial desnity of states
VB	Valence band
CB	Conduction band
TM	Transition metal
ab initio	First principal calculation
Ψ	Many-body wave function of electrons
$\hbar$	Planck's constant devised by 2π
e	Charge of the electron
m_e	Mass of the electron
M_I	Mass of the nucleus
Z_I	Charge of the nucleus
R_I	Position of the nuclei
r_i	Position of electron
T_e	Kinetic energies of the electrons
T_n	kinetic energies of the the nuclei
V_{int}	Internal potential
V_{ext}	External potential
V_{nn}	nucleus-nucleus potential
$n_H(z)$	Number of hydrogen in plan z
$n_S(z)$	Number of interstitial sites in plan z
$\rho(z)$	Density of Hydrogen in plan z
t_{eq}	Equilibrium time
t_f	Filling time
t_r	Relaxation time
V_{ee}	Electron electron potential
V_{KS}	Effective potential
$V_H(r)$	Hartree potential
$V_{xc}(r)$	Exchange-correlation potential
$\hat{H}$	Hamiltonian operator
Z	Partition function
LDA	Local density approximation
LSDA	Local Spin-Density approximation
GGA	Generalized gradient approximation
MC	Monte Carlo
MMC	Metropolis Monte Carlo
MCMC	Markov chain Monte Carlo
KMC	Kinetic Monte Carlo
ΔE	Energies difference
F	Hydrogen flux
M_{H_2}	Molecular mass of hydrogen
P_i	probability
R_i	The rate transition
R	Total rate transition
DFT	Density functional theory

Introduction

Nowadays, the increasing energy dependence is considered as one of the most issues in the modern society due to uprising population, living standards and rapid economic growth. The fossil fuels (oil, coal and natural gas) consumption and depletion of resources leads to enormous economic and environmental effects such as greenhouse gases emission, global warming, pollution and weather events etc., which threat the existence of life in the world. In this sense, developing an urgent concepts and technologies clean, practical, sustainable and safe using renewable energy has attracted attention to power vehicles. One potential solution to the intermittency problems with sustainable energy sources (solar, biomass, hydropower, wave power and wind) and non-renewable energy sources (oil, coal and natural gas) is the use of hydrogen gas (H_2) as an environmentally friendly source of energy to power fuel cells (with an energy density of 141.79 MJ/kg). However, Hydrogen storage is still one of the biggest technical challenge barriers to the broad spread commercialization of hydrogen-fueled light-duty vehicles compared with fossil fuel or hybrid vehicle markets. The United States Department of Energy (US-DOE) has set up targets for on-board hydrogen storage systems, for which an ideal hydrogen storage system must have high hydrogen gravimetric and volumetric capacities (75 g of H_2 per kg and 70 g per liter), reversible hydrogen uptake/release at around ambient conditions, fast sorption kinetics, etc.

Much effort has been made to develop hydrogen storage systems that are safe, cost-effective, environmental-friendly and more importantly with high energy densities. Current technologies used for hydrogen storage include compression in gas cylinders, liquefaction in cryogenic tanks and adsorption/absorption into solid state compounds. Compressed gas and cryogenic liquid state storage are not so suitable for practical applications due to the safety, high weight, size of the tank, evaporative losses and high maintenance and energy costs for liquefaction process (compressing and cooling). Consequently, the storage of hydrogen in solid state compounds appears to be the most

feasible solution since it is a safer and more convenient method compared to high-pressure compression and liquefaction technologies.

Generally, hydrogen storage in solid state material can be classified into two broad categories, namely physical adsorption and chemical absorption. In large surface and porous materials, the hydrogen molecules can be adsorbed on the surface and pores via physisorption through the van der Waals interactions. In metal hydrides, the hydrogen atoms are chemically bonded with metallic elements such as intermetallic hydrides, complex hydrides and elemental hydrides. These latter are potential compounds for solid-state hydrogen storage. The development of new materials with improved hydrogen storage capacities and with favorable hydrogen thermodynamics and kinetics properties remains the main focus of researchers for the last decades.

A large number of studies have been carried out to provide strategies to tackle the limitations of Mg-based hydrogen storage system. Among the most promising strategies reach that objective: reduction of size, alloying, doping/functionalization, morphology control, and engineering strain. The objective of the current study is to provide a comprehensive review of literature and industry practices in relation to energy storage systems based on perovskite hydride materials and outline their drawbacks in order to improve it, which can be divided into two aspects namely strain engineering and substitution.

For this reason, we opted for a theoretical approach, based on numerical simulation calculations, to study the hydrogen storage properties of the perovskite hydride $MgCoH_3$ and phosphorene, to understand and explain the mechanisms that operate in it. These calculations are made using the first principle method, also called ab initio calculations (DFT), to study the thermodynamic and kinetic properties. This study is organized as follows:

- The first part is devoted to the presentation of the Hydrogen Economy. It starts with a general presentation of hydrogen, as a promising energy carrier, then reviewing, different technologies and methods used for its storage. As only the solid storage is studied in this thesis, several materials for hydrogen storage are introduced and sorted by physisorption (adsorption) and chemisorption (absorption). A description of the different characteristics of those material is presented, followed by a recap of

some of the studies, reported in the literature, which tackles different approaches to improve their hydrogen storage properties.

- The second part is devoted to to introduce the theoretical frame that we use to study the hydrogen storage materials properties namely ab initio calculations based on the density functional theory. A detailled description of the code concerned with the methodology used for this study is also given in this part.

- The third part is devoted to the results and discussion the findings of the research: The chapter 3 and 4 reports the results of our investigation of the strain engineering effect and substitution by lightweight elements on the storage properties of $MgCoH_3$ within the framework of DFT. Starting with the vibrational and thermodynamic aspects, the effect on the heat of formation, desorption temperature, and gravimetric capacity were evaluated based on a detailed study of the phonon dispersion, the charge transfer, and the density of states. As for the kinetic aspect, the influence was assessed through the calculation of the activation energy. The last chapter 5 studies the potential of phosphorene as a new 2D material for molecular hydrogen storage by investing the interaction of hydrogen molecules and atoms with the surface and its impact on the diffusion behavior.

- Finally, the main conclusion gives a brief summary and criticism on our results. it includes a discussion of the impact of our findings to future research for the uses of $MgCoH_3$ and phosphorene as solid-state hydrogen storage material.

1 Literature review and analysis: Hydrogen as an energetic carrier

1.1 Introduction

Nowadays, the increasing energy dependence is considered as one of the most issues in the modern society due to uprising population, living standards and rapid economic growth [1, 2]. The fossil fuels (oil, coal and natural gas) consumption and depletion of resources leads to enormous economic and environmental effects such as greenhouse gases emission, global warming, pollution and weather events etc., which threat the existence of life in the world [3–5]. In this sense, developing an urgent concepts and technologies clean, practical, sustainable and safe using renewable energy has attracted attention to power vehicles. One potential solution to the intermittency problems with sustainable energy sources (solar, biomass, hydropower, wave power, wind and geothermal energy) and non-renewable energy sources (oil, coal and natural gas) is the use of hydrogen gas (H_2) as an environmentally friendly source of energy to power fuel cells with an energy density of $141.79 MJ/kg$ [6–12].

The development of hydrogen energy systems involves three stages: production, storage and use [13]. The methods of production and use are the subject of much research, but the Hydrogen storage is still one of the biggest technical challenge barriers to the broad spread commercialization of hydrogen-fueled light-duty vehicles [14]. This requires the search for a solution that encompasses the various fields of science and engineering in order to produce systems profitable, safe, efficient and practical [15].

This chapter deals with a bibliographic study of the hydrogen as energy vector, its characteristics and its storage. An overview is given for the differents storage methods available today with respect to the progress made recently and problems still there. We will focus specifically on hydrogen storage in the solid state and more precisely in

magnesium based hydride and 2D materials. We will describe the problems of this form of storage and solutions already proposed.

1.2 Hydrogen as a renewable energy carrier

1.2.1 History of hydrogen

Hydrogen was discovered in 1766 by Henry Cavendish and named by Lavoisier from the Greek words hydro meaning water and genes meaning generator [16],which means the element that generates water. It is the first element of the periodic table and the most abundant element in the universe, accounting for 90 percent of the universe by weight. In 1932, Harold Urey reported the discovery of a stable isotope, deuterium (^2H or D) with an atomic weight of 2, deuterium is present in natural hydrogen to the extent of 0.015% [17]. Two years later, an unstable isotope, tritium (^3H), with an atomic weight of 3 was prepared by the group of by Ernest Rutherford in 1932 [18].

1.2.2 Hydrogen properties

Hydrogen is a colorless, odorless, tasteless, and a non-poisonous gas under normal conditions on Earth. However, it is not commonly found in its pure form, since it readily combines with other elements. Hence, hydrogen is the lightest and most present element in chemical compounds: water, living matter as carbohydrates and proteins, many organic compounds, hydrocarbon, ammonia, and acids. It typically exists as a diatomic molecule, meaning each molecule has two atoms of hydrogen. this is why pure hydrogen is commonly expressed as "H_2". The Table 1.1 lists the important properties of atomic hydrogen and molecular hydrogen (H_2).

At normal conditions, hydrogen is in gaseous state. It has the second lowest boiling point and melting points of all substances. Hydrogen liquefies below 20 K at atmospheric pressure. In these conditions, the liquid is 800 times denser than the gas at ambient temperature. Gas liquefaction processes involve techniques quite complex which combine cold intake and adiabatic relaxation [19].The first liquefaction hydrogen was obtained by Claude using a cycle divided into several steps [20]. The gas is firstly cooled from the ambient to 230 K by a group mechanical refrigeration then up to 80 K using a liquid nitrogen ex-changer. Hydrogen then undergoes compression-expansion cycles which

TABLE 1.1: Atomic and Molecular Hydrogen properties

Atomic Hydrogen			
Atomic number	1	Atomic radius, non-bonded (Å)	1.10
Electron configuration	$1s^1$	Electron affinity (eV)	0.7542
Density (g cm^{-3})	0.000082	Ionisation energies (eV)	13.595
Isotopes	1H, 2H, 3H	Electronegativity (Pauling)	2.1
Molecular Hydrogen			
Bond distance (Angstrom)	0.7416	Dissociation energy (25°C, kJ mol^{-1})	435.93
Ionization potential (eV)	15.427	Density of solid (g cm^{-3})	0.08671
Density of liquid (-252.78 °C,g cm^{-3})	0.07099	Heat of combustion to water (kJ mol^{-1})	-241.82

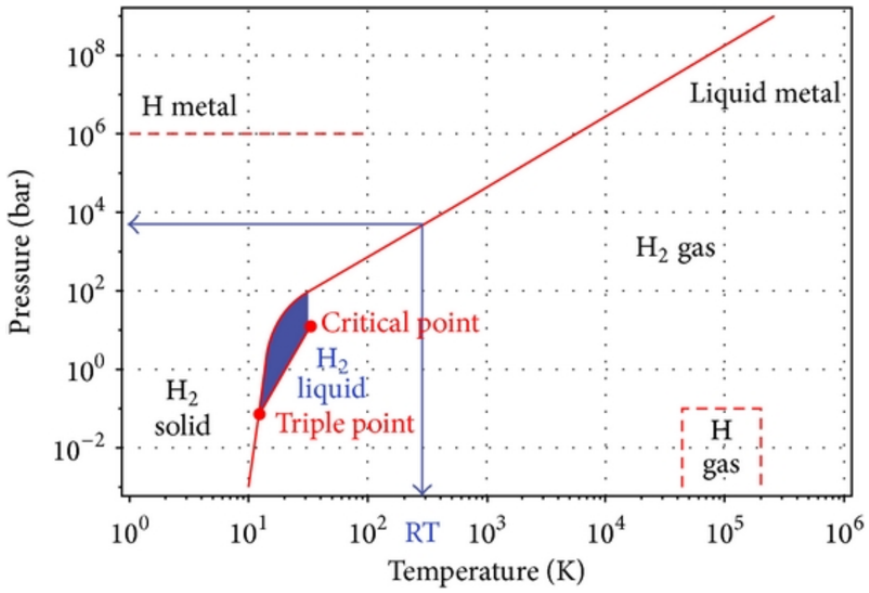

FIGURE 1.1: The primitive phase diagram of hydrogen [20]

further reduce temperature before being subjected to Joule-Thompson relaxation which leads to the liquefaction[20]. Other processes can be envisaged such as the Brayton cycle which uses the liquid helium whose liquefaction temperature is lower than that of hydrogen or Magnetometer cycle refrigeration. The hydrogen is in solid state below its melting point of -259 °C (14 K) and atmospheric pressure. The density of hydrogen at atmospheric pressure as a gas (at room temperature) is $0.09 kg.m^{-3}$, as a liquid (at -253°C) $70.8 kg.m^{-3}$ and as a solid (at -262°C) $70.6 kg.m^{-3}$. A phase diagram of hydrogen is shown in Figure 1.1, with a triple point at -259.1 °C and 0.07 bar and a critical point at -239.8 °C and 13 bars. At atmospheric pressure the boiling point (T_b) is at -253 °C and the melting point (T_m) at -259 °C. The boiling point of a fuel is a critical parameter since it defines the temperature to which it must be cooled in order to store and use it as a liquid [20].

1.2.3 Hydrogen Energy System

Today's society faces growing challenges related to the global energy demand due to increasing population and rising standards of living. Fossil fuels such as petroleum, natural gas, and coal provide more than 80% of all the energy being consumed globally [21–26]. The world energy consumption is projected to climax in 2035 while the world economy is projected to go into a long depression after 2040 [6, 26, 27] (By 2050, the energy consumption is expected to escalate to 30TW). To a great extent, major economies of the world today rely on fossil fuels. However, excessive dependence on fossil fuels has become a critical global challenge in today's economy, because they are diminishing apace [27–29]. Accordingly, fossil fuels are not expected to keep up with the increase in energy demand. Also, its reserves are getting less accessible as the easily accessible ones are consumed, and the fossil fuels prices keep increasing due to accessibility loss and political uncertainties of the countries holding world's fossil fuel supplies [30]. Along with energy and economic security issues, greenhouse gas (mainly CO_2) emissions as a result of fossil fuel utilization, and their contribution to global planet-warming, have been raising serious environmental concerns. Therefore, developing an urgent concepts and technologies clean, practical, sustainable and safe using renewable energy has attracted attention to power the vehicles. In this sense, one potential solution to the intermittency problems with sustainable energy sources (solar, biomass, hydropower, wave power and wind) and non-renewable energy sources (oil, coal and natural gas) is the use of hydrogen gas (H_2) as an environmentally friendly source of energy to power fuel cells. Hydrogen, has an even higher energy density of $142 MJ/kg$. This energy density enables a car equipped with a fuel cell and $5kg$ of H_2 to drive about $500km$, while for the same trip a normal car would require about $20kg$ ($25l$) of gasoline. It is a primary candidate for future energy application, due to its higher chemical energy when compared to other fossil fuels [30]. Table 1.2 represents the comparative energy values of different fuels. It shows that the chemical energy of hydrogen is approximately three times higher than those of petroleum fuels such as gasoline, kerosene, and diesel oil. Hydrogen can be produced in any country from numerous energy sources (e.g. Water, Algae: methods using photosynthesis, reforming fossil fuels, etc). Moreover, it can be economically competitive with traditional energies (diesel or gasoline). The use of hydrogen as an energy carrier and switch to the "hydrogen

TABLE 1.2: Chemical energy values of various fuels, adapted from [30].

Fuel	Phase	Chemical energy (MJ/kg)
Hydrogen	gas	141.79
Methane	gas	55.50
Ethane	gas	51.88
Propane	gas	50.35
Butane	gas	49.85
Ethanol	liquid	29.85
Gasoline	liquid	45.58
Kerosene	liquid	45.42
Diesel oil	liquid	45.00
oal	solid	25.58
Wood (dry)	solid	21.14
Peat (dry)	solid	22.09

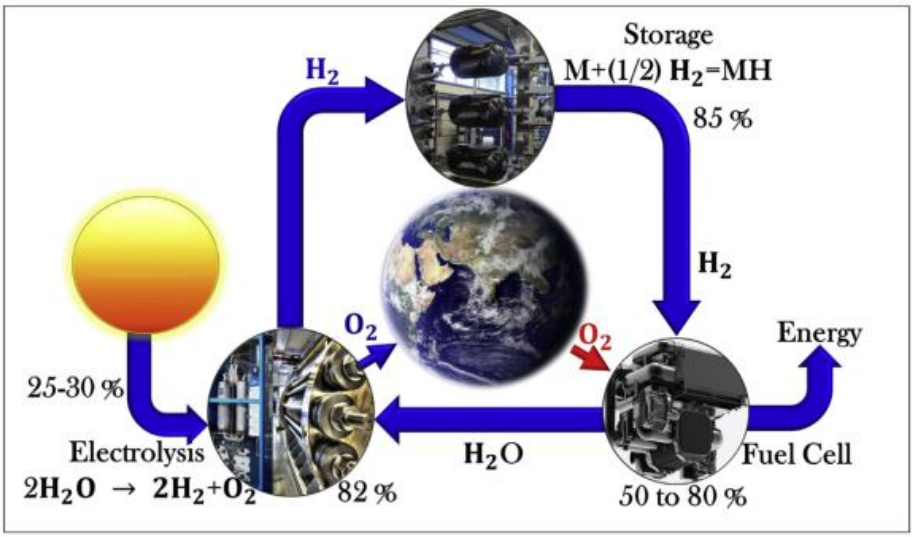

FIGURE 1.2: Solar H_2 Cycle with the typical efficiency values

economy" requires the development and use of different technologies. For this reason, H_2 can be produced from water by electrolysis using renewable energy sources such as wind, hydro, solar, and tidal energy leading to a sustainable system without any pollution [31]. Figure 1.2 provides the solar H_2-cycle along with possible efficiency in each conversion step. In fact, the H_2 economy could also lead to a distributed generation. Green H_2 can be produced wherever there is access to electricity from renewable energy systems, ultimately leading to energy security. However, for broader and more conventional usage of hydrogen energy, a few limitations and hurdles in its generation, transportation, distribution, and storage need to be successfully overcome [32, 33].

1.3 Hydrogen storage

1.3.1 Hydrogen storage issues and US-DOE criteria/targets

Whether for vehicular on-board storage or stationary bulk storage, the storage of hydrogen in high density has been the major challenge due to hydrogen's low volumetric density and its resulting high cost. Hence, hydrogen storage basically implies the reduction of the enormous volume of the hydrogen gas [34].The issues that challenge the application of hydrogen vehicle imply to find a storage method or material that satisfies the following requirements [35]:

- High gravimetric and volumetric storage capacities, which will determine the amount of energy available.
- Reversibility of the release/charge cycle at moderate temperatures in $70 - 100°C$ range to be compatible with the present generation of fuel cells.
- Fast release/charge kinetics with minimum energy barriers to hydrogen release and recharge.

To satisfy the requirements mentioned above, the materials should feature [36–41]:

- A strong enough interaction between the hydrogen and the storage material.
- A relatively weak interaction between hydrogen and the storage material in an applicable temperature.
- The reversibility for the facile release/recharge processes.
- High safety under operating conditions and public acceptance

The U.S. Department of Energy (US-DOE) hydrogen storage system targets facilitates guide researchers by shaping system necessities to realize commercially hydrogen storage [42]. The table 1.3 summarizes the US-DOE performance targets concerning the on-board hydrogen storage systems in light-duty fuel cell vehicles which beginning from 2020 [43]. The main target is the design of a light-weight storage system ($5 - 13kg$) that could enable a conventional driving range of $500km$ (or $\sim$300 miles). Regarding that the on-board hydrogen storage systems should achieve a target of 6.5wt% ($2.2kWh/kg$) for gravimetric capacity and a $0.050kg.H_2/L$ target ($1.7kWh/L$), at a cost of $\$266/kgH_2$ stored

($8/kWh$). The research and development of hydrogen storage technologies mainly focus on achieving the requirements to lower the cost and to increase both the gravimetric and volumetric storage capacity as well as efficiency. Hydrogen could be stored in

TABLE 1.3: Overview of some selected parts of the *US-DOE* technical system goals for on-board hydrogen storage for light-duty fuel cell vehicles, (data adapted from [44].

Storage parameter	Unit	2020	2025	Ultimate
Storage capacities				
System-based gravimetric capacity	kgH_2/kg system	0.045	0.055	0.065
System-based volumetric capacity	kgH_2/l system	0.030	0.040	0.050
Storage system cost	$\$/kWh$ net	10	9	8
(and fuel cost)	$\$/kgH_2$	333	300	266
Durability/Operability				
Min/Max delivery temperature	$^{\circ}C$	-40/85	-40/85	-40/85
Cycle life (1/4 tank to full)	cycles	1500	1500	1500
Min. delivery pressure from tank	bar	5	5	5
Max delivery pressure from tank	bar	12	12	12
Charging/Discharging rates	min	3-5	3-5	3-5
System fill time (for $4-10kg$)				
Fuel purity (H_2 from storage)	$\%H_2$	Meet or exceed applicable standards		

multiple ways, though with their identified strengths and weaknesses. There are two types of hydrogen storage methods available depending on the size of storage and area of application namely conventional methods (or physical storage), to store hydrogen involve compression of gas and liquefaction, and solid-state materials where hydrogen is absorbed or adsorbed on these materials (Figure 1.3). In next sections, an overview is given for the storage methods available today with respect to the progress made recently and the problems that encounter.

1.3.2 Conventional or Physical storage methods

High-pressure Storage

The most common and simple method of H_2 storage is in its natural form. Worldwide, the prevalent refueling stations adopt the gaseous storage under high pressure, which finds application in stationary, vehicular and bulk transportation [45]. The main effect of gas compression is to increase its density. Indeed, because of the very low density of hydrogen ($0.089kg/m^3$) its storage requires high pressure between $35MPa$ and $70MPa$ [34, 38]. Compressed hydrogen is a highly efficient methodology for hydrogen storage ($\sim 30-40g/l$) and the energy density considering volumetric increase with the pressure

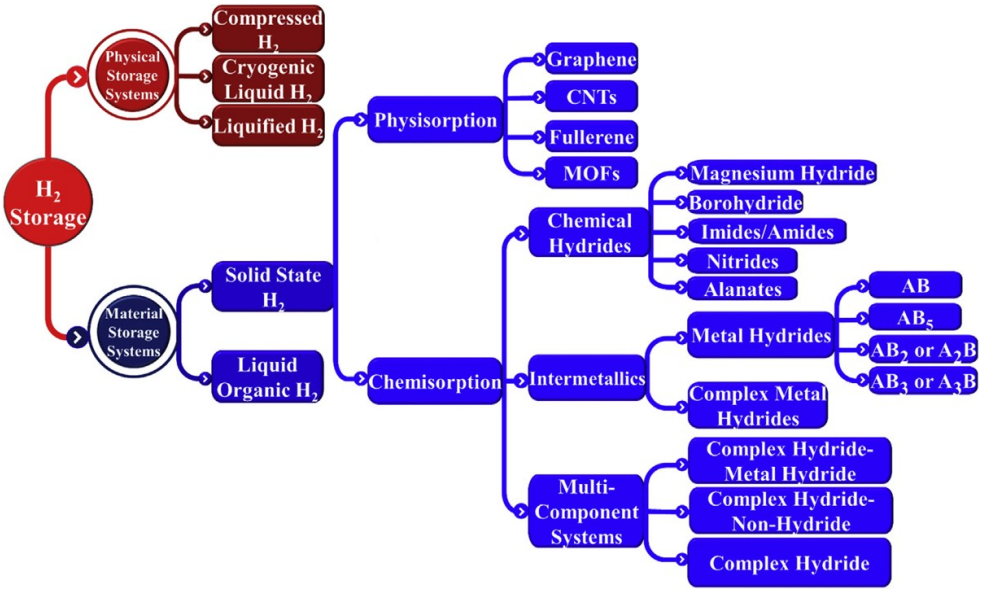

FIGURE 1.3: Classification of H_2 storage methods and materials

increase of the gas. However, between 11 and 13% of the hydrogen energy content is affected negatively by pressurizing as well as there are possibility that under high-pressure hydrogen leakage from containing vessels may ensue due to its extreme lightness [44]. High-pressure hydrogen storage requires special tanks, which can both withstand hyperbaric conditions and prevent metal embrittlement by the hydrogen molecules. To this end, four different types of high-pressure tanks are currently used (Figure 1.4) [46–49]:

- Type I metallic pressure vessel is mostly use for industrial applications with pressure of $20-30MPa$. This type has a limitation in storage efficiency, it can only able to store about $1wt.\%$ of H_2.
- Type II (pressure not limited) tank containing a metal envelope for mechanical strength, fretted by continuous fibers impregnated with resin.
- Type III (for P<45MPa) reservoir consisting of a metal shell to contain hydrogen and a continuous resin impregnated fiber envelope for mechanical holding.
- Type IV (For P<100MPa) reservoir consisting of a non-metallic envelope to contain the hydrogen and a continuous resin impregnated fiber envelope for mechanical latency.

For each type of tank, the choice of the envelope (liner) in contact with the hydrogen is of prime importance. Steel and aluminium materials are used for the traditional type

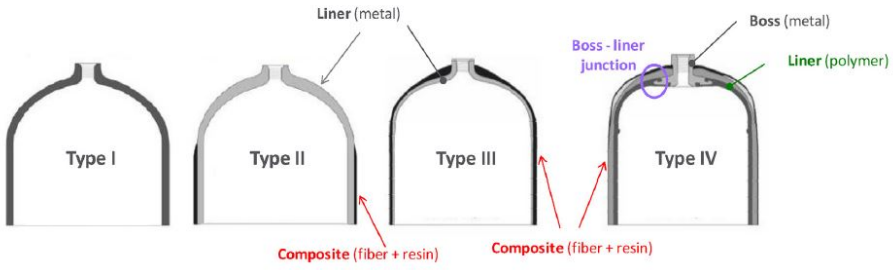

FIGURE 1.4: Different types of hydrogen compressed tank

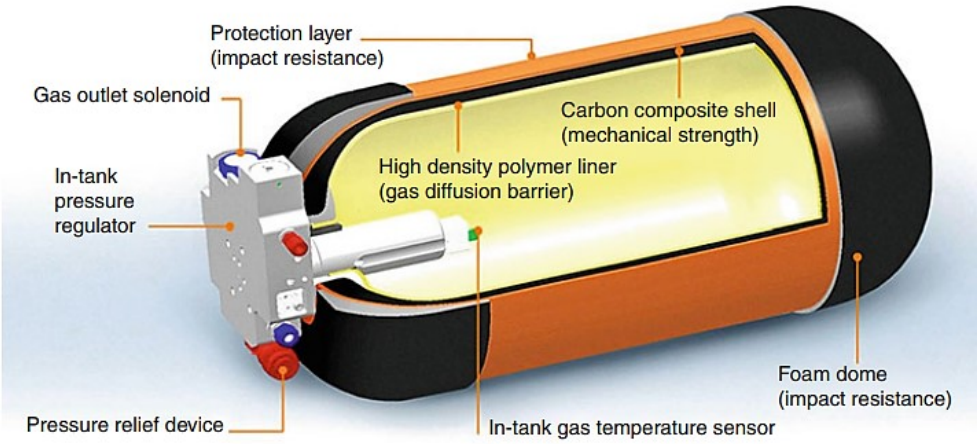

FIGURE 1.5: Type IV compressed gaseous hydrogen storage tank.

of storage vessels for commercial hydrogen. However, carbon fiber reinforced plastic composite vessel with adequate strength and impact resistance for safety during collisions, is a lighter solution but too expensive and generates another problem for future cost reduction in contrast to steel or aluminum vessels. Type IV tanks (see Figure 1.5) are the most widely used to store hydrogen at very high pressure, as they ensure the best performance. These tanks are made of carbon fiber, which reduces the weight of the storage system.Furthermore, a polymer inner lining prevents leakages. The cost of a type IV tank is around 14.75\$/kWh when considering a manufacturing rate of 500,000 tanks per year. On the contrary, types I and II are metal tanks and their use on-board is therefore difficult to envisage due to their high weight. Finally, type III tanks are made of composite materials, with an inner lining of aluminum, which makes them heavier than type IV tanks.Today, the majority of car manufacturers have chosen the high-pressure gas storage solution. This technology makes it possible to store the quantity of hydrogen necessary for a car powered by a fuel cell to travel 500 to 600km between each refueling. It is certainly the simplest storage method and it requires no special equipment to recover the gas.

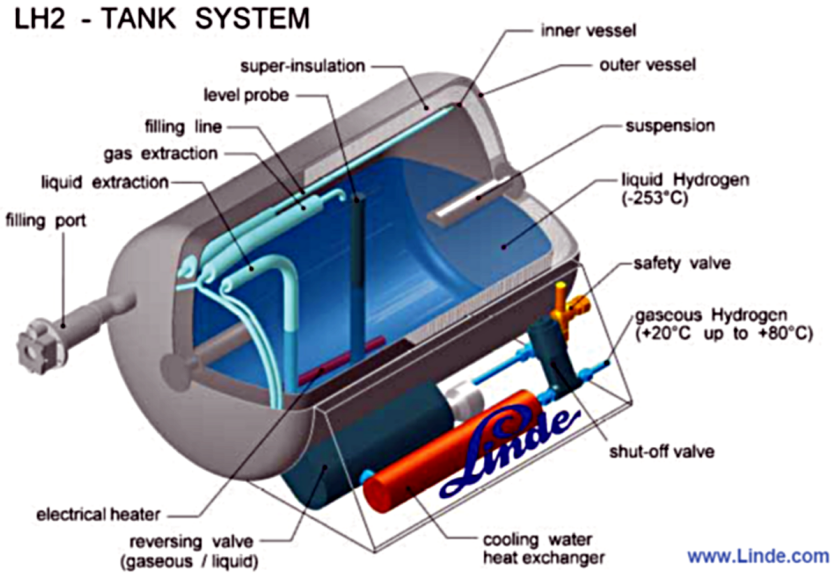

FIGURE 1.6: Cryogenic tank (or cryostat) developed by linde

Cryogenic storage

Another advanced method and technology of physical storage of hydrogen as possible in a small volume is by liquefying of the hydrogen at $-253°C(20K)$.Compared to compressed hydrogen, liquid hydrogen has a higher energy density. Liquid hydrogen has a density of about $71g/l$ at its normal boiling point of $20K$, which is approximately 1.8 times the density of hydrogen pressurized up to $70MPa$ at $288K$ ($42g/l$).The most important issues associated with liquefaction are the non-viable requirements of the process in terms of energy, time and cost. More specifically,the cooling technology of H_2 requires very low temperatures which consume about 40% of its total energy content [50, 51]. Another major issue refers to potential losses due to evaporation of H_2 as a result of temperature and pressure variations in the tank, usually described as *boil-off* mechanism. To prevent and reduce these losses, special double-walled vessels furnished with good insulation systems are essential to mitigate heat leakage (Figure 1.6).This form of storage is used for very specific applications of very high technologies such as space propulsion. For example, the "Ariane rocket" tanks designed and manufactured by "Air Liquide" contains 28 tons of liquid hydrogen used to power its central engine [12, 22, 50, 52, 53].

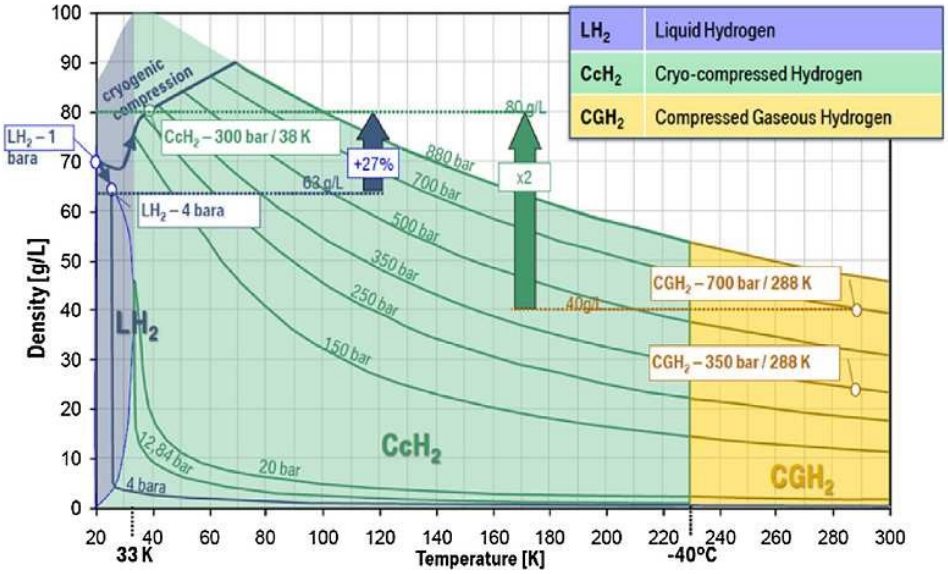

FIGURE 1.7: Temperature versus hydrogen density curve for compressed hydrogen, liquid hydrogen and cryo-compressed hydrogen; respectively

Cryo-compressed storage

The hybrid technologies; *cryo-compressed* storage method [54] consists on combining both properties of compressed gaseous hydrogen and cryogenic hydrogen systems to increase the amount of hydrogen that can be stored by volume and avoid the energy cost linked to the liquefaction of hydrogen. The cryo-compressed tank system would be used to store hydrogen at low temperatures of 80K and pressures between 200 and 400bar as presented in Figure 1.7 [55]. More compact and lighter cryogenic pressure vessels, therefore, provide better safety advantages than compressed hydrogen vessels. However, the persistent boil-off of hydrogen and too much energy required for liquefaction restrict the potential use of liquid hydrogen storage systems to applications that require high energy density as well as uses where hydrogen cost does not matter, and its consumption is within a short time, examples include air and space and automotive applications [52, 56, 57].

1.3.3 Solid hydrogen storage

In view of a hydrogen economy, storage systems need to be very safe, efficient, economical, light and compact.as mentioned earlier, the conventional pressurized hydrogen gas and cryogenic liquid hydrogen require a lot of space, bulky storage system and have safety issues plus high cost.Therefore, they fail to satisfy the future goals of a hydrogen economy [7, 30, 58, 59]. it is obvious that hydrogen storage needs a more technical breakthrough, probably in the most feasible option in contrast to pressurized hydrogen gas and cryogenic liquid Hydrogen. Specifically, for a fuel cell vehicle, storage of enough hydrogen onboard is a major hurdle to cross [34, 60–62]. To achieve the goals of high gravimetric and volumetric capacity, much attention is currently being given to storing hydrogen in solid-state materials. A solid storage material that satisfied the US-DOE target capacities (see Table 1.3) and has favorable hydrogen uptake–release characteristics within the functional temperature window of PEM fuel cells would be ideal [63]. Storage of hydrogen in the solid state is divided into two categories depending on the nature of bonding between the solid and hydrogen which is stored either by physisorption (adsorption) or chemisorption(absorption) [30, 58, 59]. Most of these storage methods are still in development, and a numerous academic researchers have addressed this question.

Physisorption

Physisorption or physical adsorption is the mechanism by which hydrogen is stored in the molecular form, that is, without dissociating, on the surface of a solid material through the van der Waals interactions (binding energy: 10-100 meV) [64]. The physical adsorption and release of H_2 is perfectly reversible and characterized by fast kinetics due to the weak nature of interactions between the solid surface of the molecular H_2 gas.This adsorption increases with the pressure of the gas and the more important that the temperature is lower and the interaction surface with the solid is greater. Although the reversibility and fast kinetics make these materials nice-looking options, low hydrogen storage capacity at ambient conditions and the requirement of extremely low temperatures for high hydrogen storage capacity place appalling constraints on the use of these materials as it touches on the practical application. Large surface area and porous materials being investigated for hydrogen storage such as carbon-based materials (activated carbons,

carbon nanotubes, nano-fibers, fullerenes, graphene, and graphene oxides, carbons from templates, etc.), zeolites, metal-organic frameworks (MOFs), covalent-organic frameworks (COFs), porous-polymers, aerogels, and boron-nitride materials [6, 65–72].

Chemisorption

In chemisorption, hydrogen molecules are split into atoms and integrated with the chemical structure of the material to form hydrides (metallic, intermetallic, complex and chemical hydrides) [73]. By suitable control of the thermodynamic conditions of gas pressure and temperature within the reservoir, it is possible to manage respectively the absorption and desorption of hydrogen. Lowering the cost, weight, and operating temperature,enhancing the charge-discharge kinetics and controlling formation of unwanted gases during desorption are the main remaining challenges facing the chemical sorption materials.
In the next sections a brief description will be given for some current based materials suitable for hydrogen storage in solid-state.

1.4 The current state of based materials for hydrogen storage

1.4.1 Metal hydride

The storage of hydrogen is intended to achieve high volumetric and gravimetric densities of hydrogen. Therefore, compared to other storage methods, storage in materials known as hydrides offers the possibility to meet the requirements for on-board storage. In metal hydride tank, hydrogen molecules bond into metal under moderate temperature and pressure, usually between 3 and 30 atm, much lower than compressed gas tanks. This makes the system safer than any other solutions since hydrogen gas leakage cannot be spontaneous or the containing tank blow up by itself [38, 40, 74]. Also, in these materials, hydrogen can be stored both reversibly and irreversibly. Reversible storage means that the host material possesses the ability to absorb hydrogen and release it later, either at room temperature or through the control of temperature and hydrogen pressure. The relative strength of the interaction of hydrogen with a storage material greatly influences the kinetics and thermodynamics of the hydrogen uptake and release. Therefore it affects the overall manner in which a hydrogen storage material will be used in a real

application. The life of a storage material is directly related to the purity of the hydrogen it is storing. Since it acts as a sponge, which absorbs hydrogen, it also absorbs any impurities introduced with it. As a result, the hydrogen released is extremely pure, but the material's lifetime and ability to store hydrogen are reduced as the impurities left behind, fill the spaces that the hydrogen once occupied.

According to authors of many works [40, 75, 76], metal hydrides are produced by the interaction of hydrogen with different metals, either pure or alloy (in granular form or particles) resulting in solid-state storage under moderate temperature and pressure which gives them the crucial safety advantage above conventional storage systems. A key contributing factor to a wide usage of metal hydrides in the field of hydrogen storage is their huge capacity to accommodate a significant amount of hydrogen in their structures [76–78]. It is possible to pack more atoms of hydrogen into a metal that forms a hydride lattice than into the same volume of liquid hydrogen.

The hydriding and dehydriding process

A metal hydride is technically formed via a chemical reaction but acts like a physical storage method. When host materials are brought in contact with gaseous hydrogen, they have the characteristic of reacting spontaneously with it, acting similar to a sponge soaking up water, forming, therefore, hydride compounds. Depending on the thermodynamics of the reaction, different temperatures apply to different metal hydrides. A typical reversible interaction between metal/alloy and hydrogen can be written as:

$$M + \frac{x}{2} H_2 \longleftrightarrow MH_x + Q \tag{1.1}$$

where M is a metal, an intermetallic alloy, or a solid solution; x is the number of hydrogen, MH_x is the formed hydride and Q is the heat generated by the exothermic reaction. A simplified model of hydrogen storage in a metal hydride is given in Figure 1.8. The hydrogen absorption mechanism can described by a direct combination of the intemetallic compound and hydrogen, according to the following steps:

(a) Transport and adsorption of the hydrogen molecule on the material surface (physisorption).

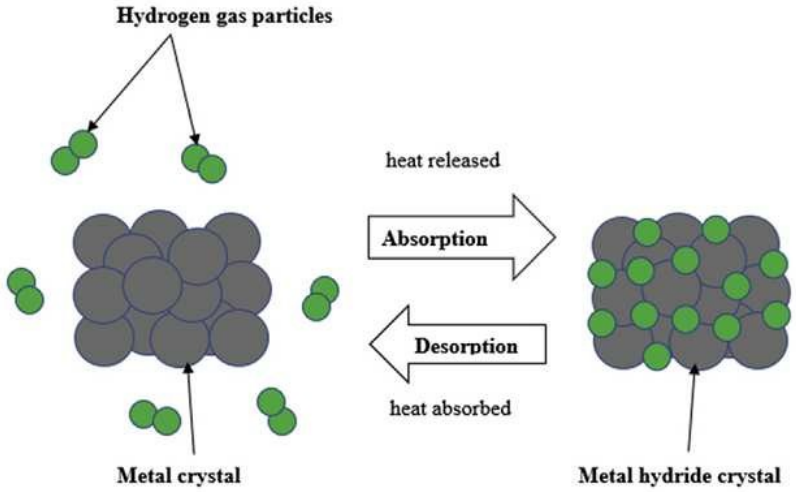

FIGURE 1.8: A simplified model of a metal hydride hydrogen storage

(b) Chemisorption and dissociation of hydrogen molecules into atoms, When the hydrogen pressure is sufficient, the penetration of hydrogen atoms into the solid structure followed by the diffusion of hydrogen from surface sites to deep sites and formation of the solid solution (noted phase α).

(c) Diffusion of hydrogen atoms inside the crystal lattice until saturation and formation of the hydride phase (noted phase β). Subsequently, this phase grows with the addition of hydrogen.

These different stages can be treated as successive or simultaneous. Regarding of the desorption process, it can be described simply as the reverse of the mechanism of absorption which has just been described. The absorption and desorption processes are continuously repeatable, and reversible metal hydrides can, therefore, be used for the storage of heat and hydrogen. Charging and discharging of the hydride tank can be performed as many times as possible in as much as the hydride material does not become contaminated [79, 80].

Pressure-composition-temperature isotherms (PCT)

The conditions of thermodynamic equilibrium between a metal and its hydride depend on the temperature, the pressure and the hydrogen composition of the system. At a given temperature, these equilibrium conditions can be plotted in a Pressure-Composition diagram (see Figure 1.9).The isothermal curve shows three regions: The solid solution

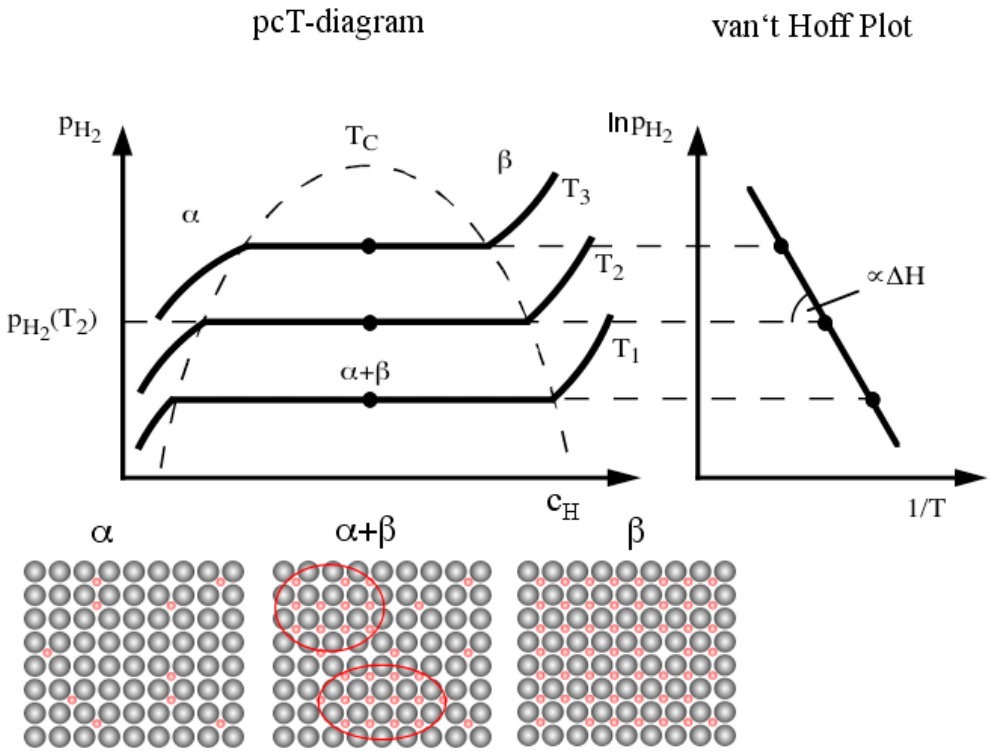

FIGURE 1.9: P-C-T diagram and Van't Hoff plot: α– solid solution of hydrogen in α-phase; β–hydride; α+ β two-phase [82]

(α-phase), the hydride phase (β-phase), and the region of the coexistence of the two phases (α/β/phase). At low hydrogen pressure a solid solution is formed, the α phase, whose equilibrium pressure increases with the rate of hydriding. When the saturation rate of the α phase is reached, a structural transition leads to the formation of a hydride of defined composition, the β phase. This transition takes place at constant pressure: there is coexistence of the α and β phases on an equilibrium plateau. Beyond this, the increase in pressure leads to saturation of the β phase, which is the preferred phase for the storage of hydrogen [81]. The plate pressure increases with temperature. Determining the equilibrium pressure as a function of temperature makes it possible to represent in a Pressure-Temperature diagram the absorption and desorption domains (Figure 1.9). Using Van't Hoff's law which describes the relationship between temperature (T) and free reaction enthalpy (ΔH), the enthalpy and standard reaction entropy (ΔS) are then calculated, the values of which are characteristic of the stability of hydride (see Equation 1.2).

$$\ln P_{eq} = \frac{\Delta H}{R.T} - \frac{\Delta S}{R} \tag{1.2}$$

Hydrogen is chemically bonded in the metal hydrides. These bonds are much stronger than the physical bonds concerned within the adsorption of hydrogen. Consequently, additional energy is required to release the chemicals bonded hydrogen. On the opposite hand, the stronger bonding permits hydrogen to be stored at high density even at ambient conditions.

The different types of metal hydrides

Prabhukhot et *al.* [44] and Ozturk and Demirbas [80] reported that both the thermodynamic and kinetic conditions are the essential requirement that must be met for hydrogen storage to occur. There are various reaction steps that kinetically may prevent a hydrogen-storing system to reach its thermodynamic equilibrium of hydrogen storage within a reasonable time. The reaction rate of a metal-hydrogen system is, therefore, a function of pressure and temperature. Hydrogen storage in metal hydrides comprises a few mechanistic steps and depends on some parameters. Essentially, the surface of the metal must be able to dissociate the hydrogen molecule and permit easy mobility of hydrogen atoms to be able to store hydrogen. Different metals have different abilities to dissociate hydrogen depending on their surface structures, morphologies, and purities. According to David [53], Lai et *al.* [83] and Khafidz et *al.* [84], metal hydrides can be categorized into low-temperature hydrides and high-temperature hydrides based on the temperature of absorption/desorption of hydrogen. Hydrogen is bound via covalent bonding in the low-temperature hydrides, and the metal hydride consists of high molecular weight material which exhibits fast kinetics and low hydrogen equilibrium pressures because of their low heat of reaction. These metal hydrides are mostly intermetallic alloy or solid solution hydrides operating at ambient to moderate temperatures. Whereas on the other hand, hydrogen is usually ionically bound in the high-temperature hydrides, and the metal hydride consists of low molecular weight material. Although the high temperature restricts the choice of high-temperature hydrides, they have been found to possess relatively higher hydrogen storage capacities than the low-temperature hydrides. Metal hydrides appear to be the safest method of storing hydrogen since metal hydrides can be operated at relatively low temperatures and pressures typical of fuel cell vehicles and the release of hydrogen from metal hydrides is an endothermic process [85]. Hydrogen can be released from metal hydrides either by an increase in

temperature rise or a decrease in external pressure [86]. However, there are a number of issues associated with hydrogen storage in metal hydrides, i.e. slow reaction kinetics, low reversibility and high dehydrogenation temperatures [87]. Nowadays, research is still ongoing to synthesize metal hydrides which will fulfill the targets for hydrogen storage systems set by the *US-DoE* for on-board vehicular applications. At present, the main alloying materials for metal hydrides are:

- Intermetallic compounds (AB_5, AB_2, AB, and A_2B), which has a hydrogen storage capacity of 1.5, 2.0, 1.8 and 3.0$wt.\%$, respectively [26]. Solid solution alloys are also available such as vanadium-based solid solution alloys and Mg-based alloys, which have a hydrogen storage capacity of approximately 2 and 5$wt.\%$ respectively [26, 53, 83, 88–93].

- Metallic hydrides (also called element hydrides or metal hydrides) composed of lightweight elements such lithium (Li), boron (B), nitrogen (N), magnesium (Mg) and aluminium (Al) have shown great potential for use as hydrogen storage materials [94].

- Complex hydrides which are the only group of metal hydrides having high volumetric and gravimetric hydrogen storage densities [95–97].

Some features of these metal hydrides will be given in next sections.

Intermetallic compounds

Hydrogen can be chemisorbed on metals and intermetallic alloys with varying degrees of storage capacity. Alloys of the type AB_5, AB_2, AB, and A_2B are promising candidates, where A represents elements with high affinity for hydrogen typically rare-earth or alkaline-earth metal (e.g., Ca, Ti, Y, Zr, Hf, La, Ce, etc.) and B represents elements with low affinity for hydrogen typically a transition metal (e.g., Cr, Mn, Fe, Co, Ni). The resultant hydrides are called intermetallic hydrides and their common formula is $A_mB_nH_x$. It has been shown that AB_5, AB_2, and A_2B type alloys have excellent hydrogen absorbing properties [98–100]. The properties of some of the most common intermetallic hydrides are summarized in Table 1.4.

The volume capacities of the intermetallic compounds make solid-state hydrogen storage

TABLE 1.4: Properties of some of the most common intermetallic metal hydrides [26]

Intermetallic compound	Intermetallic hydride	Hydrogen storage capacity (wt.%)	Temperature at 1 bar ($^{\circ}K$)
$LaNi_5$	$LaNi_5H_6$	1.37	295
$FeTi$	$FeTiH_2$	1.89	185
Mg_2Ni	Mg_2NiH_4	3.59	550
$ZrMn_2$	$ZrMn_2H_2$	1.77	440

mode very competitive compared to the gaseous and liquid modes. On the other hand, the metallic matrix weighs considerably in the low gravimetric performances. The AB_5 category represented by the $LaNi_5$ alloy have the ability to absorb hydrogen already within the room temperature, however, the stored content is only 1.37% by weight. Another cluster are AB and AB_2 type materials, associate example of which might be FeTi, that has the capacity of 1.89 wt.% [101]. The materials of this group have good thermodynamic properties, however the flaw of these categories is that the activation of the hydrogenation itself is difficult. Therefore, the materials need to be subjected to initial cycles of absorption and decomposition in high temperatures and under high vacuum [102–105]. Following generations are A_2B type alloys, eg. Mg_2Ni, which have disadvantages like high temperature of the absorption and desorption process and slow reaction dynamics, however, they need good hydrogen storage capacities of about 3.6% by mass. They have comparatively low weight and relatively expensive [101, 106]. The use of intermetallic hydrides is rather limited for on-board vehicular applications since intermetallic hydrides have low hydrogen storage capacities by weight, slow kinetics, and complicated activation procedure. Thus, much effort has been made to optimize the composition, morphology and size distribution of the metal hydride particles, modify the hydride particles surface and optimize the surface oxides via various synthesis routes in order to achieve a good compromise between degradation, kinetics and hydrogen storage capacity of the intermetallic hydrides [57]. Based on the chemical formula $A_mB_nH_x$, the partial substitution of A, B or both will alter the hydrogenation kinetics and equilibrium pressure of the metal hydride without affecting its hydrogen storage capacity [99, 107].

Complex hydrides

The main disadvantage of conventional metal hydrides such as intermetallic hydrides is their low gravimetric hydrogen storage capacities [108]. Complex hydrides are rich in hydrogen and can be classified into two families: complex hydrides of transition metals ($BaReH_9$ and Mg_2FeH_6...) and complex hydrides of metals other than transition metals (such as alanates, borohydrides, and amide: $LiAlH_4$, $NaBH_4$, and $LiNH_2$) [109–113]. Complex hydrides with light elements such as lithium (Li), boron (B) and sodium (Na) emerge as potential candidates for hydrogen storage applications due to their high hydrogen storage capacities (up to $18 wt.\% H_2$ for $LiBH_4$), high hydrogen storage densities, as well as mild dehydrogenation pressures and temperatures [114]. The gravimetric storage capacity and dehydrogenation temperatures for some selected complex hydrides are shown in Table 1.5. Unlike intermetallic hydrides, hydrogen is released via cascade

TABLE 1.5: Dehydrogenation temperature and gravimetric storage capacities of complex hydrides [63, 115–120]

Complex compound	**Heat of formation (kJ/mol)**	**Desorption temperature($^\circ C$)**	**Gravimetry (wt.%)**	**Hydrogen density (kg/m^3)**
$LiBH_4$	-194	380	18.4	121
$NaBH_4$	-191	400	10.6	114.5
KBH_4	-229	500	7.4	87.8
$LiAlH_4$	-2	125	9.5	-
$NaAlH_4$	37	210	7.4	-
$KAlH_4$	-	270	5.7	-
$Mg(AlH_4)_2$	-18	140-200	9.3	-
$Ca(BH_2)_2$	-	320	11.5	124.1

decompositions with highly stable elements and each step reactions call for different conditions, which are very challenging to refuel with hydrogen on-board a motor vehicle. Therefore, there is a large difference between the theoretical and the practically attainable hydrogen capacities. Even though complex hydrides possess interesting gravimetric storage capacities, Kinetic and thermodynamic limitations are their major drawbacks, as they expose high stability due to their iono-covalent character which makes it difficult to release hydrogen under ambient conditions (particularly for the first family). Moreover, the reversibility of these hydrides is very poor.

However, these problems can be compensated to a certain extent by thermodynamic destabilization, which involves the addition of a new element into the system by

means of cation or anion substitution, or the addition of reactive hydride composites. Nanoconfinement or the addition of catalysts can also be used for thermodynamic destabilization[121–123].

1.4.2 Recent developments in improving hydrogen storage in metal hydrides

To improve the kinetic properties of metal-based materials with considerable hydrogen storage capacities without increasing the temperature, great efforts and numerous approaches have been attempted, including the use of nanostructured particles, the use of alloys, catalyst/additive deposition and the use of thin films [124–126]. The results obtained from each effort resulted in improvements to the thermodynamic and kinetic properties, enabling researchers to study various types of materials and techniques to achieve the goals of the target hydrogen storage system in the future. In the subsequent sections, we explain some of these approaches.

Nanostructuring using ball-milling technique

The surface properties of the metal are an essential factor for the absorption as they control the dissociation of the hydrogen molecules. At first, diffusion is not considered as the limiting step because the material has not yet reacted and there are enough active sites available. On the other hand, in the case of pure magnesium, chemisorption is the slowest step. When the reaction progresses, the diffusion of hydrogen begins and the hydride layer develops forming a more or less impermeable envelope. The diffusion of hydrogen through this layer then becomes the limiting step in the hydride formation process [127]. Exposure to oxygen also reduces absorption rates through the formation of MgO at the surface (very stable and very impermeable) [128]. Andreasen et al. [129] suggested that there is an increase in activation energies in the presence of this oxide layer which inhibits the diffusion of hydrogen.

Nanostructuring using ball-milling technique appears to be a possible solution for enhancing the hydrogenation and dehydrogenation kinetics of metal-based materials [130]. These kinetics are affected by the size of the metal hydride particles. Previous studies have reported [131, 132] that reducing the particle size to the nanoscale accelerates the reaction kinetics by increasing the surface area to volume ratio, thereby providing more nucleation sites for hydrogen sorption, promoting a rapid diffusion rate and decreasing

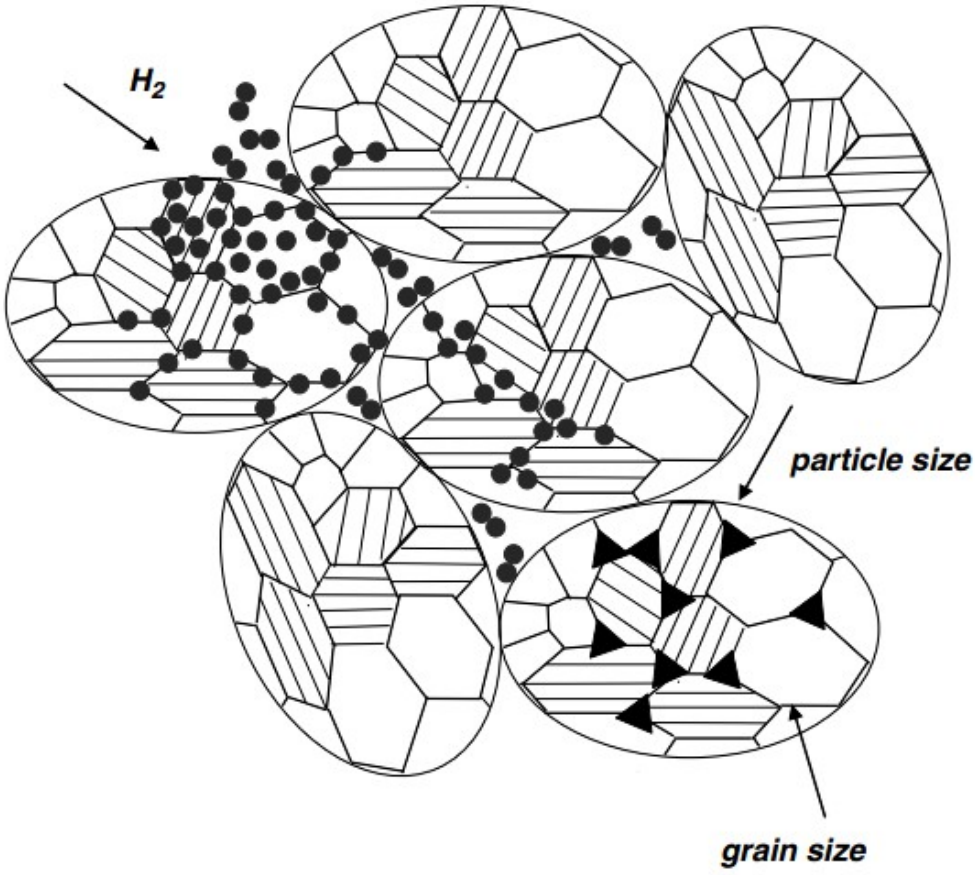

FIGURE 1.10: Particle size and grain size in a nanostructured powder

the hydrogen diffusion path length [131]. In addition, nanoscale materials offer the possibility of controlling material parameters more independently than in their bulk counterparts. Srinivasan and Sharma [133] reported that if the particle size is less than 30 nm, then the absorption of hydrogen could occur continuously. Ball milling is the most popular method used in the synthesis of materials from the micrometer to nanometer scale because of its economic price, ease of handling and simple preparation technique with low restrictions with the expectation of developing hydride storage properties [134]. Any materials exposed to ball milling can achieve a smaller grain size, wider grain boundaries, new structural features, a high surface area and grain defects [134]. If hydrogen diffuses rapidly through the grain boundary, then a new and smaller grain size with higher defect densities will improve the rates of hydrogen absorption and desorption (see Figure 1.10) [135–137].

Catalysis and alloying with other elements

Catalysis is the process of enhancing the sorption kinetics of hydrogen of metal hydride systems that facilitates dissociation of hydrogen molecules or recombination of hydrogen atoms rapidly and effectively. Common catalysts employed to improve hydriding/dehydriding kinetics of metals/alloys include various transition metals (e.g. Ti, V, Ni, Pd, Pt, Ru, Rh), metal oxides (e.g. Nb_2O_5, Cr_2O_3, Fe_3O_4, TiO_2), non-metals (e.g. carbon) and compounds [30, 59, 88, 138–140]. The catalytic effects have attracted a substantial amount of attention for improving the kinetics of metal-based materials and have exhibited a positive effect on the kinetic properties. Zaluski et al. [141] have also reported on the hydrogen molecules have a strong affinity for nickel and readily dissociate and adsorb onto surface-layer nickel clusters [142, 143]. Through the addition of 1% of nickel to magnesium, Holtz and Imam [144] achieved a 50% increase in hydrogen capacity, a decrease in the temperature for the onset of hydrogenation from 275 to 175°C, and a lowering of the dehydrogenation onset temperature from 350 to 275°C. Vanadium also acts as a catalyst for the dissociation of hydrogen molecules. It was also reported using V as a catalyst, hydrogen capacity can be increased up to 5.8wt.%H_2 while the thermodynamic parameters of MgH_2 were not altered. Titanium and vanadium block the oxidation of the alloy surface, and therefore, increase the discharge capacity over multiple cycles [145]. A nano-crystalline $Mg_{1.9}Ti_{0.1}Ni$ alloy shows good absorption kinetics at room temperature [146]. Fuurthermore, Huot et al. [147] showed that milling MgH_2 with 5 wt% of Ti, V, Mn, Fe, or Nb leads to a material that can desorb hydrogen within few minutes at 250°C and absorb hydrogen at room temperature. The high absorption rates observed are due to the appearance of grain boundaries and the porous structure of the material [148]. Interestingly, MgH_2 with 5wt%ZrO_2 exhibited a lower activation energy for the hydrogenation reaction. Notably, this composite had a hydrogen storage capacity of 6.73wt.%H_2 at 423K within 100s and still absorbed 4.0wt.%H_2 under room conditions (298K).

Thin films

An alternative method for improving the kinetic reactions of metal-based materials in hydride form is the use of thin films. Thin films provide an opportunity to create novel

structures because the hydrogen sorption is a surface phenomenon rather than a bulk phenomenon. The surface phenomenon of thin films offers a large surface area that allows for fast hydrogen absorption and desorption. For instance, research carried out on thin films of pure magnesium has made it possible to conclude that the thinner the magnesium sheet, the faster, the complete formation of MgH_2 will be reached. Tan et al. [149] synthesized the 4wt%Fe-doped Mg thin film on Al_2O_3 and Si substrate by an e-beam evaporation technique. They have found that the ΔH and ΔS of the Mg system, together with its thermodynamic stability, significantly decreased when using Fe-doped Mg film. The reported ΔH of the Mg film for hydrogen absorption and desorption is 42.7 ± 3.2 and 66.9 ± 4.1 kJ/mol, respectively [149]. In brief, these reported studies show that the ΔH of hydrogen absorption and desorption of $3D$ bulk Mg/MgH_2 are 73.9 ± 0.7 and 77.7 ± 0.8 kJ/mol, respectively [150], and are considerably higher than those of the as-prepared 2D nano-structured Mg/MgH_2 film. In the same way, the isothermal hydrogen absorption kinetics of Mg-based thin film is 56 ± 3 kJ/mol. The dimensional changes on Mg films have essentially improved the sorption kinetics and thermodynamic changes in Mg due to the thickness and surface properties of 2D nano-structured film [44, 84].

1.4.3 Porous Materials

Various classes of materials have been investigated as adsorbents for hydrogen in the literature including carbon-based materials: carbon nanotubes, fibers, fullerenes, activated carbon, zeolites, porous graphene or graphene oxide, metal-organic frameworks (MOFs) as well as covalent organic frameworks (COFs) and more recently polymers of intrinsic microporosity (PIMs). Designing an optimized adsorbent for hydrogen storage is no easy task. There are two basic requirements a storing material should fulfill [151, 152]: a large number of adsorption sites per weight and volume, (i.e. large surface areas and pore volumes). The second requirement is increasing the heat of adsorption. In the following subsectionns a brief overview description will be given for the most promising porous materials suitable for hydrogen storage such as Carbon Materials and Metal/Covalent-Organic Frameworks.

Carbon based Materials

The carbon materials are one of the most interesting materials for solid-state hydrogen storage due to its low atomic weight and microporous nature that adsorbs the hydrogen molecules at its surface through Van der Waals interaction forces. Experimental studies beyond well-known physisorption lead to a large set of various maximum hydrogen adsorption capacities.

Activated carbon (AC) is a form of processed carbon comprising graphite crystallites and amorphous carbon, fabricated from biomass resource and normally of less than 1nm pore diameter possessing a specific surface area (SSA) of $3000 m^3 g^{-1}$ [153]. Weak Van der Waal's forces enable the physisorption of hydrogen molecules as they get adsorbed and diffuse into the pores of the ACs [154]. It has been tested for AC having SSA of $2560 m^3 g^{-1}$ for hydrogen adsorption at room temperature and 77.4K. The experimentally measured maximum hydrogen storage capacity was reported as 4.5wt% at temperature of 77.4K with high adsorption kinetics and reversibility [155]. Also, AC is inexpensive and has good availability for industrial purposes, for which several studies on hydrogen storage were carried out. It is provided that hydrogen storage potential in AC it can be more efficient than compressed gas at cryogenic temperature and depends to the microstructure of the material (i.e. specific surface area (SSA) and pore volume).

Carbon nanotubes (CNTs) are graphene sheets rolled up in cylindrical shape in a seamless cylinder with a diameter in the scale of a few nanometers, and solely composed of carbon atoms. There are a variety of tubes that consist of one layer called single-walled carbon nanotubes (SWCNT) or of more than one layer, called multi-walled (MWCNT) [156, 157]. The hollow and porous structure of CNTs gives the possibility of hydrogen storage both in the inner and outer surfaces [158]. Experimental data on hydrogen adsorption was determined that the gravimetric storage density for *SWNT* at ambiante temperature is in a range of $5 - 10 wt.\%$[159].
Multi-walled (MWCNT) possess superior physical, chemical and mechanical properties and large surface areas making them promising H_2 storage physical adsorbents. *MWNTs* provide several sites such as the exterior walls, space between the nanotubes, tube channels, and interstitial space in the lattices for physical adsorption of H_2. The initial

investigations for H_2 storage on bare *MWNTs* shown a weak interactions between the *MWNTs* and H_2, which is not sufficient for efficient H_2 uptake (binding energy between 1 and 10kJ/mol). Various strategies are observed to be useful for improving the H_2 storage capacities on *MWNTs* such as surface modifications and, decoration with metals/metal oxides [160–162]. Chen et al. [163] reported that *Li*-doped and *K*-doped multi-walled Nanotubes show an uptake capacity of $20wt.\%$ and $14wt.\%$, respectively, among which the *K*-doped *MWNTs* are chemically unstable, whereas the *Li*-doped *MWNTs* are chemically stable but require elevated temperatures (473 to $673K$) for maximum adsorption and desorption of H_2.

The hydrogen storage capacities of CNTs are mainly depending on its structure, pretreatments, geometry, structural defects, operating pressure, temperature, and so on. For this reason, the use of nanotubes becomes a limitation because it is not well adjusted for storing a high capacity of H_2. Also, it requires more modifications in preparation and processing methods to achieve the high target of hydrogen capacity [164].

Metal/Covalent-Organic Frameworks

Metal-Organic Frameworks(MOFs) are the first and widely studied porous materials for hydrogen storage that operate via physisorption [165]. MOFs are crystalline porous frameworks that consist of two components secondary building units (clusters or metal ions) surrounded by organic molecules (linker). Numerous families of MOFs have been reported in the last 20 years, they are classified according to the nature of the ligands, metals (Ni, Zn, Cr, Mn, Cu, Ni, rare-earth, and alkali metals), and the geometry of the framework (symetry and pore sizes). Nevertheless, we can cite a few families of MOFs such as MIL (Matériaux de L'Institut Lavoisier), IRMOF-XX (with XX a whole number, and IR for "Isoreticulated") or even HKUST (for Hong-Kong University of science and technology) (see Figure 1.11). It has been demonstrated in MOFs that high surface areas of up to $6000m^2/g$, permanent porosity, tunable pore sizes, rigidity, structural flexibility and thermal stability make them as promising materials for H_2 storage [166–168]. Some of the rated networks (MOF-n=1–7, 8, 10, 12, 14, and 16) have been highlighted and the MOF-5 compounds were among the first to be studied for hydrogen storage (4.5 wt % at 77 K and 1 atm) [165]. Hydrogen uptake studies reveal that the hydrogen saturation uptake correlates with the preparation and handling conditions and varied

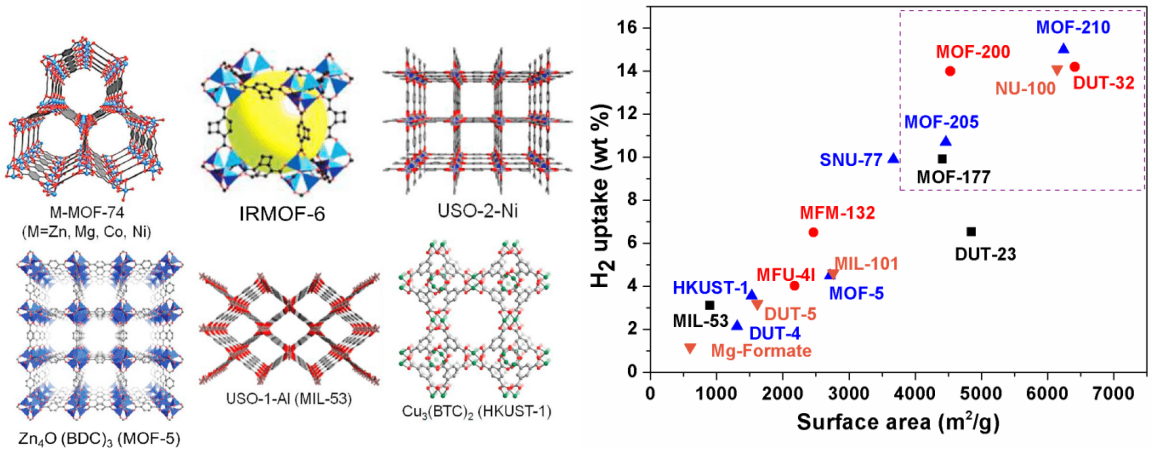

FIGURE 1.11: Common examples Porous MOFs prepared by several research groups (left) [170], H_2 uptake capacities at 77 K versus surface areas for some highly porous MOFs (right) [171]

widely with the saturation pressure reaching a strikingly high capacity of 6.7 and 7.1*wt*.% in *IRMOF*-20 and *MOF*-177 at saturation pressures of 70 and 80*bar* (at 77*K*), respectively [169]. Scientists are giving tremendous attention to *MOF* for hydrogen storage in order to maintain high hydrogen storage capacity at room temperature by manipulating the parameters mentioned above (type of metal, framework topology, surface area, and pore size...).Therefore, the exploration of new *MOFs* and developing an understanding of adsorption mechanisms are very important steps towards optimizing the hydrogen storage properties of *MOFs* at near ambient conditions.

Covalent-Organic Frameworks(COFs) , where the organic structural building units are held together by strong covalent bonds, have been presented all the advantages of MOFs (high surface area, pore-volume, low density, the rigidity of the structure) but without the drawback of the presence of heavy elements.Their molecular frameworks are constructed of light elements (carbon, oxygen, boron, hydrogen) that lower the relative weight of the structure. As one of the best COFs for hydrogen storage *COF*-8 exhibits an excess hydrogen uptake of 10*wt*.% at 77*K* and 100*bar* [74]. Moreover, the reported gravimetric uptake for COF-108 reached the value of 21wt% at 77K and 100 bar conditions and the very promising value of 4.5wt% in room temperature and 100 bar conditions [31]. These values are significantly higher than the highest values reported in *MOFs* (7*wt*.% in *MOF*-177 and 7.1*wt*.% in *MOF*-5), although the pressure employed is quite high at 77*K* [169, 172].

1.5 Summary

The hydrogen storage technology is rapidly emerging as a fast alternative to the current fossil fuels in our future energetic transition, but the challenges demand further improvements in terms of infrastructure and applications which in turn depends on the energy density, storage capacity, efficient hydrogen storing system, least safety requirements and finally low investment cost. Therefore, there are many variables that are taken into consideration for the development and deployment of hydrogen technologies in order to achieve the target of a clean and renewable economy which would depend entirely on hydrogen.

Fuel-cell vehicles are the most demanding application for hydrogen storage. At present, the only practical means of storing hydrogen on a road vehicle is as a high-pressure gas in a cylinder. High pressure limits the uses of compressed hydrogen while liquid hydrogen offers high volumetric energy density but fails as being an energy extensive method. Corrosion is another problem that occurs due to the formation of ice around the tank that leads to boil off. On the other hand, solid storage is very attractive, particularly for its safety and high gravimetric capacities compared to gas and liquid storage. Hydrogen adsorption on porous systems (physisorption) at low temperature or high pressure and the weak interaction with the H_2 molecules limits their use. Also, metal hydrides (chemical storage) offer high gravimetric capacity but require high pressure and temperature for hydride formation and hydrogen release. A comparison of properties, benefits and limitations of the different hydrogen storage methods is given in Table 1.6. Solid storage in metal hydrides appears as one of the interesting method due to its high safety under operating conditions and the high gravimetric capacity that some hydrides exhibit.

Mg and Mg-based alloy has been investigated as a great hydrogen storage material due to their advantages such as high hydrogen storage capacity which is around of 7.6 wt.% and 110 g.H_2/L for MgH_2, cyclability, relative low cost, great abundant resource and lightweight of magnesium. However, the sluggish reaction kinetics, high thermodynamic stability and working temperature for hydrogen uptake and release (>300◦C) have been hindering its practical and commercial use under adequate temperature and pressure conditions [174–179]. Despite these drawbacks, the perovskite hydrides having high hydrogen content are very attractive due to their potentials for hydrogen and energy

TABLE 1.6: Comparison between the various hydrogen storage methods [173].

Parameters	**Compressed storage**	**Liquid storage**	**Chemical storage**	**Physisorption**
Gravimetric capacity ($wt.\%$)	13	Varies	<18	20
Volumetric capacity ($Kg.m^{-3}$)	<40	70.8	150	20
Temperature (K)	273	21.5	$373-573$	Varies
Pressure (bar)	800	1	1	100
System cost ($\$kW/h$)	$12-16$	6	$8-16$	100/60
Method of storage	Compressed gas storage	Cryogenic storage	Chemical storage	Physical adsorption by porous materials
Systems	Benefits		limitations	
Compressed storage	-Lightweight -Highly beneficial for fuel purpose -Occupies smaller space and energy effective		-Requires high-pressure cylinder -volumetrically and gravimetrically inefficient	
Liquid storage	-Volumetrically and gravimetrically -Long term hydrogen storage		-Requires compressed tanks, suffers from large energy loss due to liquefaction and boil off process and high tank cost	
Chemical storage	-High storage density -low reactivity -short storage time		-Reacts violently with moist air -Cumbersome to handle -Absorption of impurities -Lack of reversibility -Desorption at elevated temperature -Slow kinetics of dehydrogenation	
Physisorption	-Fully reversible process -No accumulation of impurities -Fast cycle life and refilling time		-Clustering problem -Requires low temperature or exceedingly high pressure and shows weak interaction with the H_2	

storage applications. Recent theoretical and experimental studies have been carried out in order to improve the hydrogen storage properties. For this reason, the strain effect and the substitution effect on the perovskite-type compounds $MgCoH_3$ have been examined based on Density Functional Theory (DFT).

For H_2 storage, graphene-like structures, such as graphdiyne, honeycomb BC_3, borophene, CN and $g-C_3N_4$ layer have been also considered as efficient hydrogen storage candidates

due to their high surface area and the remarkable chemical stability [33, 180–184]. In the same frame, we investigated and illustrated the possibility of phosphorene monolayer as a prospective medium for clean energy storage using DFT approach. The theoretical framework is the subject of the following chapter.

2 Density Functional Theory: Concepts and Methods

2.1 Introduction

The understanding of the matter properties requires the study of the processes from macroscopic to microscopic scale. such as the molecular, atomic, electrons and atomic nuclei objects. Density functional theory (DFT) is a valuable tool to study physics and chemistry at this scale, and the applications of this theory, that is exact, are based on the approximation for the electron-electron interaction energy. The purpose of this chapter is to present the modeling of the physical problem that is posed to us. Since the DFT is based on of the Schrödinger equation, we will introduce approximations and different ways to solve it.

2.2 The Schrödinger equation

2.2.1 Basic knowledge

In this part, we consider the $\mathbb{R}^3 \times \mathbb{R}^+$ space, i.e. the three coordinates of space, and time. We denote by $\mathbf{q}$ the coordinates of a quantum system. $\mathbf{q}$ belongs to a space called the configuration space, composed of the spatial and temporal coordinates of the A nuclei and N electrons of the system ($\mathbb{R}^{3(K+N)} \times \mathbb{R}^+$). The state of a system is completely determined by its Ψ wave function, with values in $\mathbb{C}$[185]. By definition, the data of this function, at a given time, not only describes all the properties of the system at this moment, but also determines its behavior in all subsequent states. Mathematically, this translates into the fact that the value of the derivative $\frac{\partial}{\partial t}\Psi$ of the wave function with respect to time must, at every moment, be determined by the value of the wave function Ψ itself at this instant. In the most general form, the Schrodinger equation, which describes the evolution of the

function is given by [186]:

$$i\hbar\frac{\partial}{\partial t}\bar{\Psi} = \mathscr{H}\bar{\Psi} \tag{2.1}$$

where the Hamiltonian $\mathcal{H}$ is an hermitian linear operator, independent of time, $\hbar = \frac{h}{2\pi}$, h being the Planck constant (h=6.6260610^{-34} m^2 kg s^{-1}). At the stationary state the energy of the system is constant over time. Thus, the Schrodinger equation that depends on the time may be reduced to stationnary state Schrondinger equation:

$$\mathcal{H}\bar{\Psi}_n = \varepsilon_n\bar{\Psi}_n \tag{2.2}$$

ϵ_n being the eigenvalue or energy associated with the steady state $\bar{\Psi}_n$. It's an eigenvalue equation where the eigenvalue ϵ_n of the Hamiltonian is none other than the energy associated to the steady state $\bar{\Psi}_n$ that is independent of time. For many body systems, the information of all particles is contained in the wave function. Thus, the Schrodinger equation becomes complicated to solve in its standard form. In what follows, we will present the theory and the different approximations that simplify the problem. Considering a system of A nuclei and N electrons,the stationary state $|\Psi\rangle$ of this system can be described by a wave function:

$$\Psi\left(R_I,\vec{r}_i\right) = \left\langle \vec{R}_I,\vec{r}_i|\Psi\right\rangle = \Psi\left(\vec{R}_1,\vec{R}_2,\ldots,\vec{R}_N,\vec{r}_1,\vec{r}_2,\ldots,\vec{r}_n\right), \tag{2.3}$$

satisfying the equation of Schrödinger independent of the time [187]:

$$\hat{\boldsymbol{H}}_{tot}\Psi\left(\vec{R}_I,\vec{r}_i\right) = E_{tot}\Psi\left(\vec{R}_I,\vec{r}_i\right) \tag{2.4}$$

where E_{tot} is the total energy of the system. The total Hamiltonian operator is given by:

$$\hat{H}_T = \hat{T}_n + \hat{T}_e + \hat{V}_{ne} + \hat{V}_{ee} + \hat{V}_{nn} \tag{2.5}$$

The first terms $\hat{T}_n$ and $\hat{T}_e$ designate the kinetic energy of A nuclei and N electrons respectively. while the terms $\hat{V}_{n-e}$, $\hat{V}_{e-e}$, and $\hat{V}_{n-n}$ describe Colombian interaction electron-nuclei, electron-electron and nuclei-nuclei respectively. Its explicit expression can be

written as follow:

$$\Psi = -\sum_{i}^{N} \frac{\hbar^2}{2m} \nabla_i^2 - \sum_{I}^{A} \frac{\hbar^2}{2M} \nabla_I^2 - \sum_{i,I} \frac{Z_I e^2}{\left|\vec{r}_i - \vec{R}_I\right|} + \sum_{i<j} \frac{e^2}{\left|\vec{r}_i - \vec{r}_j\right|} + \sum_{I<J} \frac{Z_I Z_J e^2}{\left|\vec{R}_I - \vec{R}_J\right|} \tag{2.6}$$

The first two terms of the Hamiltonian are the kinetic energy operators of N electrons (indexed i, j) and Atomic nuclei (indexed I, J) respectively. The other three terms represent the different electron-nucleus,electron-electron, and nucleus-nucleus interaction potentials. As an example of a many-body system, we may quote the case of a regular crystal. The electrons are not only affected by the nuclei in their lattice sites, but also by the other electrons. An exact solution of the Schrodinger equation is impossible in the case of poly-electronic systems. It is therefore necessary to implement simplifying procedures associated with some mathematical tricks in order to make possible the obtaining of an approximate solution.

2.2.2 The Born-Oppenheimer Approximation

Max Born and Robert Oppenheimer proposed an approximation to simplify the Schrödinger equation. This approach is today the basis of many calculations in the physics of matter. The Born-Oppenheimer approximation considers the position of atomic nuclei as fixed, from the simple observation that electrons are much lighter than nuclei($M_I \gg m_i$) [188]; their kinetic energy can therefore be neglected and the interaction term between nuclei considered as a constant. Then we can decouple the nuclear and electronic movements, and the wave function of the system becomes:

$$\Psi(\{r\},\{R\}) = \Psi_{\text{elec}}(\{r\};\{R\})\Psi_{\text{nucl}}(\{R\}) \tag{2.7}$$

However, the new equation obtained represents a N-body problem whose rigorous resolution can not be obtained analytically except in very simple cases like that of the hydrogen atom. Thus, the approximation of Born-Oppenheimer is important but still insufficient for solving the **Schrodinger** equation. Thus, other approximations should be introduced.

2.2.3 Hartree-Fock approximation

The Hartree-Fock method seeks to approximately solve the electronic Schrödinger equation, and it assumes that the wavefunction can be approximated by a single Slater determinant made up of one spin orbital per electron. The objective of the Hartree-Fock method is to produce the best possible one-electron wavefunctions for use in approximating the exact wavefunction for a multi-electron system. In these models, we consider the $\mathcal{H}_{el}$ operator composed of the three operators (The kinetic operator, the interaction of an electron-nuclei and the interaction between all the electrons):

$$H_{elec} = T_e + V_{ee} + V_{en} \tag{2.8}$$

Hartree's approach

The Hartree approximation consists of replacing the interaction of each electron of the atom with all the others by the interaction with a mean field created by the nuclei and all the other electrons, that is to say that the electron moves independently in a middle field created by other electrons and nuclei [189–191]. This makes it possible to replace the potential of the type $1/r_{ij}$ which depends on the coordinates of the two electrons by an expression defining the electronic interaction which depends on the coordinates of each isolated electron. Thus, within this approximation, the correlations are neglected allowing to write:

$$\Psi_H(\{\boldsymbol{r}\}) = \psi_1(\boldsymbol{r}_1)\,\psi_2(\boldsymbol{r}_2)\ldots\psi_N(\boldsymbol{r}_N) \tag{2.9}$$

Definition of Hartree Potential the potential of Hartree or Coulomb potential V_H is defined by [189]:

$$V_{\mathbf{H}}(\mathbf{r}) = \int \mathrm{d}\mathbf{r}' \frac{n(\mathbf{r}')}{|\mathbf{r}-\mathbf{r}'|} \tag{2.10}$$

Which describes the interaction of an electron at a position $\mathbf{r}$ with an electronic cloud of density $\mathbf{n}(\mathbf{r}')$. We point out that, the equation Hartree's approximation ignores the anti-symmetry of the wave function, as long as the electron is a fermion then the total wave function must be antisymmetric with respect to the exchange of any two particles that is neglected by Hartree.

Hartree-Fock Method (1930)

To restore the wave function antisymmetry neglected in Hartree equation, Fock proposed to apply the Pauli's exclusion principle, therefore the electronic wave function is then written as a determinant of Slater [192–194]:

$$\Psi\left(r_1,\dots r_n\right)=\frac{1}{\sqrt{n!}}\begin{vmatrix}\psi_1\left(r_1\right) & \psi_1\left(r_2\right) & \dots & \psi_1\left(r_n\right)\\ \psi_2\left(r_1\right) & \psi_2\left(r_2\right) & \dots & \psi_2\left(r_n\right)\\ \vdots & \vdots & \ddots & \vdots\\ \psi_n\left(r_1\right) & \psi_n\left(r_2\right) & \dots & \psi_n\left(r_n\right)\end{vmatrix} \tag{2.11}$$

With $\frac{1}{\sqrt{n!}}$ the normalization constant. This approximation leads to good results, particularly in molecular physics. Moreover, solving the system of equations (2.11) remains difficult in the case of solids.

2.2.4 Thomas-Fermi models

Before Hohnberg and Kohn's theory of the functional density presented in the next section (2.3), Thomas and Fermi [195] independently demonstrated in the 1920s that the Y electronic density could be used as a central variable to solve the Schrödinger equation [186]. Compared with the previous expressions of energy, the calculation of kinetic energy is changed: it will also be a density function [196]. The ground state energy $\mathcal{E}^{TF}$ is obtained by minimizing according to Y:

$$\mathcal{E}^{TF}[\mathrm{Y}]=A_0\int_{\mathbb{R}^3}\mathrm{Y}(\mathbf{r})^{5/3}d\mathbf{r}+\int_{\mathbb{R}^3}V(\mathbf{r})\mathrm{Y}(\mathbf{r})d\mathbf{r}+\frac{1}{2}\iint_{\mathbb{R}^3\times\mathbb{R}^3}\frac{\mathrm{Y}(\mathbf{r})\mathrm{Y}\left(\mathbf{r}'\right)}{|\mathbf{r}-\mathbf{r}'|}d\mathbf{r}d\mathbf{r}' \tag{2.12}$$

Where $\int_{\mathbb{R}}\mathrm{Y}(r)dr=\lambda,\lambda\in\mathbb{R}^{+*}$,$A_0$ is a constant. In the general case, the density associated with the wave function of N electrons is written:

$$\mathrm{Y}(\mathbf{r})=N\int_{\mathbb{R}^{3(N-1)}}\left|\Psi\left(\mathbf{r},\mathbf{r}_2,\dots,\dots,\mathbf{r}_N\right)\right|^2d\mathbf{r}_2\dots d\mathbf{r}_N \tag{2.13}$$

But we will also have to define it from N orbitales $\psi_i(\mathbf{r})$:

$$\rho(\mathbf{r})=\sum_{i=1}^{N}|\psi_i(\mathbf{r})|^2 \tag{2.14}$$

Let's look at the physical meaning of the different terms of this energy:

- The first term would be the exact energy of a uniform gas of non-interacting electrons. When we consider a system with one nuclei, it then becomes necessary to introduce a correction, which von Weizsäcker did in 1935, thus allowing the stability of the molecules:

$$\mathcal{E}^{TFW}[\Upsilon] = \mathcal{E}^{TF}[\Upsilon] + A_2 \int_{\mathbb{R}^3} |\nabla\sqrt{\Upsilon}|^2 d\mathbf{r} \tag{2.15}$$

- compared to the hartree $\mathcal{E}^H$ and Hartree-Fock $\mathcal{E}^{HF}$ potential. Only an electronic interaction of the Hartree type (2.10) is shown here. To correct this, Dirac added in 1930 [197] a so-called exchange term to better describe the interaction between electrons [194]:

$$\mathcal{E}^{TFD}[\Upsilon] = \mathcal{E}^{TF}[\Upsilon] - A_1 \int_{\mathbb{R}^3} \Upsilon^{4/3}(\mathbf{r}) d\mathbf{r} \tag{2.16}$$

The model including the two corrections of Dirac and Von Weizsäcker is called TFDW. E. Lieb studies these different systems in detail, and P.-L. Lions demonstrates the existence and uniqueness of an electronic distribution for a neutral molecule or a positively charged ion [197–199]. The advantage of this method is that it is linear with respect to the number of electrons N.

2.3 The density functional theory

The DFT formalism was presented for the first time in an article by Hohenberg and Kohn in 1964. This article explains that the ground state is totally determined by the electronic density (*The details of density functional theory are explained in the book by R.G. Parr and W. Yang. [200]*). It is based on two theorems [201]:

Theorem 1 : The total energy of the fundamental state of the system is a single universal functional function of the electronic density for a given external potential; whether $E = E[\rho(\vec{r})]$. There are two classes of electrons, the spin-up electrons and the spin-down electrons. So the total energy is a functional (both electronic density of spin up and spindown $E = E\left[\rho_\uparrow(\vec{r}), \rho_\downarrow(\vec{r})\right]$. The general expression of the total energy is:

$$E[\rho(\vec{r})] = F_{HK}[\rho(\vec{r})] + \int \hat{V}_{ext}(\vec{r})\rho(\vec{r}) d\vec{r} \tag{2.17}$$

In which $F_{\mathrm{HK}}\left[\rho(\bar{r})\right]$ represents the universal functional of Hohenberg-Kohn.

Theorem 2 : A universal functional for the energy E[n] in terms of the density $n(r)$ can be defined, valid for any external potential $V_{ext}(r)$. The exact ground state energy of the system is the global minimum of this functional and the density that minimizes the functional is the exact ground state density $n_0(r)$. This reduces the very complex problem of finding all ground state physical properties of a system to finding the minimum of the energy with respect to the electron density. The energy functional is as follows:

$$E_{HK}[n] = T[n] + E_{int}[n] + \int V_{ext}(\mathrm{r})n(\mathrm{r})d\mathbf{r} + E_{nn} \tag{2.18}$$

where $E_{HK}[n]$ is the total energy functional, T[n] its kinetic energy part, $E_{int}[n]$ the part coming from the electronic interactions and E_{nn} is the energy of nuclei interaction. E_{nn} does not depend on the density and is due to the nuclei-nuclei interaction. It should be noted that although the first Hohenberg-Kohn theorem requires a nondegenerate ground state, degenerate ground states are also allowed by the Levy formulation. It should also be noted that using the Hohenberg- Kohn formulation of DFT implies that we are working at $T = 0$K.

2.3.1 The Kohn-Sham equation

Kohn and Sham have shown that there is a way to map the problem of solving Eq. 2.18 to the one of solving a system of non-interacting electrons moving in an effective potential from all the (other) electrons. According to Theorem 2, the true electron density will minimize the total energy, but all means of finding it are valid. It could be guessed or, as suggested by Kohn and Sham, calculated from a reference system of non-interacting electrons moving in an effective potential. Thus, developing this variation with the full energy functional added (eq. 2.18), under the condition that the sum of the density throughout the molecule or solid should be constant and equal to the number of electrons,

$$\int_V n(\mathbf{r})d\mathbf{r} = n_e \tag{2.19}$$

finally gives the Schrödinger-like equations called the Kohn-Sham equations:

$$\mathcal{H}\phi_i = \left[-\frac{1}{2}\nabla^2 + V_{eff}(\mathbf{r})\right]\phi_i = \epsilon_i\phi_i \tag{2.20}$$

$\mathcal{H}$ is the one electron Hamiltonian and $V_{eff}(r)$ the effective potential in which the electron moves. The effective potential is given by

$$V_{eff}(\mathbf{r}) = V_{ext} + V_H + V_{XC} = V_{ext}(\mathbf{r}) + \int \frac{n(\mathbf{r}')}{|\mathbf{r}-\mathbf{r}'|}d\mathbf{r}' + \frac{\delta E_{XC}[n(\mathbf{r})\mid}{\delta[n(\mathbf{r})]} \tag{2.21}$$

Since the electron density,

$$n(\mathbf{r}) = \sum_{i=1}^{\infty} |\phi_i(\mathbf{r})|^2 \tag{2.22}$$

is needed to calculate the last two terms, which are the Coulomb potential from all electrons and the exchange-correlation potential, the Kohn-Sham equations need to be solved self-consistently. The new term, the exchange correlation potential, appearing here contains all the many-body effects that are not present in the classical Hartree interaction term. The initial electron density can be chosen, for example, as a superposition of atomic densities. The Kohn-Sham equations can now be solved instead of finding the minimum of Eq. (2.18), and the orbitals $\phi_i(r)$ then give the electron density according to Eq. 2.22 above. These orbitals are often called Kohn-Sham orbitals and in the case of a non-spin-polarized system, each of these orbitals contain two electrons.

2.3.2 The exchange-correlation approximations

The functional LDA : The simplest physical way to approximate the exchange-correlation energy is the Local Density Approximation (LDA). In this approximation two assumptions are made: i) the local exchange-correlation energy per particle only depends on the local density (hence the name of the approximation) and ii) is equal to the exchange-correlation energy per particle of a homogeneous electron gas, that has the same density, in a neutralizing positive background (jellium background). The total exchange-correlation energy E_{XC} is then given by the sum of the contributions of each point in space, where it is assumed that the contribution of one point only depends on the density of that particular

point, independent of the other points. So:

$$E_{XC}^{LDA}[n] = \int n(r)\epsilon_{XC}^{hom}[n(r)]dr \tag{2.23}$$

Where $E_{XC}[n(r)]$ is the exchange-correlation energy per particle of a uniform electron gas of density $n(r)$. The quantity $E_{XC}[n(r)]$ can be further split into exchange and correlation contributions,

$$\epsilon_{XC}(n(\mathbf{r})) = \epsilon_X(n(\mathrm{r})) + \epsilon_C(n(\mathbf{r})) \tag{2.24}$$

The exchange part, E_x, represents the exchange energy of an electron in a uniform electron gas and is given by:

$$\epsilon_X = -\frac{3}{4}\sqrt[3]{\frac{3n(\mathrm{r})}{\pi}} \tag{2.25}$$

The correlation part, E_C, is determined using quantum Monte-Carlo simulations of the homogeneous electron gas as proposed by Ceperly and Alder [202]. This approximation is more accurate for systems with slowly varying densities, as it is assumed that the density is locally a constant. While being a simple approximation, the results of this approximation are surprisingly good. In general, LDA almost always leads to a correct picture of binding trends across the periodic table. Also, structures, bond lengths, vibrational energies, phonon spectra and other properties are predicted correctly, or with a systematic deviation. Binding energies of solids and molecules are usually overestimated, which leads to an underestimation of the bond lengths. Band gaps are also underestimated (a notorious example of this is the bandgap of bulk Ge, which is predicted to be metallic).

Generalized Gradient Approximation (GGA) In LDA, one uses the knowledge of the density in a point r. In real systems the density varies in space. A logical improvement of the LDA approximation would be to include also information of this rate of change in the functional. This can be done by adding gradient terms. This approach is called the gradient-expansion approximation. In this class of approximation, one tries to systematically calculate gradient-corrections of the form $|\nabla n(r)|, |\nabla n(r)|^2, \left|\nabla^2 n(r)\right|$, etc., to the LDA. In practice, the inclusion of low-order gradient corrections almost never

improves on the LDA, and often even worsens it. Moreover, higher-order corrections are exceedingly difficult to calculate and little is known about them. It was realized that instead of power-series like systematic gradient expansions one could experiment with more general functions of $n(r)$ and $\mid \nabla n(r) \mid$ which needs not proceed order by order. Such functionals, of the general form:

$$E_{XC}^{GGA} = \int \epsilon x_C \left(n, |\nabla n|, \nabla^2 n\right) d\mathbf{r} \tag{2.26}$$

are known as generalized-gradient approximations (GGAs). The current GGAs seem to give reliable results for all main types of chemical bonds and are popular in computational chemistry. Overall, GGA type functionals, like PBE, are expected to be more accurate than LDA typefunctionals, meaning a GGA functional should give better results for a larger array of systems than an LDA functional. LDA functionals may perform better than GGA functionals for a particular system or a particular group of systems, but overall GGA functionals should give better result than LDAs functional.

2.3.3 Methods for electronic structure calculations

The Kohn-sham equation is solved self-consistent according to figure 2.1. This figure includes the following steps:

1. The first step consists in choosing an initial density in $n(r)$ based on the eigen densities of the free atoms of the solid
2. We then calculate the effective Kohn-Sham potential using the density defined in first step.
3. We solve the Schrodinger equation in order to obtain the wave functions of the system.
4. We recalculate the density

In the next sections we will briefly discuss themost popular methods that are used to calculate the electronic structure of materials.

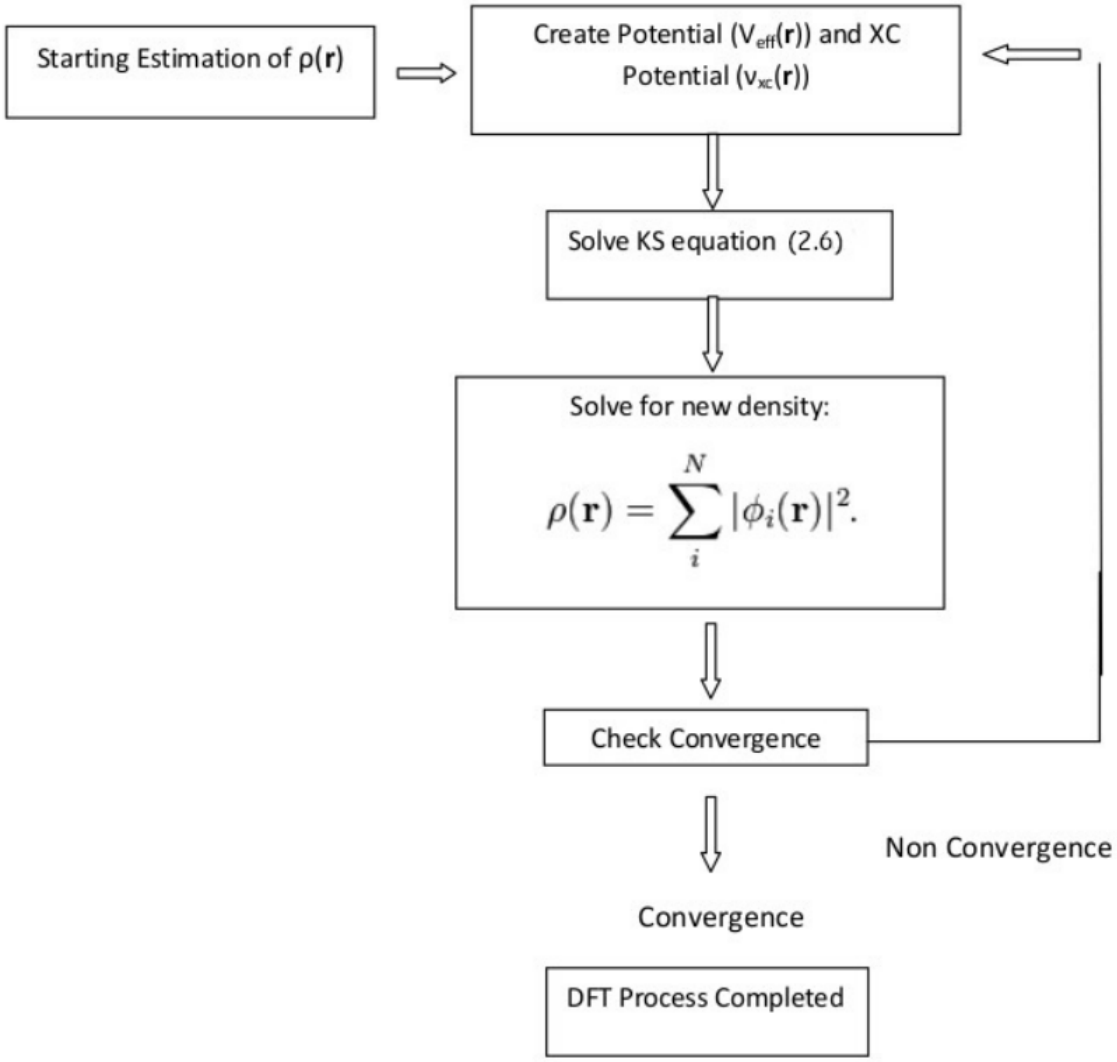

FIGURE 2.1: Diagram representing the Kohn-Sham equation solved in a self-consistent way

2.4 Crystal structure and Bloch Theorem

In the case of solids, the situation is more complicated than that of a single atom or molecule, because the properties of the solid can depend on a very large number of electrons, since there are a large number of atoms distributed in a macroscopic volume. For standard calculation methods, that would be a huge cost in time, even for powerful computers if we were to try to calculate the electronic structure of the whole system. In the case of crystal structures, this process is greatly simplified because the network is periodic. Since the same structure, or supercell is generally small, and has just repeated a large number of times, which allows to consider just this cell for the purpose of calculations (something that cannot be done in a non-crystalline structure). This is done in the calculation using periodic boundary conditions, which comes from the cell which are repeated again and again in the simulation, just like in a real solid. Another theorem useful for these solid state calculations is called Bloch's theorem. A Bloch wave is defined as the wave function of a particle (in terms of interest here an electron) inside a periodic potential. The definition of this theorem is given below;

Bloch theorem [203] : The proper function of such a system can be written as the product of a plane wave envelope function and a periodic function (of periodic function Bloch) $\mu_{nk}(r)$ which has the same periodicity as the potential:

$$\Psi_{nk}(r) = e^{ikr}\mu_{nk}(r) \tag{2.27}$$

The importance of this theorem is that the part of the envelope of the plane wave can be extended as a series of plane waves, allowing all functions of electrons to be expressed by plane-wave. It will become important and is discussed further in the following sections.

2.5 Plane-Waves

One of the most common methods for DFT when working in solids is the pseudopotential plane wave method [204]. It basically works out of a set of approximations and symmetries that work well in periodic boundary conditions of a crystal lattice. It is based on the theorem of Bloch identified as periodic boundary conditions as well as to create a set

of basic wave plane. Returning to the previous section, it has shown that the electronic wave functions can be expressed as plane-waves. Another approximation, known as pseudopotential is also integrated to simplify the basic set plane wave and is discussed in the next section. The basis of the theory is that it could go to infinity, that the great values of k will result in electrons with high kinetic energy. Since the DFT calculations are for the ground state, we can reasonably suppose that the wave functions of electrons can be given with a reduced basic set which will contain only the plane waves lower than the cutting energy (denoted E_{cut}). Basically after a certain value of k (denoted k_{cut}), the coefficients for the plane-waves will become very low, and can be overlooked because they are higher than the energy of electrons. However, we must be careful to choose the right value of the cut-off energy, because a too low a value can lead to inaccurate results.

2.6 Plane wave pseudopotential method

Plane waves offer a natural choice as a basis set to expand the periodic functions $u_{nk}(\mathrm{r})$ as:

$$u_{nk}(\mathrm{r}) = \sum_{\mathrm{G}} c_{n\mathrm{k,G}} e^{i\mathrm{G}\cdot\mathrm{r}} \tag{2.28}$$

where the summation is over all the reciprocal lattice vectors G of the system under study. Thus, the electronic wave functions can be written as:

$$\phi_{nk}(\mathrm{r}) = \sum_{G} c_{nk,G} e^{i(k+G)\cdot r} \tag{2.29}$$

The electronic wave functions at each k-point are now expressed in terms of a discrete plane wave basis set. In principle this Fourier series is infinite. However, in practice we cannot work with an infinite basis set, it has to be truncated. The number of plane waves can be restricted by placing an upper boundary to the kinetic energy of the plane waves. This boundary is called energy cut-off Ecut and only plane-waves satisfying the condition:

$$\frac{|\mathrm{k}+\mathrm{G}|^2}{2} < E_{\mathrm{cut}} \tag{2.30}$$

are considered in the computation. With DFT, the complexity of the problem has reduced appreciably. However, for systems with a large number of electrons still remains

computationally very expensive. Pseudopotentials helped in a crucial way to make the calculations tractable. Using the fact that the physical properties of solids depend mainly on valence electrons, the computational effort can be minimized considerably. In the pseudopotential approximation, the core electrons are removed and the strong ionic potential is replaced by the weaker pseudo potential V_{pseudo} that acts on a set of pseudo wave functions Ψ_{pseudo} rather than the true valence wave functions (Ψ). The pseudopotential and pseudo wave functions are generated in such a way that they are identical to the true potential and wave function beyond a certain radius known as cut-off radius r_c. In the core region the pseudo wave function is constructed such that all the nodes are removed but the norm is conserved. Also, since the nodes of the core states are removed, the number of plane-wave basis functions required to describe this wave function in the core region is much less resulting in reduced computational effort. This leads to a popular plane wave pseudopotential method for electronic structure calculations. In this thesis, we use this method to calculate the DFT band structure within the GGA approximation. These calculations are performed using the Quantum espresso code.

2.7 Projector augmented wave method (PAW)

An approach that lies half-way between the LAPW and the pseudopotential methods has been introduced by Bloch 2.4 known as the projector augmented waves (PAW) method. This approach retains the all-electron character, but it uses a decomposition of the all-electron wave function in terms of a smooth pseudo-wave function, and a rapidly varying contribution localized within the core region. The true and pseudo-wave functions are related by a linear transformation:

$$\left|\Psi_n^{AE}\right\rangle = \left|\Psi_n^{PS}\right\rangle + \sum_i \left(\left|\phi_i^{AE}\right\rangle - \left|\phi_i^{PS}\right\rangle\right) \left\langle p_i^{PS} \mid \Psi_n^{PS}\right\rangle \tag{2.31}$$

The pseudo-wave functions Ψ_n^{PS}, where n is the band index, are the variational quantities and are expanded in plane waves. In the regions between the PAW spheres surrounding the atoms, the Ψ^{PS}, n are identical to the all-electron wave functions Ψ_n^{AE} , but inside the spheres Ψ^{PS} are only a bad approximation to the exact wave functions, they are

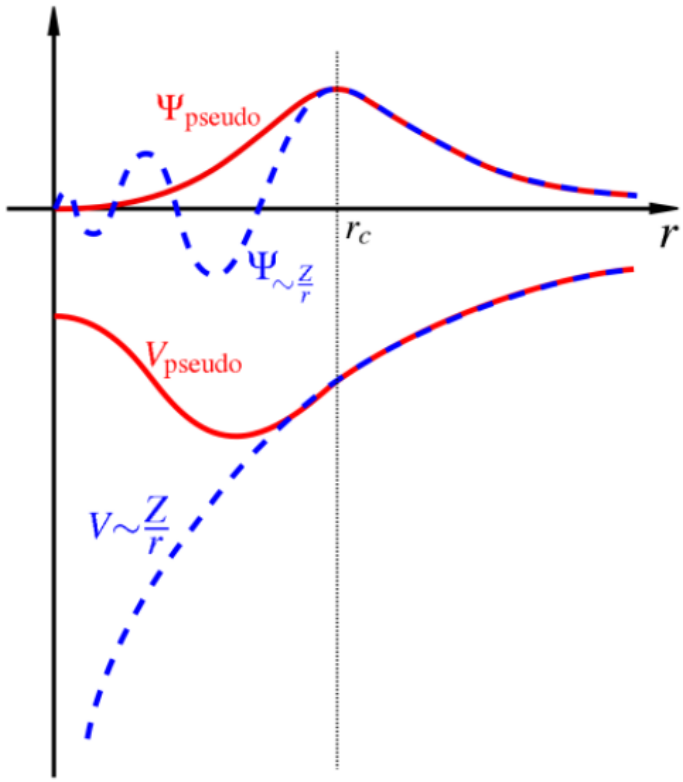

FIGURE 2.2: Schematic representation of pseudopotential and the pseudo wave function

used only as a computational tool. The all-electron partial waves ϕ_i^{AE} are solutions of the spherical scalar-relativistic Schrödinger equation for a non-spin-polarized atom at a reference energy E_i in the valence regime and for an angular momentum I_i,

$$\left(-\frac{1}{2}\nabla^2 + v_{eff}^{AE}\right)\left|\phi_i^{AE}\right\rangle = \varepsilon_i \left|\phi_i^{AE}\right\rangle \tag{2.32}$$

where V_{eff}^{AE} is the spherical component of the AE potential. The index i contains the reference energy ε_i the angular momentum quantum numbers (I_i, m_i), and the atomic coordinates R_i. The PS partial waves ϕ_i^{PS} are nodeless and identical to the AE partial wave outside a core radius r_c (approximately equal to half the nearest-neighbor distance) and match continuously to ϕ_i^{AE} inside these spheres. The projector functions p_i^{PS} are constrained to be dual to the partial waves, they are constructed by two-step procedure: First, intermediate functions χ_i are computed via

$$|\chi_i\rangle = \left(\varepsilon_i + \frac{1}{2}\nabla^2 - v_{eff}^{PS}\right)\left|\phi_i^{PS}\right\rangle \tag{2.33}$$

where V_{eff}^{PS} is the spherical component of the effective pseudopotential, which can be chosen arbitrarily inside the radius r_c but must match V_{eff}^{PS} for $r \geq r_c$. The projector functions are linear combinations of the χ_i with

$$\left|\phi_i^{PS}\right\rangle = \sum_j \left(B^{-1}\right)_{ji} |\chi_j\rangle \,, B_{ij} = \left\langle \phi_i^{PS} \mid \chi_j \right\rangle \tag{2.34}$$

such that the ϕ_i^{PS} and p_i^{PS} are dual, $\left\langle p_i^{PS} \mid \phi_j^{PS} \right\rangle = \delta_{ij}$ and $\langle r \mid p_i^{PS} \rangle = 0$ for $r \geq r_c$

2.8 Quantum Espresso

In this thesis, all calculations were performed using the Quantum Espresso (PWSCF) code [205]. Quantum ESPRESSO stands for op**E**n **S**ource **P**ackage for **R**esearch in **E**lectronic **S**tructure, **S**imulation and **O**ptimization. It is a free software, released under the GNU General Public License. The code is designed to perform density functional theory calculations of the electronic structure. It uses plane wave basis sets and pseudopotential in its applications. Its features range from the calculation of ground-state energy and Kohn-Sham orbitals to the calculation of atomic forces, stresses, and structural

optimization, molecular dynamics on the ground state Born-Oppenheimer surface, Nudged Elastic Band (NEB) and Fourier String Method Dynamics. Quantum ESPRESSO is also able to perform other calculations such as; phonon frequencies and eigenvectors at a generic wave vector, effective charges and dielectric tensors, electron-phonon interaction coefficients for metals, Infrared and Raman (non-resonant) crosssection etc. [206, 207]. The main advantages of QE over VASP in the context of this work are as follows: first, QE is able to characterize the vibrational frequencies into either Raman or infrared active modes. Secondly, QE assigns modes on the basis of the degeneracy of the vibrational frequencies (single, double or triple). In addition, QE tells you to which irreducible representation a mode belongs. This makes it easy to interpret the results of Raman and infrared spectra. Quantum Espresso is presently divided into several executable, performing different types of calculations, although some of them have overlapping functionalities. Typically, there is single set of functions or a single Fortran 90 module that perform each specific task, but there are still important exceptions to this rule, reflecting the different origin and different styles of the original components. Quantum Espresso has in fact built out of the merging and re-engineering of different packages.

2.9 Phonon calculation

Crystallography is generally concerned with the static properties of crystals, describing features such as the average positions of atoms and the symmetry of a crystal. Solid state physics takes a similar line as far as elementary electronic properties are concerned [207, 208]. We know, however, that atoms actually move around inside the crystal structure and that are these motions which gave rise to the concept of temperature. The static lattice model, which is only concerned with the average positions of atoms and neglects their motions, can explain a large number of material features. Calculating the phonon spectrum (=lattice vibrations) can provide you with an additional check. The phonon frequencies stand for the (effective) interatomic spring constants associated with vibrational normal modes. In a solely theoretical context, phonon calculations may indeed provide a hint towards the stability of the calculated structure. If some phonon frequency is particularly small, then this means that a distortion along this normal coordinate costs very little energy. In the extreme case, the energy curvature along some coordinate might

turn out to be negative, then you know for sure that (within the chosen model) the structure is unstable. Otherwise, knowing the phonon spectrum, one can also compute the phonon contribution to specific heat, which could yet be another basic material property of interest. In conjunction with symmetry analysis, you can determine which phonons are Raman or IR active and which ones are "silent" modes.

2.9.1 Crystal structure

There are three types of heat carriers in solids: photons, phonons and electrons. The photons transport heat in semi-transparent media, such as glass, by radiation; electrons are mainly responsible for conduction in metals and phonons explain most of the thermal and dynamical stability behavior of semiconductors and insulators. Matter is generally found in three forms: solid, liquid and gas [1]. Within of the solid state, we can also differentiate certain states according to their atomic organization. Crystals are structures for which the atoms (or ions) constituting the matter are organized according to a periodic pattern. Conversely, the amorphous state corresponds to an arrangement of atoms such that it is not possible to define periodicity. Depending on the pressure and temperature conditions, the number of covalent bonds, the charge static, the elements crystallize according to a particular elementary pattern. We distinguish in crystallography 14 Bravais networks; 14 ways to organize the material according to regular patterns. A crystal is usually described by its representation in reciprocal space, which corresponds to the Fourier transform of the real crystal structure. A basis of this space is defined by the vectors wave, K_x, K_y and K_z, as shown in Figure 2.3.

2.9.2 Lattice dynamics

Within the crystal, the atoms (ions) are not fixed. They vibrate, under the effect of thermal excitement , around an equilibrium position. These vibrations generate waves which can propagate in the structure. Within the framework of quantum theory, we can associate a particle with any wave and vice versa. A phonon is then the particle associated with a wave generated by the vibrations of atoms around their equilibrium position. In order to characterize these vibrations. To obtain the modes of vibration,

[1] We can also define a fourth state called plasma where the electrons are no longer linked to the nuclei atoms and a fifth state at temperatures close to absolute zero called "Bose-Einstein" condensate.

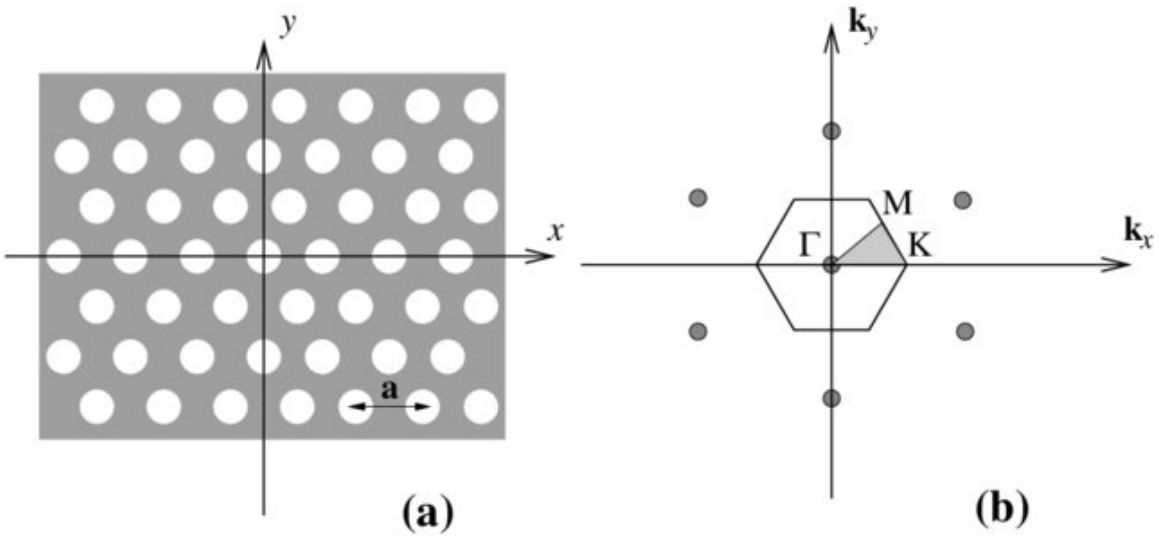

FIGURE 2.3: Example of a two-dimensional crystal structure (a) and associated reciprocal (b).

we will follow a procedure similar to a classical one. Suppose we have a cell with a single atom in a cubic lattice. As a first approximation, we can represent the interactions between adjacent sites by springs. Each atom is then connected only to its immediate neighbors. The main difference that we will find at the atomic scale is that we cannot consider only the first neighbors.The second neighbor has an effect, but as the force considered is due to the stretching of a cord, the influence of the more distant neighbors is only indirect through their influence on the position of the first neighbor. Since the force we now consider is the Coulomb force between two charges, an atom can be directly affected by the movement of a distant neighbor. The important point that remains is that we will still consider a linear relationship between displacement of an atom and the resulting force on another atom as in the equation of the exerted force. Force constants are generated based on finite displacement method. Crystal symmetry is used to reduce the calculation cost and numerical noise of the force constants. Firstly a symmetry reduced set of atomic displacements is generated. After the atomic force calculations, the set of atomic displacements are expanded using the symmetry and then all the elements of force constants between atoms in a primitive cell and the supercell are fit to the symmetry expanded forces of atoms in supercells. This procedure may considered as a variant of Parlinski-Li-Kawazoe method [209]. In case of 3D harmonic crystal the force constant

matrix is presented by the folowing equation:

$$\Phi_{\alpha\beta}\left(il, jl'\right) = \frac{\partial^2 E}{\partial r_\alpha(l)\partial r_\beta\left(l'\right)} = -\frac{\partial F_\alpha(il)}{\partial r_\beta\left(jl'\right)} \tag{2.35}$$

where $r(jl)$ is the point of the $j_t h$ atom in the $l_t h$ unit cell. The α, β are the Cartesian indices, j, j' are the indices of atoms in a unit cell, and l, l', are the indices of unit cells. By convention, the dynamical matrix is used as follows:

$$D_{\alpha\beta}\left(jj', \mathbf{q}\right) = \frac{1}{\sqrt{m_j m_{j'}}} \sum_{l'} \Phi_{\alpha\beta}\left(j0, j'l'\right) \exp\left(i\mathbf{q} \cdot \left[\mathbf{r}\left(j'l'\right) - \mathbf{r}(j0)\right]\right) \tag{2.36}$$

Where m is the atomic mass and q is the wave vector, and the eigenvector of the band index at q is obtained by the diagonalization of D(q). After diagonalisation we get :

$$e(\mathbf{q}) \cdot \Omega(\mathbf{q}) = D(\mathbf{q}) \cdot e(\mathbf{q}) \tag{2.37}$$

The force constant matrix $\Phi_{\alpha\beta}\left(il, jl'\right)$ can be obtained either from finite-deplacement calculations, or by using the density-Functional Perturbation Theory (DFPT). In our calculations, we carried out to extract the force matrix from the self-Consistent Field (SCF) calculation by quantum espresso code. The number of displacements which need to be evaluted to construct the dynamical matrix can be reduced by symmetry. The phonon density of state (or vibration spectrum) is calculated, as for the electrons. Thus one can define a density of states of modes:

$$g(\omega) = \frac{1}{N} \sum_{\lambda} \delta\left(\omega - \omega_\lambda\right) \tag{2.38}$$

where N is the number of unit cells and $\lambda = (\mu, q)$ with μ as the band index and q as the q-point, ω is a frequency and k is a Wave-vector . Based on the phonon frequencies, the thermodynamic functions can be also obtained. The Helmholtz free energy could be written as:

$$F = E + H_{vib} + TS_{vib} \tag{2.39}$$

where, E, H_{vib} and S_{vib} are the static electronic energy of the crystal, internal energy and entropy contributing to the lattice vibration. Within the harmonic approximation these

contributions are given by:

$$H_{vib}(T) = \sum_i \frac{1}{2}\hbar\omega_i + \hbar\omega_i \left[\exp\left(\frac{\hbar\omega_i}{K_\beta T}\right) - 1\right]^{-1} \tag{2.40}$$

$$S_{vb}(T) = k_\beta \sum_i \frac{\frac{\hbar\omega_i}{K_\beta T}}{\exp\left(\frac{\hbar\omega_i}{k_\beta T}\right) - 1} - \ln\left[1 - \exp\left(-\frac{\hbar\omega_i}{k_\beta T}\right)\right] \tag{2.41}$$

Where the sums run over vibrational frequencies, K_β is the Boltzmann factor and T is the absolute temperature. The Constant volume heat capacity is gevin by the equation :

$$\begin{aligned} C_V &= \left(\frac{\partial E}{\partial T}\right)_V \\ &= \sum_{\mathbf{q}\nu} k_\mathrm{B} \left(\frac{\hbar\omega(\mathbf{q}\nu)}{k_\mathrm{B}T}\right)^2 \frac{\exp\left(\hbar\omega(\mathbf{q}\nu)/k_\mathrm{B}T\right)}{\left[\exp\left(\hbar\omega(\mathbf{q}\nu)/k_\mathrm{B}T\right) - 1\right]^2} \end{aligned} \tag{2.42}$$

Beyond Harmonic Approximation

The harmonic approximation is a very powerful tool for studying excitations in solids. In general, the assumption that the ions remain close to their equilibrium positions holds good in most materials below their melting points. Despite its undeniable qualities, the description harmonic of solids suffers from its inability to explain fairly common phenomena like thermal expansion of materials. It is very instructive to identify the reason for this failure of the model.

Thermal expansion and quasi-harmonic approximation The limitations of the Harmonic Approximation are well-known: zero thermal expansion, temperature independence of elastic constants and bulk modulus, equality of constant-pressure and constant-volume specific heats, infinite thermal conductivity and phonon lifetimes, etc. The simplest way for correcting most of the above mentioned deficiencies of the HA is represented by the QHA, according to which the Helmholtz free energy of a crystal is written retaining the same harmonic expression but introducing an explicit dependence of vibration phonon frequencies on volume:

$$G(T, p) = \min_V \left[U(V) + F_{\text{phonon}}(T; V) + pV\right] \tag{2.43}$$

Where U(V) electronic internal energy, F_{phonon} is the phonon Helmholtz free energy, T temperature, p pressure and, $\min_V[$ function of $V]$ means to achieve unique minimum value in the brackets by changing volume. Since volume dependencies of energies in electronic and phonon structures are different, volume giving the minimum value of the energy function in the square brackets shifts from the value calculated only from electronic structure even at 0 K. By increasing temperature, the volume dependence of phonon free energy changes, then the equilibrium volume at temperatures changes. This is considered as thermal expansion under this approximation.

The heat capacity at constant pressure Cp are given by equation:

$$C_p(T,p) = -T\frac{\partial^2 G(T,p)}{\partial T^2} = C_v(T,V(T,p)) + T\frac{\partial V(T,p)}{\partial T}\frac{\partial S(T,V)}{\partial V}\bigg|_{V=V(T,p)} \tag{2.44}$$

The coefficient of thermal expansion (CTE) relates the change in volume of a material to change in temperature and it is given by:

$$\alpha_v = \frac{1}{V}\left(\frac{\partial V}{\partial T}\right)_p \tag{2.45}$$

3 Hydrogen storage properties of $MgCoH_3$ under strain effect

3.1 Introduction

During the last decades, Mg and Mg-based alloys have been broadly examined due to their advantages such as great abundance, lightweight and large capacity absorbed hydrogen, which is of order 7.65 wt.% [174–179, 210]. However, the high thermodynamic stability of the magnesium hydride and its poor kinetics of ad/desorption of hydrogen (excess of 300°C at 1bar H_2) prevents its application concerning the hydrogen storage under adequate temperature and pressure conditions [211–215]. To overcome such issues, many theoretical and experimental works have been performed to enhance the stability and desorption temperature. Among the most promising strategies reach that objective: reduction of size [216, 217], alloying [218, 219], doping/functionalization [220–222], morphology control [222, 223], and engineering strain [224–226].

Computational methods such as density functional theory has been proven to provide extensive structural, physical and mechanical properties as well as analyzing stabilities of compounds without complexity and cost of any experiments. In this sense, this study adopts density functional theory in order to suggest and thoroughly investigate new type of perovskite materials for solid state storage of hydrogen. To use Perovskite hydride $MgCoH_3$ as energy carrier in mobile application, it is necessary to improve its thermodynamic and kinetics properties. In this chapter, the role of biaxial compressive strain on the Perovskite hydride $MgCoH_3$ and its effect on the stability, crystal structure, phonon dispersion, thermodynamic properties, the distributions of charge density and hydrogenation kinetics was investigated by using the first-principles calculations.

3.2 Model and computational details

All calculations have been carried out according to the first-principles calculations based on a density functional theory (DFT) approach [227, 228] and using plane wave pseudo potential method (PWSCF) in the Quantum Espresso code (QE) to solve the Kohn-Shame equation [205]. The electronic exchange-correlation functional corrections included through a generalized gradient approximation (GGA-PBE) was used [229]. All pseudopotentials are constructed using the ultra-soft pseudopotential method, with cutoff kinetic energy of 59 Ry (800 eV) and the k-point grids [230] for the Brillouin zone integration are sited to be 11x11x11 and 6x6x6 for the primitive unit-cell and supercell, respectively, which is large enough to make the error from calculations of the energy below 0.01eV. The positions of atoms and the cell parameters, including the cell volume were all relaxed by minimizing the Hellmann-Feynman forces and stresses without any symmetry constraint using the Broyden–Fletcher–Goldfarb–Shanno method (BFGS)[231] and the convergence energy in the self-consistent cycle was selected to be 10^{-8} Ry. The atomic structures are plotted by the VESTA program [232].

The phonon frequencies and thermal properties are calculated using density functional theory implemented in QE code in combination with phonopy software [233]. In order to analyze the stability of compound structure, the phonon dispersion is studied using a finite displacement method according to the Parlinski-Li-Kawazoe method [234]. The displacements of atomic position of 0.02 Å were used to extract the force constants. A huge displacement was employed to avoid possible numerical inaccuracies in the system. A complete force constant matrix was obtained, and the phonon frequencies (ω) were then calculated by the dynamical matrix diagonalization, over the electronic density of states. The lattice c was completely relaxed in the bi-axial strain. The mechanical bi-axial strains rate for each direction is defined by equation 3.1 and Figure 3.1

$$\epsilon_{xx} = \epsilon_{yy} = \frac{a(b) - a_0(b_0)}{a_0(b_0)} \tag{3.1}$$

Where $a(b)$ and $a_0(b_0)$represent the lattice constants in x(y) axis direction of $MgCoH_3$ unit cell with and without strain, respectively. In order to simulate either the compression strain state in the x and y axes indicated by negative value or the tension strain represented by positive value.

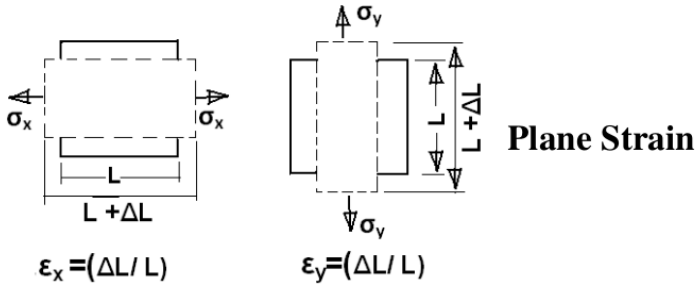

FIGURE 3.1: Illustration of bi-axial strain

TABLE 3.1: Lattice parameters (a), Volume (V) and interatomic distances (d) between different neighboring atoms of MgCo and $MgCoH_3$ systems

System	Parameters (Å)	Volume (Å^3)	Interatomic distances (Å)		
			Mg-Co	Co-H	Mg-H
MgCo (221-Pm-3m)	2.99 (this work) 3.026[221] 3.07[235]	26.73 27.70	2.59	-	-
$MgCoH_3$ (221-Pm-3m)	3.278 (this work) 3.31[221] 3.33[235] 3.288[236]	35.23 36.26[221] 36.9[235]	2.84	1.64 1.665[235]	2.32

3.3 Perovskite-type hydride structure of $MgCoH_3$

The bulk Perovskite hydride $MgCoH_3$ crystallizes in body-centered cubic (BCC) with space group Pm-3m (No.221). The unit-cell of the Perovskite compound contains five atoms, i.e. a magnesium atom located at corner (0,0,0), the Co atom at the center and the three hydrogen atoms are placed at octahedral sites at the face centers; (0.5, 0.5, 0.0), (0.5, 0.0, 0.5) and (0.0, 0.5, 0.5). The cell parameter of the relaxed structure is found to be a_0=3.278 Å, which is close to the results obtained in previous studies [221, 235, 236]. Crystal lattice of the cubic $MgCoH_3$ compound are illustrated in Figure 3.2. The relaxed lattice constants a_0 and cells volumes for all systems (intermetallic and their hydrides) are listed in Table 3.1.

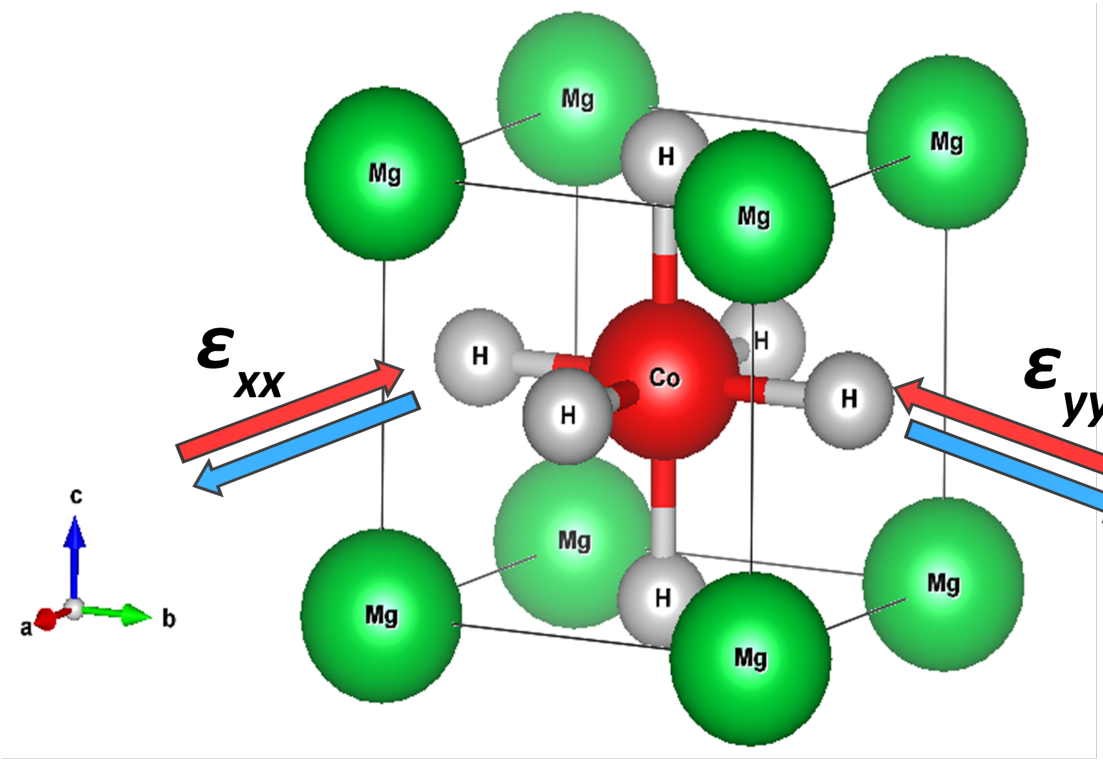

FIGURE 3.2: Unit-cell crystal structure of the cubic Perovskite hydride $MgCoH_3$

3.3.1 Electronic properties

The electronic band structure of the Perovskite hydride $MgCoH_3$ compound along the high symmetry directions in Brillouin zone, the total density of states (DOS) and the projected density of states (PDOS) obtained from the calculated equilibrium lattice constants are displayed in Figure 3.3. From the band structure graph (see Figure 3.3(a)) it is noticed that there is no forbidden energy gap at the Fermi level for $MgCoH_3$ compounds. In other words, the compound shows a metallic character due to overlap of the valence and conduction bands with each other at the fermi level. Furthermore, total DOS of free-strain $MgCoH_3$ is divided into two distinct parts. The first part covers the band energy range from -12.00 to -3.00 eV, which is composed of a strong hybridization between H-s, Mg-(s, p) and Co-d states. The second part, with an energy ranging from -2.00 to 2.00 eV, the fermi level almost formed by the contribution of the d-orbitals of Co atoms (see Figure 3.3(b), (c) and (d)).

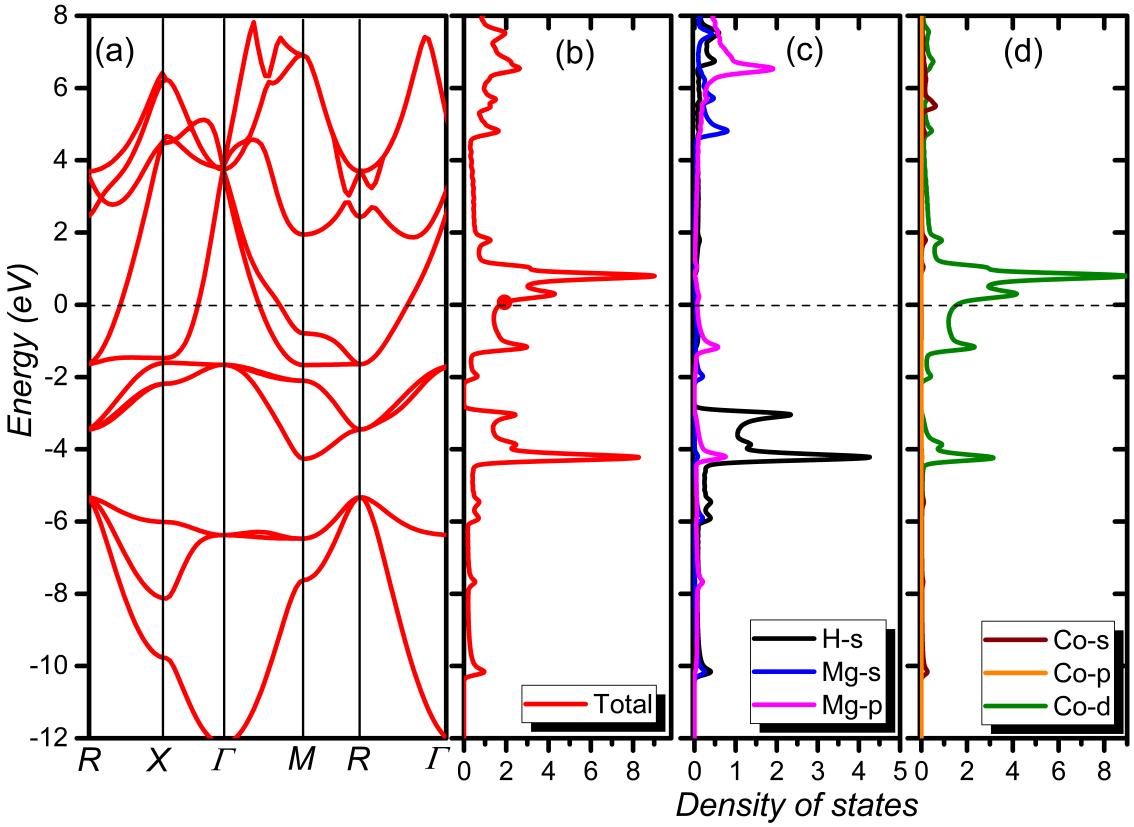

FIGURE 3.3: (a) Electronic band structure for the cubic phase $MgCoH_3$, (b), (c) and (d) the corresponding density of states

3.3.2 Phonon dispersion

Once the converged parameters structure were obtained, we directly evaluated the vibrational properties. The method uses a phonon calculated at 0K to see if there are imaginary phonon modes, also called soft mode. The unit-cell of $MgCoH_3$ contains five basis atoms, and therefore there are 15 vibrations modes (equal to 3N, where N represents the number of atoms exist in the unit cell), which are constituted of three acoustics modes (A) and twelve optical (O) modes (3N-3) for any chosen k point. The calculated phonon dispersion relations along high symmetry lines within the first Brillouin zone (BZ) are plotted in Figure 3.4 together with the vibration density of states. As seen in Figure 3.4, the presence of a gap between the acoustic (low frequencies) and optic (high frequencies) phonon modes is due to the large difference in mass between the Mg, Co and H atoms. This gap value is computed to be 30.9 THz, which close to the value 28.53 THz obtained by A. Candan et al. [236]. The calculated phonon frequencies at Γ point obtained under harmonic approximation are 5.66-15.54-16.96-47.01THz. They are close to the theoretical values of 5.27-17.12-18.83-47.48THz [236]. The absence of any imaginary or negative phonon frequencies in the entire Brillion zone (BZ) confirms that $MgCoH_3$ structure is dynamically stable. The vibrational density of state shows two branches of optical phonons separated from the phonon branches of lower frequencies (acoustic phonon). The reason for separation of these branches in the dispersion plot comes from the presence of the light H atoms in the structure. The vibrational density of state curves (VDOS) shows that Mg and Co atoms in the $MgCoH_3$ compound vibrate in the acoustic region (0-7.4THz) while only H atoms are vibrated only in the optical region (15.45-47.21THz).

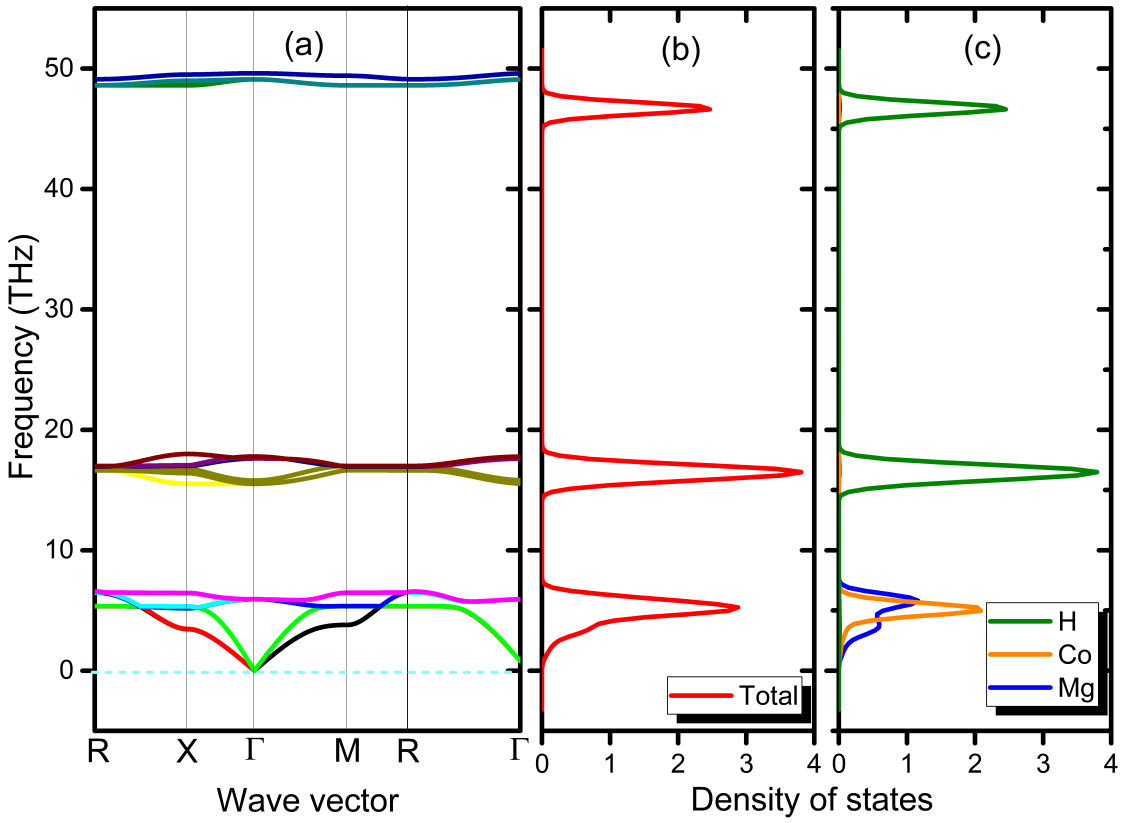

FIGURE 3.4: (a) Phonon band structure with VDOS, (b) and (c) the corresponding vibrational density of states of $MgCoH_3$

3.4 Hydride formation energies and Storage capacities

Hydrogen storage in metal hydrides was possible due to many metals readily able to react with hydrogen, forming a stable metal hydride. Formation energies ΔH_f are an important manner to identify if the predicted phases are likely to be stable (if $\Delta H_f < 0$ the hydride is stable and vice versa). The reaction related to the formation of Perovskite hydride $MgCoH_3$ in our study is:

$$MgCo + \frac{3}{2}H_2 \rightarrow MgCoH_3 \quad \{1\}$$

Based on these reactions, the formation energy of hydride $MgCoH_3$ could be defined as the difference of the total energies between the hydride phase $MgCoH_3$ and sum of H_2 in the gas phase and the energy of MgCo alloy and is firstly calculated by using equation 3.2:

$$\Delta H_f = E_{tot}(MgCoH_3) - E_{tot}(MgCo) + \frac{3}{2}E_{tot}(H_2) \quad (3.2)$$

The hydrogen molecule is simulated by putting its center in the center of a giant cube of parameter a = 30Å, to reduce the interaction between the molecules, while respecting the distance of 0.74Å which separates the centers of the two H atoms. The calculated formation energy value of stain-free $MgCoH_3$ is $-71.30 kJ.mol^{-1}.H_2$, which is in good agreement with the theoretical value -73.32 kJ.mol^{-1}.H_2 obtained in our previous works using the all-electron full-potential local-orbital minimum-basis scheme FPLO9.0034 [221], close to -73.80 kJ.mol^{-1}.H_2 calculated by A. Candan et al. [236] and in the measured interval of some Mg-Co-H systems [79.00, 70.00 kJ.mol^{-1}.H_2] [237, 238]. It can be seen that the formation energy of $MgCoH_3$ is considerably higher, compared with the optimum value -40 kJ.mol^{-1}.H_2 [238, 239], that explains the high stability of the compound. Furthermore, the desorption temperature T_d is an important parameter for the classification of materials applied for hydrogen storage. The formation energy ΔH_f obtained above is used to determine the desorption temperature of the studied compound using the following equation :

$$T_d = \frac{\Delta H_f}{\Delta S} \quad (3.3)$$

Where $\Delta S \approx \Delta S(H_2)$ = 130.7 J.mol^{-1}.K is the entropy variation at standard pressure and temperature of the dehydrogenation reaction. The estimated desorption temperature of Perovskite hydride $MgCoH_3$ is T_d= 545.52 K. Noticeably, this value is still higher than the required range of desorption temperature for practical applications from 289 to 393 K [14]. The formation energies, desorption temperatures and gravimetric/volumetric capacity of the studied systems are reported in Table 3.2.

TABLE 3.2: Formation energy ΔH_f, Desorption temperature T_d and Storage capacities C_g/C_v for unstrained $MgCoH_3$ compound.

System	ΔH_f (kJ.mol^{-1}.H_2)	T_d (°K)	C_g(wt%)	C_v (g.H_2mol^{-1})
The unstrained $MgCoH_3$	-71.30	545.52	3.505	142.52
	-73.32[221]		3.483[221]	137.38[221]
	-62.72[235]	482.42[235]		
	-73.80[236]	560.97[240]		

3.5 Strain effect on the Perovskite-type $MgCoH_3$ structure

3.5.1 Structural properties under strain

Based on the previous results, Perovskite hydride $MgCoH_3$ show high stability and also high decomposition temperature making it thermodynamically stable which prevents its application for mobile hydrogen storage. The application of biaxial strain by values ranging from -6% to $+6\%$ along the a[100] and b[010] directions of $MgCoH_3$ unit-cell was used to reduce this stability, which can lead to an improvement of the dehydrogenation temperature. The unit-cell parameters c/a and cell volume variation under strain of $MgCoH_3$ are represented in Figure 3.5. As a result, the lattice parameter c of $MgCoH_3$ unit-cell is elongated under biaxial compressive strain, resulting in an increase of the ratio c/a compared to that ($\approx$ 1) of strain-free state. The c/a ratio reaches a highest value of 1.0767 at the compressive strain of -6%. Comparatively, under biaxial tensile strain, the $MgCoH_3$ lattice along z axis direction shrinks, giving a decreasing of c/a ratio relative to that of unstrained state. A minimum of 0.933 is found at the tensile strain of $+6\%$. Furthermore, by increasing the strain conditions applied to Perovskite hydride $MgCoH_3$, the volume increases in the opposite direction from 31.37 Å^3 at -6% to 38.97 Å^3 at $+6\%$ strain. The same comportment is reported for $LiBH_4$ and MgH_2 under strain conditions [225, 226]. So, it can be concluded that the biaxial tensile/compressive strain is

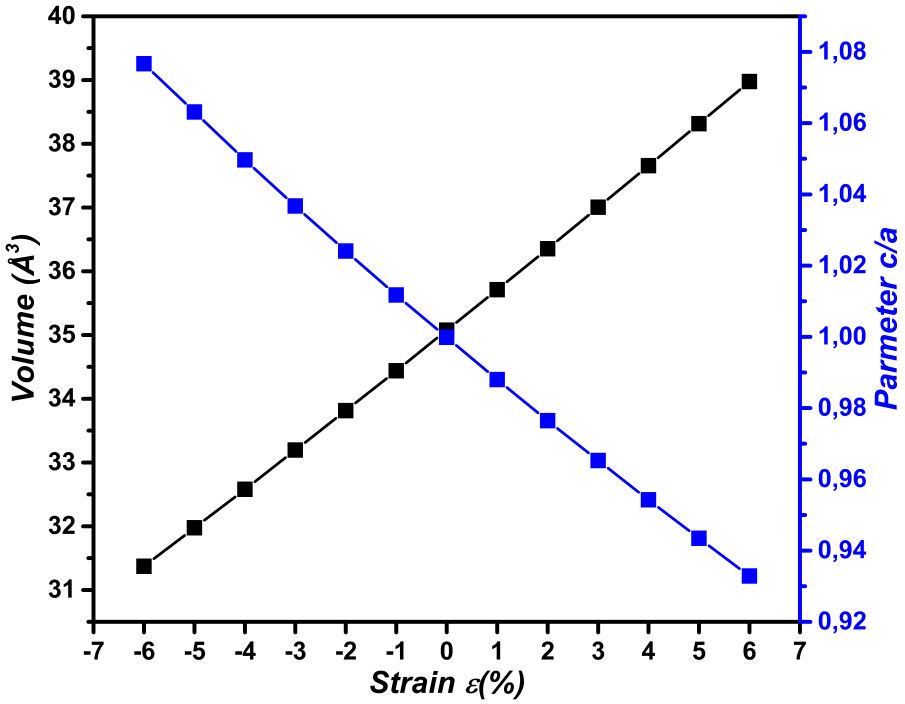

FIGURE 3.5: Representation of c/a parameter and volume in terms of the biaxial strain on $MgCoH_3$

probably to cause a structural and interatomic distance deformation of $MgCoH_3$ crystal and the distortion lattice becomes severe with increasing of biaxial strain. Figure 3.6 shows the phonon dispersion of $MgCoH_3$ compound under compressive strains. Based on the findings results plotted in the Figure 3.6, the absence of the negative frequencies is observed for the Perovskite hydride $MgCoH_3$ compound under strain. This means that the strained compound is also dynamically stable. The vibration of the hydrogen of strained $MgCoH_3$ is more independent than that of the free one because of the increase on lattice distortion, which explain the reduction of stability for strained $MgCoH_3$ lattice (increase of the formation energy).

3.5.2 Dehydrogenation properties

The formation energy of strained $MgCoH_3$ systems are calculated using the same method, by proposing that the strained hydrides are decomposed completely into the strain-free solid $MgCo$ and gaseous H_2 molecule and the desorption temperature were also calculated by using equation 3.2. The obtained results of the formation energy and desorption temperature as function of biaxial strain in $MgCoH_3$ unit cell are plotted in Figure 3.7.

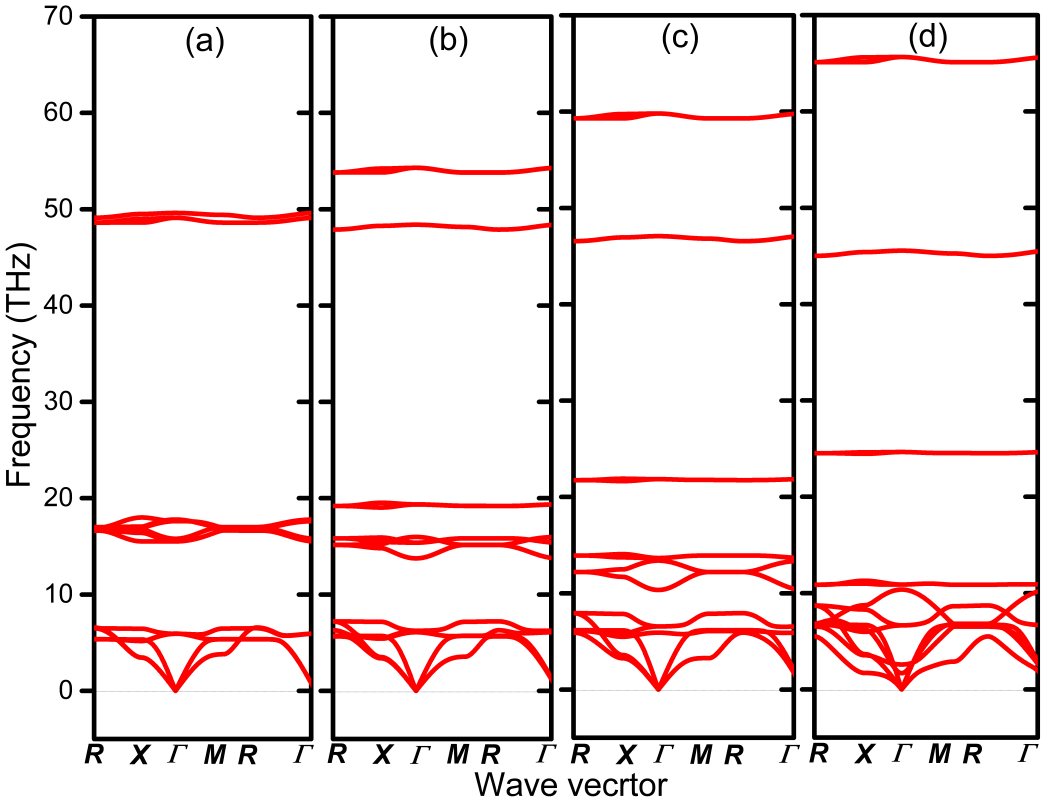

FIGURE 3.6: Phonon dispersion curves of $MgCoH_3$ hydride under biaxial strain of (a) 0%, (b) -2%, (c) -4% and (d) -6%.

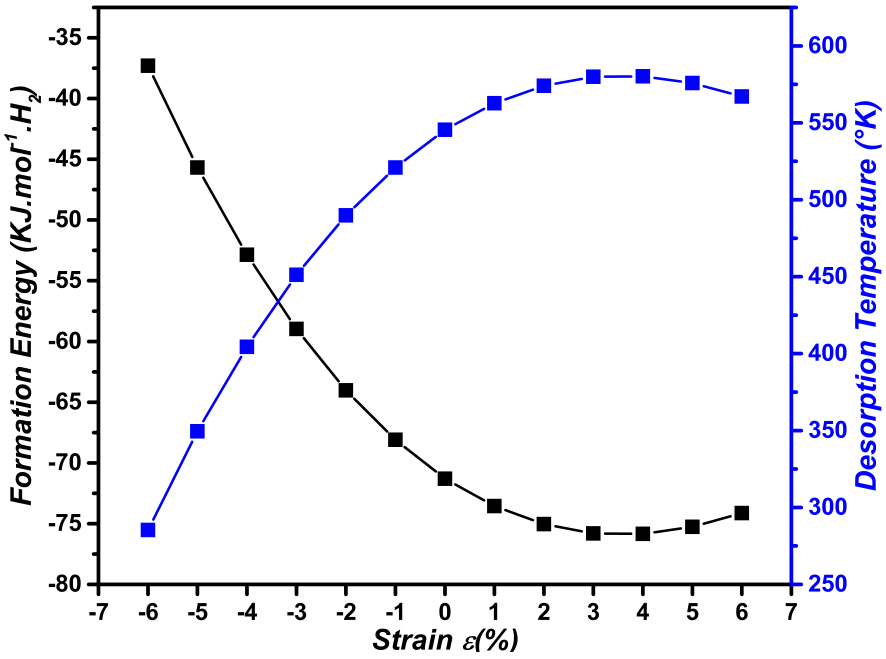

FIGURE 3.7: The formation energy and desorption temperature according to biaxial strain $\epsilon(\%)$ in the structure $MgCoH_3$.

It can be seen from Figure 3.7 that under biaxial compression, the calculated formation energies all strained $MgCoH_3$ systems are all increased with increasing strain magnitude as compared with that of strain-free one, which reduces the stability and the desorption temperature of the hydride. The obtained results show that the formation energy shifted from -71.30 kJ/mol.H_2 for the free-strain $MgCoH_3$ structure to -37.29 kJ/mol.H_2 for the $MgCoH_3$ structure under the compression of -6% strain. Therefore, the gain of 34 kJ/mol.H_2 was obtained for $MgCoH_3$ compound by application of biaxial compression strain. This suggests that effect of the either biaxial compressive strain to $MgCoH_3$ material is efficacy for the enhancement of dehydrogenation thermodynamics because of strain energy contribution. Noticeably, the compression strain effect is found to be more remarkable than that of tensile one due to the relatively higher formation energy values as well as the desorption temperature.

3.5.3 Diffusion activation energy of hydrogen

The dehydrogenation mechanism in metal hydrides systems, is complex and mainly includes hydrogen atom or vacancy diffusion, nucleation, phase growth and surface desorption [241]. Among of them, the hydrogen diffusion and migration in hydride

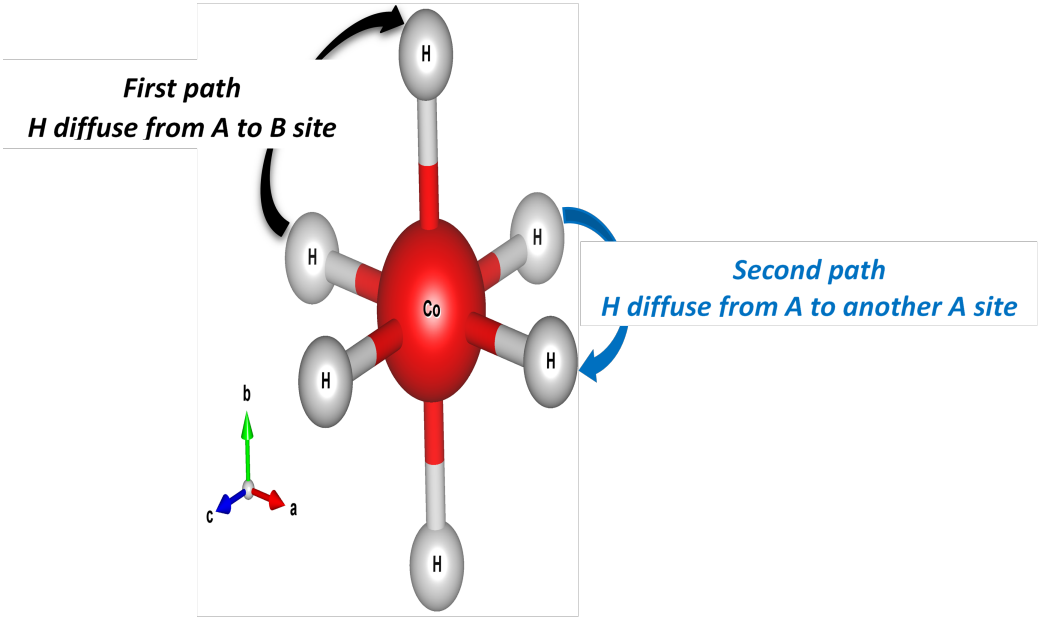

FIGURE 3.8: Schematic view of the diffusion pathways of hydrogen atom from A to B site or from A to another A site in $MgCoH_3$.

phase has been found to be an important rate-limiting step. In order to estimate the energy barrier for diffusion through the Perovskite hydride model and to evaluate the dehydrogenation kinetics, two diffusion paths of hydrogen atom in $MgCoH_3$ super-cell are considered in the present work: In the same distance, each hydrogen atom has eight nearest neighbors available sites, which is illustrated by the first path (diffusion from A to B site after H desorption) and the second path (diffusion from A to A site). The two different pathways for the diffusion of hydrogen atom are presented in Figure 3.8. Figure 3.9(a) and (b) shows the diffusion energy profiles, i.e. activation energies of H for the first and second pathways respectively in the (un)strain structure of $MgCoH_3$. The free strain diffusion energy barrier of hydrogen atom for the first path is 0.55 eV similar with that of the second path, which is slightly lower than the value obtained previously (0.67 eV). It can be concluded that the hydrogen atom diffusion behavior along the first and second pathways is almost identical. Moreover, the diffusion energy barriers values of first and second paths in all strained $MgCoH_3$ (compression) are all determined from Figure 3.9. Based on the results, under the compression strain, the diffusion energy barrier of hydrogen atom along the first path increase from 0.55 eV to 0.635 eV. Otherwise, the diffusion activation energy of hydrogen atom decreases by increasing the compression, from 0.552 eV to 0.518 eV for the second path, which means that the hydrogen atom

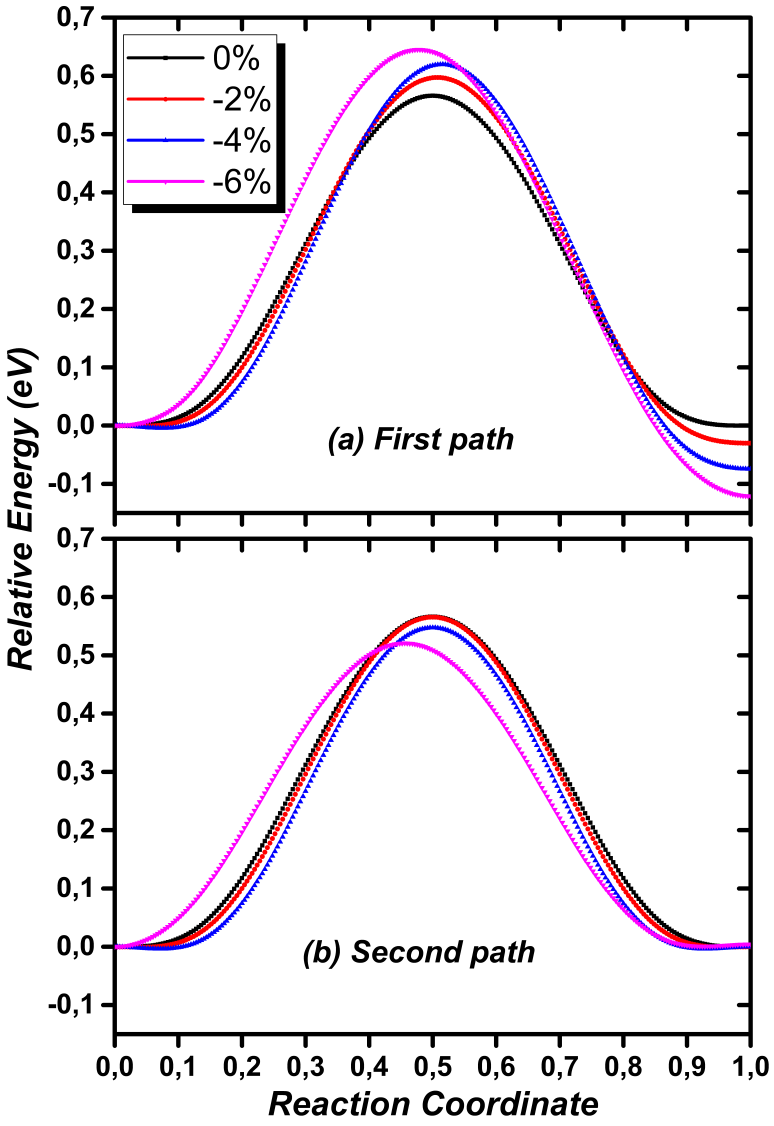

FIGURE 3.9: Energy curves for diffusing hydrogen between two interstitial sites along (a) the first path and (b) second path as function of biaxial strain in $MgCoH_3$.

prefers to diffuse along X and Y direction instead of moving vertically with compression strain effect. The decrease of diffusion energy barriers suggests the improvement of the dehydrogenation kinetics in Perovskite hydride $MgCoH_3$. The reasons of the above obtained results using biaxial compression strain effect can be explained by two things: The interatomic distances between hydrogen and the others atoms and the diffusion paths. For the first path, the interatomic distances between hydrogen and magnesium atom become small (from 2.32Å for 0% to 1.96Å for -6%) in the directions of stain effect and also the increase in diffusion paths for hydrogen atoms making the activation barriers more important under compression strain. Otherwise, for the second path, the reduction

in diffusion paths for hydrogen atoms make the barrier smaller in comparison with the first path.

3.5.4 Electronic charge density

To identify the bonding nature between the elements forming the $MgCoH_3$ compound, the calculations density distributions were investigated and displayed in the Figure 3.10 for different planes as function of compression strain magnitude. For unstrained $MgCoH_3$, the Co-H bond contours are not completely isolated which indicate that the Co-H bond exhibits a mixture of an ionic-covalent bond (see Figure 3.10(a)). The applying compressive strain leads to decrease/increase the bond lengths and to change the distribution of density around the hydrogen and cobalt atoms. Also, the bond length between atoms become shorter in the biaxial strain direction than the free one. It should be mentioned also, that for the –6% a bridge between Co and H atoms is formed leading to a strong charge transfer in both directions comparing to the unstrained case, which weakens the ionic bonding between Co and H and makes it easy to remove hydrogen from the perovskite framework. Moreover, the application of compression enhances the electronic charge overlapping between Cobalt and hydrogen. This leads to the localization of charges between Co and H atoms and thus increases the covalent bonds between them (Figure 3.10(b), (c), and (d)).

3.6 Thermodynamic properties

3.6.1 Vibrational enthalpy and Entropy

Based on phonon frequencies throughout the BZ, the thermodynamic properties of hydride $MgCoH_3$ can be determined with the variation of temperature within the quasi-harmonic approximation listed in the chapter 2 using Phonopy software. Thermodynamic quantities, such as Helmholtz Free Energy F, Internal Energy H_{vib}, Entropy S_{vib}, and Constant-Volume Heat C_v help to evaluate some important features of a material like its behavior under temperature. Figure 3.11 shows the change in the Helmholtz Free Energy and volume with increasing temperature from 0 to 1000 K, respectively. By increasing the temperature, the volume dependence of the phonon free energy changes, hence the equilibrium volume of stain-free $MgCoH_3$ changes at each given temperature

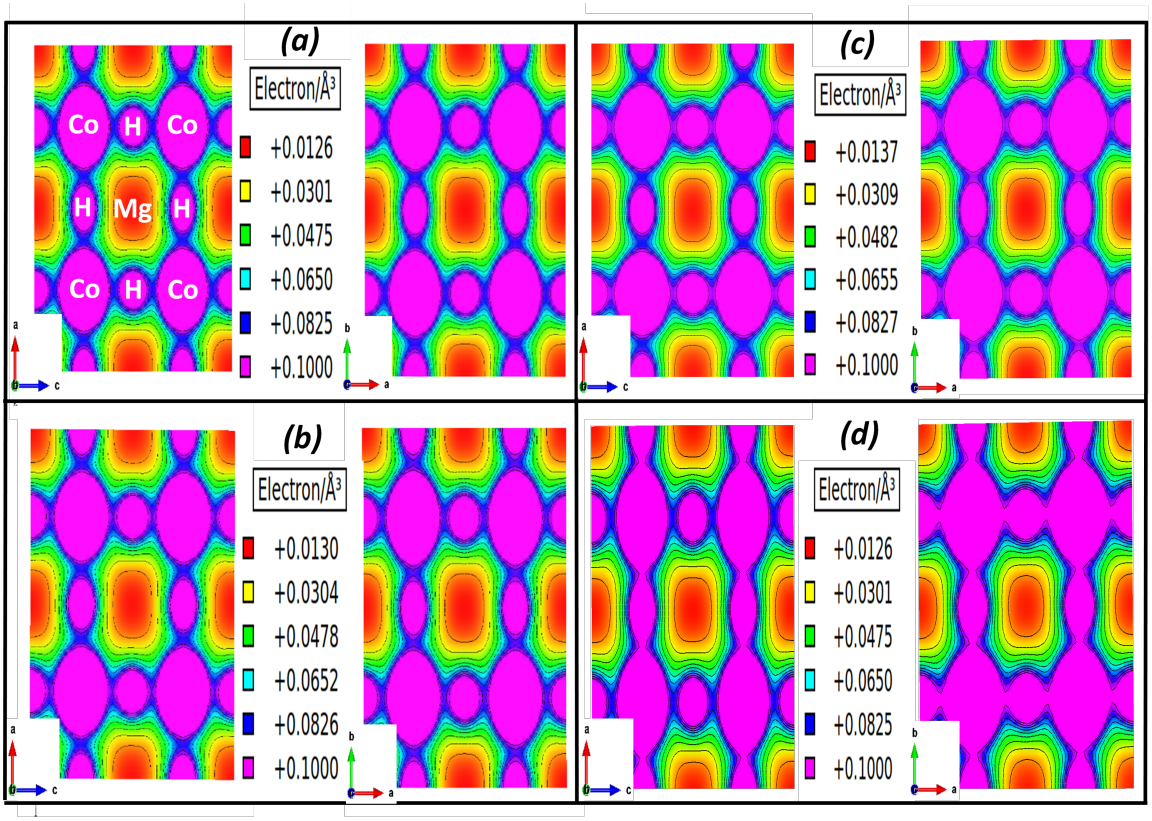

FIGURE 3.10: Electron density distribution for $MgCoH_3$ for different values of strain. (a) 0%, (b) -2%, (c) -4% and (d) -6%. The magnitude of the charge density showed by different colors.

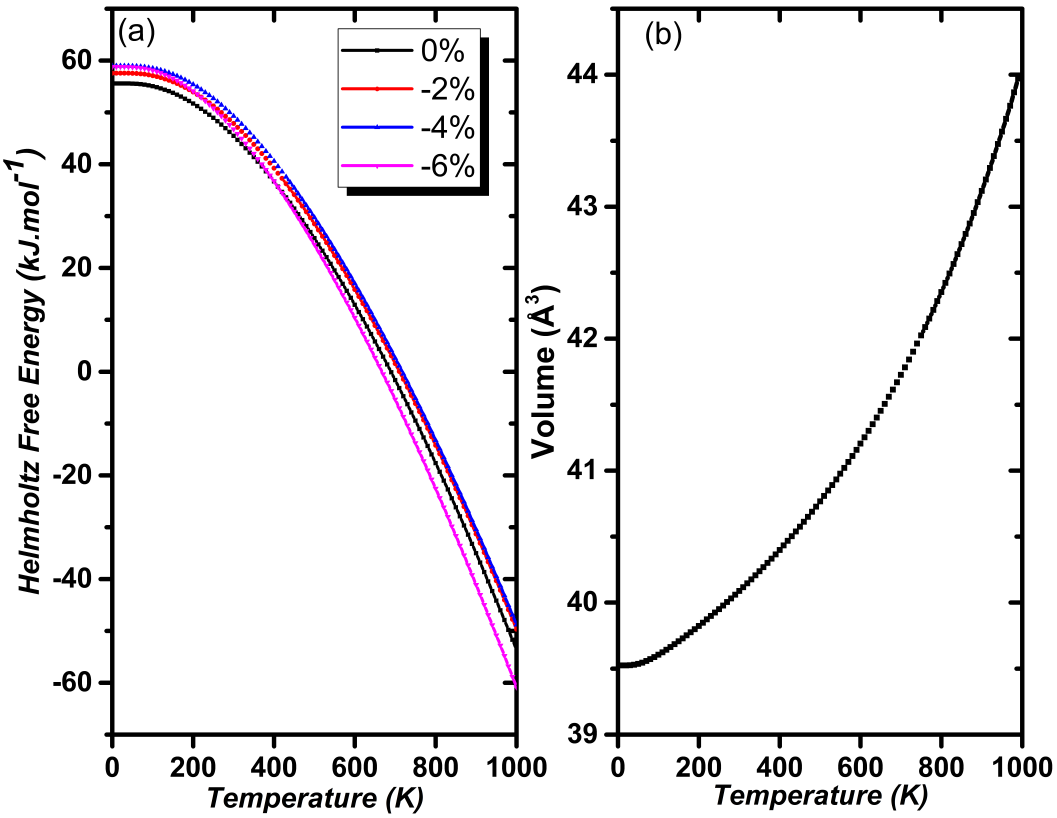

FIGURE 3.11: (a) Helmholtz free energy versus temperature under compressive strain and (b) the variation of volume on unstrained $MgCoH_3$.

and it becomes higher with increase of temperature (see Figure 3.11(b)). The Helmholtz Free Energy decreases from about 53.483 to $-58.907 kJ/mol$ (for stain-free $MgCoH_3$) when the temperature increases from 0 to 1000 K (Figure 3.11(a)). It is worthwhile noting that the zero-point energy ZPE can be found from the expression of H_{vib} at T= 0K (equation 2.40). The Figure 3.12 presents the computed H_{vib} and S_{vib} of $MgCoH_3$ compound in terms of temperature and for different compressive strain values. The functions H_{vib} and S_{vib} exhibit similar temperature dependencies for the $MgCoH_3$ structure. It can be observed from Figure 3.11(a) that the ZPE is found to be $53.48 kJ.mol^{-1}$ for unstrained system and slightly increase with the strain magnitude. The internal energy H_{vib} increase almost linearly when the temperature becomes greater than 300 K, tending to display $k_\beta.T$ behavior for all systems.

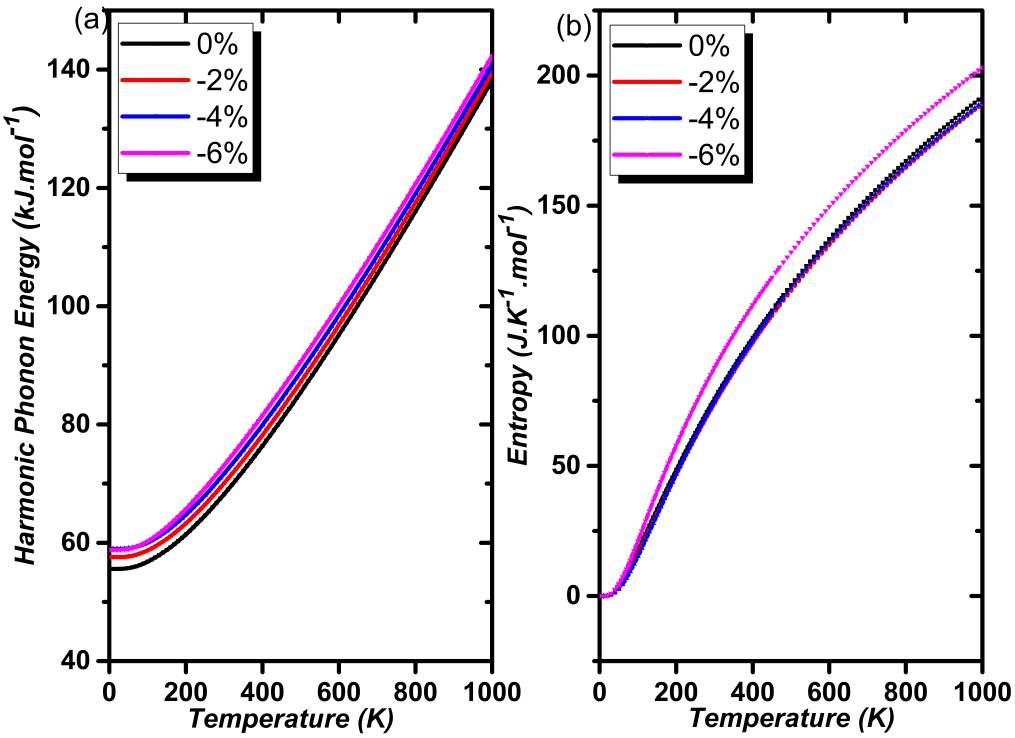

FIGURE 3.12: (a) Harmonic phonon energy and (b) Entropy versus temperature under compressive strain.

3.6.2 Heat capacity

The molar heat capacity C_v has importance in terms of energy, time and costs involved in changing temperatures of objects. Hence it is important as it will present a notion of how much energy will be appropriate to heat or cool an object of a given mass by a given supply. This will give information as to how long the heating or cooling process will take under a given supply. The classic Dulong-petit law reported that the heat capacity per mole of many solid elements is about 3R, where R presents the gas constant in joule per kelvin per mole. The $MgCoH_3$ unit cell contains five atoms, based on the Dulong-petit law, the specific heat per primitive cell is 15R. this value can be obtained using the equation 2.42 when the temperature tends to infinity. As illustrates in Figure 3.13, it is observed that the specific heat capacity at constant-volume (C_v) tends to $C_v \propto T^3$ behavior at low temperature, while the C_v is close to a constant value limit of $124.71 J.K^{-1}.mol^{-1}$ at high temperature. According to Figure 3.13, the C_v of unstrained $MgCoH_3$ increases quickly from 0 to about $80 J.K^{-1}.mol^{-1}$ when the temperature increases from 0 to 300 K and after that the C_v increase slowly approaching to the classical Dulong-Petit asymptotic

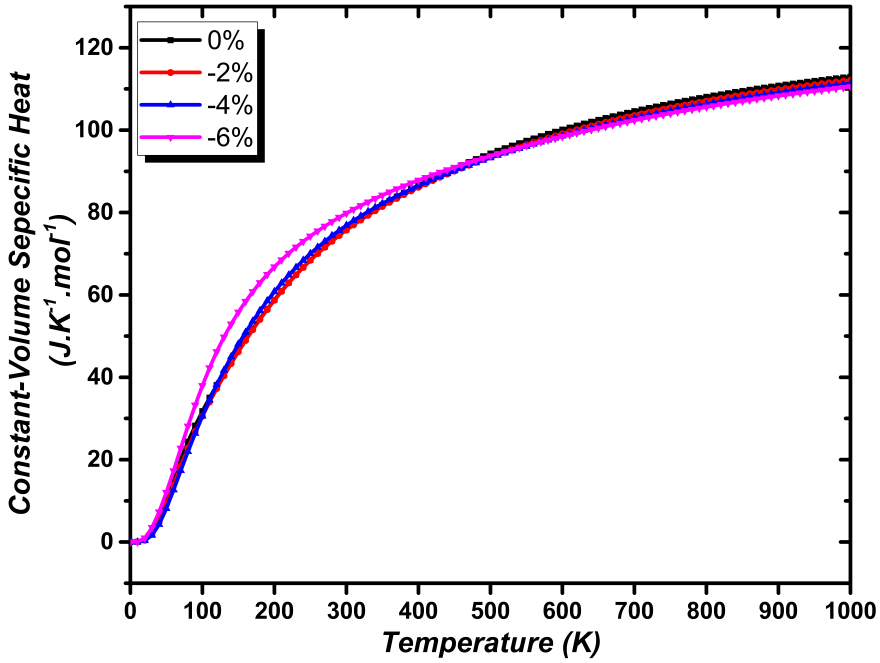

FIGURE 3.13: Heat capacity of $MgCoH_3$ under biaxial strain versus temperature.

limit discussed above. Our finding value of the specific heat of unstrained material is in complete agreement with the previous reported theoretical value of specific heat. At low temperature, with the increasing of strain magnitude the lattice heat capacities of the systems have small increases as compared with the unstrained perovskite compound $MgCoH_3$.

3.7 Conclusion

First-principles calculations were used to study the biaxial compressive strain effect on the structural, vibrational, stability, dehydrogenation thermodynamic and kinetic properties in Perovskite $MgCoH_3$ hydride. Using the DFT method, we have shown on the one hand that the strain improves the thermodynamic properties and kinetics hydrogenation of the material as summarized in what follow:

- The biaxial compressive strain tends to lead to the structural deformation of $MgCoH_3$ crystal, and the lattice distortion becomes severe with increasing magnitude of strain.

- Due to the contribution of strain energy, the formation energy, desorption temperature as well as hydrogen diffusion activation energies for strained $MgCoH_3$ hydride are all improved relative to that of strain-free system.
- The formation energy shifted from -71.30 kJ.mol^{-1}.H_2 to -37.29 kJ.mol^{-1}.H_2 under the compression of -6% strain and the hydrogen release started at 285.34 K compared with 545.52 K for free strained $MgCoH_3$.
- All system of $MgCoH_3$ perovskite-type hydrides are found to be energetically, mechanically and dynamically stable.

4 Effect of doping in hydrogen storage properties of Perovskite $MgCoH_3$

4.1 Introduction

The perovskite compounds with ABX_3 formula have taken attention in recent years due to their desirable properties and potential technological applications such as sunlight-to-fuel conversion, solar cells, light emitting devices, hydrogen storage, sensors photodetectors and lasers [242, 243]. In this case, the possible combinations of ABX_3 perovskite consist of considering the A and B elements as monovalent and/or divalent cations and X as an anion [244–246]. The perovskite hydride ABH_3 having high hydrogen content are very attractive due to their potentials for hydrogen and energy storage applications [247, 248]. Recent theoretical and experimental studies have been also carried out to examine the hydrogen storage properties of perovskite type materials [249, 250]. From this viewpoint, the theoretical analysis of all properties of the perovskite-type $MgCoH_3$ such as structural, electronic, thermodynamic, vibrational and stabilities have been done using density functional theory (DFT). However, its high thermodynamic stability ($71.30 kJ/mol.H_2$) and high desorption temperature ($545.52 K$) is still an issue that needs to be overcome and limits its large-scale industrial and technological applications. For this reason, the substitution effect on the perovskite-type compounds $MgCoH_3$ with lightweight element boron (B) or lithium (Li) has been examined in order to improve its hydrogen storage characteristics and to be close to the optimum targets for the practical application ($289 - 393 K$ and $-40 kJ.mol^{-1}.H_2$) [238, 239].

4.2 Computational details

The calculations have been done using Quantum Espresso code (QE) by implementing the plane wave pseudo potential method (PWSCF) within the framework of density functional theory (DFT) [227, 228] in order to solve the Kohn-Shame equation [205]. The electronic exchange correlation potential was performed within the generalized gradient approximation (GGA) in the form of Perdew-Burke-Ernzerhof (PBE) functional [229]. The plane wave cutoff kinetic energy for all calculations was set to $59Ry$ ($800eV$) and the k-point grids [230] for the Brillouin zone integration was sited to be 6x6x6 for the supercell, which ensures a high accuracy in our calculations. By minimizing the Hellmann-Feynman forces and stresses, The atomic positions, the cell parameters and the cell volume were all relaxed without any symmetry constraint using the Broyden–Fletcher–Goldfarb–Shanno method (BFGS) [231]. The convergence energy in the self-consistent cycle was selected to be $10^{-10}Ry$ and the visualization of all atomic structures were performed using the VESTA program [232]. In order to guarantee dynamic stability, the phonon dispersion curves of the perovskite hydrides have been calculated with phonopy software [233] based on the finite-displacement and Parlinski-Li-Kawazoe method [234]. Furthermore, the lattice thermal properties such as Helmholtz Free Energy, Internal Energy, Entropy, and Constant-Volume Heat were evaluated by employing the quasi-harmonic approximation (QHA).

4.3 Lightweight element substituted Perovskite-type $MgCoH_3$

4.3.1 Crystal structure and optimization

The hydride $MgCoH_3$ crystallizes in body-centered cubic (BCC). Its space group is Pm-3m (No.221) and the cell parameter is found to be $a_0 = 3.278$Å. The $MgCoH_3$ structure has 5 formula units (f.u) per cell, where Mg and Co occupy the Wyckoff positions 1a(0, 0, 0) and 1b(1/2, 1/2, 1/2), respectively. The H atoms occupy the octahedral sites 3c(1/2, 1/2, 0), (1/2, 0, 1/2) and (0, 1/2, 1/2). To study the hydrogenation properties of $MgCo_{1-x}M_xH_3$ (M=Li or B; x = 0.125, 0.25 and 0.50), the calculations have been carried out using a 2×2×2 supercell, which allows us to reach such concentrations (see Figure 4.1(b)). The proposed substitution compositions (12.5%,25% or 50%) are achieved by substituting the

TABLE 4.1: Lattice parameters (a), Volume (V) and interatomic distances (d) between different neighboring atoms of $MgCo_{1-x}M_x$ and $MgCo_{1-x}M_xH_3$ systems (M=Li or B and x=0, 0.125, 0.25 or 0.50)

System	a(Å)	V(Å^3)	d(Å)					
			Mg-Co	Co-H	Mg-H	M-H	M-Mg	M-Co
$MgCo$	2.99 3.026[221] 3.07[235]	26.73 27.70[221]	2.59	-	-	-	-	-
$MgCoH_3$	3.27 3.31[221] 3.33[235] 3.281[236]	35.23 36.26 36.9[235]	2.84	1.64 1.665[235]	2.32	-	-	-
$MgCo_{0.875}Li_{0.125}$	3.07	28.93	2.65	-	-	-	2.67	3.07
$MgCo_{0.875}Li_{0.125}H_3$	3.285	35.49	2.85	1.58/ 1.63	2.32/ 2.82	1.7	2.86	4.64
$MgCo_{0.75}Li_{0.25}$	3.083	29.30	2.61/ 2.64	-	-	-	2.58	3.04
$MgCo_{0.75}Li_{0.25}H_3$	3.287	35.51	2.84	1.59 1.64	2.32	1.699	2.846	4.648
$MgCo_{0.5}Li_{0.125}$	3.12	30.34	2.7	-	-	-	2.70	3.12
$MgCo_{0.5}Li_{0.5}H_3$	3.294	35.76	2.85	1.60	2.33	1.691	2.853	4.659
$MgCo_{0.875}B_{0.125}$	3.038	28.04	2.616	-	-	-	2.585	3.038
$MgCo_{0.875}B_{0.125}H_3$	3.281	35.32	2.837	1.62/ 1.75	2.31/ 2.33	1.52	2.846	4.626
$MgCo_{0.75}B_{0.25}$	3.022	27.56	2.618	-	-	-	2.618	3.02
$MgCo_{0.75}B_{0.25}H_3$	3.259	34.61	2.82	1.63/ 1.74	2.307	1.518	2.82	4.61

Co atoms with either Li or B. The optimized structures are given in Figure 4.1. The equilibrium parameter constant, cells volumes and interatomic distances (intermetallic and their hydrides) are summarized in the table 4.1 along with the available theoretical values [221, 235, 236]. The results that are obtained in this study are in accordance with other investigations. For these systems, it can be concluded that the incorporation of light element (Li or B) with contents range from 12.5% to 50%, generates a slight variation of the cell volume and lattice parameters because of the different atomic radius of Co (152pm), Li (167pm) and B (85pm). However, the new systems compositions preserve the crystal periodicity and the same cubic structure as pure $MgCoH_3$.

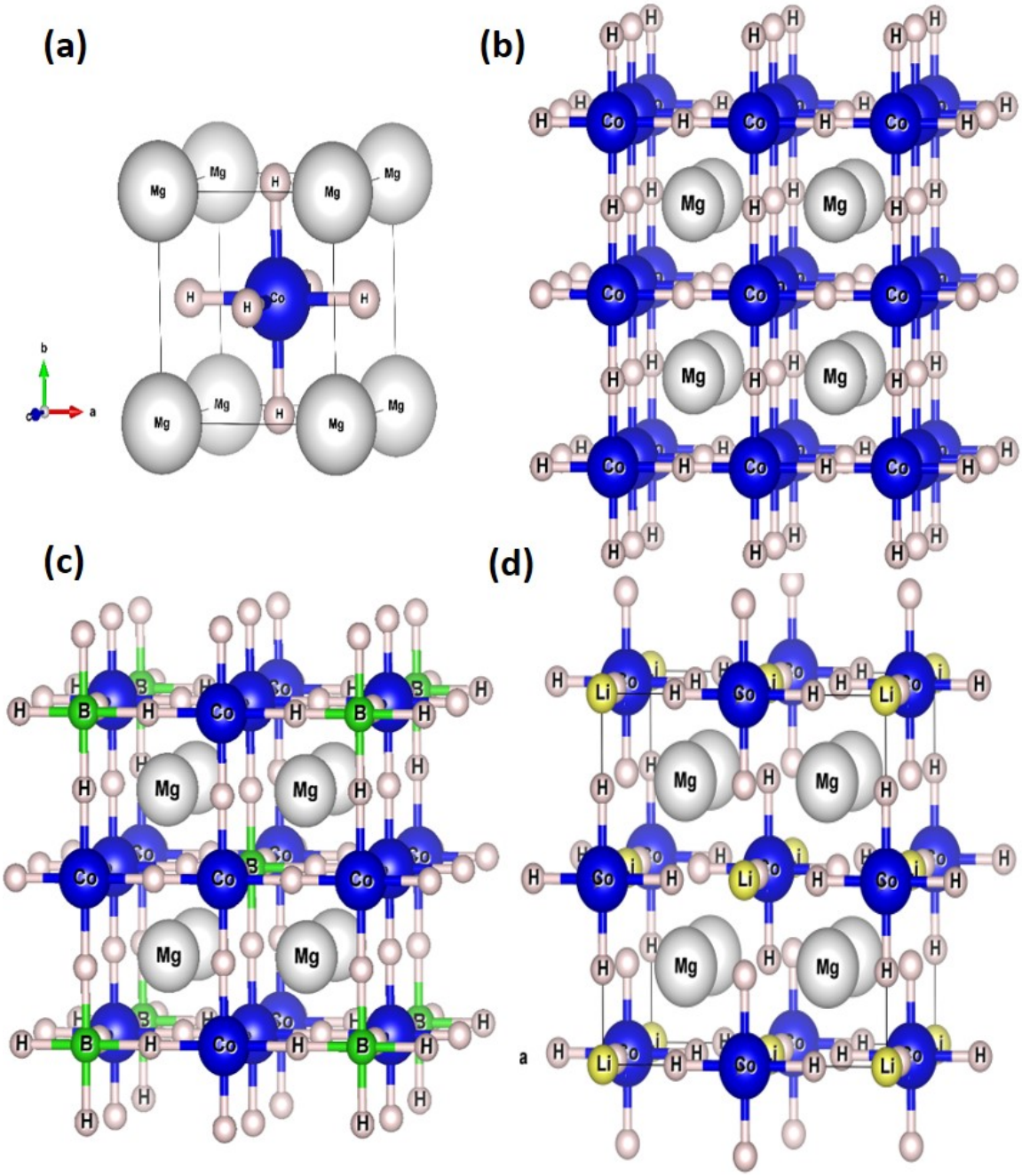

FIGURE 4.1: Crystal structure (a) unit-cell, (b) 2x2x2 super-cell of $MgCoH_3$ (c) $MgCo_{0.75}B_{0.25}H_3$ and (d) $MgCo_{0.50}Li_{0.50}H_3$

4.3.2 Hydrogen storage properties

The formation energy ΔH_f is an excellent way employed to characterize and identify hydrogen storage materials stability. The hydrides with a lower formation energy are considered to be more stable, which leads to difficult release of the hydrogen from hydrides and therefore the need for a high temperature. The formation energy required for ideal materials for hydrogen storage should be around to the optimum value $-40\text{kJ.mol}^{-1}.H_2$ [238, 239]. To analyze the possibility of forming compound of $MgCoH_3$ substituted by either Li or B with different contents x, the following chemical reactions is considered in our study:

$$\text{MgCo} + \frac{3}{2}\text{H}_2 \rightarrow \text{MgCoH}_3 \qquad \{2\}$$

$$\text{MgCo}_{1-x}\text{M}_x + \frac{3}{2}\text{H}_2 \rightarrow \text{MgCo}_{1-x}\text{M}_x\text{H}_3 \qquad \{3\}$$

Where M=Li or B and x=0.125,0.25 or 0.50. The formation energy of hydride $MgCoH_3$ and the related $MgCo_{1-x}M_xH_3$ were calculated by Hess's law as the difference between the total energies of products and reactants. Based on these reactions, the formation energies of $MgCoH_3$ and $MgCo_{1-x}M_xH_3$ hydrides are defined using the following equations:

$$\Delta H_f = E_{tot}(MgCoH_3) - E_{tot}(MgCo) + \frac{3}{2}E_{tot}(H_2) \qquad (4.1)$$

$$\Delta H_f = E_{tot}(MgCo_{1-x}M_xH_3) - E_{tot}(MgCo_{1-x}M_x) + \frac{3}{2}E_{tot}(H_2) \qquad (4.2)$$

Furthermore, the desorption temperature T_d represents an important parameter for the selection of materials applied for hydrogen storage. The formation energy ΔH_f is used to estimate the desorption temperature of the studied hydrides using the equation $\Delta H_f = T_d.\Delta S$, where $\Delta S \approx \Delta S(H_2)$ = 130.7 J.mol^{-1}.K is the variation of the entropy of the dehydrogenation reaction at standard conditions. Noticeably, the required value of desorption temperature for practical applications should be in the range from $289K$ to $393K$ [14]. The formation energies, desorption temperatures and gravimetric/volumetric capacity of the evaluated systems are listed in Table 4.2.

As shown in Table 4.2, the formation energy and the desorption temperature of perovskite-type $MgCoH_3$ are found equal to $\Delta H_f = -71.30\text{kJ.mol}^{-1}.H_2$ and $T_d = 545.52K$, respectively, which is in good accordance with the theoretical values $\Delta H_f =$

$-73.80\text{kJ.mol}^{-1}.H_2$ calculated by A. Candan et al. [236]. We mention that these values are also close to the theoretical values $\Delta H_f = -73.32\text{kJ.mol}^{-1}.H_2$ and $T_d = 560.97K$ obtained previously by the authors using the all-electron full-potential local-orbital minimum-basis scheme FPLO9.0034 [221]. Since the perovskite-type hydride $MgCoH_3$ is relatively stable hydride with high desorption temperature, Co has been replaced by lighter elements Li or B with concentrations of 12.5% and 25%.

According to the obtained results, it is shown that the substitution of Co by Li and B with various concentration x increases the formation energy (see Table 4.2), which reduces the stability and the desorption temperature of the hydrides. The obtained values are equal to $\Delta H_f = -44.68\text{kJ.mol}^{-1}.H_2$, $Td = 341.87K$ for $MgCo_{0.5}Li_{0.5}H_3$ and $\Delta H_f = -39.56\text{kJ.mol}^{-1}.H_2$, $Td = 302.67K$ for $MgCo_{0.75}B_{0.25}H_3$. The destabilization effect on $MgCo_{1-x}M_xH_3$ becomes important in the case of boron compared to lithium by increasing the concentration x and consequently, reach the optimum characteristics range ($-40\text{kJ.mol}^{-1}.H_2$ and $289-393K$) for PEMFC application [14].

It follows from the obtained results above (see Table 3.1) that the substitution of Co by light elements leads to an expansion of volume in the case of $MgCo_{0.875}Li_{0.125}H_3$, $MgCo_{0.75}Li_{0.25}H_3$ and $MgCo_{0.5}Li_{0.5}H_3$, and a contraction of $MgCo_{0.75}B_{0.25}H_3$. The expansion of the volume leads to a small decrease in the volumetric capacity of $MgCoH_3$ doped Li from 142.52 to $140.4\text{g}.H_2.\text{L}^{-1}$, while the volume contraction leads to an increase in volumetric capacity for $MgCoH_3$ doped B to $145.02\text{g}.H_2.\text{L}^{-1}$. On the other hand, it was proved that the substitution of perovskite-type $MgCoH_3$ with light elements Li or B affects positively the system gravimetric capacities. The gravimetric capacity shifted to $5.017wt\%$ for $MgCo_{0.5}Li_{0.5}H_3$ and $4.073wt\%$ for $MgCo_{0.75}B_{0.25}H_3$ compared with the value $3.505wt\%$ for pure $MgCoH_3$.

It can be concluded that the hydrides $MgCo_{0.75}B_{0.25}H_3$ and $MgCo_{0.50}Li_{0.50}H_3$ will satisfy several requirements for hydrogen storage material in solid-state: (i) stability $-40\text{kJ.mol}^{-1}.H_2$; (ii) desorption temperature in the range $289-393K$; (iii) volumetric capacity of $30-50\text{g}.H_2\text{mol}^{-1}$ and gravimetric capacity $4.5-5.5wt\%$ for practical use as reported by the US-DOE (United states Department of Energy). Hence, it can be considered as a promising candidate material for H_2 storage at room temperature.

TABLE 4.2: Formation energy ΔH_f, Desorption temperature T_{des} and Storage capacities C_g/C_v for perovskite hydride compounds.

Systems	ΔH_f (kJ.mol^{-1}.H_2)	T_d (°K)	C_g(wt%)	C_v (g.H_2.mol^{-1})
$MgCoH_3$	-71.30 -73.32[221] ,-62.72[235] -73.80[236]	545.52 482.41[235] 560.97[236]	3.505 3.483[221]	142.52 137.38[221]
$MgCo_{0.875}Li_{0.125}H_3$	-61.1	467.34	3.791	141.6
$MgCo_{0.75}Li_{0.25}H_3$	-58.02	443.93	4.127	141.4
$MgCo_{0.50}Li_{0.50}H_3$	-44.68	341.87	5.017	140.41
$MgCo_{0.875}B_{0.125}H_3$	-51.61	394.89	3.768	143.49
$MgCo_{0.75}B_{0.25}H_3$	-39.56	302.67	4.073	145.02

4.3.3 Electronic properties of doped systems

To understand and explain the de/hydrogenation performance of $MgCoH_3$ associated with the substitution of Co by lightweight elements Li or B, the total density of states (DOS) and the projected density of states (PDOS) of pure and modified $MgCoH_3$ structure have been performed. The total and partial density of state curves of both pure $MgCoH_3$ and substituted $MgCo_{1-x}M_xH_3$ (M=Li or B, x=0.125, 0.25 or 0.50) are computed and presented in figure 4.2 . As a reference, the Fermi level (E_F) is set to zero (dotted line). According to DOS and PDOS of $MgCoH_3$ (see Figure 4.2 (a)), it is noticed that the compound exhibits a metallic character due to the overlap between the valence and conduction bands at the fermi level. Furthermore, the valence band of pure $MgCoH_3$ is divided into two distinct regions. The region I covers the band energy range from -10.00 to -5.00 eV, which is composed of a strong hybridization between H-s, Mg-(s, p) and Co-d states. The region II, with an energy between -4.00 and -0.00 eV consists of the d-orbitals of Co atoms, s- and p-orbitals of Mg atom. Beyond the Fermi level, the DOS is dominated by the Mg-(s, p) states. The strong hybridization between H, Mg and Co states may explain the high stability and high decomposition temperature obtained earlier for the pure $MgCoH_3$ system.

On the other hand, the influence of substituting Co by light element (M=Li or B) on both stability and desorption temperature of the $MgCoH_3$ compound has been explained using the density of state. As shown in figure 4.2(b)-(f), the overall shapes of the electronic structure are similar to each other, signifying that the system preserves the same electronic behavior as observed in pure $MgCoH_3$. It is also important to observe that the valence

band (VB) reveals the creation of a new orbital hybridization between Co-M(s,p), Mg-M(s,p), and H-M(s,p). However, the contribution of the conduction band (CB) is fully ascribed to Mg(s,p) and M(s,p) states. As expected, after the substitution of Co by light elements M (M=Li or B), the creation of a novel bond between elements weakens the existing strong bonding between elements and interstitial hydrogen, which comes at the expense of the already existing bond in the case of pure $MgCoH_3$. Consequently, substitution reduces simultaneously the stability and the desorption temperature of the systems, which is in agreement with the results discussed above.

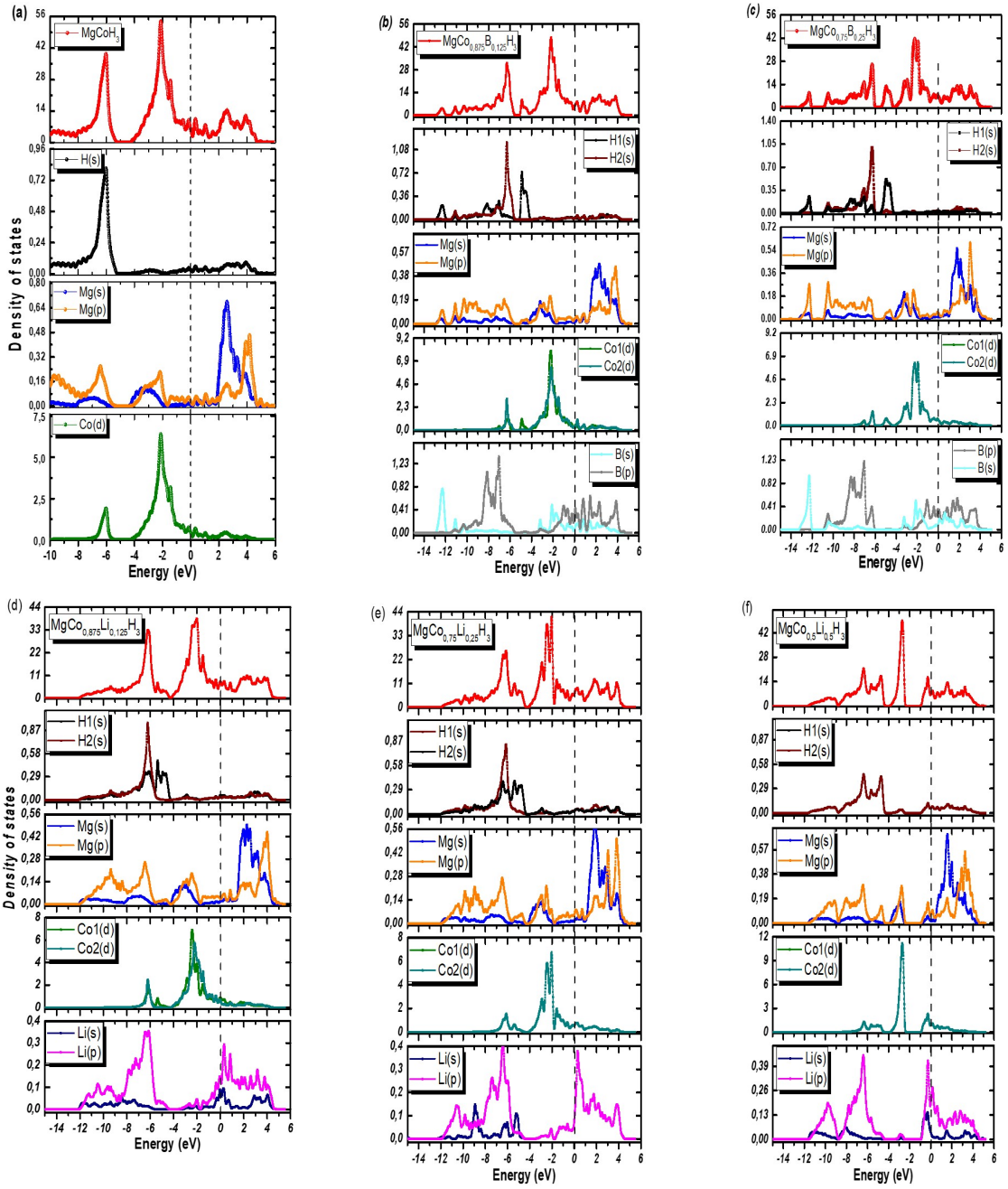

FIGURE 4.2: The calculated total and the projected density of states of $MgCo_{1-x}M_xH_3$ (M=Li or B, x=0, 0.125, 0.25 or 0.50)

4.3.4 Lattice dynamical properties

Phonon calculations are carried out to provide the dynamical stability information and vibrational contribution for $MgCo_{1-x}M_xH_3$ (M=Li or B, x=0, 0.125, 0.25 or 0.50) compounds. Based on the harmonic approximation, the phonon frequencies have been calculated using PHONON software and negative or imaginary frequencies of phonons indicate that the compound is dynamically unstable. Figure 4.3 shows the vibrational density of states (VDOS) for $MgCo_{1-x}M_xH_3$ compounds. As seen from this figure, the absence of any imaginary or negative phonon frequencies in the entire Brillion zone (BZ) means that the dynamical stability of the pure $MgCoH_3$ structure. Also, the phonon modes can be grouped into three regions, one branches of the acoustic modes (lower frequencies) and two branches of optical phonons. The H atom which is lighter than Mg and Co give contributions to high frequencies while Mg and Co the elements having highest mass in the pure $MgCoH_3$ structure contribute to low frequencies. In the case of the $MgCo_{1-x}M_xH_3$ (M=Li or B, x=0, 0.125, 0.25 or 0.50) structure a small phonon branches in the negative frequency range of -10THz are observed. This means that all compounds $MgCo_{1-x}M_xH_3$ are considered mechanically stable. These imaginary phonons may be eliminated by introducing the van der Waals interaction with substrates or external pressure [251, 252]. In addition, due to the substitution effect by light elements (Li or B) with different contents x, the frequencies of the acoustic and optic branches are close to each other that can be related to the change of thermal conductivities of the $MgCo_{1-x}M_xH_3$ compounds and the large mass difference between atoms. Furthermore, the vibration of the hydrogen becomes more independent than that of the pure perovskite-type hydride, which explains the reduction of desorption enthalpies for modified $MgCoH_3$ lattice.

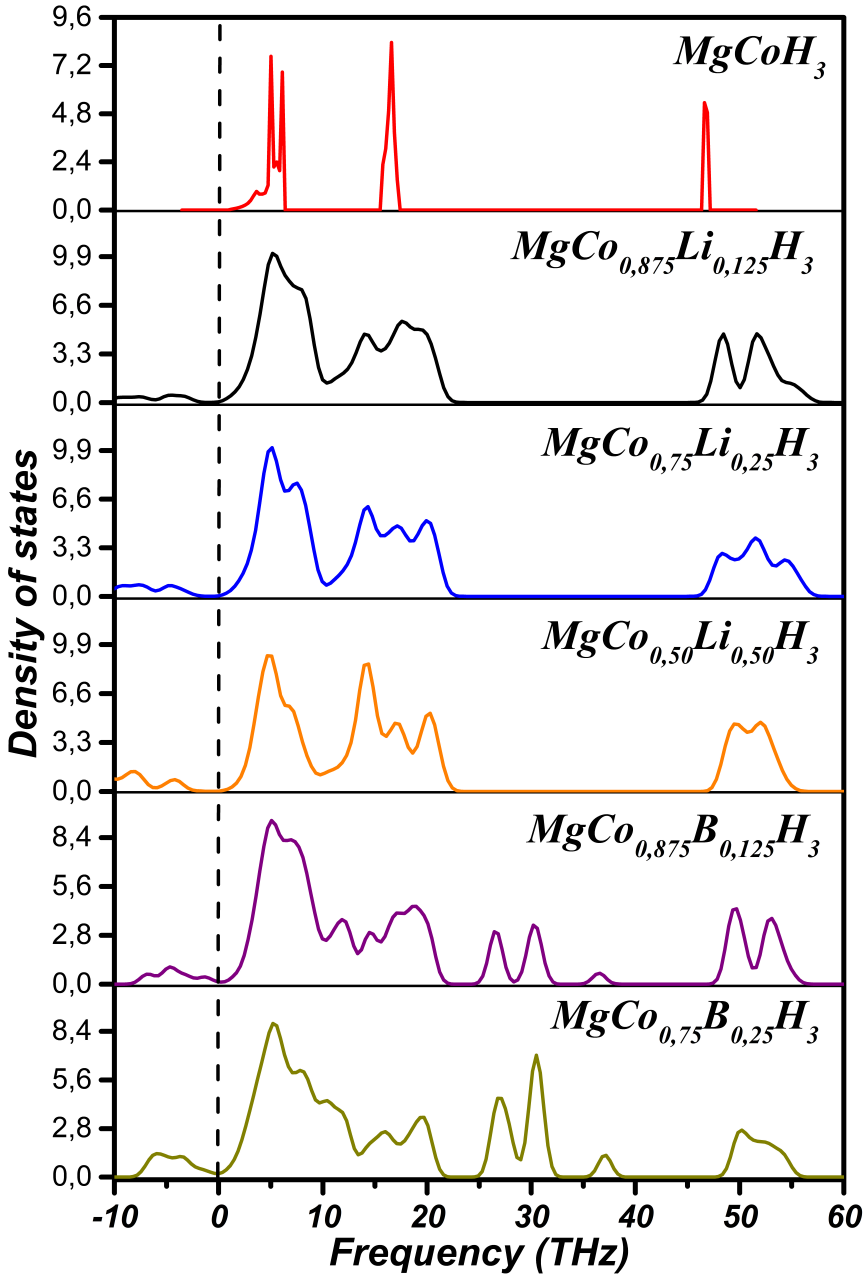

FIGURE 4.3: Phonon density of states of $MgCo_{1-x}M_xH_3$ (M=Li or B, x=0, 0.125, 0.25 or 0.50)

4.3.5 Lattice thermodynamic properties

Knowledge of thermal characteristics of crystal plays significant role to get information about the response of the material in term of temperature. For that, several thermodynamic parameters of perovskite-type hydrides $MgCo_{1-x}M_xH_3$ (M=Li or B, x=0, 0.125, 0.25 or 0.50) such Helmholtz Free Energy (F), Entropy (S), Harmonic Phonon Energy (H_{vib}) and specific heat capacity were determined through the quasi-harmonic approximation (QHA) using the phonopy package. The temperature dependencies of thermodynamic parameters are calculated and presented for $MgCo_{1-x}M_xH_3$ compounds in Figure 4.4. It can be seen that all hydrides compounds showed the same behavior with temperature variation. As one can notice, from 0 to 100 K, the free energy is nearly constant and decreases linearly with increasing temperature from $T \succ 100K$. Inversely, the entropy increases with increasing temperature for all systems due to the increase in thermal vibrations of atoms (phonon frequency). As we know, the specific heat capacity is an important thermodynamic parameter which gives insight into heat loss or retention of materials. It is apparent from Figure 4.4 that the heat capacity increases rapidly below 200 K ($C_v \propto T^3$ behavior at low temperature) whereas these increments slowdown in the temperature region above 400 K and finally it reaches a saturation value called the classical Dulong-Petit asymptotic limit. Moreover, with the increase of light elements (Li or B) substitutions concentrations x in $MgCo_{1-x}M_xH_3$, the free energy, entropy and heat capacity gradually decrease.

4.3.6 Diffusion activation energy of hydrogen atom

The diffusion kinetics analysis of hydrogen into the supercell perovskite-type hydrides lattice $MgCo_{1-x}M_xH_3$ (M=Li or B, x=0, 0.125, 0.25 or 0.50) is one of the key properties for the hydride formation and hydrogen desorption process. The diffusion paths and activation energy profiles of H translation in space between nearby H atoms are investigated and illustrated in figures 4.5 and 4.6. Impact of boron or lithium doping content x on the hydrogen diffusion in hydride have been studied and the potential barriers values for $MgCo_{1-x}M_xH_3$ systems are determined by finding the minimum energy path (MEP) and its saddle point using NEB method.

The two different pathways considered for the diffusion of hydrogen atom in

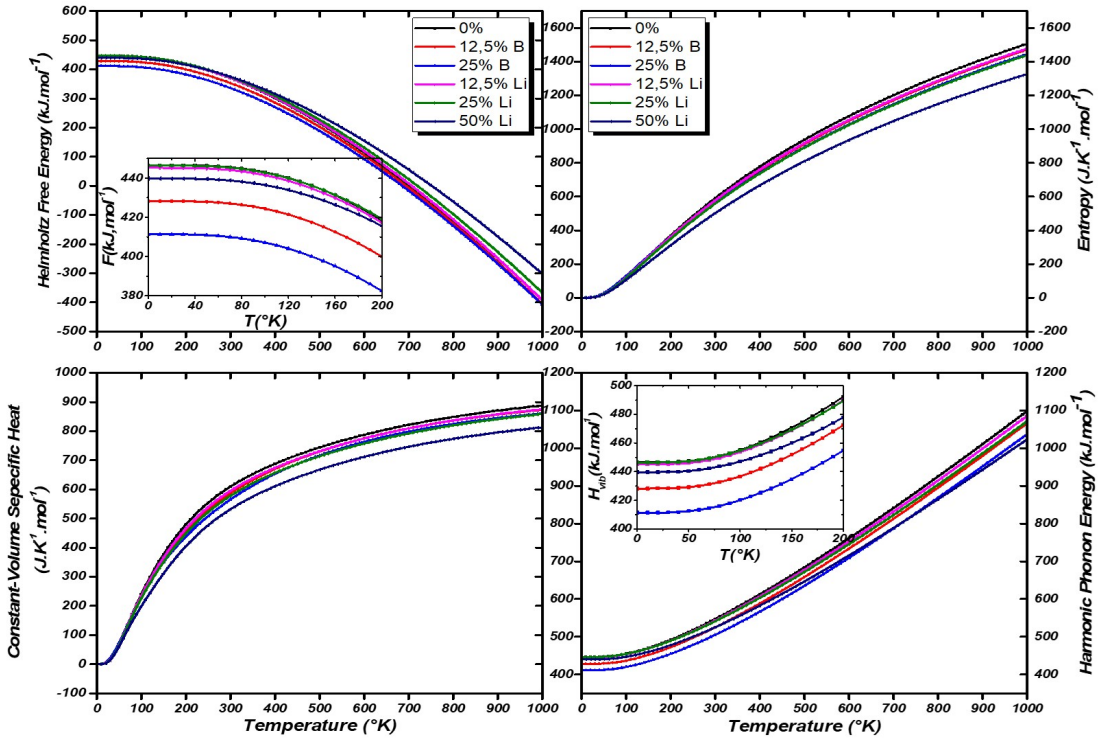

FIGURE 4.4: Temperature dependencies of Helmholtz free energy (F), entropy (S), heat capacity (C_v) and harmonic phonon energy (H_{vib}) of $MgCo_{1-x}M_xH_3$ (M=Li or B, x=0, 0.125, 0.25 or 0.50)

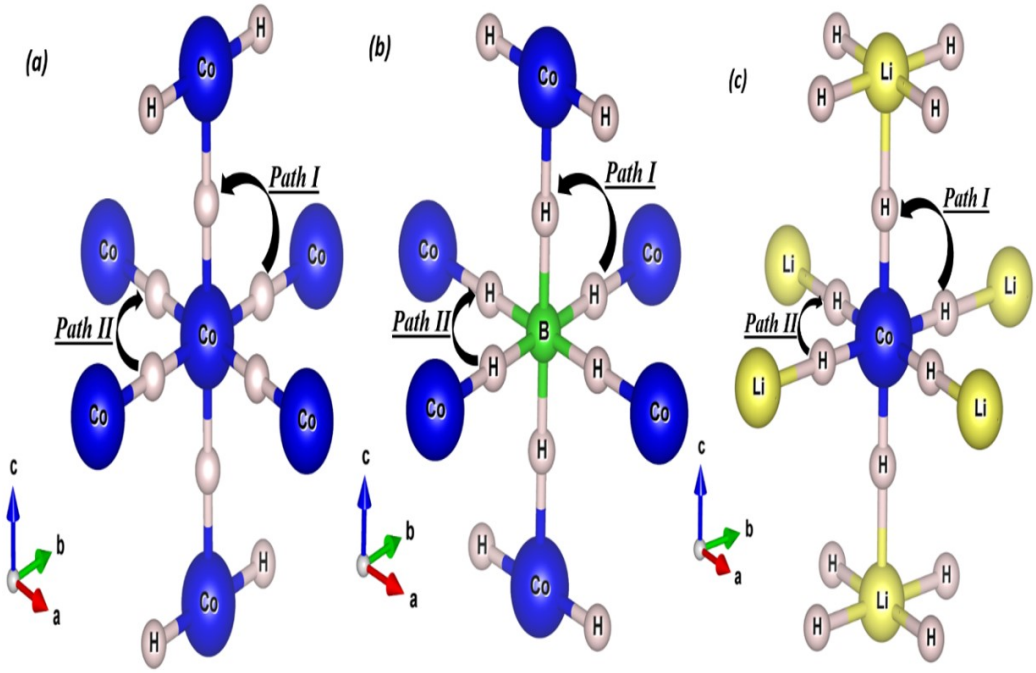

FIGURE 4.5: Schematic view of the diffusion pathways of hydrogen atom in (a) $MgCoH_3$ (b) $MgCo_{0.75}B_{0.25}H_3$ and (c) $MgCo_{0.5}Li_{0.5}H_3$

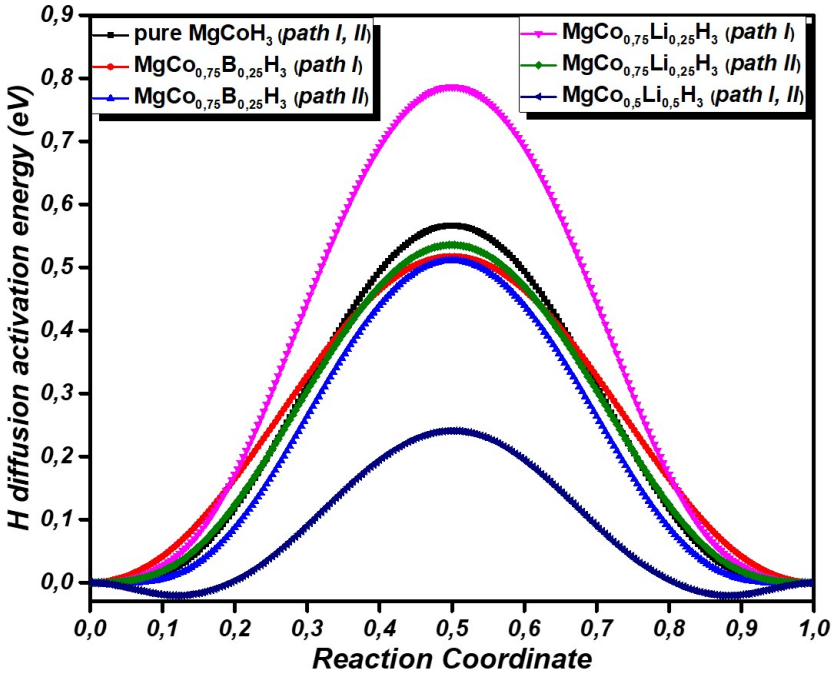

FIGURE 4.6: Energy curves for diffusing hydrogen between two interstitial sites in $MgCo_{1-x}M_xH_3$ (M=Li or B, x=0, 0.125, 0.25 or 0.50)

$MgCo_{1-x}M_xH_3$ super-cell systems are presented in figure 4.5. The activation energy values were estimated from the data illustrated in figure 4.6. The initial and final points of translation curves in the pure and doped conditions have the same energy because of the structure symmetry. A notably decrease in the diffusion energy barriers from 0.566 eV ($MgCoH_3$) to 0.241 eV ($MgCo_{0.5}Li_{0.5}H_3$) due to the incorporation action is observed.

4.3.7 Charge density distribution

The calculation of the electronic charge density informs about the charge transfer and therefore on the ionic or covalent nature of the bonds between the elements forming the $MgCo_{1-x}M_xH_3$ (M=Li or B, x=0, 0.125, 0.25 or 0.50) compounds. Figure 4.7 indicates the electron-density contour map of the $MgCo_{1-x}M_xH_3$ in the two planes (001) and (101) in order to verify the bonding behavior of the structures. The amount of electronic charge at every point in space is determined and all points having the same electron density value in the plane are joined by a line, a contour line. As can see from figure 4.7(a) that for the pure $MgCoH_3$ there is an equal sharing of charge density between cobalt and hydrogen which is interpreted by the covalent bonding. This covalency strength decreases with doping by boron atom (figure 4.7(b)). The reason is that boron atom attracts hydrogen more

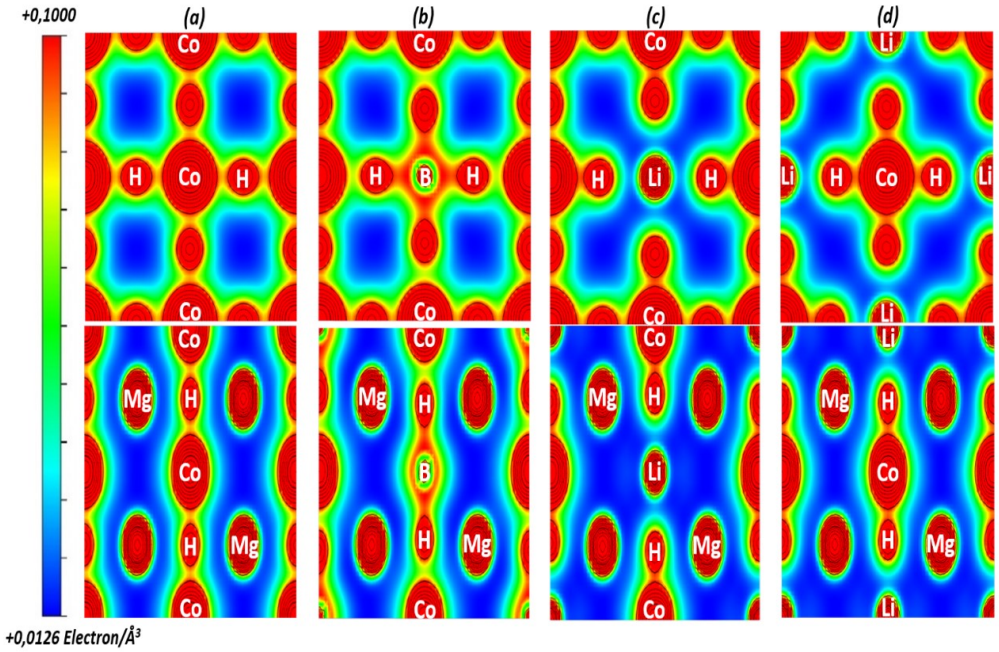

FIGURE 4.7: Electron charge density distribution of (001) and (101) planes for (a) $MgCoH_3$, (b) $MgCo_{0.75}B_{0.25}H_3$ (c) $MgCo_{0.75}Li_{0.25}H_3$ and (d) $MgCo_{0.5}Li_{0.5}H_3$. The magnitude of the charge density showed by different colors.

closely than Co/Mg and tends to share its electrons with neighboring H atoms like in BH_4^- group. In this regard, the $B-H$ bond is more covalent than $Co-H$ bond, so the charge is more concentrated in $B-H$ bonding region leading to charge depletion in the region between the Co and H atoms. On the other hand, the substitution of lithium enhances the electronic charge overlapping between Cobalt and hydrogen (closest to Li)(see figure 4.7(c) and (d)). The result of the incorporation of lightweight elements into $MgCoH_3$ hydride may be explained by the reduction of the interactions between interstitial H atoms and the $Mg-Co$ host, which leads to a decrease in the system stability. Thus, this finding confirms the relation between charge density and stability as reported in previous sections.

4.4 Conclusion

In summary, the structural, electronic, hydrogen storage, stability and lattice dynamical characteristics of perovskite-type hydrides $MgCo_{1-x}M_xH_3$ (M=Li or B, x=0, 0.125, 0.25 or 0.50) have been presented using the first principle calculations. Formation energy, desorption temperature, volumetric/gravimetric capacities and diffusion activation barriers of $MgCo_{1-x}M_xH_3$ are analyzed in order to reveal their potentials in hydrogen

technology. The possibility of the synthetization of these systems was confirmed by the negative formation energies and the weak soft modes in phonon dispersion. The obtained results indicated that the substitution of cobalt with lightweight elements (Lithium or Boron) enhances the thermodynamic properties and kinetics as well volumetric and gravimetric capacities. It was found that the formation energy shifted from $-71.30\text{k}J.\text{m}ol^{-1}$ per H_2 to $-44,68$ and $-39.56\text{k}J.\text{m}ol^{-1}$ per H_2 for $MgCo_{0.5}Li_{0.5}H_3$ and $MgCo_{0.75}B_{0.25}H_3$ compounds, respectively. Furthermore, the hydrogen release started at $341.87K$ and $302.67K$ compared with $545.52K$ of the pure $MgCoH_3$, which is requested for the practical hydrogen storage applications ($289-393K$, $-40\text{k}J.\text{m}ol^{-1}$ per H_2). In addition, the substitution with lightweight elements accompanied by an increase of the gravimetric and/or volumetric capacities from $3,5wt\%$, $142,5g.H_2/L$ ($MgCoH_3$) to $5,02wt\%$, $140,41g.H_2/L$ for $MgCo_{0.5}Li_{0.5}H_3$ and $4,07wt\%$, $145,02g.H_2/L$ for $MgCo_{0.75}B_{0.25}H_3$. Precisely, the improvement of the hydrogen storage properties of $MgCo_{1-x}M_xH_3$ systems was attributed the decrease of cobalt atom concentration in perovskite hydrides. Finally, vibrational properties were used to represent and analyze the thermal characteristics of all $MgCo_{1-x}M_xH_3$ systems as function of temperature and doping content x including the vibrational enthalpy, entropy, phonon Helmholtz free energy and the molar specific heat capacity etc. All results are in good agreement with the available theoretical data and verified that the systems of $MgCo_{1-x}M_xH_3$ perovskite-type hydrides are found to be energetically, mechanically and dynamically stable.

5 Phosphorene: A promising candidate for molecular hydrogen storage

5.1 Introduction

Since the discovery of graphene, the field of two-dimensional (2D) nanomaterials has tremendously grown not only in energy storage but also in the field of spintronics, gas sensing, catalysis and hydrogen production applications. In the context of H_2 storage, graphene-like structures, such as graphdiyne, honeycomb BC_3, borophene, CN and $g-C_3N_4$ layer have been considered as efficient hydrogen storage candidates due to their high surface area and the remarkable chemical stability [184, 253–256]. Meanwhile, research into exploiting the capability of other two-dimensional (2D) nanostructures, such as boron nitride (BN), boron arsenide (BAs), germanium carbide ($g-GeC$), and Boron and Gallium monochalcogenides ($BX, X = S, Se$ or Te) has significantly expanded [256–263]. Single-layer black phosphorus, labeled "phosphorene", is a new material in the family of 2D nanostructures. It can be obtained by mechanical exfoliation of the black phosphorus, which is a stable compound with a natural layered structure [264]. Very recently, phosphorene with a thickness of only few nanometers has been produced by several groups worldwide [265]. Theoretical and experimental investigations have demonstrated the potential of the application of phosphorene as a transistor material, as a photocatalyst and as anodes in batteries [266–270], but the use of this material for hydrogen storage solid state remains limited. the main aim of the present work is to study, using density functional theory (DFT), the potential of phosphorene application as a new 2D material for hydrogen storage by investing the interaction of hydrogen molecules and

atoms with the surface and its impact on the diffusion behavior. The work is organized as follows: at first, the adsorption of hydrogen molecules on the surface will be evaluated and the results will be compared with the pristine graphene. Next, the energy barriers for hydrogenation reaction, diffusion, and dissociation of hydrogen located at a phosphorene surface are simulated. All the possible dissociation and diffusion pathways are analyzed to find the diffusion and dissociation barriers.

5.2 Computational method

All calculations are performed within density functional theory (DFT) [227, 228] using the Quantum espresso program [205]. The PBE generalized gradient approximation [229] and the projector-augmented wave potential [271] are employed to describe the exchange-correlation energy and the electron–ion interaction, respectively. It has been found that the van der Waals (vdW) interactions are quite important for black phosphorus, thus it was included by using the self-consistent correction scheme of vdW-DF2 [272] as implemented by Kyuho lee et al. [273], and the exchange functional (C09) developed by Cooper [274, 275]. The cutoff energy for the plane wave expansion is set to 40 Ry (544 eV), which is large enough to make the error from calculations of the adsorption energy below 0.01 eV. To model the phosphorene monolayer, a rectangular 9.24x6.60Å supercell with 16 phosphorus atoms was used (see Figure 5.2(a)). The atomic positions of all the atoms including hydrogen molecules in the supercell were fully relaxed using the Broyden–Fletcher–Goldfarb–Shanno (BFGS) minimization method [276]. The electronic ground-state steps were allowed to converge to an accuracy of 10-10 eV and convergence tolerance for forces were set less than 0.05 eV/Å, displacement of atoms less than $2x10^{-3}$Å and stress less than 0.02 GPa. The Brillouin zones of the unit cells are represented by Monkhorst-Pack special k-points scheme with a 5x3x1 grid mesh [277]. Computational settings such as plane wave cutoff energy, the number of k-points and convergence criteria were carefully chosen to control the numerical accuracy. To determine activation barriers for dissociation and diffusion of hydrogen on phosphorene surface, the nudged elastic band (NEB) method [278, 279] was used, which has been employed to find out the minimum energy path (MEP) and the corresponding energy barrier for the dissociation and diffusion of hydrogen molecule and hydrogen atom on the phosphorene surface. This

method involves the optimization of a chain of images, obtained by linear interpolation, between the initial and final states. In most of the cases, the total number of images used is equal to 10, which is sufficient to map the MEP accurately. Each image is allowed to move in all direction.

5.3 Optimized structure of the phosphorene sheets

Black Phosphorus (BP) is a layered material in which atomic layers are bound by van der Waals (vdW) interactions and exhibits AB stacking (see Figure 5.1(a)). In each single layer of BP, unlike to the planar graphene sheet, phosphorus atoms form a puckered honeycomb structure which each phosphorus atom is covalently bonded to three adjacent P atoms. The top and side view of the optimized monolayer phosphorene is shown in Figure 5.1(b). The relaxed lattice constant of the single layer phosphorene is a = 4.62Å and b = 3.30Å along the armchair and zigzag directions, respectively, which are in good agreement with the previous results. The calculated P-P bond lengths are $R_1 = 2.22$Å for the horizontal (in the zigzag direction) bonds and $R_2 = 2.27$Å for the bonds in other directions (armchair direction). The corresponding bond angles are $\theta_1 = 95.81^\circ$ and $\theta_2 = 104.1^\circ$, respectively (see Figure 5.1(c)), which are in agreement with the previous results. The band structure is presented in Figure 5.2. The band gap is located at the Γ point with a direct band gap of 0.9 eV, which is also in excellent agreement with previous results [280–282].

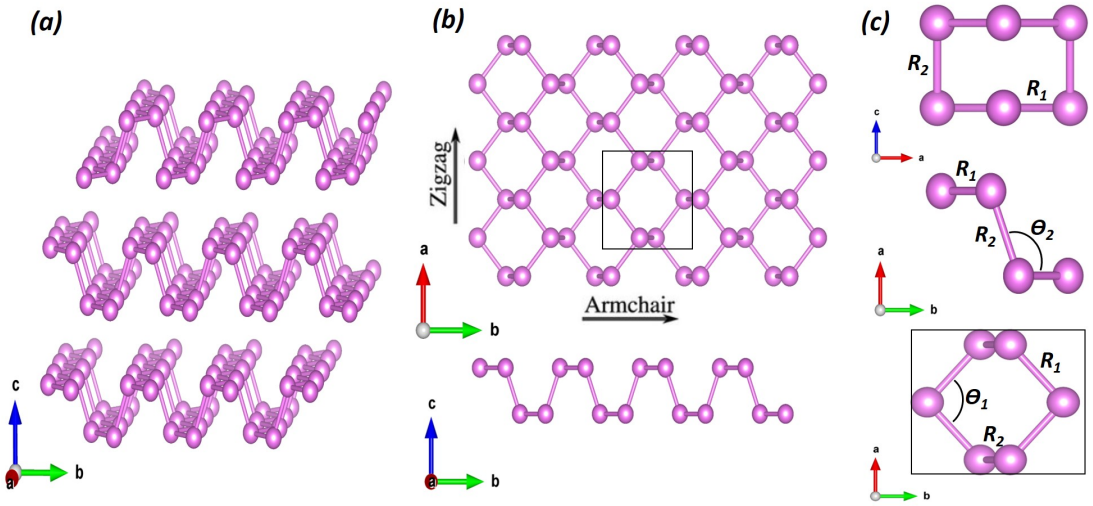

FIGURE 5.1: Crystal structure of (a) Black Phosphorus (BP) (b) and (c) Monolayer phosphorene. R_1 and R_2 indicate the intra-planar and inter-planar P-P bond length, θ_1 and θ_2 show the intra-planar and inter-planar bond angle.

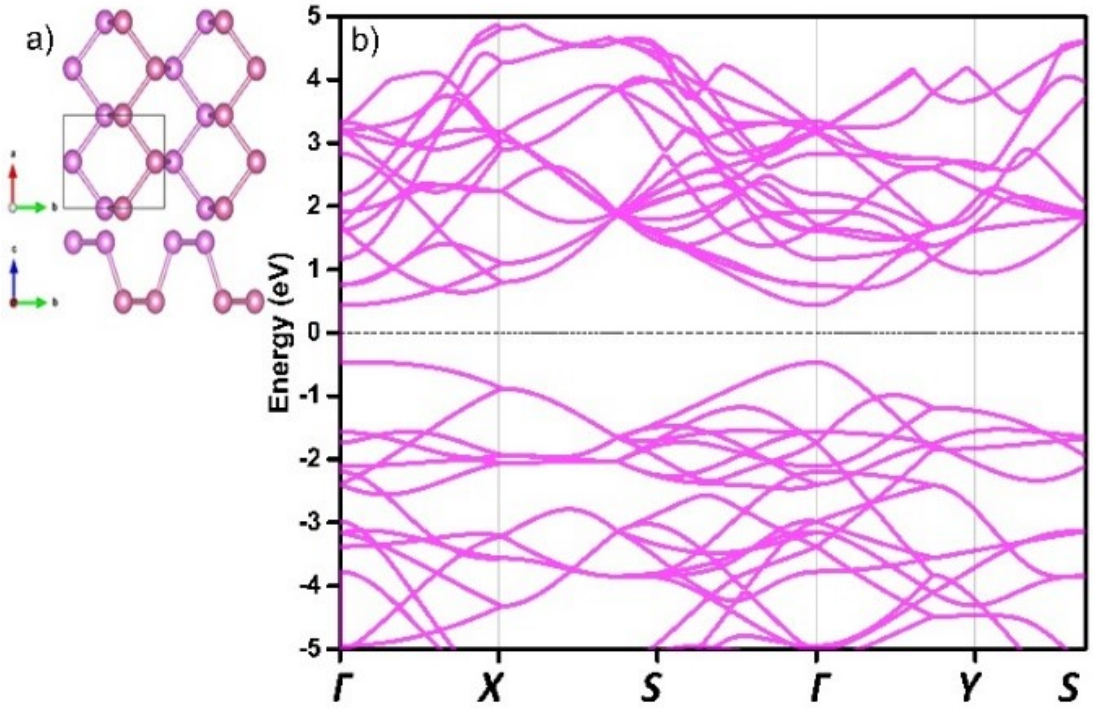

FIGURE 5.2: (a) Optimized geometry and (b) Band structure plot of pristine Phosphorene.

5.4 Single H_2 molecular adsorption properties

In this section, equilibrium properties of molecular hydrogen on phosphorene are calculated. Four adsorption sites of H_2 on phosphorene are investigated: H (hollow site, in the center of the phosphorus hexagon), T (top site, on top of the phosphorus atom), B and B′ (bridge site, above the middle-point of the bottom and top P-P bond). Also, several orientations of the H_2 molecule with respect to the phosphorene surface are considered at each adsorption site, as presented in Figure 5.3. In configurations H1, H2, B1, B′1, T1, and T2, the axis of the H_2 molecule (H-H axis) is parallel to phosphorene surface. Whereas configurations H3, B2, B′2 and T3 correspond to the cases where the H-H axis is perpendicular to the phosphorene plane. The total energies of the hydrogen-phosphorene systems were computed for different configurations, where the separation z between the phosphorene substrate and the center of mass of the H_2 molecule was varied between 2 and 6.5 Å, thus allowing for the computation of the adsorption potential E_{ads} in the relevant separation range and for the location of the energy minimum value and position. The adsorption potential E_{ads} of H_2 molecule (at the equilibrium distance z_{min}) to various adsorption sites on phosphorene is obtained using the formula:

$$E_{ads}(z_{min}) = E_{tot} - (E_{sub} + E_{H_2}) \tag{5.1}$$

where E_{tot}, E_{sub}, and E_{H_2} are the total minimized energies of H_2 plus substrate, substrate, and H_2, respectively. z_{min} is the vertical equilibrium distance from the center of mass of H_2 to the phosphorene layer provided that all the energies are minimized. Figure 5.4 shows $E_{ads}(z)$ on the B′2 site, as computed using different approximations. The higher energy curve represents the results of the PBE-DFT calculations without the inclusion of vdW interactions. When the van der walls (vdW) interactions are taken into account with the different methods, the calculated binding energy becomes more attractive and its value at the minimum decrease with respect to the PBE-DFT results. The results obtained by the vdW-DF2-C09x method [283], in particular, give a minimum binding energy of -292 meV at a distance of 3.36 Å, which corresponds to the requirement for appropriate hydrogen storage with a binding energy of -0.2 $\sim$ -0.6 eV/H_2 [284, 285]. The hydrogen remains at the molecule state with a bond length of 0.75 Å. The values of the adsorption potential and the vertical distances of H_2 for all configurations sites are obtained using the equation 5.2 and

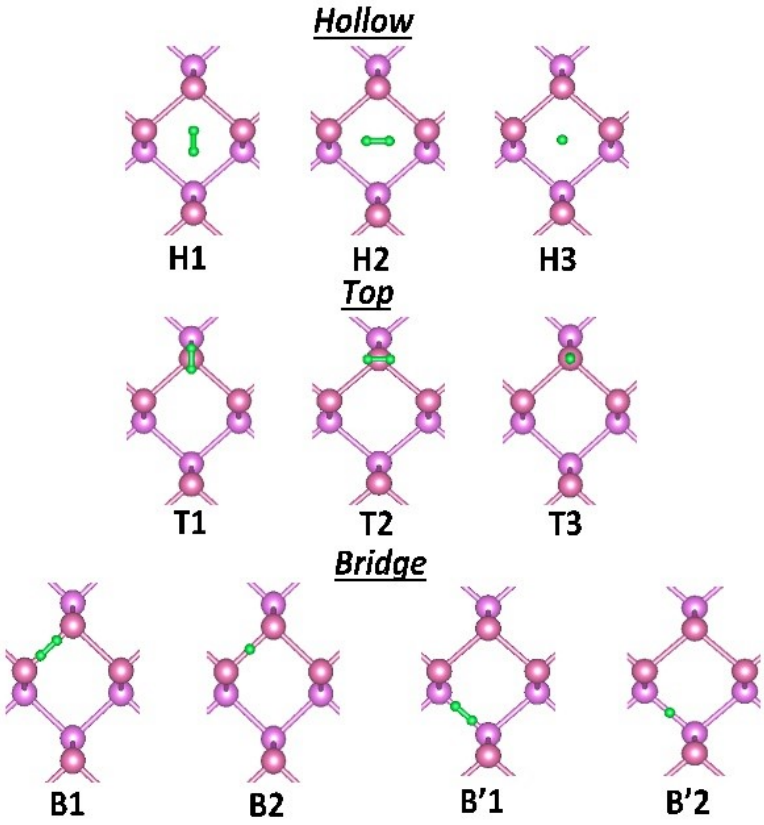

FIGURE 5.3: The various molecular hydrogen adsorption configurations studied: Hollow (H), Top (T) and Bridge (B and B′).

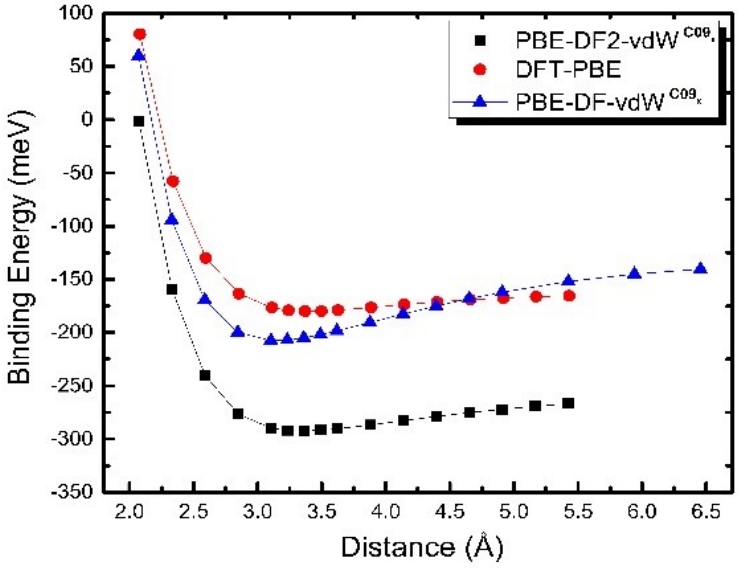

FIGURE 5.4: Physisorption of H_2 on phosphorene, in the bridge configuration. Pure DFT calculation, DFT/vdW-DF-C09x and DFT/ vdW-DF2-C09x.

TABLE 5.1: Equilibrium distances and potential minima of H_2 to various adsorption sites on phosphorene.

		DFT/PBE		DFT/vdW-DF2-C09$_x$		graphene-DFT/vdW	
		$E_{ads}(meV)$	z_{min}(Å)	$E_{ads}(meV)$	z_{min}(Å)	$E_{ads}(meV)$	z_{min}(Å)
Hollow	H1	-170	3.33	-283	3.13	-54	3.2
	H2	-163	3.00	-279	2.99	-48	3.0
	H3	-174	3.37	-286	3.36	-47	3.5
Top	T1	-170	3.74	-282	3.59	-39	3.4
	T2	-164	3.73	-278	3.63	-43	3.6
	T3	-169	3.39	-280	3.37	-38	3.1
Bridge1	B1	-169	3.54	-280	3.42	-43	3.6
	B2	-166	3.37	-277	3.36	-43	3.3
Bridge2	B'1	-164	3.04	-281	2.99	-	-
	B'2	-180	3.37	-292	3.36	-	-

reported in Table 5.1 along with the obtained results for graphene.From the analysis of the results of H_2 adsorption on phosphorene using the PBE-DFT and when introducing the vdW forces, the hydrogen prefers to be adsorbed on the middle-point of the bottom P-P bond with its molecular axis perpendicular to the phosphorene surface (bridge2, B'2). The intermediate adsorption potential energy of hydrogen molecule on phosphorene implies stable hydrogen storage at ambient conditions and subsequent facile release. It is noted that the E_{ads} of H_2 on phosphorene is much larger than that of H_2 on pristine graphene (283 versus 54 meV/H_2 for the case of H1 hollow calculated using vdW-DF2) [64], which suggests a higher working temperature for using phosphorene as the hydrogen adsorbent [286], better than that found for graphene, which limits the use of graphene as an absorbent of hydrogen. The desorption temperature of hydrogen molecule T_{des} can be estimated using the well-known thermodynamics relation:

$$T_{des} = \frac{\Delta H}{\Delta S} \tag{5.2}$$

For most of the dehydrogenation reactions, it is estimated that ΔS is about 140 J/mol.K [226, 287]. Taking the above value of E_{ads} and the value of the entropy, we get T_{des}= 297K. However, since the density of bulk phosphorene is about 23% larger than that of graphite, implying a smaller gravimetric value of the hydrogen storage than graphite. Nevertheless, the highly flexible and puckered honeycomb structure of phosphorene implies a higher possibility for increasing the chemical affinity for hydrogen with convex

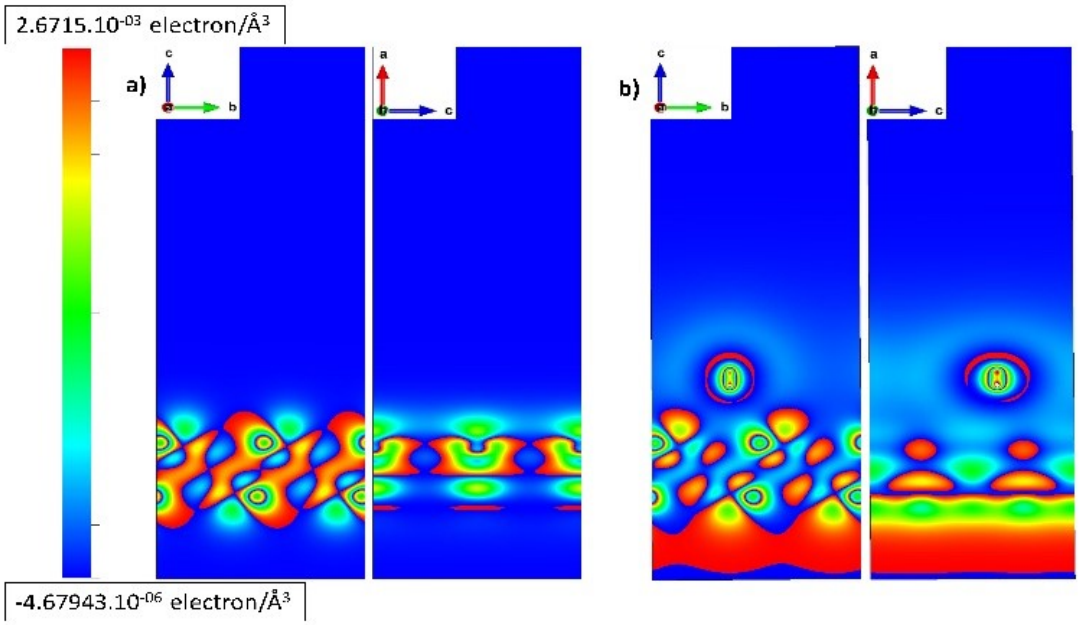

FIGURE 5.5: Electron density distributions in (a) phosphorene sheet (b) H_2 adsorbed on 3 x 4 supercell phosphorene sheet

areas of phosphorene surfaces, which has been demonstrated in fullerenes, nanotubes, and graphene by controlling curvature or creating ripples [288–290]. To analyze the electronic interaction between H_2 molecule and phosphorene, the electron density distributions was investigated and plotted in figure 5.5. For the system of H_2 adsorbed on phosphorene, it can be seen that there is an accumulation of charge around the far hydrogen atom and a depletion of electron around the lower H atom from substrate, which lead to a slight polarization of the H_2 molecule. Additionally, a small amount of charge transfer from phosphorene layer to the hydrogen molecule means that H_2 exhibits physisorption on phosphorene sheet. These findings are in good agreement with results of Zhiyuan Yu et al. [291] and Murugan Lalitha et al. [292].

5.5 Single H_2 molecular diffusion

The diffusion barriers for the hydrogen molecule moving across the surface from various configurations have been calculated as the difference between the initial physisorption state and the transition state. The calculation of barrier using the NEB method [279] is described pictorially in Figure 5.6 and the results are reported in Table 5.2. The barriers found are rather low compared to graphene [64, 293] and hence the physisorbed molecules

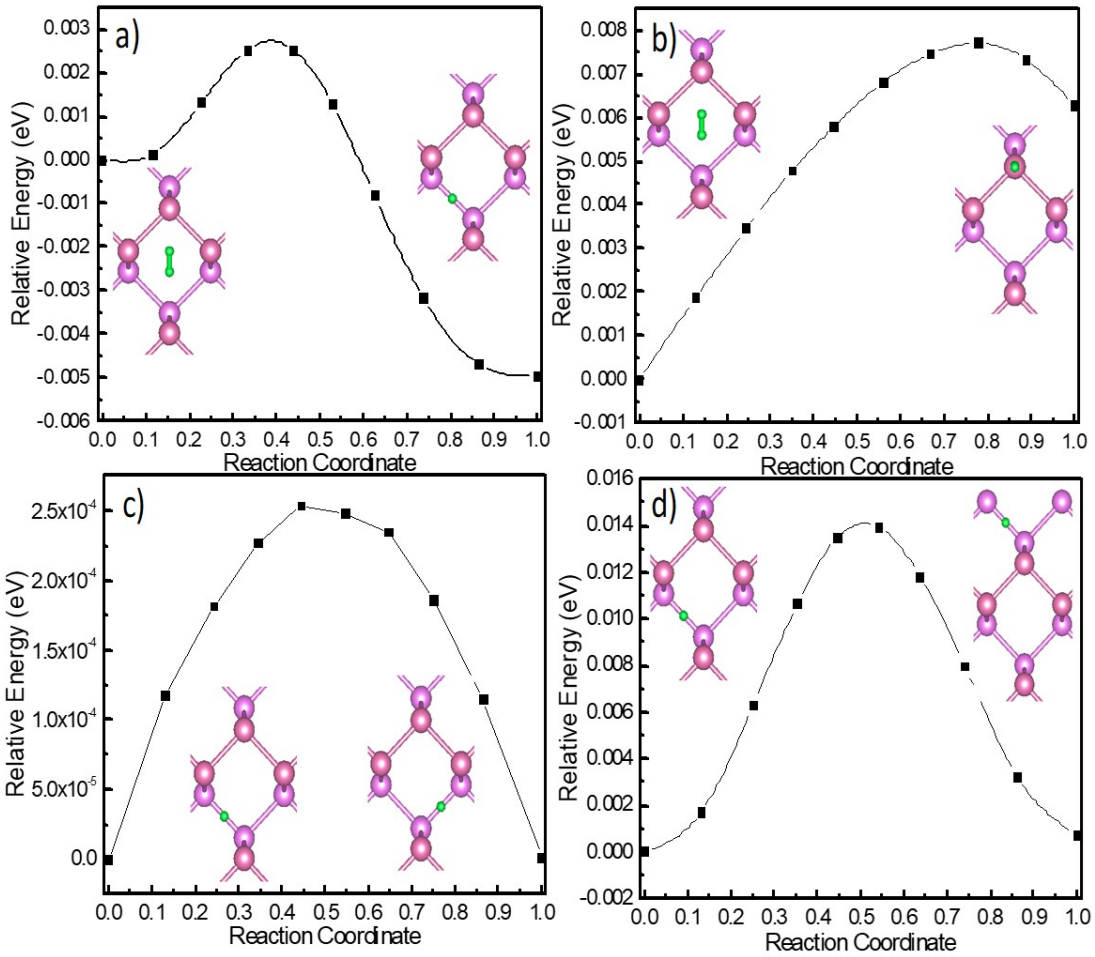

FIGURE 5.6: Examples of configuration migration of H_2 on phosphorene from various initial to final sites: (a) Hollow (H1) to Bridge2 (B'2), (b) Hollow (H1) to Top (T3), (c) and (d) Bridge2 (B'2) to Bridge2 (B'2) with zigzag and armchair direction, respectively.

are expected to be quite mobile on phosphorene. The main difference in the barriers is the configuration migration. It can also be noted that the hydrogen molecule can easily diffuse into the convex zone (zigzag direction) than the armchair or diagonal direction with a barrier nearly zero (0.3 meV).

5.6 Single H_2 molecular dissociation

We now discuss the possibility of adsorption of hydrogen atoms from the molecular gas phase. To get insight into the energetic favorability of such a process, it is important to take energy barriers resulting from the molecular dissociation into account. For this calculation, we consider two possible chemisorbed configurations of H atoms on phosphorene after the dissociation of a diatomic molecule (para and Meta). The energetically favored

TABLE 5.2: Migration energy barriers of H_2 on phosphorene from various initial to final sites.

Configuration		Migration direction	The activation energy (meV) This work	The activation energy (meV) (graphene)
Initial state	Final state			
B′2	H1	Diagonal	2.5	
H1	T3	armchair	7.7	≈14meV
H1	B′2	Diagonal	7.5	Arellano et al. [285]
T3	H1	armchair	1.4	≈10 meV
B′2	B′2	armchair	14.0	Costanzo et al. [277]
B′2	B′2	zigzag	0.3	

TABLE 5.3: Activation barriers for the H_2 Dissociation..

Configuration	The activation energy (eV) This work	The activation energy (eV) (graphene)
B′2 $\longleftrightarrow$ Top (meta)	2.32	
B′2 $\longleftrightarrow$ Top (para)	2.77	2.68-3.86
H1 $\longleftrightarrow$ Top (para)	2.64	Costanzo et al. [277]
H1 $\longleftrightarrow$ Top (meta)	2.26	
H3 $\longleftrightarrow$ Top (para)	2.64	

configuration is found when two H atoms are adsorbed on the opposite vertices diagonal (Meta position) of the same hexagon ring of phosphorene (final state in Figure 5.7(a) and 5.7(d)). Figure 5.7 shown the pathway calculated from differences between H_2 physisorbed state and the chemisorbed state of 2H on phosphorene. One can see that the energy of the final dissociated configuration is higher than that of the physisorbed one, thus characterizing this hydrogenation process as an endothermic reaction. The path connecting the H1 configuration to the Meta configuration has the lowest energy barrier, 2.26 eV (Figure 5.7(d)). Table 5.3 reports all energy barriers for the explored paths from physisorbed to chemisorbed states for H_2 on phosphorene surface. The transition state (TS) is characterized by a broken H-H bond and by the formation of a new P-H bond (1.44 Å length), with a substantial distortion of the substrate. The results of barriers for H_2 dissociation on the phosphorene surface are lowered compared with the case of graphene, which shows the remarkable effect of the substrate curvature in promoting hydrogen dissociation [294, 295].

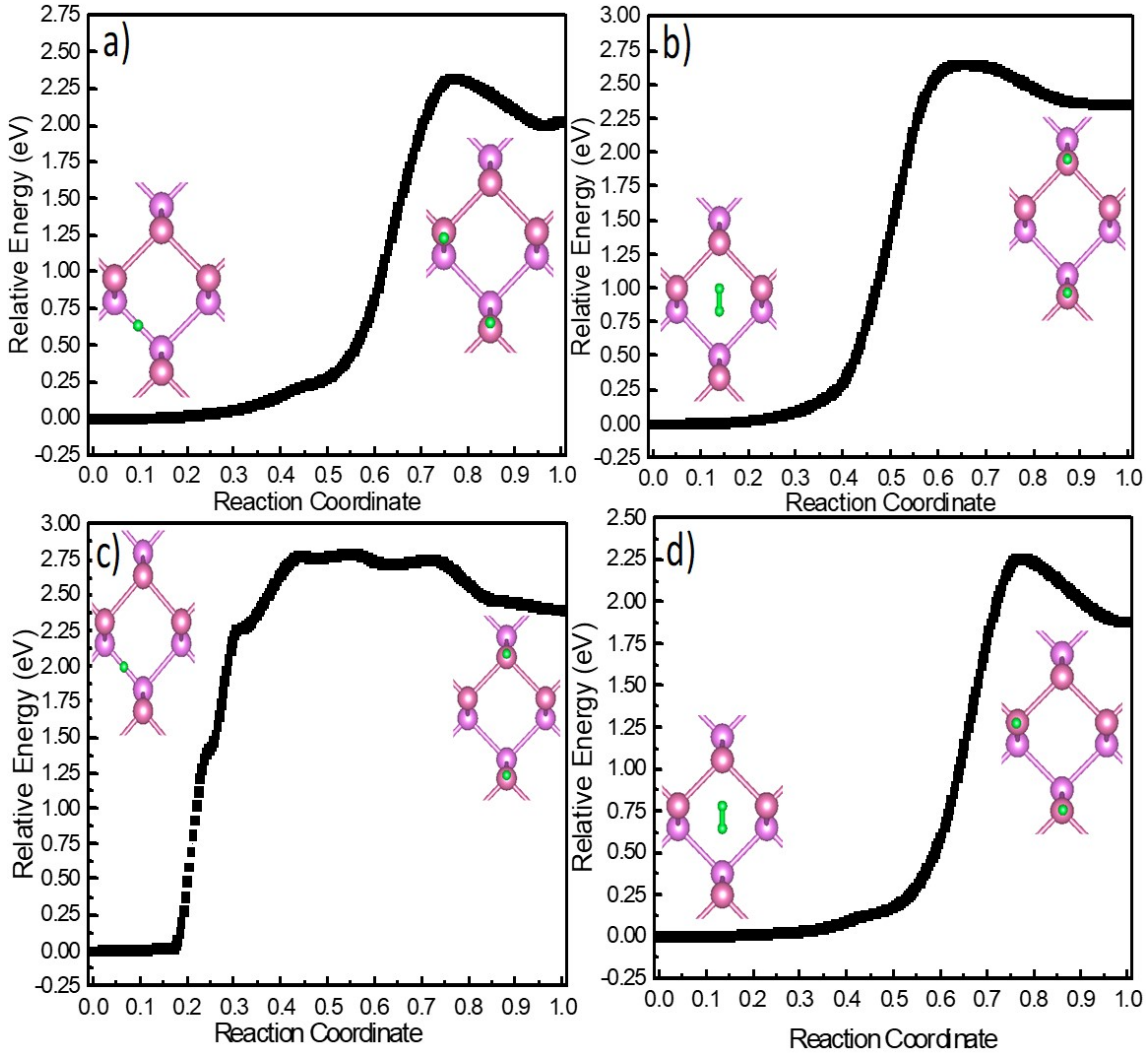

FIGURE 5.7: Chemisorption reaction path of H_2 on phosphorene, from the physisorbed state to the chemisorbed state: (a) Bridge2(B′2) to Top(meta), (b) Hollow(H1) to Top(para), (c) Bridge2(B′2) to Top(para) (d) Hollow(H1) to Top(meta).

5.7 Coverage of the surface by H atoms

To get more inside, we perform adsorption calculations for the hydrogen atom of each phosphorene sites. Our results show that the decomposition of hydrogen molecule suggests a decomposition of phosphorene into weakly bonded one-dimensional 1D chains arranged in the zigzag direction (Figure 5.8(b)). As we know phosphorus atoms have five valence electrons, each phosphorus atom becomes saturated by making a covalent σ-bond, two at the same plane while another is on a neighboring plane via 3p orbitals leaving a mono-electron pair oriented out-of-plane, orbitals giving rise to sp^3 hybridization. In the presence of hydrogen atom, the general mechanism of the bond formation between phosphorene and hydrogen atom redistribute, one σ-orbital form covalent bond with the hydrogen atom, two others keep covalent bonds with phosphorus atoms in plane and the last doubly occupied orbital forms alone pair pointing in the direction of the other phosphorus plane, which suggests an increase of distance between two plans of phosphorus which is significantly large value of 3.54Å (2.13Å before the hydrogenation). To study the reversibility of hydrogen atom chemisorbed in phosphorene, we evaluate a calculation of hydrogen desorption (Figure 5.8(c)). It can be seen from this figure that the distortion of phosphorene structure during the hydrogen atom desorption induces an across of the phosphorene chain after fully hydrogen desorbed. It is noticed that the chemisorption of hydrogen atom is not likely reversible. However, the chemisorption of hydrogen atom in phosphorene does not seem to be directly observable from the adsorption of hydrogen molecule due to high energy barriers governed by molecular dissociation and atomic migration.

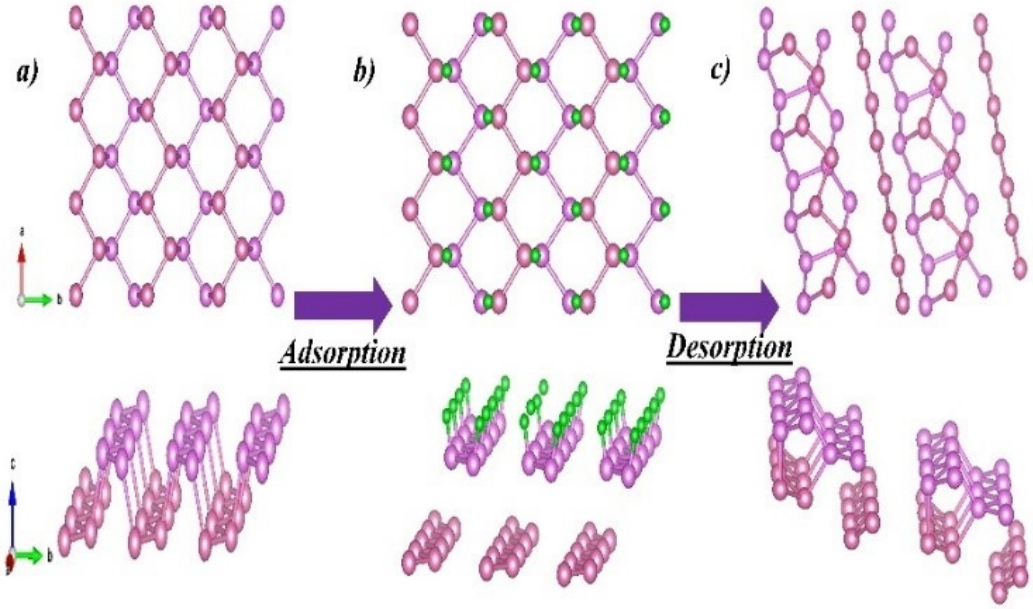

FIGURE 5.8: Optimized atomic structures of adsorption and desorption of hydrogen on single sides phosphorene.

5.8 Hydrogen storage capacity and stability

In order to understand the adsorption behaviors, hydrogen storage capacity and stability of substrate, we gradually increased the number of adsorbed H_2 molecules on both side of phosphorene layer. The different adsorption sites are also considered during such process (see Figure 5.9) and the adsorption energy per H_2 is calculated using the following term:

$$\overline{E_{ads}} = \frac{1}{n}(E_{syst} - E_{sub} - n.E_{H_2}) \tag{5.3}$$

where E_{syst} and E_{sub} are the total minimized energies of substrate with and without H_2 respectively, and E_{H2} is the total energy of the H_2 molecule and n is the number of adsorbed H_2 molecules. Table 5.4 lists the adsorption energies per H_2 on the range distance of H_2 molecules from substrate for different number of adsorbed H_2 and as well as H-H bond length. It was also noted that the H_2 molecules do not move away from the substrate indicating adsorption to phosphorene layer. From Figure 5.9 and Table 5.4, by increasing of the number of H_2 in one or both sides, the adsorbed hydrogen molecules with non-uniform manner and the calculated adsorption energies per H_2 for the most

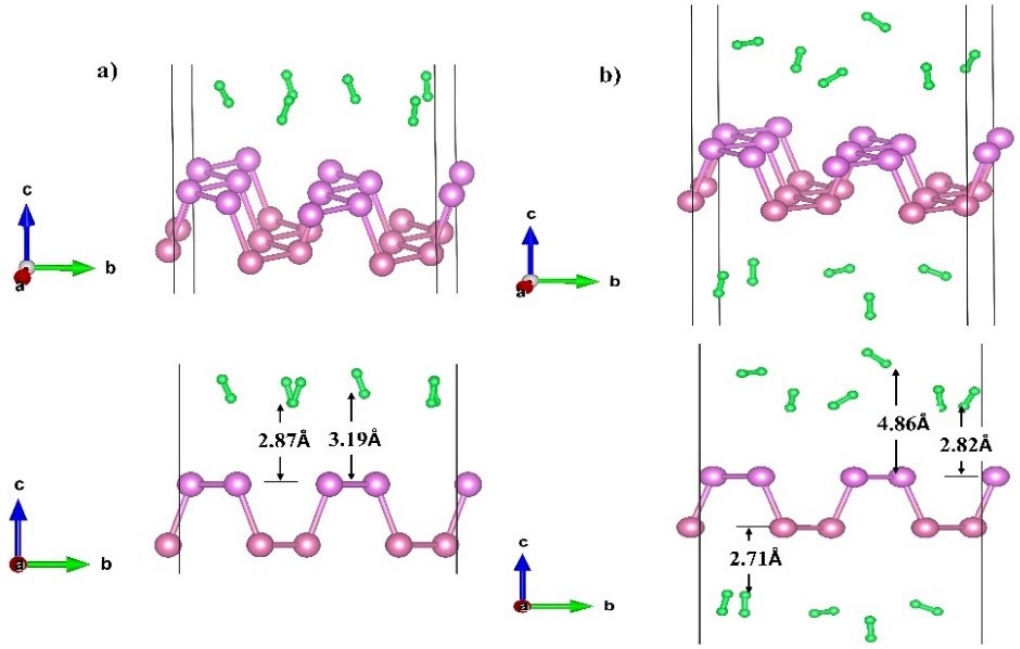

FIGURE 5.9: Optimized structures of phosphorene saturated with H_2 molecules on (a) one side and (b) both sides.

TABLE 5.4: Calculated adsorption energies of H_2 molecules (meV/H_2) on phosphorene, average height between H_2 and substrate (Å) and H-H bond length (Å).

Number of H_2	Adsorption energies per H_2 (meV)	Adsorbate height (Å)	H-H bond length (Å)
1	-292.4	2.98	0.7562
2	-307.3	2.98	0.7557
3	-300.8	2.98	0.7557
4	-298.2	2.98	0.7551-0.7556
5	-198.8	2.92-2.95	0.7484-0.7556
6	-268.2	2.87-3.19	0.7531-0.7548
7	-271.9	2.86-3.2	0.7534-0.7556
8	-275	2.86-3.2	0.7534-0.7562
9	-279.7	2.78-3.57	0.7537-0.7558
10	-280.9	2.78-3.57	0.7537-0.7558
11	-281.5	2.71-4.86	0.7539-0.7559

stable configuration are in the range from -198.8 to -307.3 meV/H_2, which satisfies the requirement of effective hydrogen storage material specified by US-DOE (stable storage and release at near ambient conditions). It can be seen that all the relaxed H-H bond lengths are between 0.7484–0.7562 Å. Such result is in good agreement with the length 0.75 Å of a free H_2 molecule, which indicates that all hydrogen remains in the molecular state. As a result, the saturate of the H_2 molecules adsorption is 11 and the maximum gravimetric density of adsorbed hydrogen on phosphorene should be around 4.45wt%. Finally, due to the large dissociation energies, the phosphorene monolayer preferably adsorbs hydrogen molecules rather than dissociates hydrogen molecules. The H_2 molecules were adsorbed in a non-uniform manner and the distance to the H_2 molecules from the substrate increased due to the steric interaction between the adsorbed H_2 molecules.

5.9 Conclusion

Several adsorption sites and the orientation of hydrogen molecule relative to the phosphorene surface were explored. The most stable physisorbed state is in the bridge B' site, with a binding energy of -292 meV. This value, which is obtained using the DFT/vdW-DF2-C09x approach including the vdW interactions, is higher than obtained from graphene (-54 $\sim$ -38 meV) and fulfills the requirement for appropriate hydrogen storage with a binding energy of -0.2 $\sim$ -0.6 eV/H_2. The analysis of reaction pathways diffusion among physisorbed states shows that molecular hydrogen can easily diffuse on phosphorene at room temperature across sites separated by energy barriers of just a few meV. The situation is different when the hydrogen molecules approach the phosphorus surface and dissociate. In particular, we calculated the activation energy of dissociation from H_2 molecule on highly symmetric sites of phosphorene. The lowest dissociation barrier of 2.26 eV is the one that corresponds to the transition from the H_2 physisorbed state to the meta chemisorbed state. Other energy paths are characterized by higher activation barriers ($\sim$ 2.77 eV).

General Conclusion and Perspectives

At the present time, a sustainable provision of energy is one of the greatest challenges for mankind. It requires ground-breaking scientific ideas, bold monetary investments and innovative public actions to initiate technological, economical and social transitions. Energy generated from sustainable sources has to be transported and stored in an eficient, ecologically friendly way and at low cost. At this point, hydrogen offers an elegant solution to the environment crucible. As a very flexible energy carrier, hydrogen can offer a global, clean, integrated and multisectoral energy approach, which will allow to make a contribution to solving the environmental problem and to guarantee of the future Earth's energy. However, it is crucial to find safe, compact and cost efiective methods for storing hydrogen to enhance the future realization of the sustainable energy economy. Due to the complexity of developing hydrogen storage systems, scientific research at a fundamental level is required. The present thesis is devoted to the first-principles study of the hydrogen storage properties of a set of promising bulk and 2D systems.

The main interest of this work is devoted to the bulk systems of the perovskite-type hydride $MgCoH_3$. Strain engineering and substitution with lightweight elements aims at enhancing the kinetic and the thermodynamic properties of the perovskite hydride $MgCoH_3$. We showed that the biaxial strains plays a key role in improving the de/absorption thermodynamic and kinetic properties of $MgCoH_3$ compound. Due to the contribution of strain energy, the formation energy, desorption temperature as well as hydrogen diffusion activation energies for strained $MgCoH_3$ hydride are all improved relative to that of strain-free system. Precisely, the formation energy shifted from -71.30kJ/mol per H_2 to -37.29kJ/mol per H_2 under the compression of -6% strain and the hydrogen release started at 285.34K compared with 545.52K for free strained $MgCoH_3$, which is very interesting for the practical hydrogen storage applications (289-393K, -40kJ/mol per H_2). The second strategy used to improve the properties of de/rehydrogenation is the substitution of cobalt by the Lithium or Boron atom in the stable

structure of the perovskite-type hydride $MgCoH_3$. The formation energy, desorption temperature, volumetric/gravimetric capacities and diffusion activation barriers of $MgCo_{1-x}M_xH_3$ are analyzed in order to reveal their potentials in hydrogen technology. The possibility of the synthetization of these systems was confirmed by the negative formation energies and the weak soft modes in phonon dispersion. The obtained results indicated that the substitution of cobalt with lightweight elements enhance the thermodynamic properties and kinetics as well volumetric and gravimetric capacities. It was found that the formation energy shifted from -71.30 kJ/mol per H_2 to -44,68 and -39.56 kJ/mol per H_2 for $MgCo_{0.50}Li_{0.50}H_3$ and $MgCo_{0.75}B_{0.25}H_3$ compounds, respectively. Furthermore, the hydrogen release started at 341.87K and 302.67K compared with 545.52K of the pure $MgCoH_3$, which is requested for the practical hydrogen storage applications. In addition, the substitution with lightweight elements accompanied by an increase of the gravimetric and/or volumetric capacities from 3,5wt%, 142,5g.H_2/L ($MgCoH_3$) to 5,02wt%, 140,41 g.H_2/L for $MgCo_{0.5}Li_{0.5}H_3$ and 4,07wt%, 145,02 g.H_2/L for $MgCo_{0.75}B_{0.25}H_3$. Precisely, the improvement of the hydrogen storage properties of $MgCo_{1-x}M_xH_3$ systems was attributed the decrease of cobalt atoms in perovskite hydrides. All results are in good agreement with the available theoretical data and verified that the strained or substituted systems of $MgCoH_3$ perovskite-type hydrides are found to be energetically, mechanically and dynamically stable.

Phosphorene is considered as a material suitable for the hydrogen storage in molecular form. A significant advantage of molecular hydrogen storage over chemical storage in atomic form, which requires dissociation of the hydrogen bond and the formation of a hydride, is the improved kinetics. Our results show that the adsorption energy (-292 to -277 meV) of H_2 on phosphorene is appropriate for storage. The analysis of diffusion pathways between different physisorbed states on phosphorene shows that a single hydrogen molecule diffuses very easily along the open channel (less than 1 meV along the zigzag direction), as compared to 14 meV for diffusion across the channels (along the armchair direction). The potential energy surfaces for the dissociative chemisorption of H_2 was computed on highly symmetric sites of phosphorene and the highest activation barrier was found to be 2.77 eV. The very large dissociation energy coupled with a strong physisorption of H_2 and easy diffusion, makes this 2D material a promising candidate for H_2 storage at room temperature.

Computational materials science is playing a fundamental role in the development of energy storage and energy conversion systems. Particularly, the development of efficient computational infrastructure, codes, and faster high performance computers is increasing the connection between simulations and experimental studies. For the energy storage application, ab-initio studies have the potential to aid in the design of systems that utilize hydrogen as an energy carrier. Future investigations should be focused on the novel perovskite-type hydrides comprising Mg-based mixtures with lightweight metals and 2D materials in an effort to find a suitable candidate for on-board hydrogen storage. We are also wondering how far the thermodynamic properties for hydrogen storage may be improved by considering nanoparticles of perovskite hydride.

Bibliography

[1] S. Sorrell, *Renewable and Sustainable Energy Reviews* **2015**, *47*, 74–82.

[2] E. Shove, G. Walker, *Theory Culture & Society* **2014**, *31*, 41–58.

[3] M. R. Allen, O. P. Dube, W. Solecki, F. Aragón–Durand, W. Cramer, S. Humphreys, M. Kainuma, J. Kala, N. Mahowald, Y. Mulugetta, R. Perez, M. Wairiu, K. Zickfeld, 1-Farming and Context, techreport, **2018**, **pages** 47–92.

[4] R. Tuckett, *US EIA - Short-Term Energy Outlook* **2018**, 1–48.

[5] British Petroleum, BP statistical review of world energy. London, techreport, **2018**, **page** 40.

[6] J. Ren, N. M. Musyoka, H. W. Langmi, M. Mathe, S. Liao, *International Journal of Hydrogen Energy* **2017**, *42*, 289–311.

[7] Y. huan ZHANG, Z. chao JIA, Z. ming YUAN, T. YANG, Y. QI, D. liang ZHAO, *Journal of Iron and Steel Research International* **2015**, *22*, 757–770.

[8] I. Jain, *International Journal of Hydrogen Energy* **2009**, *34*, IWBT 2008, 7368–7378.

[9] B. Zhang, Y. Wu, *Progress in Natural Science: Materials International* **2017**, *27*, SI-HYDROGEN STORAGE MATERIALS, 21–33.

[10] M.-D. Iordache, A. Okujeni, S. van der Linden, J. M. Bioucas-Dias, A. Plaza, B. Somers **in**2014 6th Workshop on Hyperspectral Image and Signal Processing: Evolution in Remote Sensing (WHISPERS) **2014**, **pages** 1–4.

[11] M. Deveci, *International Journal of Hydrogen Energy* **2018**, *43*, 9353–9368.

[12] K. Mazloomi, C. Gomes, *Renewable and Sustainable Energy Reviews* **2012**, *16*, 3024–3033.

[13] H. Nazir, N. Muthuswamy, C. Louis, S. Jose, J. Prakash, M. E. Buan, C. Flox, S. Chavan, X. Shi, P. Kauranen, T. Kallio, G. Maia, K. Tammeveski, N. Lymperopoulos, E. Carcadea, E. Veziroglu, A. Iranzo, A. M. Kannan, *International Journal of Hydrogen Energy* **2020**, *45*, 20693–20708.

[14] S. Satyapal, J. Petrovic, C. Read, G. Thomas, G. Ordaz, *Catalysis Today* **2007**, *120*, Proceedings of the Korea Conference on Innovative Science and Technology (KCIST-2005):Frontiers in Hydrogen Storage Materials and Technology, 246–256.

[15] G. W. Crabtree, M. S. Dresselhaus, M. V. Buchanan, *Physics Today* **2004**, *57*, 39–44.

[16] H. Cavendish, *Philosophical Transactions of the Royal Society of London* **1766**, *56*, 141–184.

[17] F. G. Brickwedde, *Physics Today* **1982**, *35*, 34–39.

[18] M. L. Oliphant, P. Harteck, Rutherford, Transmutation effects observed with heavy hydrogen [1], **1934**.

[19] U.S. Department of Energy, Hydrogen Storage | Department of Energy, techreport 1, **2012**, n/a.

[20] A. Züttel, *Naturwissenschaften* **2004**, *91*, 157–172.

[21] I. Iordache, A. V. Gheorghe, M. Iordache, *International Journal of Hydrogen Energy* **2013**, *38*, 12231–12240.

[22] P. E. deJongh, P. Adelhelm, *ChemSusChem* **2010**, *3*, 1332–1348.

[23] T. N. Veziroglu, *Energy Procedia* **2012**, *29*, WHEC 2012 Conference Proceedings – 19th World Hydrogen Energy Conference, 654–656.

[24] T. N. Veziroğlu, S. Şahi˙n, *Energy Conversion and Management* **2008**, *49*, ICENES'2007, 13th International Conference on Emerging Nuclear Energy Systems, June 3–8, 2007, İstanbul, Turkiye, 1820–1831.

[25] Y. Sun, C. Shen, Q. Lai, W. Liu, D.-W. Wang, K.-F. Aguey-Zinsou, *Energy Storage Materials* **2018**, *10*, 168–198.

[26] N. Rusman, M. Dahari, *International Journal of Hydrogen Energy* **2016**, *41*, 12108–12126.

[27] X. Luo, J. Wang, M. Dooner, J. Clarke, *Applied Energy* **2015**, *137*, 511–536.

[28] F. Mueller-Langer, E. Tzimas, M. Kaltschmitt, S. Peteves, *International Journal of Hydrogen Energy* **2007**, *32*, TMS06: Symposium on Materials in Clean Power Systems, 3797–3810.

[29] D. Durbin, C. Malardier-Jugroot, *International Journal of Hydrogen Energy* **2013**, *38*, 14595–14617.

[30] T. Sadhasivam, H.-T. Kim, S. Jung, S.-H. Roh, J.-H. Park, H.-Y. Jung, *Renewable and Sustainable Energy Reviews* **2017**, *72*, 523–534.

[31] H. Nazir, C. Louis, S. Jose, J. Prakash, N. Muthuswamy, M. E. Buan, C. Flox, S. Chavan, X. Shi, P. Kauranen, T. Kallio, G. Maia, K. Tammeveski, N. Lymperopoulos, E. Carcadea, E. Veziroglu, A. Iranzo, A. M. Kannan, *International Journal of Hydrogen Energy* **2020**, *45*, 13777–13788.

[32] A. F. Dalebrook, W. Gan, M. Grasemann, S. Moret, G. Laurenczy, *Chem. Commun.* **2013**, *49*, 8735–8751.

[33] V. Tozzini, V. Pellegrini, *Phys. Chem. Chem. Phys.* **2013**, *15*, 80–89.

[34] H. T. Hwang, A. Varma, *Current Opinion in Chemical Engineering* **2014**, *5*, Energy and environmental engineering / Reaction engineering, 42–48.

[35] S. Sharma, S. K. Ghoshal, *Renewable and Sustainable Energy Reviews* **2015**, *43*, 1151–1158.

[36] D. Durbin, C. Malardier-Jugroot, *International Journal of Hydrogen Energy* **2013**, *38*, 14595–14617.

[37] Y. Jia, C. Sun, S. Shen, J. Zou, S. S. Mao, X. Yao, *Renewable and Sustainable Energy Reviews* **2015**, *44*, 289–303.

[38] T. Ozturk, A. Demirbas, *Energy Sources Part A: Recovery Utilization and Environmental Effects* **2007**, *29*, 1415–1423.

[39] G. Han, Y. Kwon, J. B. Kim, S. Lee, J. Bae, E. Cho, B. J. Lee, S. Cho, J. Park, *Applied Energy* **2020**, *259*, 114175.

[40] B. Sakintuna, F. Lamari-Darkrim, M. Hirscher, *International Journal of Hydrogen Energy* **2007**, *32*, 1121–1140.

[41] Giovanni Mazzolai, Recent Patents on Materials Science, 2012 , 5, 137-148.

[42] DOE Technical Targets for Fuel Cell Systems and Stacks for Transportation Applications | Department of Energy, **2020**.

[43] M. M. Whiston, I. L. Azevedo, S. Litster, K. S. Whitefoot, C. Samaras, J. F. Whitacre, *Proceedings of the National Academy of Sciences of the United States of America* **2019**, *116*, 4899–4904.

[44] J. Abe, A. Popoola, E. Ajenifuja, O. Popoola, *International Journal of Hydrogen Energy* **2019**, *44*, 15072–15086.

[45] J. Bellosta von Colbe, J.-R. Ares, J. Barale, M. Baricco, C. Buckley, G. Capurso, N. Gallandat, D. M. Grant, M. N. Guzik, I. Jacob, E. H. Jensen, T. Jensen, J. Jepsen, T. Klassen, M. V. Lototskyy, K. Manickam, A. Montone, J. Puszkiel, S. Sartori, D. A. Sheppard, A. Stuart, G. Walker, C. J. Webb, H. Yang, V. Yartys, A. Züttel, M. Dornheim, *International Journal of Hydrogen Energy* **2019**, *44*, A special issue on hydrogen-based Energy storage, 7780–7808.

[46] H Barthelemy, M Weber, F Barbier, *International Journal of Hydrogen Energy* **2017**, *42*, 7254–7262.

[47] D Mori, K Hirose, *International Journal of Hydrogen Energy* **2009**, *34*, 4569–4574.

[48] S. W. Jorgensen, *Current Opinion in Solid State and Materials Science* **2011**, *15*, 39–43.

[49] R. Janot, M. Latroche, A. Percheron-Guégan, *Materials Science and Engineering: B* **2005**, *123*, 187–193.

[50] A. Midilli, M. Ay, I. Dincer, M. Rosen, *Renewable and Sustainable Energy Reviews* **2005**, *9*, 255–271.

[51] C. Webb, *Journal of Physics and Chemistry of Solids* **2015**, *84*, Focus issue on the Study of matter at extreme conditions and related phenomena, 96–106.

[52] D. Schitea, M. Deveci, M. Iordache, K. Bilgili, Z. Akyurt, I. Iordache, *International Journal of Hydrogen Energy* **2019**, *44*, 8585–8600.

[53] E. David, *Journal of Materials Processing Technology* **2005**, *162-163*, AMPT/AMME05, 169–177.

[54] S. M. Aceves, F. Espinosa-Loza, E. Ledesma-Orozco, T. O. Ross, A. H. Weisberg, T. C. Brunner, O. Kircher, *International Journal of Hydrogen Energy* **2010**, *35*, 1219–1226.

[55] R. Ahluwalia, T. Hua, J.-K Peng, S. Lasher, K. McKenney, J. Sinha, M. Gardiner, *International Journal of Hydrogen Energy* **2011**, *35*, 4171–4184.

[56] K. Mazloomi, C. Gomes, *Renewable and Sustainable Energy Reviews* **2012**, *16*, 3024–3033.

[57] *Journal of Alloys and Compounds* **2020**, *827*, 153548.

[58] A. Eftekhari, B. Fang, *International Journal of Hydrogen Energy* **2017**, *42*, 25143–25165.

[59] X. Shan, J. H. Payer, W. D. Jennings, *International Journal of Hydrogen Energy* **2009**, *34*, 363–369.

[60] S. Sleiman, J. Huot, Inorganics 2017, 5, 300-308.

[61] L. Zhang, J. Zheng, X. Xiao, X. Wang, X. Huang, M. Liu, Q. Wang, L. Chen, *International Journal of Hydrogen Energy* **2017**, *42*, 20046–20055.

[62] A. Ozarslan, *International Journal of Hydrogen Energy* **2012**, *37*, HYFUSEN, 14265–14277.

[63] T. K. Mandal, D. H. Gregory, *Proceedings of the Institution of Mechanical Engineers Part C: Journal of Mechanical Engineering Science* **2010**, *224*, 539–558.

[64] F. Costanzo, P. L. Silvestrelli, F. Ancilotto, *Journal of Chemical Theory and Computation* **2012**, *8*, PMID: 26596745, 1288–1294.

[65] M. Jehan, D. Fruchart, *Journal of Alloys and Compounds* **2013**, *580*, SI : MH2012, S343–S348.

[66] M. V. Lototskyy, M. W. Davids, I. Tolj, Y. V. Klochko, B. S. Sekhar, S. Chidziva, F. Smith, D. Swanepoel, B. G. Pollet, *International Journal of Hydrogen Energy* **2015**, *40*, 11491–11497.

[67] G Rambach, C Hendricks, 1996.

[68] N. Zhevago, A. Chabak, E. Denisov, V. Glebov, S. Korobtsev, *International Journal of Hydrogen Energy* **2013**, *38*, 6694–6703.

[69] N. Zhevago, E. Denisov, V. Glebov, *International Journal of Hydrogen Energy* **2010**, *35*, 169–175.

[70] H. Langmi, D. Book, A. Walton, S. Johnson, M. Al-Mamouri, J. Speight, P. Edwards, I. Harris, P. Anderson, *Journal of Alloys and Compounds* **2005**, *404-406*, Proceedings of the 9th International Symposium on Metal-Hydrogen Systems, Fundamentals and Applications (MH2004), 637–642.

[71] R. Ströbel, J. Garche, P. Moseley, L. Jörissen, G. Wolf, *Journal of Power Sources* **2006**, *159*, 781–801.

[72] Y. Xia, Z. Yang, Y. Zhu, *J. Mater. Chem. A* **2013**, *1*, 9365–9381.

[73] Z. Abdin, K. R. Khalilpour **in***Polygeneration with Polystorage for Chemical and Energy Hubs* (**editor**: K. R. Khalilpour), Academic Press, **2019**, **pages** 77–131.

[74] S. S. Han, H. Furukawa, O. M. Yaghi, W. A. Goddard, *Journal of the American Chemical Society* **2008**, *130*, PMID: 18683924, 11580–11581.

[75] A. Züttel, *Materials Today* **2003**, *6*, 24–33.

[76] J. L. Blackburn, P. A. Parilla, T. Gennett, K. E. Hurst, A. C. Dillon, M. J. Heben, *Journal of Alloys and Compounds* **2008**, *454*, 483–490.

[77] A. López-Suárez, *International Journal of Hydrogen Energy* **2010**, *35*, Indo-French Workshop on Biohydrogen: from Basic Concepts to Technology, 10404–10411.

[78] K. L. Lim, H. Kazemian, Z. Yaakob, W. R. W. Daud, *Chemical Engineering & Technology* **2010**, *33*, 213–226.

[79] M. Paskevicius, D. Sheppard, K. Williamson, C. Buckley, *Energy* **2015**, *88*, 469–477.

[80] A. Demirbas, *Energy Sources* **2002**, *24*, 601–610.

[81] J. Huot, F. Cuevas, S. Deledda, K. Edalati, Y. Filinchuk, T. Grosdidier, B. C. Hauback, M. Heere, T. R. Jensen, M. Latroche, S. Sartori, *Materials* **2019**, *12*.

[82] M. Dornheim in Thermodynamics-Interaction Studies-Solids, Liquids and Gases,

[83] Q. Lai, M. Paskevicius, D. A. Sheppard, C. E. Buckley, A. W. Thornton, M. R. Hill, Q. Gu, J. Mao, Z. Huang, H. K. Liu, Z. Guo, A. Banerjee, S. Chakraborty, R. Ahuja, K.-F. Aguey-Zinsou, *ChemSusChem* **2015**, *8*, 2789–2825.

[84] N. Z. Abd.Khalim Khafidz, Z. Yaakob, K. L. Lim, S. N. Timmiati, *International Journal of Hydrogen Energy* **2016**, *41*, 13131–13151.

[85] R. Jain, A. Jain, S. Agarwal, N. Lalla, V. Ganesan, D. Phase, I. Jain, *Journal of Alloys and Compounds* **2007**, *440*, 84–88.

[86] I. Jain, C. Lal, A. Jain, *International Journal of Hydrogen Energy* **2010**, *35*, Novel Hydrogen Production Technologies and Applications, 5133–5144.

[87] A. Tlahuice-Flores, *The Journal of Physical Chemistry C* **2018**, *122*, 14971–14978.

[88] B. D. Adams, A. Chen, *Materials Today* **2011**, *14*, 282–289.

[89] K. Shashikala, A. Kumar, C. Betty, S. Banerjee, P. Sengupta, C. Pillai, *Journal of Alloys and Compounds* **2011**, *509*, 9079–9083.

[90] V. Zadorozhnyy, G. Milovzorov, S. Klyamkin, M. Zadorozhnyy, D. Strugova, M. Gorshenkov, S. Kaloshkin, *Progress in Natural Science: Materials International* **2017**, *27*, SI-HYDROGEN STORAGE MATERIALS, 149–155.

[91] A. W. C. van den Berg, C. O. Areán, *Chem. Commun.* **2008**, 668–681.

[92] L Zaluski, A Zaluska, J. Ström-Olsen, *Journal of Alloys and Compounds* **1997**, *253-254*, 70–79.

[93] R. Chamoun, U. B. Demirci, P. Miele, *Energy Technology* **2015**, *3*, 100–117.

[94] V. Yartys, M. Lototskyy, E. Akiba, R. Albert, V. Antonov, J. Ares, M. Baricco, N. Bourgeois, C. Buckley, J. Bellosta von Colbe, J.-C. Crivello, F. Cuevas, R. Denys, M. Dornheim, M. Felderhoff, D. Grant, B. Hauback, T. Humphries, I. Jacob, T. Jensen, P. de Jongh, J.-M. Joubert, M. Kuzovnikov, M. Latroche, M. Paskevicius, L. Pasquini, L. Popilevsky, V. Skripnyuk, E. Rabkin, M. Sofianos, A. Stuart, G. Walker, H. Wang, C. Webb, M. Zhu, *International Journal of Hydrogen Energy* **2019**, *44*, A special issue on hydrogen-based Energy storage, 7809–7859.

[95] R. A. Varin, T Czujko, Z Wronski, *Nanotechnology* **2006**, *17*, 3856–3865.

[96] H. Furukawa, O. M. Yaghi, *Journal of the American Chemical Society* **2009**, *131*, PMID: 19496589, 8875–8883.

[97] K. Kumar, M. Alam, D. Rakshit, V. Dutta, *Energy Conversion and Management* **2019**, *187*, 176–190.

[98] J. Farrell, W. E. Wallace, *Inorganic Chemistry* **1966**, *5*, 105–109.

[99] A. Lys, J. O. Fadonougbo, M. Faisal, J.-Y. Suh, Y.-S. Lee, J.-H. Shim, J. Park, Y. W. Cho, *Hydrogen* **2020**, *1*, 38–63.

[100] Y. HATANO, K. ISOBE, R. HITAKA, M. SUGISAKI, *Journal of Nuclear Science and Technology* **1996**, *33*, 944–949.

[101] J. Bellosta von Colbe, J. R. Ares, J. Barale, M. Baricco, C. Buckley, G. Capurso, N. Gallandat, D. M. Grant, M. N. Guzik, I. Jacob, E. H. Jensen, T. Jensen, J. Jepsen, T. Klassen, M. V. Lototskyy, K. Manickam, A. Montone, J. Puszkiel, S. Sartori, D. A. Sheppard, A. Stuart, G. Walker, C. J. Webb, H. Yang, V. Yartys, A. Züttel, M. Dornheim, *International Journal of Hydrogen Energy* **2019**, *44*, 7780–7808.

[102] B. D. MacDonald, A. M. Rowe, *Journal of Power Sources* **2006**, *161*, 346–355.

[103] J. Chen, N. Kuriyama, H. T. Takeshita, H. Tanaka, T. Sakai, M. Haruta, *Electrochemical and Solid-State Letters* **2000**, *3*, 249–252.

[104] G. Mohan, M. Prakash Maiya, S. Srinivasa Murthy, *International Journal of Hydrogen Energy* **2007**, *32*, 4978–4987.

[105] B. Sakintuna, F. Lamari-Darkrim, M. Hirscher, Metal hydride materials for solid hydrogen storage: A review, **2007**.

[106] M. Dornheim **in***Thermodynamics* (**editor**: J. C. Moreno-Pirajan), IntechOpen, Rijeka, **2011**, **chapter** 33.

[107] S.-F. Wang, Y.-X. Liu, Y.-F. Hsu, C.-J. Li, P. Jasinski, *International Journal of Applied Ceramic Technology* **2017**, *14*, 84–93.

[108] H. Leng, T. Ichikawa, H. Fujii, *The Journal of Physical Chemistry B* **2006**, *110*, PMID: 16805600, 12964–12968.

[109] O. Dolotko, S. Gupta, T. Kobayashi, E. McDonald, I. Hlova, E. Majzoub, V. P. Balema, M. Pruski, V. K. Pecharsky, *International Journal of Hydrogen Energy* **2019**, *44*, 7381–7391.

[110] Z. Jiang, J. Yuan, H. Han, Y. Wu, *Journal of Alloys and Compounds* **2018**, *743*, 11–16.

[111] G. Afonso, A. Bonakdarpour, D. P. Wilkinson, *The Journal of Physical Chemistry C* **2013**, *117*, 21105–21111.

[112] P. Javadian, C. Zlotea, C. M. Ghimbeu, M. Latroche, T. R. Jensen, *The Journal of Physical Chemistry C* **2015**, *119*, 5819–5826.

[113] G. Severa, E. Rönnebro, C. M. Jensen, *Chem. Commun.* **2010**, *46*, 421–423.

[114] S. Srinivasan, D. Escobar, Y. Goswami, E. Stefanakos, *International Journal of Hydrogen Energy* **2008**, *33*, 2268–2272.

[115] S.-i. Orimo, Y. Nakamori, J. R. Eliseo, A. Züttel, C. M. Jensen, *Chemical Reviews* **2007**, *107*, PMID: 17848101, 4111–4132.

[116] M. Ismail, Y. Zhao, X. B. Yu, A. Ranjbar, S. X. Dou, *International Journal of Hydrogen Energy* **2011**, *36*, 3593–3599.

[117] T. B. Lee, D. Kim, D. H. Jung, S. B. Choi, J. H. Yoon, J. Kim, K. Choi, S. H. Choi, *Catalysis Today* **2007**, *120*, 330–335.

[118] B. Bogdanovic, M. Felderhoff, G. Streukens, *Journal of the Serbian Chemical Society* **2009**, *74*, 183–196.

[119] L. George, S. K. Saxena, Structural stability of metal hydrides, alanates and borohydrides of alkali and alkali- earth elements: A review, **2010**.

[120] B. Bogdanović, M. Felderhoff, S. Kaskel, A. Pommerin, K. Schlichte, F. Schüth, *Advanced Materials* **2003**, *15*, 1012–1015.

[121] O. Zavorotynska, A. El-Kharbachi, S. Deledda, B. C. Hauback, *International Journal of Hydrogen Energy* **2016**, *41*, 14387–14403.

[122] Z. Huang, Z. Guo, A. Calka, D. Wexler, C. Lukey, H. Liu, *Journal of Alloys and Compounds* **2006**, *422*, 299–304.

[123] M. B. Ley, L. H. Jepsen, Y.-S. Lee, Y. W. Cho, J. M. Bellosta von Colbe, M. Dornheim, M. Rokni, J. O. Jensen, M. Sloth, Y. Filinchuk, J. E. Jørgensen, F. Besenbacher, T. R. Jensen, *Materials Today* **2014**, *17*, 122–128.

[124] M. Zhu, Y. Lu, L. Ouyang, H. Wang, *Materials* **2013**, *6*, 4654–4674.

[125] I. Jain, P. Jain, A. Jain, *Journal of Alloys and Compounds* **2010**, *503*, 303–339.

[126] P. E. de Jongh, P. Adelhelm, *ChemSusChem* **2010**, *3*, 1332—1348.

[127] G. Friedlmeier, M. Groll, *Journal of Alloys and Compounds* **1997**, *253-254*, 550–555.

[128] A Zaluska, L Zaluski, J. Ström–Olsen, *Journal of Alloys and Compounds* **1999**, *288*, 217–225.

[129] A. Andreasen, T. Vegge, A. S. Pedersen, *The Journal of Physical Chemistry B* **2005**, *109*, PMID: 16851363, 3340–3344.

[130] E. Boateng, A. Chen, *Materials Today Advances* **2020**, *6*, 100022.

[131] K.-F. Aguey-Zinsou, J.-R. Ares-Fernández, *Energy Environ. Sci.* **2010**, *3*, 526–543.

[132] B. Zahiri, B. S. Amirkhiz, D. Mitlin, *Applied Physics Letters* **2010**, *97*, 083106.

[133] S. S. Srinivasan, P. C. Sharma, *Catalysts* **2012**, *2*, 434–446.

[134] R. A. Varin, L. Zbroniec, M. Polanski, J. Bystrzycki, *Energies* **2011**, *4*, 1–25.

[135] P Tessier, H Enoki, M Bououdina, E Akiba, *Journal of Alloys and Compounds* **1998**, *268*, 285–289.

[136] T. Klassen, W. Oelerich, R. Bormann **in**Metastable, Mechanically Alloyed and Nanocrystalline Materials 2000 Trans Tech Publications Ltd, **2001**, **pages** 603–608.

[137] R Schulz, J Huot, G Liang, S Boily, G Lalande, M. Denis, J. Dodelet, *Materials Science and Engineering: A* **1999**, *267*, 240–245.

[138] H.‥Young, Conceiving the Indian Buddhist Patriarchs in China, 2015, 1--24

[139] P. Jain, C. Gosselin, N. Skryabina, D. Fruchart, J. Huot, *Journal of Alloys and Compounds* **2015**, *636*, 375–380.

[140] Z. G. Yang, K. S. Weil, M. P. Brady, *International Journal of Hydrogen Energy* **2007**, *32*, TMS06: Symposium on Materials in Clean Power Systems, 3609.

[141] L. Zaluski, A. Zaluska, J. Ström-Olsen, *Journal of Alloys and Compounds* **1995**, *217*, 245–249.

[142] R. Baer, Y. Zeiri, R. Kosloff, *Phys. Rev. B* **1997**, *55*, 10952–10952.

[143] J. Bloch, M H. Mintz, Journal of Alloys and Compounds, 1997, 253—254, 1—2

[144] A. Baran, M. Polański, *Materials* **2020**, *13*.

[145] C. Iwakura, S. Nohara, S. G. Zhang, H. Inoue, *Journal of Alloys and Compounds* **1999**, *285*, 246–249.

[146] G. Liang, J. Huot, S. Boily, A. Van Neste, R. Schulz, *Journal of Alloys and Compounds* **1999**, *282*, 286–290.

[147] J Huot, J. Pelletier, G Liang, M Sutton, R Schulz, *Journal of Alloys and Compounds* **2002**, *330-332*, Proceedings of the International Symposium on Metal-Hydrogen Systems, Fundamentals and Applications (MH2000), 727–731.

[148] G. Liang, S. Boily, J. Huot, A. V. Neste, R. Schulz, *Journal of Alloys and Compounds* **1998**, *268*, 302–307.

[149] Z. Tan, C. Chiu, E. J. Heilweil, L. A. Bendersky, *International Journal of Hydrogen Energy* **2011**, *36*, European Fuel Cell 2009, 9702–9713.

[150] H. Lu, C. Poh, L. Zhang, Z. Guo, X. Yu, H. Liu, *Journal of Alloys and Compounds* **2009**, *481*, 152–155.

[151] R. Morris, P. Wheatley, *Angewandte Chemie International Edition* **2008**, *47*, 4966–4981.

[152] J. Germain, J. M. J. Fréchet, F. Svec, *Small* **2009**, *5*, 1098–1111.

[153] S. Tedds, A. Walton, D. P. Broom, D. Book, *Faraday Discuss.* **2011**, *151*, 75–94.

[154] M. Hirscher, B. Panella, *Journal of Alloys and Compounds* **2005**, *404-406*, 399–401.

[155] Y. Xia, Z. Yang, Y. Zhu, *Journal of Materials Chemistry A* **2013**, *1*, 9365–9381.

[156] C. Liu, Y. Chen, C. Z. Wu, S. T. Xu, H. M. Cheng, *Carbon* **2010**, *48*, 452–455.

[157] H. M. Cheng, Q. H. Yang, C. Liu, *Carbon* **2001**, *39*, 1447–1454.

[158] M. Mohan, V. K. Sharma, E. A. Kumar, V. Gayathri, *Energy Storage* **2019**, *1*, e35.

[159] S. M. Lee, Y. H. Lee, *Applied Physics Letters* **2000**, *76*, 2877–2879.

[160] A. Lueking, R. T. Yang, *Journal of Catalysis* **2002**, *206*, 165–168.

[161] A. Reyhani, S. Mortazavi, A. Moshfegh, A. N. Golikand, M. Amiri, *Journal of Power Sources* **2009**, *188*, 404–410.

[162] S. Z. Mortazavi, P. Parvin, A. Reyhani, R. Malekfar, S. Mirershadi, *RSC Adv.* **2013**, *3*, 1397–1409.

[163] Chen, Wu, Lin, Tan, *Science* **1999**, *285 5424*, 91–3.

[164] A. M. Abdalla, S. Hossain, O. B. Nisfindy, A. T. Azad, M. Dawood, A. K. Azad, *Energy Conversion and Management* **2018**, *165*, 602–627.

[165] N. L. Rosi, J. Eckert, M. Eddaoudi, D. T. Vodak, J. Kim, M. O'Keeffe, O. M. Yaghi, *Science* **2003**, *300*, 1127–1129.

[166] K. K. Gangu, S. Maddila, S. B. Mukkamala, S. B. Jonnalagadda, *Inorganica Chimica Acta* **2016**, *446*, 61–74.

[167] K. K. Gangu, S. Maddila, S. B. Jonnalagadda, *Inorganica Chimica Acta* **2017**, *466*, 308–323.

[168] K. K. Gangu, S. Maddila, S. B. Mukkamala, S. B. Jonnalagadda, *Journal of Molecular Structure* **2017**, *1143*, 153–162.

[169] A. G. Wong-Foy, A. J. Matzger, O. M. Yaghi, *Journal of the American Chemical Society* **2006**, *128*, PMID: 16536503, 3494–3495.

[170] V. R. Bakuru, M. E. DMello, S. B. Kalidindi, *ChemPhysChem* **2019**, *20*, 1177–1215.

[171] Y. Basdogan, S. Keskin, *CrystEngComm* **2015**, *17*, 261–275.

[172] S. S. Kaye, A. Dailly, O. M. Yaghi, J. R. Long, *Journal of the American Chemical Society* **2007**, *129*, PMID: 17967030, 14176–14177.

[173] S. Niaz, T. Manzoor, A. H. Pandith, *Renewable and Sustainable Energy Reviews* **2015**, *50*, 457–469.

[174] R. Hardian, C. Pistidda, A.-L. Chaudhary, G. Capurso, G. Gizer, H. Cao, C. Milanese, A. Girella, A. Santoru, D. Yigit, H. Dieringa, K. Kainer, T. Klassen, M. Dornheim, *International Journal of Hydrogen Energy* **2018**, *43*, 16738–16748.

[175] H. Yong, S. Guo, Z. Yuan, Y. Qi, D. Zhao, Y. Zhang, *International Journal of Hydrogen Energy* **2019**, *44*, 16765–16776.

[176] M. Tian, C. Shang, *International Journal of Hydrogen Energy* **2019**, *44*, State of the Art Materials for Hydrogen Energy, 338–344.

[177] L. Ouyang, Z. Cao, H. Wang, J. Liu, D. Sun, Q. Zhang, M. Zhu, *Journal of Alloys and Compounds* **2014**, *586*, 113–117.

[178] J. Zhang, S. Yan, L. Yu, X. Zhou, T. Zhou, P. Peng, *International Journal of Hydrogen Energy* **2018**, *43*, 21864–21873.

[179] Q. Luo, J. Li, B. Li, B. Liu, H. Shao, Q. Li, *Journal of Magnesium and Alloys* **2019**, *7*, 58–71.

[180] S. Haldar, S. Mukherjee, F. Ahmed, C. V. Singh, *International Journal of Hydrogen Energy* **2017**, *42*, 23018–23027.

[181] W. Lei, H. Zhang, Y. Wu, B. Zhang, D. Liu, S. Qin, Z. Liu, L. Liu, Y. Ma, Y. Chen, *Nano Energy* **2014**, *6*, 219–224.

[182] X. Tan, H. A. Tahini, S. C. Smith, *ACS Applied Materials & Interfaces* **2016**, *8*, PMID: 27934167, 32815–32822.

[183] C. Tan, X. Cao, X.-J. Wu, Q. He, J. Yang, X. Zhang, J. Chen, W. Zhao, S. Han, G.-H. Nam, M. Sindoro, H. Zhang, *Chemical Reviews* **2017**, *117*, PMID: 28306244, 6225–6331.

[184] A. Hashmi, M. U. Farooq, I. Khan, J. Son, J. Hong, *J. Mater. Chem. A* **2017**, *5*, 2821–2828.

[185] D. J. Griffiths, D. F. Schroeter, *Introduction to quantum mechanics*, Cambridge University Press, **2018**.

[186] E. Schrödinger, *Phys. Rev.* **1926**, *28*, 1049–1070.

[187] U. Peskin, N. Moiseyev, *The Journal of Chemical Physics* **1993**, *99*, 4590–4596.

[188] M Born, R Oppenheimer, *Annalen der Physik* **1927**, *389*, 457–484.

[189] D. R. Hartree, *Mathematical Proceedings of the Cambridge Philosophical Society* **1928**, *24*, 111–132.

[190] J. C. Slater, *Physical Review* **1928**, *32*, 339–348.

[191] J. A. Gaunt, *Mathematical Proceedings of the Cambridge Philosophical Society* **1928**, *24*, 328–342.

[192] J. C. Slater, Physical Review, 1930, 35, 210—211.

[193] V. Fock, *Zeitschrift für Physik* **1930**, *61*, 126–148.

[194] V. Fock, *Zeitschrift für Physik* **1930**, *62*, 795–805.

[195] L. H. Thomas, *Mathematical Proceedings of the Cambridge Philosophical Society* **1927**, *23*, 542–548.

[196] E. Teller, *Reviews of Modern Physics* **1962**, *34*, 627–631.

[197] R. G. Parr, Chemical and Engineering News, 1990, 68, 45.

[198] R. G. Parr **in***Horizons of Quantum Chemistry* Springer Netherlands, Dordrecht, **1980**, **pages** 5–15.

[199] S. Seriy, *Open Journal of Modelling and Simulation* **2015**, *03*, 96–103.

[200] J.-L. Calais, *International Journal of Quantum Chemistry* **1993**, *47*, 101–101.

[201] P. Hohenberg, W. Kohn, *Physical Review* **1964**, *136*, B864.

[202] D. M. Ceperley, B. J. Alder, *Phys. Rev. Lett.* **1980**, *45*, 566–569.

[203] F. Bloch, *Zeitschrift für Physik* **1929**, *52*, 555–600.

[204] A. Dal Corso **in**Springer, Berlin, Heidelberg **1996**, **pages** 155–178.

[205] P. Giannozzi, S. Baroni, N. Bonini, M. Calandra, R. Car, C. Cavazzoni, D. Ceresoli, G. L. Chiarotti, M. Cococcioni, I. Dabo, A. D. Corso, S. de Gironcoli, S. Fabris, G. Fratesi, R. Gebauer, U. Gerstmann, C. Gougoussis, A. Kokalj, M. Lazzeri, L. Martin-Samos, N. Marzari, F. Mauri, R. Mazzarello, S. Paolini, A. Pasquarello, L. Paulatto, C. Sbraccia, S. Scandolo, G. Sclauzero, A. P. Seitsonen, A. Smogunov, P. Umari, R. M. Wentzcovitch, *Journal of Physics: Condensed Matter* **2009**, *21*, 395502.

[206] P Giannozzi, O Andreussi, T Brumme, O Bunau, M. B. Nardelli, M Calandra, R Car, C Cavazzoni, D Ceresoli, M Cococcioni, N Colonna, I Carnimeo, A. D. Corso, S de Gironcoli, P Delugas, R. A. DiStasio, A Ferretti, A Floris, G Fratesi, G Fugallo, R Gebauer, U Gerstmann, F Giustino, T Gorni, J Jia, M Kawamura, H.-Y. Ko, A Kokalj, E Küçükbenli, M Lazzeri, M Marsili, N Marzari, F Mauri, N. L. Nguyen, H.-V. Nguyen, A Otero-de-la Roza, L Paulatto, S Poncé, D Rocca, R Sabatini, B Santra, M Schlipf, A. P. Seitsonen, A Smogunov, I Timrov, T Thonhauser, P Umari, N Vast, X Wu, S Baroni, *Journal of Physics: Condensed Matter* **2017**, *29*, 465901.

[207] S. Baroni, P. Giannozzi, A. Testa, *Physical Review Letters* **1987**, *59*, 2662–2665.

[208] P. Giannozzi, S. De Gironcoli, P. Pavone, S. Baroni, *Physical Review B* **1991**, *43*, 7231–7242.

[209] K. Parlinski, Z. Q. Li, Y. Kawazoe, *Phys. Rev. Lett.* **1997**, *78*, 4063–4066.

[210] J. Li, J. Xu, B. Li, L. He, H. Lin, H.-W. Li, H. Shao, **2018**, 12.

[211] A. Bhatnagar, M. Shaz, O. Srivastava, *International Journal of Hydrogen Energy* **2019**, *44*, 6738–6747.

[212] P. Pluengphon, T. Bovornratanaraks, P. Tsuppayakorn-aek, U. Pinsook, B. Inceesungvorn, *International Journal of Hydrogen Energy* **2019**, *44*, 21948–21954.

[213] D. Meggiolaro, G. Gigli, A. Paolone, F. Vitucci, S. Brutti, *The Journal of Physical Chemistry C* **2013**, *117*, 22467–22477.

[214] T. K. Nielsen, K. Manickam, M. Hirscher, F. Besenbacher, T. R. Jensen, *ACS Nano* **2009**, *3*, PMID: 19883120, 3521–3528.

[215] B. Li, J. Li, H. Zhao, X. Yu, H. Shao, *International Journal of Hydrogen Energy* **2019**, *44*, 6007–6018.

[216] A. Schneemann, J. L. White, S. Kang, S. Jeong, L. F. Wan, E. S. Cho, T. W. Heo, D. Prendergast, J. J. Urban, B. C. Wood, M. D. Allendorf, V. Stavila, *Chemical Reviews* **2018**, *118*, 10775–10839.

[217] N. S. Norberg, T. S. Arthur, S. J. Fredrick, A. L. Prieto, *Journal of the American Chemical Society* **2011**, *133*, PMID: 21671640, 10679–10681.

[218] C. Mui, S. F. Bent, C. B. Musgrave, *The Journal of Physical Chemistry B* **2004**, *108*, PMID: 18950120, 6336–6350.

[219] F. Zhang, Y. Wang, M. Y. Chou, *The Journal of Physical Chemistry C* **2012**, *116*, 18663–18668.

[220] H. Benzidi, M. Lakhal, M. Abdellaoui, M. Garara, A. Benyoussef, A. El kenz, M. Loulidi, M. Hamedoun, O. Mounkachi, *International Journal of Hydrogen Energy* **2019**, *44*, 16793–16802.

[221] M. Abdellaoui, M. Lakhal, H. Benzidi, O. Mounkachi, A. Benyoussef, A. El Kenz, M. Loulidi, *International Journal of Hydrogen Energy* **2020**, *45*, 11158–11166.

[222] E. German, R. Gebauer, *The Journal of Physical Chemistry C* **2016**, *120*, 4806–4812.

[223] F. S. Sangsefidi, M. Salavati-Niasari, *ACS Applied Energy Materials* **2018**, *1*, 4840–4848.

[224] J.-J. Tang, X.-B. Yang, M. Chen, M. Zhu, Y.-J. Zhao, *The Journal of Physical Chemistry C* **2012**, *116*, 14943–14949.

[225] J. Zhang, Y. Zhou, Z. Ma, L. Sun, P. Peng, *International Journal of Hydrogen Energy* **2013**, *38*, 3661–3669.

[226] H. Benzidi, M. Lakhal, A. Benyoussef, M. Hamedoun, M. Loulidi, A. El kenz, O. Mounkachi, *International Journal of Hydrogen Energy* **2017**, *42*, 19481–19486.

[227] P. Suryanarayana, K. Bhattacharya, M. Ortiz, *Journal of the Mechanics and Physics of Solids* **2013**, *61*, 38–60.

[228] R. van Meer, O. Gritsenko, E. Baerends, *Chemical Physics Letters* **2015**, *639*, 315–319.

[229] J. P. Perdew, K. Burke, M. Ernzerhof, *Phys. Rev. Lett.* **1996**, *77*, 3865–3868.

[230] F. G. VanGessel, P. W. Chung, *Computer Methods in Applied Mechanics and Engineering* **2017**, *317*, 1012–1036.

[231] J. D. Head, M. C. Zerner, *Chemical Physics Letters* **1985**, *122*, 264–270.

[232] K. Momma, F. Izumi, *Journal of Applied Crystallography* **2011**, *44*, 1272–1276.

[233] A. Togo, I. Tanaka, *Scripta Materialia* **2015**, *108*, 1–5.

[234] K. Parlinski, Z. Q. Li, Y. Kawazoe, *Phys. Rev. Lett.* **1998**, *81*, 3298–3298.

[235] T. Vegge, L. S. Hedegaard-Jensen, J. Bonde, T. R. Munter, J. K. Nørskov, *Journal of Alloys and Compounds* **2005**, *386*, 1–7.

[236] A. Candan, M. Kurban, *Solid State Communications* **2018**, *281*, 38–43.

[237] A Reiser, B Bogdanović, K Schlichte, *International Journal of Hydrogen Energy* **2000**, *25*, 425–430.

[238] R. Gremaud, C. Broedersz, D. Borsa, A. Borgschulte, P. Mauron, H. Schreuders, J. Rector, B. Dam, R. Griessen, *Advanced Materials* **2007**, *19*, 2813–2817.

[239] M. Ramzan, S. Lebègue, R. Ahuja, *International Journal of Hydrogen Energy* **2010**, *35*, Indo-French Workshop on Biohydrogen: from Basic Concepts to Technology, 10373–10376.

[240] Y. Kojima, *International Journal of Hydrogen Energy* **2019**, *44*, 18179–18192.

[241] T. Vegge, *Phys. Rev. B* **2004**, *70*, 035412.

[242] Q. Chen, N. De Marco, Y. M. Yang, T.-B. Song, C.-C. Chen, H. Zhao, Z. Hong, H. Zhou, Y. Yang, *Nano Today* **2015**, *10*, 355–396.

[243] M. Becker, T. Klüner and M. Wark, Dalton Trans journal, 2017, 46, 3500-3509.

[244] R. E. Schaak, T. E. Mallouk, *Chemistry of Materials* **2000**, *12*, 3427–3434.

[245] M. Becker, T. Klüner, M. Wark, *Dalton Trans.* **2017**, *46*, 3500–3509.

[246] B. Kamecki, J. Karczewski, P. Jasiński, S. Molin, *Advanced Materials Interfaces* **2021**, *8*, 2002227.

[247] K. Ikeda, T. Sato and S.-i. Orimo, International Journal of Materials Research, 2008, 99, 471–479.

[248] A. Reshak, *International Journal of Hydrogen Energy* **2015**, *40*, 16383–16390.

[249] Y. Li, J. S. Chung, S. G. Kang, *ACS Combinatorial Science* **2019**, *21*, PMID: 31613590, 736–742.

[250] D. Pottmaier, E. R. Pinatel, J. G. Vitillo, S. Garroni, M. Orlova, M. D. Baró, G. B. M. Vaughan, M. Fichtner, W. Lohstroh, M. Baricco, *Chemistry of Materials* **2011**, *23*, 2317–2326.

[251] H. Zhou, Y. Cai, G. Zhang, Y.-W. Zhang, *Nanoscale* **2018**, *10*, 480–487.

[252] C. Setty, M. Baggioli, A. Zaccone, *Physical Review B* **2021**, *103*, 2469–9969.

[253] G. M. Psofogiannakis, G. E. Froudakis, *The Journal of Physical Chemistry C* **2012**, *116*, 19211–19214.

[254] T. Hussain, D. Searles, K. Takahashi, *The Journal of Physical Chemistry Part A: Molecules Spectroscopy Kinetics Environment and General Theory* **2016**, *120*, 2009–2013.

[255] K. Alhameedi, A. Karton, D. Jayatilaka, T. Hussain, *Applied Surface Science* **2019**, *471*, 887–892.

[256] P. Mishra, D. Singh, Y. Sonvane, R. Ahuja, *International Journal of Hydrogen Energy* **2020**, *45*, 12384–12393.

[257] N. Khossossi, A. Banerjee, Y. Benhouria, I. Essaoudi, A. Ainane, R. Ahuja, *Phys. Chem. Chem. Phys.* **2019**, *21*, 18328–18337.

[258] G. Kern, G. Kresse, J. Hafner, *Phys. Rev. B* **1999**, *59*, 8551–8559.

[259] M. Wu, H. Fu, L. Zhou, K. Yao, X. C. Zeng, *Nano Letters* **2015**, *15*, PMID: 25844524, 3557–3562.

[260] Z. Chen, J. Zhao, L. Yin, Z. Chen, *J. Mater. Chem. A* **2019**, *7*, 13284–13292.

[261] S. R. Naqvi, G. S. Rao, W. Luo, R. Ahuja, T. Hussain, *ChemPhysChem* **2017**, *18*, 513–518.

[262] B. Mortazavi, T. Rabczuk, *Energies* **2018**, *11*.

[263] P. Mishra, D. Singh, Y. Sonvane, R. Ahuja, *Journal of Applied Physics* **2020**, *127*, 184305.

[264] Z. Zhu, D. Tománek, *Phys. Rev. Lett.* **2014**, *112*, 176802.

[265] Y. Jing, X. Zhang, Z. Zhou, *WIREs Computational Molecular Science* **2016**, *6*, 5–19.

[266] B. Sa, Y.-L. Li, J. Qi, R. Ahuja, Z. Sun, *The Journal of Physical Chemistry C* **2014**, *118*, 26560–26568.

[267] X. Han, H. M. Stewart, S. A. Shevlin, C. R. A. Catlow, Z. X. Guo, *Nano Letters* **2014**, *14*, PMID: 24992160, 4607–4614.

[268] J. Hu, B. Xu, S. A. Yang, S. Guan, C. Ouyang, Y. Yao, *ACS Applied Materials & Interfaces* **2015**, *7*, PMID: 26461467, 24016–24022.

[269] M. Z. Rahman, C. W. Kwong, K. Davey, S. Z. Qiao, *Energy Environ. Sci.* **2016**, *9*, 709–728.

[270] C. Chowdhury, A. Datta, *The Journal of Physical Chemistry Letters* **2017**, *8*, PMID: 28598171, 2909–2916.

[271] P. E. Blöchl, *Phys. Rev. B* **1994**, *50*, 17953–17979.

[272] D. G. Truhlar, *Journal of Computational Chemistry* **2007**, *28*, 73–86.

[273] K. Lee, E. D. Murray, L. Kong, B. I. Lundqvist, D. C. Langreth, *Phys. Rev. B* **2010**, *82*, 081101.

[274] V. R. Cooper, *Phys. Rev. B* **2010**, *81*, 161104.

[275] I. Hamada, M. Otani, *Phys. Rev. B* **2010**, *82*, 153412.

[276] C. G. BROYDEN, *IMA Journal of Applied Mathematics* **1970**, *6*, 222–231.

[277] J. D. Pack, H. J. Monkhorst, *Phys. Rev. B* **1977**, *16*, 1748–1749.

[278] G. Henkelman, B. P. Uberuaga, H. Jónsson, *The Journal of Chemical Physics* **2000**, *113*, 9901–9904.

[279] G. Henkelman, H. Jónsson, *The Journal of Chemical Physics* **2000**, *113*, 9978–9985.

[280] Q.-F. Li, C.-G. Duan, X. G. Wan, J.-L. Kuo, *The Journal of Physical Chemistry C* **2015**, *119*, 8662–8670.

[281] T. Hu, J. Hong, *The Journal of Physical Chemistry C* **2015**, *119*, 8199–8207.

[282] A. Sibari, A. Marjaoui, M. Lakhal, Z. Kerrami, A. Kara, M. Benaissa, A. Ennaoui, M. Hamedoun, A. Benyoussef, O. Mounkachi, *Solar Energy Materials and Solar Cells* **2018**, *180*, 253–257.

[283] B. Panella, M. Hirscher, S. Roth, *Carbon* **2005**, *43*, 2209–2214.

[284] Q. Wang, Q. Sun, P. Jena, Y. Kawazoe, *ACS Nano* **2009**, *3*, PMID: 19256516, 621–626.

[285] E. H. Song, S. H. Yoo, J. J. Kim, S. W. Lai, Q. Jiang, S. O. Cho, *Phys. Chem. Chem. Phys.* **2014**, *16*, 23985–23992.

[286] Y. Cai, Q. Ke, G. Zhang, Y.-W. Zhang, *The Journal of Physical Chemistry C* **2015**, *119*, 3102–3110.

[287] M. Lakhal, M. Bhihi, A. Benyoussef, A. El Kenz, M. Loulidi, S. Naji, *International Journal of Hydrogen Energy* **2015**, *40*, 6137–6144.

[288] S. Goler, C. Coletti, V. Tozzini, V. Piazza, T. Mashoff, F. Beltram, V. Pellegrini, S. Heun, *The Journal of Physical Chemistry C* **2013**, *117*, 11506–11513.

[289] V. Tozzini, V. Pellegrini, *The Journal of Physical Chemistry C* **2011**, *115*, 25523–25528.

[290] D. W. Boukhvalov, M. I. Katsnelson, *The Journal of Physical Chemistry C* **2009**, *113*, 14176–14178.

[291] Z. Yu, N. Wan, S. Lei, H. Yu, *Journal of Applied Physics* **2016**, *120*, 024305.

[292] M. Lalitha, Y. Nataraj, S. Lakshmipathi, *Applied Surface Science* **2016**, *377*, 311–323.

[293] J. Petucci, C. LeBlond, M. Karimi, G. Vidali, *The Journal of Chemical Physics* **2013**, *139*, 044706.

[294] G. Mpourmpakis, E. Tylianakis, G. E. Froudakis, *Nano Letters* **2007**, *7*, PMID: 17580924, 1893–1897.

[295] S. Park, D. Srivastava, K. Cho, *Nano Letters* **2003**, *3*, 1273–1277.

A List of publications

1. **M Garara**, H Benzidi, M Abdellaoui, M Lakhal, A El kenz, A Benyoussef, O Mounkachi, M Loulidi. *Hydrogen storage properties of perovskite-type $MgCoH_3$ under strain effect*. **Materials Chemistry and Physics**, 254 (2020), p. 123417.

2. M Abdellaoui, M Lakhal, H Benzidi, **M Garara**, A Benyoussef, A El Kenz, O Mounkachi, M Loulidi, H Ez-Zahraouy. *Enhancing of hydrogen storage properties of perovskite-type $MgNiH_3$ by introducing cobalt dopant ($MgCo_xNi_{1-x}H_3$) using first-principle calculations*. **Applied Physics A, Materials Science & Processing**, 125 (2019), pp. 1-8.

3. **M Garara**, H Benzidi, M Lakhal, M Loulidi, H Ez-Zahraouy, A El Kenz, M Hamedoun, A Benyoussef, A Kara and O Mounkachi1. *Phosphorene: A promising candidate for H_2 storage at room temperature*. **International Journal of Hydrogen Energy**, 44 (2019), pp. 24829-24838.

4. H Benzidi, M Lakhal, **M Garara**, M Abdellaoui, A Benyoussef, O Mounkachi. *Arsenene monolayer as an outstanding anode material for (Li/Na/Mg)-ion batteries: density functional theory*. **Physical Chemistry Chemical Physics**, 21 (2019), pp. 19951-19962.

5. H Benzidi, M Lakhal, M Abdellaoui, **M Garara**, A Benyoussef, M Loulidi, M Hamedoun, O Mounkachi. *Improved thermodynamic properties of doped $LiBH_4$ for hydrogen storage: First-principal calculation*. **International Journal of Hydrogen Energy** 2019, accepted.

6. H Benzidi, **M Garara**, M Lakhal, M Abdalaoui, A Benyoussef, M Louilidi, M Hamedoun, O Mounkachi. *Vibrational and thermodynamic properties of $LiBH_4$ polymorphs from first-principles calculations*. **International Journal of Hydrogen Energy** 2018;43(13):6625-6631

B List of communications

1. 1st International Materials Science and Engineering for Green Energy Conference, Ifrane, Morocco, May 10-12, 2017.
   Oral: Catalytic Effects of Subsurface Ni in the adsorption, dissociation and diffusion of Hydrogen on a Mg(0001) Surface: an Ab-initio Study.

2. MSDA workshop 2019 ''Modeling of electronic structure in material science", Mohammed VI Polytechnic University, Benguerir-Morocco, 28 March 2019.
   Oral: The potential of 2D germanium carbide as a Water Splitting Photocatalyst.

3. 8th International Renewable and Sustainable Energy Conference (IRSEC'20),Tetouan-Morocco, from 25th to 28th, November 2020.
   Oral: Effect of doping in hydrogen storage properties of Perovskite-type $MgCoH_3$

4. The fourth Conference on Nano-Materials: Theory and Experiments "Nano-TN 2020", Marrakech, Morocco, February 19-22, 2020.
   Oral: Phosphorene: A promising candidate for H_2 storage at room temperature.

C Published papers on hydrogen storage

Materials Chemistry and Physics 254 (2020) 123417

Contents lists available at ScienceDirect

Materials Chemistry and Physics

journal homepage: www.elsevier.com/locate/matchemphys

Hydrogen storage properties of perovskite-type $MgCoH_3$ under strain effect

M. Garara [a,*], H. Benzidi [a], M. Abdellaoui [a], M. Lakhal [a], A. El kenz [a], A. Benyoussef [a,b], O. Mounkachi [a], M. Loulidi [a]

[a] Laboratory of Condensed Matter and Interdisciplinary Sciences, Physics Department, Faculty of Sciences, Mohammed V University, Rabat, Morocco
[b] Materials and Nanomaterials Center, MAScIR Foundation, Rabat Design Center, Rue Mohamed Al Jazouli Madinat Al Irfane, Rabat, 10 100, Morocco

HIGHLIGHTS

- Thermodynamic and kinetic properties of $MgCoH_3$ under strain conditions are studied.
- The compression strain effect enhances the hydrogen storage properties.
- The obtained values are close to optimum values for the practical application.
- The $MgCoH_3$ systems are found to be energetically, mechanically and dynamically stable.

ARTICLE INFO

Keywords:
Hydrogen storage
Density functional theory
Phonon dispersion
Formation energy
Perovskite hydride

ABSTRACT

In the present study, the crystal structure, phonon dispersion curves, stability, de/hydrogenation thermodynamic and kinetic properties of Perovskite $MgCoH_3$ hydride under biaxial compression strain conditions were studied using the density functional theory (DFT) calculations. Our findings show that the biaxial strains played a key role in improving the de/absorption thermodynamic properties of $MgCoH_3$ compound. Precisely, the formation energy shifted from −71.30 kJ mol^{-1} per H_2 for unstrained $MgCoH_3$ to −37.29 kJ mol^{-1} per H_2 under the compression of −6% strain and the desorption temperature also decrease to 285.34 K compared with 545.52 K for free strained $MgCoH_3$, which is close to optimum values for the practical application (289–393 K and −40 kJ mol^{-1} per H_2). Noteworthy, the diffusion barrier energy of hydrogen atom in strained $MgCoH_3$ is also calculated using the nudged elastic band method (NEB) and the obtained values decrease with the strain magnitude, which can accelerate the kinetic of hydrogenation process of $MgCoH_3$. In addition, the band structures, phonon dispersion curves, the corresponding partial and total phonon density of states, also the thermal properties including the specific heat capacity, entropy and phonon free energy in terms of temperature with the variation of strain magnitude are predicted within the harmonic approximation. The analysis of phonons results revealed that crystal structure of $MgCoH_3$ is dynamically and mechanically stable.

1. Introduction

Actually, hydrogen has been considered as one of the most promising energy carriers alternatively to the fossil fuels including oil, coal and natural gas. However, the development of hydrogen faces a significant problem concerning its storage [1–4]. Alternative storage methods have been proposed and among them the hydrogen storage through hydrides (e.g. Magnesium hydride), which is very promising because of the high hydrogen storage capacities (gravimetric and volumetric) of those materials. During the last decades, Mg and Mg-based alloys have been broadly examined due to their advantages such as great abundance, lightweight and large capacity absorbed hydrogen, which is of order 7.65 wt% [5–11]. However, the high thermodynamic stability of the magnesium hydride and its poor kinetics of ad/desorption of hydrogen (excess of 300 °C at 1 bar H_2) prevents its application concerning the hydrogen storage under adequate temperature and pressure conditions [12–16]. The de/hydrogenation kinetics have mainly been affected by the resistance to hydrogenation by the oxide layer covering the Mg surface, the poor dissociation rate of the hydrogen molecule at the magnesium surface and the highly surface stability of hydride film blocking the hydrogen atoms diffusion into the magnesium sheet [17–19].

* Corresponding author.
E-mail address: garara.mourad@gmail.com (M. Garara).

https://doi.org/10.1016/j.matchemphys.2020.123417
Received 23 January 2020; Received in revised form 9 June 2020; Accepted 12 June 2020
Available online 30 June 2020
0254-0584/

To overcome such issues, many theoretical and experimental works have been performed to enhance the stability and desorption temperature. Among the most promising strategies reach that objective: reduction of size [20,21], alloying [22,23], doping/functionalization [24–26], morphology control [27,28], and engineering strain [29–31]. Alloying Mg with transition metals (TMs) appears to be the best way to overcome the poor kinetics of MgH_2 hydride without a large reduction of their hydrogen storage capacities [32–34]. Especially, Ni-Co is known by its beneficial effects to improve the slow kinetics of ab/desorption of H_2 and reduces the high hydride formation enthalpy of Mg-based alloys [34,35]. The single and double substitution with lightweight elements like Boron (B) and Lithium (Li) ameliorates considerably the thermodynamic properties and the storage capacities of the material [24,36]. The results reported that the co-doped MgH_2 with Lithium (Li) and TMs (Ti, V, Sc, Cr, Zr, Nb, Y, Mo) affects the thermodynamic properties and storage capacities, where the reduction of heat of formation/desorption and preservation of the optimum gravimetric capacity [37]. Du et al. [38] within DFT show that the activation barrier of the molecular hydrogen dissociation on the Ti-doped Mg surface is considerably reduced because of the strong binding between the hydrogen s orbital and the Ti d orbital. However, strong interaction of the two hydrogen atoms close to the Ti site hinders easy diffusion, reducing therefore the efficacy of the catalyst for Mg hydrogenation. Furthermore, Pozzo et al. [39,40] were investigated a systematic theoretical analysis of H_2 dissociation and the subsequent diffusion of the atomic H on TMs (Ti, V, Zr, Fe, Ru, Ni, Co, Rh, Ag, Pd, Cu)-doped Mg(0001) surface.

There are several structures for Mg alloys (BCC, FCC and HCP). Body-centred cubic (BCC) has more interstitial space than the face-centred cubic (FCC) and the hexagonal close-packed (HCP) lattices since it absorbs more hydrogen [41]. Thus, BCC alloys are more attractive candidates to be explored as hydrogen storage materials. At this view point, earlier study of Vegge et al. [42] with $MgXH_3$ type Perovskite hydride structures have reported the hydride formation energies for X = Ti, V, Cr, Mn, Fe, Co, Ni, Cu, Sc and Zn 3d transition metals. It has been found that the stability of this alloys hydrides tends to reduce from Mg-Sc to Mg-Fe alloys, with an exception for Mg-Cu and Mg-Zn systems. It should be mention that the synthetization of Mg-Co and Mg-Ni BCC systems have been successfully done by the mechanical alloying (MA) method [43–45]. Other groups have also developed a simple model explaining the observed trends [42,46]. Novel compositions of magnesium-based alloys system at different pression values were predicted and the calculations indicate that the new predicted phases are dynamically and mechanically stable. The investigation points out that the hydrides $MgNi_3H_2$ and $MgCuH_3$ seems to be very interesting for hydrogen storage and transportation applications [47]. Also, the calculated enthalpy of formation of $MgNi_2H_3$ is about 30 kJ/mol-H_2, which is consistent with the stability of the hydride at normal conditions [48]. Moreover, the crystal structure, vibration dispersion and the bonding properties of metal-hydrogen in the Perovskite hydride $MgNaH_3$ were investigated for hydrogen storage [49–52]. Also, using high-energy ball milling, Z. Wang et al. were synthesized the perovskite hydrides $NaMgH_3$ in the presence of a dopant K_2TiF_6. The $NaMgH_3$-0.042K_2TiF_6 sample exhibited better dehydriding properties compared with the $NaMgH_3$ sample, the release of hydrogen started approximately at 328 K (580 K for $NaMgH_3$) and 90% of hydrogen was desorbed within 20 min [53]. The family of $XNiH_3$ (X = Li, Na and K) [54] attracted researches attention due to their moderate hydrogen storage capacities of 4.4 wt%, 3.57 wt% and 3.30 wt %, respectively, and lowest hydrogen decomposition temperature of 446.3 K ($LiNiH_3$), 419.5 K ($NaNiH_3$) and 367.5 K ($KNiH_3$), respectively. Among the perovskite hydrides, $MgKH_3$, $MgRbH_3$ and $MgCsH_3$ having available crystallographic information were also studied and synthesized [51,55,56]. Interestingly, new theoretical calculations investigations contain hydrogen storage, structural, elastic, mechanical, electronic and thermodynamic behavior of $MgNiH_3$ (3.51 wt%), $MgCuH_3$ (3.32 wt%), $CaMnH_3$ (3.09 wt%), $CaFeH_3$ (3.06 wt%) and $CaCoH_3$ (2.97 wt%) perovskite hydrides have been made [57]. The results revealed that the $MgNiH_3$ and $MgCuH_3$ hydrides are mechanically/dynamically stable and have a ductile nature and experimentally synthesizable [58]. Furthermore, calculated hydride formation energies of magnesium-Co alloys using BCC Perovskite structure $MgCoH_3$ hydride have been done [25,46,59]. On the other hand, the anti-perovskite materials Ca_3CH_x (x = 1, 4, 7, 9, and 10) have been theoretically investigated and the result show that these compounds was energetic stable and synthesizable [60].

The studies in the literature show that strain or pressure have considerable effects on the crystal structure of materials [61,62]. In this regard, the mono/biaxial tensile or compressive strain enhanced the dehydrogenation and kinetics properties of different hydrides materials such magnesium hydride MgH_2 and lithium borohydride $LiBH_4$. The results obtained by J. Zhang et al. [30] report that the desorption enthalpies, desorption temperature as well as hydrogen diffusion activation of strained MgH_2 are all decrease simultaneously relative to the free-strain state. Also, the complex lithium borohydride $LiBH_4$ showed a gain of 20 kJ/mol for desorption enthalpy under 6% of compression strain [29]. Further, the diffusion activation energy of hydrogen dropped from value of 665.702 to 603.24 kJ/mol under tensile strain.

The role of biaxial compressive strain on the Perovskite hydride $MgCoH_3$ and their effect on the stability, crystal structure, phonon dispersion, thermodynamic properties, the distributions of charge density and hydrogenation kinetics was investigated in this work, by using the first-principles calculations. In addition, we expect the possibility of reducing the desorption temperature of hydrogen and an enhancement in the hydrogenation reversibility of the strained MgCoH3 structure compared to free one.

2. Models and computational details

The present calculations have been carried out according to the first-principles calculations based on a density functional theory (DFT) approach [63,64] and using plane wave pseudo potential method (PWSCF) in the Quantum Espresso code (QE) [65]. The electronic exchange-correlation functional corrections included through a generalized gradient approximation (GGA-PBE) was used [66]. All pseudopotentials are constructed using the ultra-soft pseudopotential method, with cutoff kinetic energy of 59 Ry (800 eV) and the k-point grids [67] for the Brillouin zone integration are sited to be 11x11x11 and $6 \times 6 \times 6$ for the primitive unit-cell and supercell, respectively, which is large enough to make the error from calculations of the energy below 0.01eV. The positions of atoms and the cell parameters, including the cell volume were all relaxed by minimizing the Hellmann-Feynman forces and stresses without any symmetry constraint using the Broyden–Fletcher–Goldfarb–Shanno method (BFGS) [68] and the convergence energy in the self-consistent cycle was selected to be 10^{-10}Ry. The atomic structures are plotted by the VESTA program [69].

The phonon frequencies and thermal properties are calculated using density functional theory implemented in QE code in combination with phonopy software [70]. In order to analyze the stability of compound structure, the phonon dispersion is studied using a finite displacement method according to the Parlinski-Li-Kawazoe method [71]. The displacements of atomic position of 0.02 Å were used to extract the force constants. A huge displacement was employed to avoid possible numerical inaccuracies in system. A complete force constant matrix was obtained, and the phonon frequencies (ω) were then calculated by the dynamical matrix diagonalization, over the electronic density of states.

Likewise, the thermodynamic functions properties of $MgCoH_3$ can be easily determined by the phonon frequencies spectrum throughout the whole Brillouin zone (BZ), such as Helmholtz free energy F, the internal energy H, entropy S, and constant-volume specific heat capacity C_V. For lattice properties calculations, the Helmholtz free energy is calculated using the formula below:

$$F = E + H_{vib} + TS_{vib} \quad (1)$$

where E, H_{vib} and S_{vib} are the ground state electronic energy of the crystal, the lattice vibration contribution to the harmonic phonon energy (internal energy) and entropy, respectively. The harmonic phonon energy H_{vib}, the entropy S_{vib} and the constant-volume specific heat C_v at a given temperature T can be directly calculated within the harmonic approximation using the following equations:

$$H_{vib}(T) = \sum_i \frac{1}{2}\hbar\omega_i + \hbar\omega_i \left[\exp\left(\frac{\hbar\omega_i}{K_\beta T}\right) - 1\right]^{-1} \quad (2)$$

$$S_{vib}(T) = k_\beta \sum_i \frac{\frac{\hbar\omega_i}{K_\beta T}}{\exp\left(\frac{\hbar\omega_i}{k_\beta T}\right) - 1} - \ln\left[1 - \exp\left(-\frac{\hbar\omega_i}{k_\beta T}\right)\right] \quad (3)$$

$$C_v = \left(\frac{\partial E}{\partial T}\right)_v = \sum_i k_\beta \left(\frac{\hbar\omega_i}{k_\beta T}\right)^2 \frac{\exp\left(\frac{\hbar\omega_i}{k_\beta T}\right)}{\left[\exp\left(\frac{\hbar\omega_i}{k_\beta T}\right) - 1\right]^2} \quad (4)$$

In these expressions, ω_i are the phonon frequencies, ħ and *kB* are the reduced Planck constant and the Boltzmann constant, respectively.

To determine activation barriers for diffusion of hydrogen on $MgCoH_3$ structure, the nudged elastic band method (NEB) was used [72,73], which has been employed to determine the energy barrier correspond to the minimum energy profiles (MEP). This method implies the optimization of a chain of images between the initial states and final state, obtained by linear interpolation. The total images number used to map the MEP accurately was 10, which is sufficient. A smaller set of k-point (6 × 6 × 6) and a lower energy cutoff (500 eV) were used for NEB calculations due to their computational expense.

3. Result and discussion

3.1. Intrinsic structural and electronic properties of (un)strained $MgCoH_3$

The bulk Perovskite hydride $MgCoH_3$ crystallizes in body-centred cubic (BCC) with space group Pm-3m (No.221). The unit-cell of the Perovskite compound contains five atoms, i.e. a magnesium atom located at corner (0,0,0), the Co atom at the center and the three hydrogen atoms are placed at octahedral sites at the face centers; (0.5, 0.5, 0.0), (0.5, 0.0, 0.5) and (0.0, 0.5, 0.5). The cell parameter of the relaxed structure is found to be $a_0 = 3.278$ Å, which is close to the results obtained in previous studies [42,46,74]. Crystal lattice of the cubic $MgCoH_3$ compound are illustrated in Fig. 1. The relaxed lattice constants

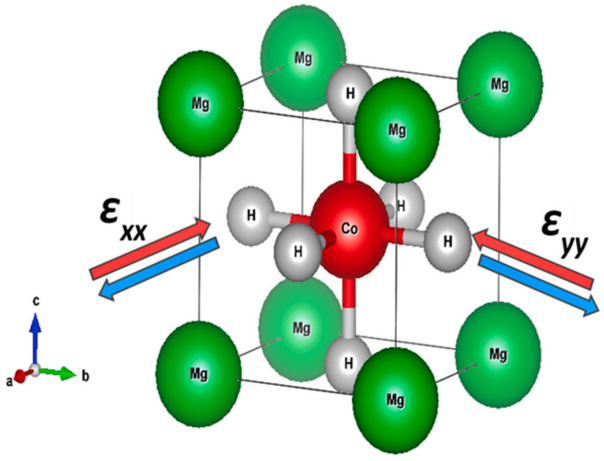

Fig. 1. Unit-cell crystal structure of the cubic Perovskite hydride $MgCoH_3$.

a_0 and cells volumes for all systems (intermetallic and their hydrides) are listed in Table 1.

Once the relaxed lattice constants of free $MgCoH_3$ unit cell are calculated, the mechanical biaxial isotropic strains will be imposed along the directions of x[100] and y[010] axes by equivalently constraining the lattice constants a and b. Then, the mechanical biaxial strains ε_{xx} and ε_{yy} is defined as:

$$\varepsilon_{xx}(\%) = \varepsilon_{yy}(\%) = \frac{a(b) - a_0(b_0)}{a_0(b_0)} \times 100\% \quad (5)$$

where a(b) and $a_0(b_0)$ represent the lattice constants in x(y) axis direction of $MgCoH_3$ unit cell with and without strain, respectively. In order to simulate either the compression indicated by negative strain value or the tension represented by positive strain value, the relaxation of the crystal is freely calculated along the c axis for every given value of a and b.

First, a different biaxial strain is applied by values ranging from −6% to +6% along the [100] and [010] directions of $MgCoH_3$ unit-cell. Fig. 2 illustrates the $MgCoH_3$ unit-cell parameters c/a and cell volume variation under strain. As a result, the lattice parameter c of $MgCoH_3$ unit-cell is elongated under biaxial compressive strain, resulting in an increase of the ratio c/a compared to that (≈1) of strain-free state. The c/a ratio reaches a highest value of 1.0767 at the compressive strain of −6%. Comparatively, under biaxial tensile strain, the $MgCoH_3$ lattice along z axis direction shrinks, giving a decreasing of c/a ratio relative to that of unstrained state. A minimum of 0.933 is found at the tensile strain of 6%. Furthermore, by increasing the strain conditions applied to Perovskite hydride $MgCoH_3$, the volume increases in the opposite direction from 31.37 $Å^3$ at −6% to 38.97 $Å^3$ at +6% strain. The same comportment is reported for $LiBH_4$ and MgH_2 under strain conditions [29,30]. So, it can be concluded that the biaxial tensile/compressive strain is probably to cause a structural and interatomic distance deformation of $MgCoH_3$ crystal and the distortion lattice becomes severe with increasing of biaxial strain.

The electronic band structure of the Perovskite hydride $MgCoH_3$ compound along the high symmetry directions in Brillouin zone, the total density of states (DOS) and the projected density of states (PDOS) obtained from the calculated equilibrium lattice constants are displayed in Fig. 3. From the band structure graph (Fig. 3 (a)) it is noticed that there is no forbidden energy gap at the Fermi level for $MgCoH_3$ compounds. In other words, the compound shows a metallic character due to overlap of the valence and conduction bands with each other at the fermi level. Furthermore, total DOS of free-strain $MgCoH_3$ is divided into two distinct parts. The first part covers the band energy range from −12.00 to −3.00 eV, which is composed of a strong hybridization between H-s, Mg-(s, p) and Co-d states. The second part, with an energy ranging from −2.00 to 2.00 eV, the fermi level almost formed by the contribution of the d-orbitals of Co atoms (see Fig. 3(b), (c) and (d)).

Table 1
Lattice parameters (a), Volume (V) and interatomic distances (d) between different neighboring atoms of MgCo and $MgCoH_3$ systems.

	Parameters a (Å)	Volume V ($Å^3$)	Interatomic distances d(Å)		
			Mg-Co	Co-H	Mg-H
MgCo (221-Pm-3m)	2.99 (this work) 3.026 [74] 3.07 [42]	26.73 27.70 [74]	2.59	–	–
MgCoH3 (221-Pm-3m)	3.278 (this work) 3.31 [74] 3.33 [42] 3.28815 [46]	35.23 36.26 [74] 36.9 [42]	2.84	1.64 1.665 [42]	2.32

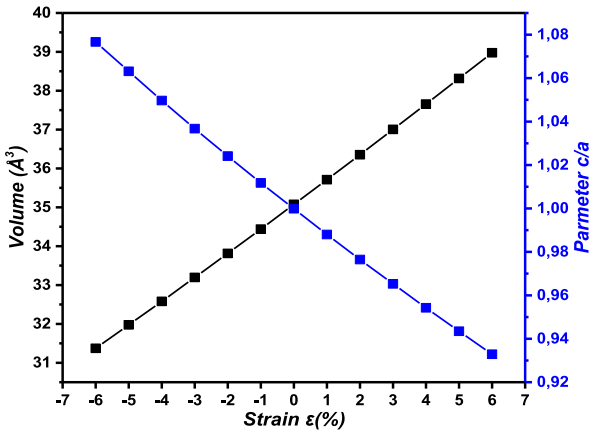

Fig. 2. Representation of c/a parameter and volume in terms of the biaxial strain on $MgCoH_3$.

3.2. Lattice dynamic stability

The calculated phonon dispersion relations along high symmetry lines within the first Brillouin zone (BZ) are plotted in Fig. 4 together with the vibration density of states. The unit-cell of $MgCoH_3$ contains five basis atoms, and therefore there are 15 vibrations modes (equal to 3 N, where N represents the number of atoms exist in the unit cell), which are constituted of three acoustics modes (A) and twelve optical (O) modes (3N-3) for any chosen k point. As seen in Fig. 4, the presence of a gap between the acoustic (low frequencies) and optic (high frequencies) phonon modes due to the large difference in mass between the Mg, Co and H atoms. This gap value is computed to be 30.9 THz, which close to the value 28.53 THz obtained by A. Candan et al. [46]. The calculated phonon frequencies at Γ point are obtained under harmonic approximation and the values was 5.66–15.54-16.96-47.01 THz. These values are close to the theoretical values of 5.27–17.12-18.83-47.48 THz [46].

From Fig. 4, The absence of any imaginary or negative phonon frequencies in the entire Brillion zone (BZ) confirms that $MgCoH_3$ structure is dynamically stable. The vibrational density of state shows two branches of optical phonons separated from the phonon branches of lower frequencies (acoustic phonon). The reason for separation of these branches in the dispersion plot is from the present of the light H atoms in the structure. The vibrational density of state curves (VDOS) shows that Mg and Co atoms in the $MgCoH_3$ compound vibrate in the acoustic region (0-7.4 THz) while only H atoms are vibrated only in the optical region (15.45–47.21 THz). Fig. 5 shows the phonon dispersion of $MgCoH_3$ compound under compressive strains. Based on the findings results plotted in Fig. 5, the absence of the negative frequencies is observed for the Perovskite hydride $MgCoH_3$ compound under strain. This means that the strained compound is also dynamically stable. The vibration of the hydrogen of strained $MgCoH_3$ is more independent than that of the free one because of the increase on lattice distortion, which explain the reduction of stability for strained $MgCoH_3$ lattice (increase of the formation energy).

3.3. Thermodynamic properties

Furthermore, based on phonon frequencies throughout the BZ, the thermodynamic functions of hydride $MgCoH_3$ can be determined with the variation of temperature using Phonopy software, such as Helmholtz Free Energy F, Internal Energy H, Entropy S, and Constant-Volume Heat C_V. Fig. 6 shows the change in the Helmholtz Free Energy and volume with increasing temperature from 0 to 1000 K, respectively. By increasing the temperature, the volume dependence of the phonon free energy changes, hence the equilibrium volume of stain-free $MgCoH_3$ changes at each given temperature and it becomes higher with increase of temperature (see Fig. 6(b)). Also, the Helmholtz Free Energy decreases from about 53.483 to −58.907 kJ mol^{-1} (for stain-free $MgCoH_3$) when the temperature increases from 0 to 1000 K (Fig. 6(a)).

It is worthwhile noting that the zero-point energy ZPE can be found from the expression of H_{vib} at T = 0 (equation (2)). Fig. 7 presents the computed H_{vib} and S_{vib} of $MgCoH_3$ compound in terms of temperature and for different compressive strain values. The functions H_{vib} and S_{vib} exhibit similar temperature dependencies for the $MgCoH_3$ structure. It can be observed from Fig. 7(a) that the ZPE is found to be 53.48 kJ mol^{-1} for unstrained system and slightly increase with the strain magnitude. The internal energy H_{vib} increase almost linearly when the temperature becomes greater than 300 K, tending to display *kB*.T behavior for all systems.

The classic Dulong-petit law reported that the heat capacity per mole of many solid elements is about 3R, where R presents the gas constant in

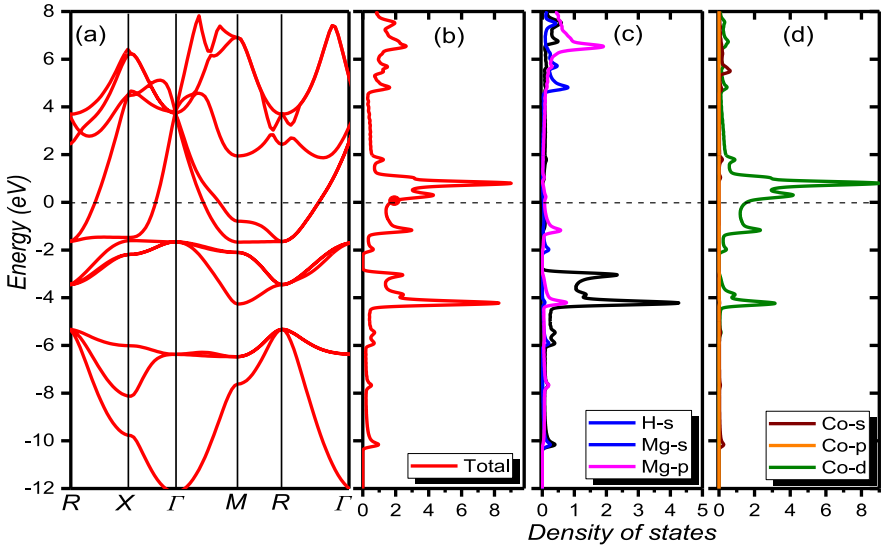

Fig. 3. (a) Electronic band structure for the cubic phase $MgCoH_3$, (b), (c) and (d) the corresponding density of states.

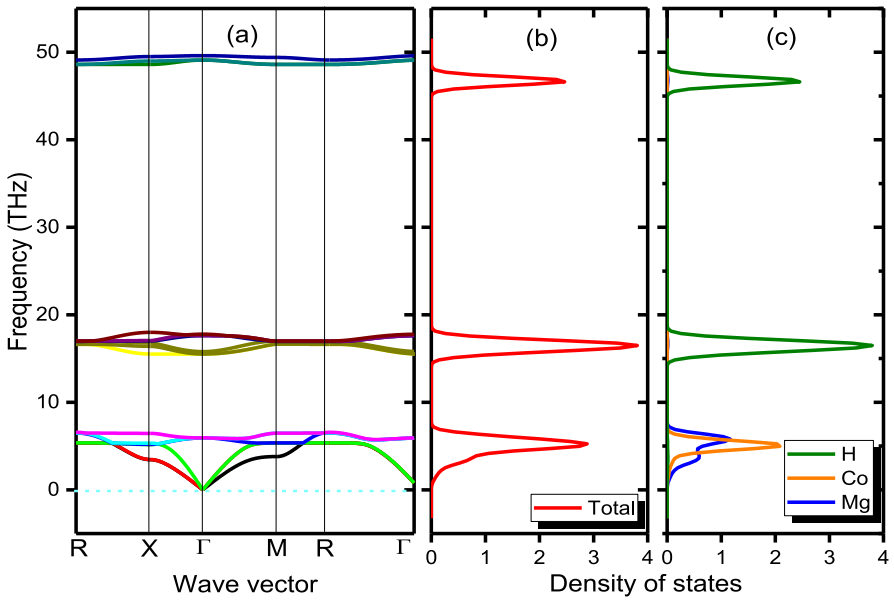

Fig. 4. (a) Phonon band structure with VDOS, (b) and (c) the corresponding vibrational density of states of $MgCoH_3$.

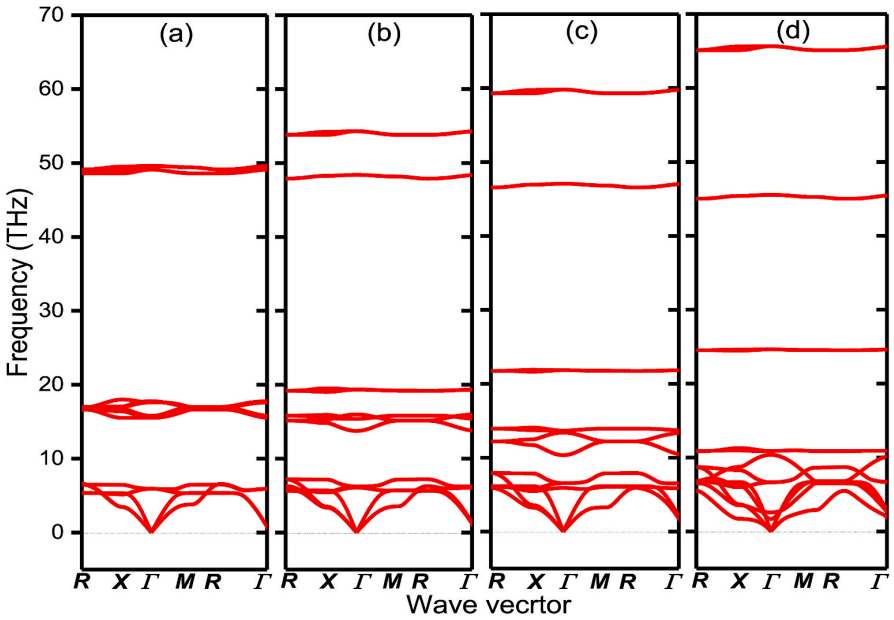

Fig. 5. Phonon dispersion curves of $MgCoH_3$ hydride under biaxial strain of (a) 0%, (b) −2%, (c) −4% and (d) −6%.

joule per kelvin per mole. The $MgCoH_3$ unit cell contains five atoms, based on the Dulong-petit law, the specific heat per primitive cell is 15R. this value can be obtained using equation (4) when the temperature tends to infinity. As illustrates in Fig. 8, it is observed that the specific heat capacity at constant-volume (C_v) tends to $C_v \propto T^3$ behavior at low temperature, while the C_v is close to a constant value limit of 124.71J. $K^{-1}.mol^{-1}$ at high temperature. According to Fig. 8, the C_v of unstrained $MgCoH_3$ increases quickly from 0 to about 80 J mol^{-1} K^{-1} when the temperature increases from 0 to 300 K and after that the C_v increase slowly approaching to the classical Dulong-Petit asymptotic limit discussed above. Our finding value of the specific heat of unstrained material is in complete agreement with the previous reported theoretical value of specific heat [46]. At low temperature, with the increasing of strain magnitude the lattice heat capacities of the systems have small increases as compared with the unstrained perovskite compound $MgCoH_3$.

3.4. Hydride formation energies and storage capacities

Hydrogen storage in metal hydrides was possible due to many metals readily able to react with hydrogen, forming a stable metal hydride. Formation energies ΔH_f are an important manner to identify if the

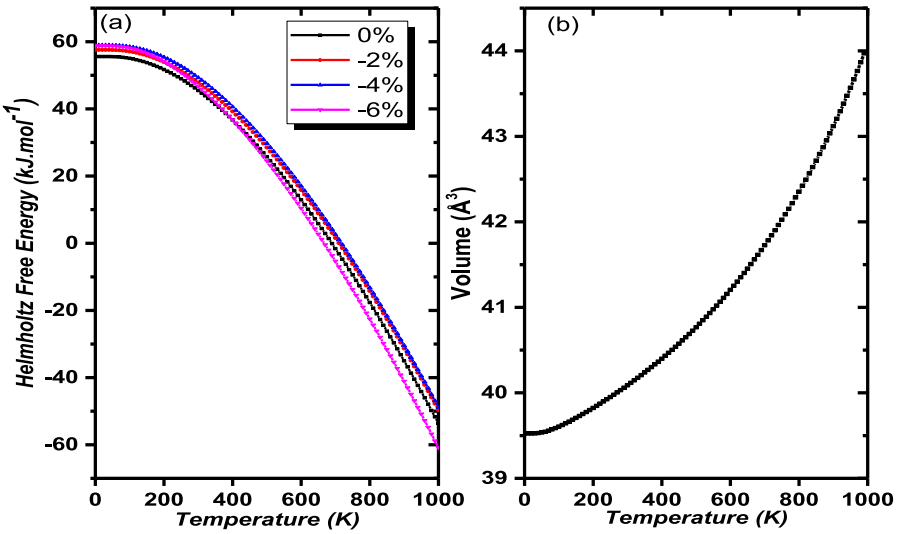

Fig. 6. (a) Helmholtz free energy versus temperature under compressive strain and (b) the variation of volume on unstrained $MgCoH_3$.

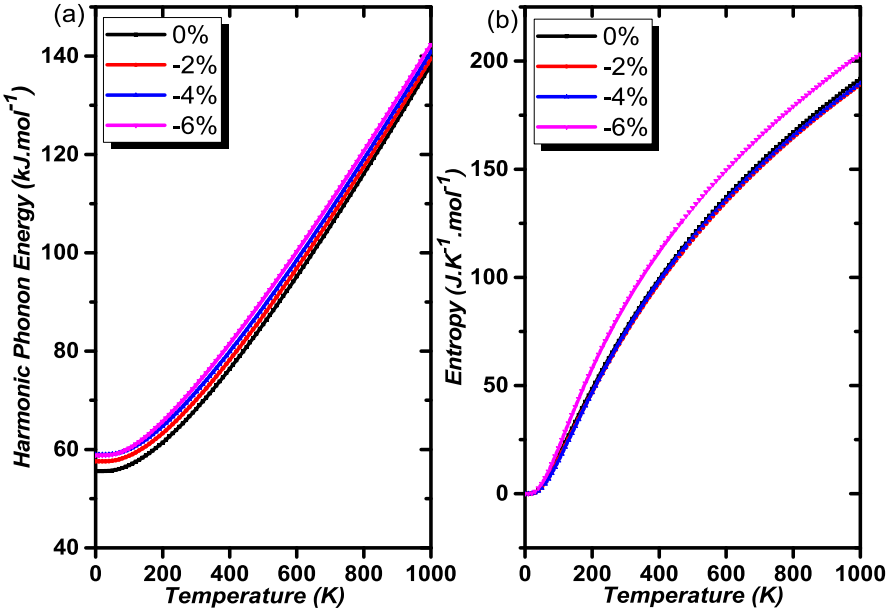

Fig. 7. (a) Harmonic phonon energy and (b) Entropy versus temperature under compressive strain.

predicted phases are likely to be stable (if $\Delta H_f < 0$ the hydride is stable and vice versa). The reaction related to the formation of Perovskite hydride $MgCoH_3$ in our study is:

$$MgCo + {}^{3}/_{2}H_2 \rightarrow MgCoH_3 \quad (6)$$

Based on these reactions, the formation energy of hydride $MgCoH_3$ could be defined as the difference of the total energies between the hydride phase $MgCoH_3$ and sum of H_2 in the gas phase and the energy of MgCo alloy and is firstly calculated by using Eq. (7):

$$\Delta H_f = E(MgCoH_3) - E(MgCo) - 3/2E(H_2) \quad (7)$$

The calculated formation energy value of stain-free $MgCoH_3$ is -71.30 kJ mol^{-1} per H_2, which is in good agreement with the theoretical value -73.32 kJ mol^{-1}.H_2 obtained in our previous works using the all-electron full-potential local-orbital minimum-basis scheme FPLO9.0034 [74], close to -73.80 kJ mol^{-1}.H_2 calculated by A. Candan et al. [46] and in the measured interval of some Mg-Co-H systems [79.00,70.00 kJ mol^{-1}.H_2] [75,76]. It can be seen that the formation energy of $MgCoH_3$ is considerably higher, compared with the optimum value -40 kJ mol^{-1}.H_2 [77,78], that explains the high stability of the compound. Furthermore, the desorption temperature T_d is an important parameter for the classification of materials applied for hydrogen storage. The formation energy ΔH_f obtained above is used to determine the desorption temperature of the studied compound using the following term:s

$$T_d = \frac{\Delta H_f}{\Delta S} \quad (8)$$

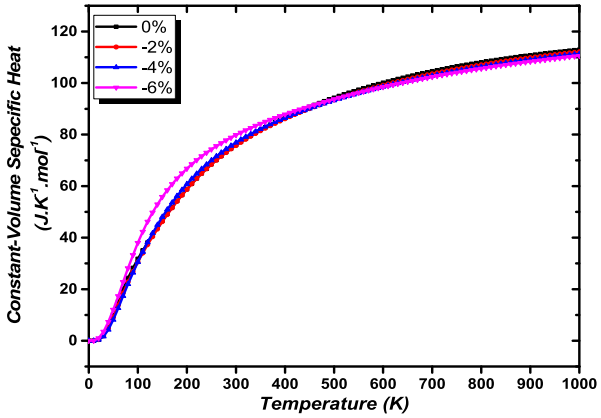

Fig. 8. Heat capacity of $MgCoH_3$ under biaxial strain versus temperature.

where $\Delta S \approx \Delta S(H_2) = 130.7$ J mol^{-1} K^{-1} is the entropy variation at standard pressure and temperature of the dehydrogenation reaction. The estimated desorption temperature of Perovskite hydride $MgCoH_3$ is $T_d = 545.52$ K. Noticeably, this value is still higher than the required range of desorption temperature for practical applications from 289 K to 393 K [79]. The formation energies, desorption temperatures and gravimetric/volumetric capacity of the studied systems are reported in Table 2.

Perovskite hydride $MgCoH_3$ show high stability and also high decomposition temperature, the biaxial strain effect was used to enhance its thermodynamics properties. The formation energy of strained $MgCoH_3$ systems are calculated using the same method, by proposing that the strained hydrides are decomposed completely into the strain-free solid MgCo and gaseous H_2 molecule and the desorption temperature were also calculated by using equation (8). These obtained results of the formation energy and desorption temperature as function of biaxial strain in $MgCoH_3$ unit cell are plotted in Fig. 9.

It can be seen from Fig. 9 that under biaxial compression, the calculated formation energies all strained $MgCoH_3$ systems are all increased with increasing strain magnitude as compared with that of strain-free one, which reduces the stability and the desorption temperature of the hydride. The obtained results show that the formation energy shifted from −71.30 kJ/mol.H_2 for the free-strain $MgCoH_3$ structure to −37.29 kJ/mol.H_2 for the $MgCoH_3$ structure under the compression of −6% strain. Therefore, the gain of 34 kJ/mol.H_2 was obtained for $MgCoH_3$ compound by application of biaxial compression strain.

This suggests that effect of the either biaxial compressive strain to $MgCoH_3$ material is efficacy for the enhancement of dehydrogenation thermodynamics because of strain energy contribution. Noticeably, the compression strain effect is found to be more remarkable than that of tensile one due to the relatively higher formation energy values as well as the desorption temperature.

Table 2
Formation energy ΔH_f, Desorption temperature T_{des} and Storage capacities C_g/C_v for unstrained Perovskite hydride compound.

System	ΔH_f (KJ. mol^{-1}.H_2)	T_{des} (°K)	C_g (wt %)	C_v (g.H_2.L^{-1})
The unstrained $MgCoH_3$	−71.30 (this work) −73.32 [74] −62.72 [42] −73.80 [46]	545.52 (this work) 560.97 [46] 482.42 [42]	3.505 (this work) 3.483 [74]	142.52 (this work) 137.38 [74]

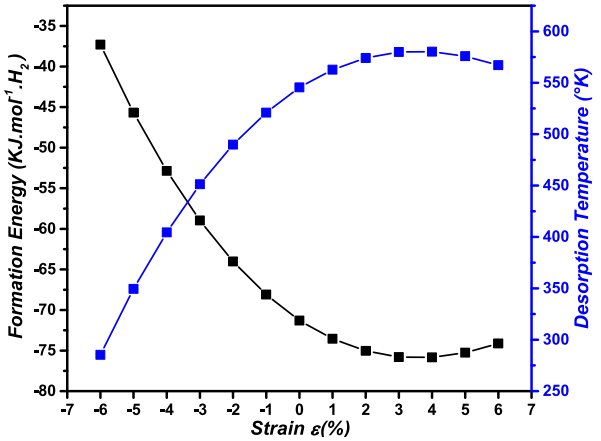

Fig. 9. The formation energy and desorption temperature according to biaxial strain ε (%) in the structure $MgCoH_3$.

3.5. Diffusion activation energy of hydrogen

The dehydrogenation mechanism in metal hydrides systems, is complex and mainly includes hydrogen atom or vacancy diffusion, nucleation, phase growth and surface desorption [80]. Among of them, the hydrogen diffusion and migration in hydride phase has been found to be an important rate-limiting step. In order to estimate the energy barrier for diffusion through the Perovskite hydride model and to evaluate the dehydrogenation kinetics, two diffusion paths of hydrogen atom in $MgCoH_3$ super-cell are considered in the present work: In the same distance, each hydrogen atom has eight nearest neighbors available sites, which is illustrated by the first path (diffusion from A to B site after H desorption) and the second path (diffusion from A to A site). The two different pathways for the diffusion of hydrogen atom are presented in Fig. 10.

Fig. 11(a) and (b) shows the diffusion energy profiles, i.e. activation energies of H for the first and second pathways respectively in the (un) strain structure of $MgCoH_3$. The free strain diffusion energy barrier of hydrogen atom for the first path is 0.55 eV similar with that of the second path, which is slightly lower than the value obtained by previously (0.67 eV). It can be concluded that the hydrogen atom diffusion behavior along the first and second pathways is almost identical. Moreover, the diffusion energy barriers values of first and second paths in all strained $MgCoH_3$ (compression) are all determined from Fig. 11. Based on the results, under the compression strain, the diffusion energy barrier of hydrogen atom along the first path increase from 0.55eV to 0.635eV. Otherwise, the diffusion activation energy of hydrogen atom decreases by increasing the compression, from 0.552eV to 0.518eV for the second path, which is mean that the hydrogen atom prefers to diffuse along X and Y direction instead of moving vertically with compression strain effect. The decrease of diffusion energy barriers suggesting the improved dehydrogenation kinetics in Perovskite hydride $MgCoH_3$.

The reasons for the results obtained above using biaxial compression strain effect can be explained by two things: The interatomic distances between hydrogen and the others atoms and the diffusion paths. For the first path, the interatomic distances between hydrogen and magnesium atom become small (from 2.32 Å for 0% to 1.96 Å for −6%) in the directions of stain effect and also the increase in diffusion paths for hydrogen atoms making the activation barriers more important under compression strain. Otherwise, for the second path, the reduction in diffusion paths for hydrogen atoms make the barrier smaller in comparison with the first path.

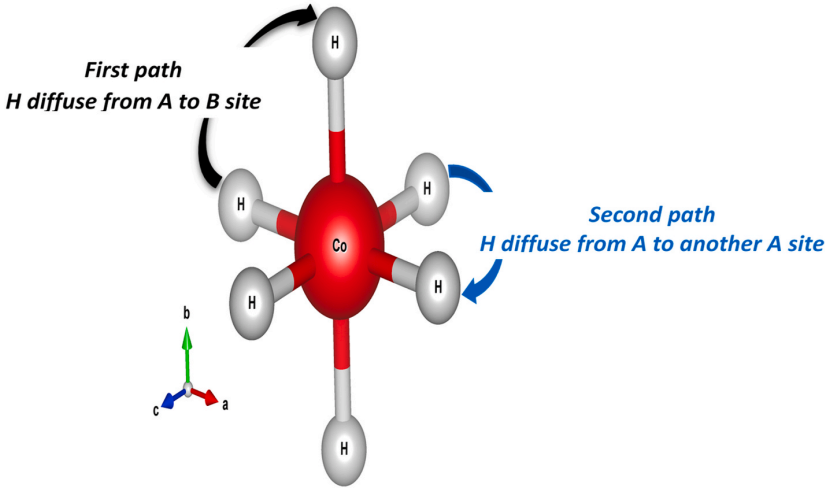

Fig. 10. Schematic view of the diffusion pathways of hydrogen atom from A to B site or from A to another A site in $MgCoH_3$.

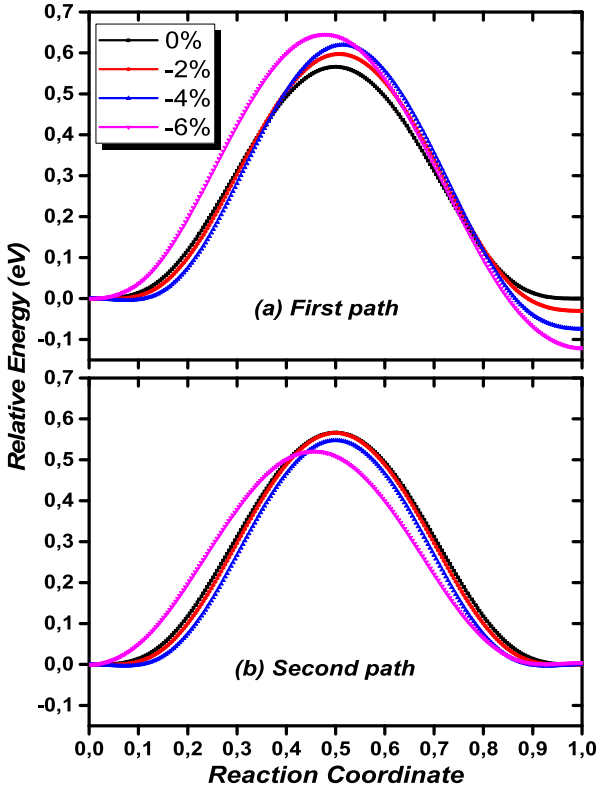

Fig. 11. Energy curves for diffusing hydrogen between two interstitial sites along (a) the first path and (b) second path as function of biaxial strain in $MgCoH_3$.

3.6. Electron density

To identify the bonding nature between the elements forming the $MgCoH_3$ compound, the calculations density distributions were investigated and displayed in Fig. 12 for different planes as function of compression strain magnitude. For unstrained $MgCoH_3$, the Co-H bond contours are not completely isolated which indicate that the Co-H bond exhibits a mixture of an ionic-covalent bond (see Fig. 12(a)). The applying compressive strain leads to decrease/increase the bond lengths and to change the distribution of density around the hydrogen and cobalt atoms. Also, the bond length between atoms become shorter in the biaxial strain direction than the free one. It should be mentioned also, that for the – 6% a bridge between Co and H atoms which makes strong charge transfer it the both direction comparing to without strain, which weaken the ionic bonding between Co and H and makes it easy to remove hydrogen from the perovskite framework. Moreover, the application of compression enhances the electronic charge overlapping between Cobalt and hydrogen. This leads to the localization of charges between Co and H atoms and thus increases the covalent bonds between them (Fig. 12(b), (c), and (d)).

4. Conclusion

First-principles calculations combined with a harmonic approximation method were used to study the biaxial compressive strain effect on the structural, vibrational, stability, dehydrogenation thermodynamic and kinetic properties of Perovskite $MgCoH_3$ hydride. The calculated lattice parameters are in good agreement with the available theoretical data. The phonon calculations show that no imaginary phonon frequency is observed in the whole BZ and also the high phonon frequencies are mainly contributed by the vibrations of H atoms, while the low phonon frequencies are produced by the vibrations of Mg and Co atoms due to smaller mass of hydrogen compared with the Mg and Co atoms masses.

Due to the contribution of strain energy, the formation energy, desorption temperature as well as hydrogen diffusion activation energies for strained $MgCoH_3$ hydride are all improved relative to that of strain-free system. Precisely, the formation energy shifted from −71.30 kJ mol^{-1} per H_2 to −37.29 kJ mol^{-1} per H_2 under the compression of −6% strain and the hydrogen release started at 285.34 K compared with 545.52 K for free strained $MgCoH_3$, which is very interesting for the practical hydrogen storage applications (289–393 K, −40 kJ mol^{-1} per H_2).

Computed vibrational properties were used to illustrate thermal properties of $MgCoH_3$ phase as function of temperature and strain like the vibrational enthalpy, entropy, phonon Helmholtz free energy and the molar specific heat capacity etc. Our obtained results are in good agreement with existing data and verified that crystal structure of strained $MgCoH_3$ is also mechanically stable.

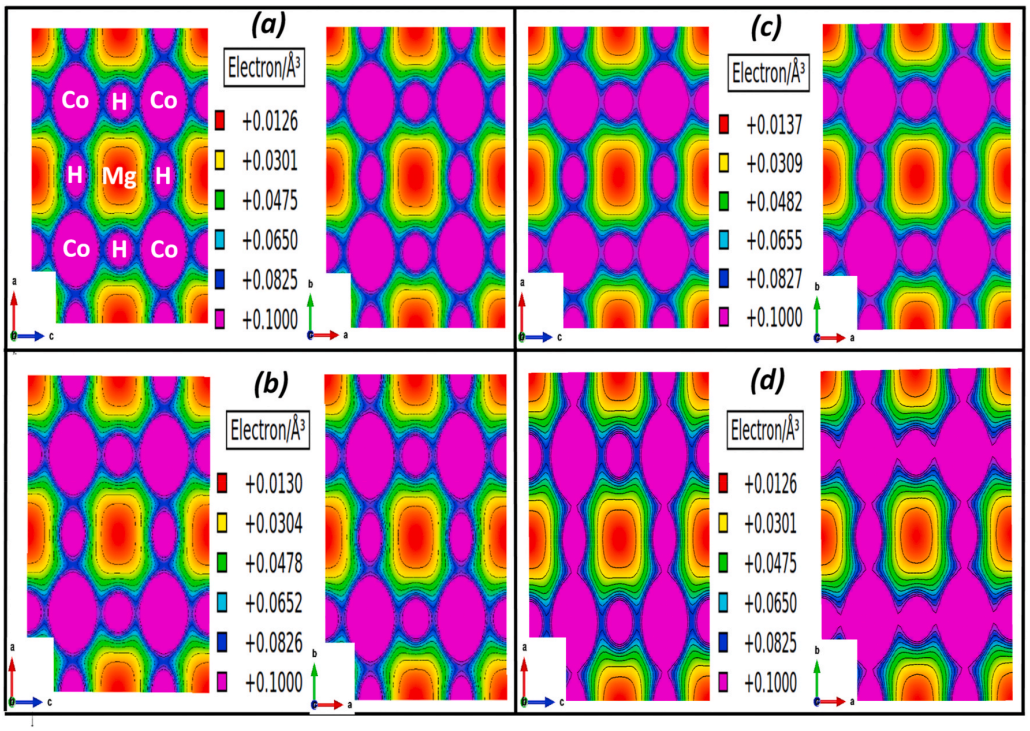

Fig. 12. Electron density distribution for $MgCoH_3$ for different values of strain. (a) 0%, (b) −2%, (c) −4% and (d) −6%. The magnitude of the charge density showed by different colors. (For interpretation of the references to color in this figure legend, the reader is referred to the Web version of this article.)

Ethical procedure

- The research meets all applicable standards with regard to the ethics of experimentation and research integrity, and the following is being certified/declared true.
- As an expert scientist and along with co-authors of concerned field, the paper has been submitted with full responsibility, following due ethical procedure, and there is no duplicate publication, fraud, plagiarism, or concerns about animal or human experimentation.

Declaration of competing interest•

None of the authors of this paper has a financial or personal relationship with other people or organizations that could inappropriately influence or bias the content of the paper.•

It is to specifically state that "No Competing interests are at stake and there is No Conflict of Interest" with other people or organizations that could inappropriately influence or bias the content of the paper.

CRediT authorship contribution statement

M. Garara: Conceptualization, Methodology, Software, Visualization, Writing - original draft. **H. Benzidi:** Software, Formal analysis, Data curation. **M. Abdellaoui:** Methodology, Investigation. **M. Lakhal:** Methodology, Investigation. **A. El kenz:** Validation, Writing - review & editing. **A. Benyoussef:** Validation, Writing - review & editing. **O. Mounkachi:** Resources. **M. Loulidi:** Validation, Supervision, Writing - review & editing.

References

[1] Y. Kojima, Hydrogen storage materials for hydrogen and energy carriers, Int. J. Hydrogen Energy 44 (2019) 18179–18192, https://doi.org/10.1016/J.IJHYDENE.2019.05.119.

[2] K. Mazloomi, C. Gomes, Hydrogen as an energy carrier: prospects and challenges, Renew. Sustain. Energy Rev. 16 (2012) 3024–3033, https://doi.org/10.1016/J.RSER.2012.02.028.

[3] G. Cipriani, V. Di Dio, F. Genduso, D. La Cascia, R. Liga, R. Miceli, et al., Perspective on hydrogen energy carrier and its automotive applications, Int. J. Hydrogen Energy 39 (2014) 8482–8494, https://doi.org/10.1016/J.IJHYDENE.2014.03.174.

[4] K.T. Møller, T.R. Jensen, E. Akiba, H. Li, Hydrogen - a sustainable energy carrier, Prog. Nat. Sci. Mater. Int. 27 (2017) 34–40, https://doi.org/10.1016/J.PNSC.2016.12.014.

[5] R. Hardian, C. Pistidda, A.-L. Chaudhary, G. Capurso, G. Gizer, H. Cao, et al., Waste Mg-Al based alloys for hydrogen storage, Int. J. Hydrogen Energy 43 (2018) 16738–16748, https://doi.org/10.1016/J.IJHYDENE.2017.12.014.

[6] H. Yong, S. Guo, Z. Yuan, Y. Qi, D. Zhao, Y. Zhang, Improved hydrogen storage kinetics and thermodynamics of RE-Mg-based alloy by co-doping Ce–Y, Int. J. Hydrogen Energy 44 (2019) 16765–16776, https://doi.org/10.1016/J.IJHYDENE.2019.04.281.

[7] M. Tian, C. Shang, Mg-based composites for enhanced hydrogen storage performance, Int. J. Hydrogen Energy 44 (2019) 338–344, https://doi.org/10.1016/J.IJHYDENE.2018.02.119.

[8] L.Z. Ouyang, Z.J. Cao, H. Wang, J.W. Liu, D.L. Sun, Q.A. Zhang, et al., Enhanced dehydriding thermodynamics and kinetics in Mg (in)– MgF 2 composite directly synthesized by plasma milling, J. Alloys Compd. 586 (2014) 113–117, https://doi.org/10.1016/j.jallcom.2013.10.029.

[9] J. Zhang, S. Yan, L.P. Yu, X.J. Zhou, T. Zhou, P. Peng, Enhanced hydrogen storage properties and mechanisms of magnesium hydride modified by transition metal dissolved magnesium oxides, Int. J. Hydrogen Energy 43 (2018) 21864–21873, https://doi.org/10.1016/J.IJHYDENE.2018.10.017.

[10] Q. Luo, J. Li, B. Li, B. Liu, H. Shao, Q. Li, Kinetics in Mg-based hydrogen storage materials: enhancement and mechanism, J Magnes Alloy 7 (2019) 58–71, https://doi.org/10.1016/J.JMA.2018.12.001.

[11] J. Li, J. Xu, B. Li, L. He, H. Lin, H.-W. Li, et al., Advanced SEM and TEM techniques applied in Mg-based hydrogen storage research, Scanning 2018 (2018) 1–12, https://doi.org/10.1155/2018/6057496.

[12] B. Li, J. Li, H. Zhao, X. Yu, H. Shao, Mg-based metastable nano alloys for hydrogen storage, Int. J. Hydrogen Energy 44 (2019) 6007–6018, https://doi.org/10.1016/J.IJHYDENE.2019.01.127.

ARTICLE IN PRESS

INTERNATIONAL JOURNAL OF HYDROGEN ENERGY XXX (XXXX) XXX

Available online at www.sciencedirect.com

ScienceDirect

journal homepage: www.elsevier.com/locate/he

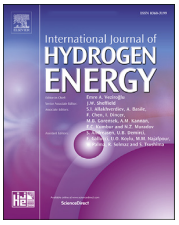

Phosphorene: A promising candidate for H_2 storage at room temperature

M. Garara [a], H. Benzidi [a], M. Lakhal [a], M. Louilidi [a], H. Ez-Zahraouy [a], A. El Kenz [a], M. Hamedoun [a], A. Benyoussef [a], A. Kara [b], O. Mounkachi [a,*]

[a] Laboratory of Condensed Matter and Interdisciplinary Sciences, Physics Department, Faculty of Sciences, Mohammed V University, Rabat, Morocco

[b] Department of Physics, University of Central Florida, Orlando, FL, 32816, United States

HIGHLIGHTS

- Physisorption, diffusion and chemisorption pathways of H_2 Molecule on hosphorene.
- Room temperature reversible hydrogen storage in phosphorene.
- First-principles calculations.

ARTICLE INFO

Article history:
Received 2 March 2019
Received in revised form
27 June 2019
Accepted 25 July 2019
Available online xxx

Keywords:
Density functional theory
Van der waals
Hydrogen storage
Phosphorene
Diffusion

ABSTRACT

Owing to the existence of periodic channels in phosphorene, this 2D material can be a good candidate for room temperature reversible hydrogen storage. The density functional theory calculations (DFT), including van der Waals interactions (vdW-DF2) coupled with the cooper exchange functional (C09), has been applied to study the potential of phosphorene as a new 2D material for hydrogen storage. Our results show that the adsorption energy (−292 to −277 meV) of H_2 on phosphorene is appropriate for storage. The analysis of diffusion pathways between different physisorbed states on phosphorene shows that a single hydrogen molecule diffuses very easily along the open channel (less than 1 meV along the zigzag direction), as compared to 14 meV for diffusion across the channels (along the armchair direction). The potential energy surfaces for the dissociative chemisorption of H_2 was computed on highly symmetric sites of phosphorene and the highest activation barrier was found to be 2.77 eV. The very large dissociation energy coupled with a strong physisorption of H_2 on phosphorene and facile diffusion, makes this 2D material a promising candidate for H_2 storage at room temperature.

Introduction

In recent years, a great emphasis has been placed on developing concepts and technologies to power the vehicles using renewable energies. One potential solution is the use of hydrogen gas as an energy vector to power fuel cells [1,2]. However, Hydrogen storage continues to be one of the most technically challenging barriers to the widespread commercialization of hydrogen-fueled light-duty vehicles, which will

* Corresponding author.
E-mail address: o.mounkachi@gmail.com (O. Mounkachi).

https://doi.org/10.1016/j.ijhydene.2019.07.194
0360-3199/

Please cite this article as: Garara M et al., Phosphorene: A promising candidate for H_2 storage at room temperature, International Journal of Hydrogen Energy, https://doi.org/10.1016/j.ijhydene.2019.07.194

compete with fossil fuel in the hybrid vehicle markets [3,4]. According to the US-DOE (United states Department of Energy) requirements, the future hydrogen tank should ultimately store 75 g of H_2 per kg (or liter) of storing system [5–7]. Among hydrogen storage technologies, compressed gas storage is not so suitable for transportation applications due to the high weight and size of the tank, whereas cryogenic liquid state storage suffers from evaporative losses and high energy cost for liquefaction. On the other hand, solid-state storage technologies such as metal hydride techniques and physisorption on high surface area materials have the potential to become a viable technology [7–9]. Although there has been a variety of experimental and theoretical research studies on solid state hydrogen storage systems, especially on metal hydrides and carbon nanomaterials, finding a suitable novel material for hydrogen storage tanks is still an open-ended problem [10–13]. It should be mentioned that dual-tuning effects of the thermodynamics and kinetics properties is one of the keys for hydrogen economy and hydrogen-storage materials issues [14]. Thus, can be partially achieved by doping [15–17], changing the reaction pathway [18] or by reducing the particle size using a ball milling process assisted by dielectric barrier discharge plasma technique (P-milling) [19,20]. Novel two-dimensional (2D) materials (e.g. graphene, BN, MoS_2, WSe_2, C_2N, etc.) [21–27] have attracted much attention due to their unique properties and numerous possible applications. In particular, one of the key domains that can be addressed with the 2D materials refers to the energy conversion and storage [28–32]. The germanium nanoparticles (NPs) wrapped with few-layer graphene sheet prepared by P-milling process show an excellent structure nanocomposite anode material for lithium ion batteries applications (LIBs) [33] because of the better electrical conductivity, low initial capacity loss, good/stable cycling capability, and rate resilience compared with Ge NPs with graphene sheets electrodes prepared by conventional milling. Furthermore, L.Z. Ouyang et al. [34] reported that the addition of graphene to $La_{11.3}Mg_{6.0}Sm_{7.4}Ni_{61.0}Co_{7.2}Al_{7.1}$ ($AB_{3.0}$) alloy electrodes and the P-milling technique improve the electrochemical properties and kinetics because of the increased surface area of the P-milling particles and the good conductivity of the introduced graphene. Carbon-based nanomaterials adsorb hydrogen very well because of their compatibility as materials for gas storage. However, for carbon in any form, the interaction with H_2 happens through the van der Waals (vdW) forces with low adsorption energies for storage at ambient conditions [35]. To understand the hydrogen adsorption/desorption storage mechanisms on carbon nanotubes CNTs and graphite nanofibers (GNFs) several investigations have been performed [35–39]. Single-layer black phosphorus, labeled "phosphorene", is a new material in the family of 2D nanostructures. It can be obtained by mechanical exfoliation of the black phosphorus, which is a stable compound with a natural layered structure [40,41]. Very recently, phosphorene with a thickness of only a few nanometers has been produced by several groups worldwide [42,43]. Theoretical and experimental investigations have demonstrated the potential of the application of phosphorene as a transistor material, as a photocatalyst and as anodes in batteries [44–48], but the use of this material for hydrogen storage solid state remains limited. Qing-Fang Li et al. [49] indicate that Li-decorated monolayer black phosphorus (MBP) can improve the hydrogen storage properties and achieve a hydrogen storage capacity of about 8.11 wt %. Zhiyuan Yu et al. [50] in contrast to Qing-Fang Li show that phosphorene decorated by Li can dramatically enhance the adsorption energy to 0.2 eV with a hydrogen storage capacity of 4.4 wt %. Thus, several finding and properties of this system remain incomplete and need further investigation. Therefore, the main aim of the present work is to study, using density-functional theory (DFT), the potential of phosphorene application as a new 2D material for hydrogen storage by investing the interaction of hydrogen molecules and atoms with the surface and its impact on the diffusion behavior. The work is organized as follows: at first, the adsorption of hydrogen molecules on the surface will be evaluated and the results will be compared with the pristine graphene. Next, the energy barriers for hydrogenation reaction, diffusion, and dissociation of hydrogen located at a phosphorene surface are simulated. All the possible dissociation and diffusion pathways are analyzed to find the diffusion and dissociation barriers. Finally, in the last section, a summary of the important findings is given.

Computational method

All calculations are performed within density functional theory (DFT) [51,52] using the Quantum espresso program [53]. The PBE generalized gradient approximation [54] and the projector-augmented wave potential [55] are employed to describe the exchange-correlation energy and the electron–ion interaction, respectively. It has been found that the van der Waals (vdW) interactions are quite important for black phosphorus, thus it was included by using the self-consistent correction scheme of vdW-DF2 [56] as implemented by Kyuho lee et al. [57], and the exchange functional (C09) developed by Cooper [58,59]. The cutoff energy for the plane wave expansion is set to 40 Ry (544 eV), which is large enough to make the error from calculations of the adsorption energy below 0.01 eV. To model the phosphorene monolayer, a rectangular 9.24 × 6.60 Å supercell with 16 phosphorus

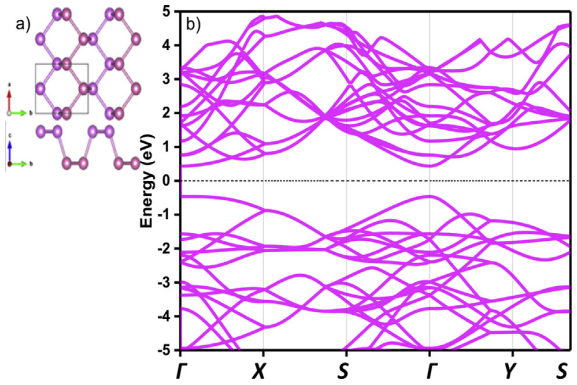

Fig. 1 – (a) Optimized geometry and (b) Band structure plot of pristine Phosphorene.

Please cite this article as: Garara M et al., Phosphorene: A promising candidate for H_2 storage at room temperature, International Journal of Hydrogen Energy, https://doi.org/10.1016/j.ijhydene.2019.07.194

atoms was used (see Fig. 1a). The atomic positions of all the atoms including hydrogen molecules in the supercell were fully relaxed using the Broyden–Fletcher–Goldfarb–Shanno (BFGS) minimization method [60]. The electronic ground-state steps were allowed to converge to an accuracy of 10^{-10} eV and convergence tolerance for forces were set less than 0.05 eV/Å, displacement of atoms less than 2×10^{-3} Å and stress less than 0.02 GPa. The Brillouin zones of the unit cells are represented by Monkhorst-Pack special k-points scheme with a $5 \times 3 \times 1$ grid mesh [61]. Computational settings such as plane wave cutoff energy, the number of k-points and convergence criteria were carefully chosen to control the numerical accuracy. To determine activation barriers for dissociation and diffusion of hydrogen on phosphorene surface, the nudged elastic band (NEB) method [62,63] was used, which has been employed to find out the minimum energy path (MEP) and the corresponding energy barrier for the dissociation and diffusion of hydrogen molecule and hydrogen atom on the phosphorene surface. This method involves the optimization of a chain of images, obtained by linear interpolation, between the initial and final states. In most of the cases, the total number of images used is equal to 10, which is sufficient to map the MEP accurately. Each image is allowed to move in all direction.

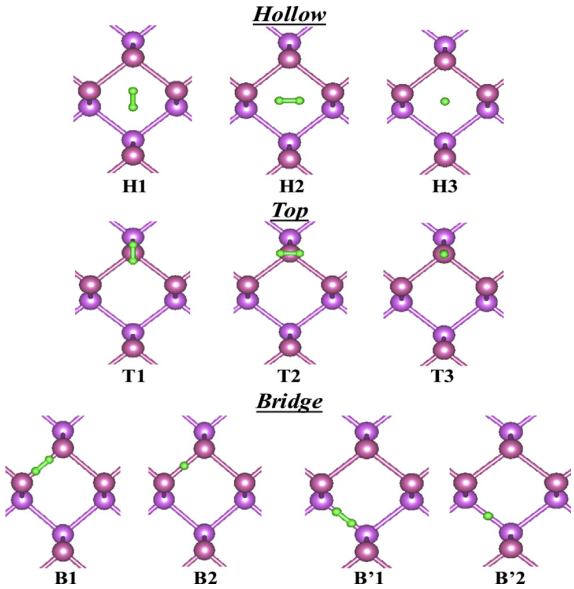

Fig. 2 – The various molecular hydrogen adsorption configurations studied: Hollow (H), Top (T) and Bridge (B and B′).

Result and discussion

The optimized phosphorene layer has a puckered honeycomb structure (in contrast with the planar sheet of graphene) with each phosphorus atom covalently bonded to three adjacent P atoms. The top and side view of the optimized monolayer phosphorene is shown in Fig. 1a. The relaxed lattice constant of the single layer phosphorene is a = 4.62 Å and b = 3.30 Å along the armchair and zigzag directions, respectively, which are in good agreement with the previous results [64]. The calculated P–P bond lengths are 2.22 Å for the horizontal (in the zigzag direction) bonds and 2.27 Å for the bonds in other directions (armchair direction). The corresponding bond angles are 95.81° and 104.1°, respectively, which are in agreement with the previous results [65]. The band structure is presented in Fig. 1b. The band gap is located at the Γ point with a direct band gap of 0.9 eV, which is also in excellent agreement with previous results [49,66,67].

In this section, equilibrium properties of molecular hydrogen on phosphorene are calculated. Four adsorption sites of H_2 on phosphorene are investigated: H (hollow site, in the center of the phosphorus hexagon), T (top site, on top of the phosphorus atom), B and B' (bridge site, above the middle-point of the bottom and top P–P bond). Also, several orientations of the H_2 molecule with respect to the phosphorene surface are considered at each adsorption site, as presented in Fig. 2. In configurations H1, H2, B1, B′1, T1, and T2, the axis of the H_2 molecule (H–H axis) is parallel to phosphorene surface. Whereas configurations H3, B2, B′2 and T3 correspond to the cases where the H–H axis is perpendicular to the phosphorene plane. The total energies of the hydrogen–phosphorene systems were computed for different configurations, where the separation z between the phosphorene substrate and the center of mass of the H_2 molecule was varied between 2 and 6.5 Å, thus allowing for the computation of the adsorption potential E_{ads} in the relevant separation range and for the location of the energy minimum value and position.

The adsorption potential E_{ads} of H_2 molecule (at the equilibrium distance z_{min}) to various adsorption sites on phosphorene is obtained using the formula:

$$E_{ads}(z_{min}) = E_{tot} - (E_{sub} + E_{H_2}) \quad (1)$$

where E_{tot}, E_{sub}, and E_{H2} are the total minimized energies of H_2 plus substrate, substrate, and H_2, respectively. z_{min} is the

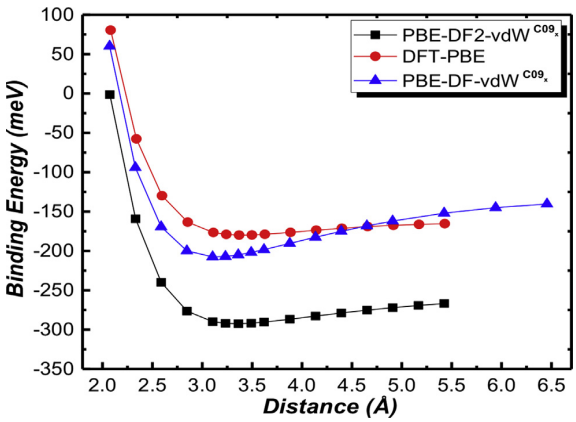

Fig. 3 – Physisorption of H_2 on phosphorene, in the bridge configuration. Pure DFT calculation, DFT/vdW-DF-C09x and DFT/vdW-DF2-C09x.

Please cite this article as: Garara M et al., Phosphorene: A promising candidate for H_2 storage at room temperature, International Journal of Hydrogen Energy, https://doi.org/10.1016/j.ijhydene.2019.07.194

vertical equilibrium distance from the center of mass of H_2 to the phosphorene layer provided that all the energies are minimized. Fig. 3 shows $E_{ads}(z)$ on the B′2 site, as computed using different approximations. The higher energy curve represents the results of the PBE-DFT calculations without the inclusion of vdW interactions. When the van der walls (vdW) interactions are taken into account with the different methods, the calculated binding energy becomes more attractive and its values at the minimum decrease with respect to the PBE-DFT results. The results obtained by the vdW-DF2-C09x method [35,36], in particular, give a minimum binding energy of −292 meV at a distance of 3.36 Å, which correspond to the requirement for appropriate hydrogen storage with a binding energy of −0.2 ~ −0.6 eV/H_2 [68–70]. The hydrogen remains at the molecule state with a bond length of 0.75 Ă.

The values of the adsorption potential and the vertical distances of H_2 for all configurations sites are obtained using the equation (1) and reported in Table 1 along with the results obtained for graphene. From the analysis of the results of H_2 adsorption on phosphorene using the PBE-DFT and when introducing the vdW forces, the hydrogen prefers to be adsorbed on the middle-point of the bottom P–P bond with its molecular axis perpendicular to the phosphorene surface (bridge2, B′2). The intermediate adsorption potential energy of hydrogen molecule on phosphorene implies stable hydrogen storage at ambient conditions and subsequent facile release. It is noted that the E_{ads} of H_2 on phosphorene is much larger than that of H_2 on pristine graphene (283 versus 54 meV/H_2 for the case of H1 hollow calculated using vdW-DF2) [71], which suggests a higher working temperature for using phosphorene as the hydrogen adsorbent [72], better than that found for graphene, which limits the use of graphene as an absorbent of hydrogen. The desorption temperature of hydrogen molecule T_{des} can be estimated using the well-known thermodynamics relation:

$$T_{des} = \Delta H/_{\Delta S} \quad (2)$$

For most of the dehydrogenation reactions, it is estimated that ΔS is about 140 J/mol.K [73,74]. Taking the above value of E_{ads} and the value of the entropy, we get $T_{des} = 297$ K. However, since the density of bulk phosphorene is about 23% larger than that of graphite, implying a smaller gravimetric value of the hydrogen storage than graphite. Nevertheless, the highly flexible and puckered honeycomb structure of phosphorene implies a higher possibility for increasing the chemical affinity for hydrogen with convex areas of phosphorene surfaces, which has been demonstrated in fullerenes, nanotubes, and graphene by controlling curvature or creating ripples [75–77].

To analyze the electronic interaction between H_2 molecule and phosphorene, the electron density distributions was investigated and plotted in the Fig. 4. For the system of H_2 adsorbed on phosphorene, it can be seen that there is an accumulation of charge around the far hydrogen atom and a depletion of electron around the lower H atom from substrate, which lead to a slight polarization of the H_2 molecule. Additionally, a small amount of charge transfer from phosphorene layer to the hydrogen molecule mean that H_2 exhibits physisorption on phosphorene sheet. These findings are in good agreement with results of Zhiyuan Yu [50] et al. and Murugan Lalitha et al. [78].

The diffusion barriers for the hydrogen molecule moving across the surface from various configurations have been calculated as the difference between the initial physisorption state and the transition state. The calculation of barrier using the NEB method [63] is described pictorially in Fig. 5 and the results are reported in Table 2. The barriers found are rather low compared to graphene [71,79] and hence the physisorbed molecules are expected to be quite mobile on phosphorene. The main difference in the barriers is the configuration migration. It can also be noted that the hydrogen molecule can easily diffuse into the convex zone (zigzag direction) than the armchair or diagonal direction with a barrier nearly zero (0.3 meV).

We now discuss the possibility of adsorption of hydrogen atoms from the molecular gas phase. To get insight into the energetic favorability of such a process, it is important to take energy barriers resulting from the molecular dissociation into account. For this calculation, we consider two possible chemisorbed configurations of H atoms on phosphorene after the dissociation of a diatomic molecule (para and Meta). The energetically favored configuration is found when two H atoms are adsorbed on the opposite vertices diagonal (Meta position) of the same hexagon ring of phosphorene (final state in Fig. 6(a) and (d)). Fig. 6 shown the pathway calculated from differences between H_2 physisorbed state and the chemisorbed state of 2H on phosphorene. One can see that the energy of the final dissociated configuration is higher than that of the physisorbed one, thus characterizing this

Table 1 – Equilibrium distances and potential minima of H_2 to various adsorption sites on phosphorene.

		DFT/PBE		DFT/vdW- DF2-C09$_x$		Graphene-DFT/vdW	
		E_{ads} (meV)	z_{min}(Å)	E_{ads} (meV)	z_{min}(Å)	E_{ads} (meV)	z_{min}(Å)
Hollow	H1	−170	3.33	−283	3.13	−54	3.2
	H2	−163	3.00	−279	2.99	−48	3.0
	H3	−174	3.37	−286	3.36	−47	3.5
Top	T1	−170	3.74	−282	3.59	−39	3.4
	T2	−167	3.73	−278	3.63	−43	3.6
	T3	−169	3.39	−280	3.37	−38	3.1
Bridge1	B1	−169	3.54	−280	3.42	−43	3.6
	B2	−166	3.37	−277	3.36	−43	3.3
Bridge2	B′1	−164	3.04	−281	2.99	–	–
	B′2	−180	3.37	−292	3.36	–	–

Please cite this article as: Garara M et al., Phosphorene: A promising candidate for H_2 storage at room temperature, International Journal of Hydrogen Energy, https://doi.org/10.1016/j.ijhydene.2019.07.194

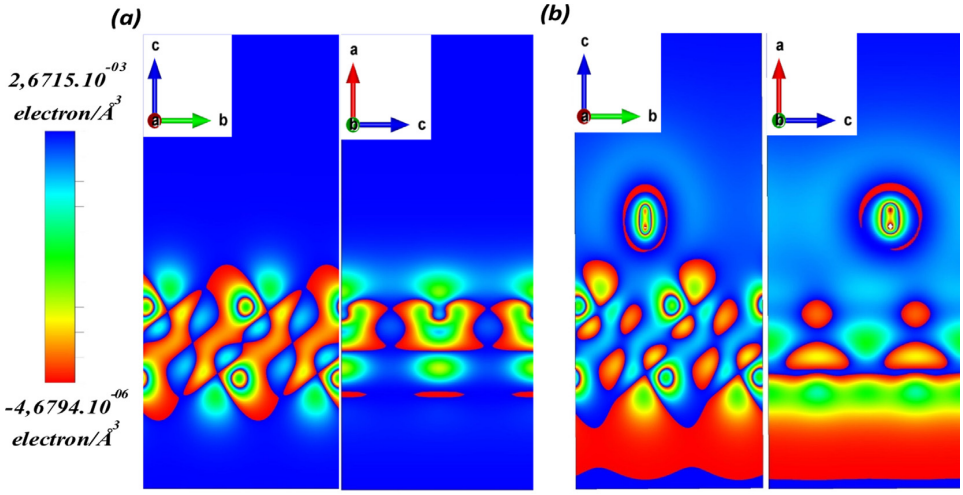

Fig. 4 – Electron density distributions in (a) phosphorene sheet (b) H_2 adsorbed on 3 × 4 supercell phosphorene sheet.

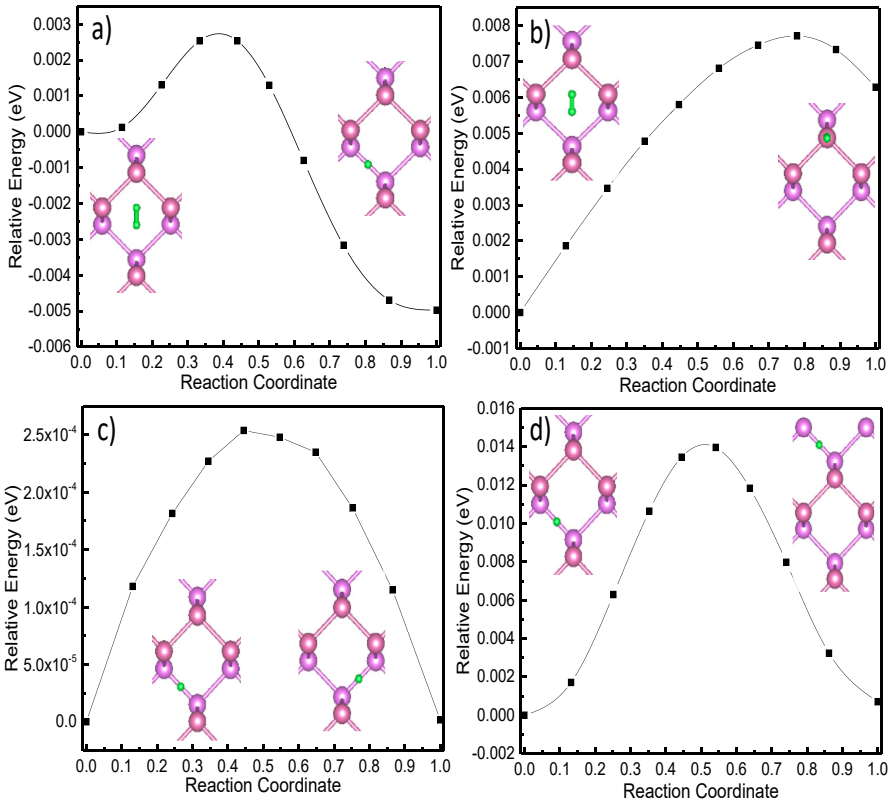

Fig. 5 – Examples of configuration migration of H_2 on phosphorene from various initial to final sites: (a) Hollow (H1) to Bridge2 (B′2), (b) Hollow (H1) to Top (T3), (c) and (d) Bridge2 (B′2) to Bridge2 (B′2) with zigzag and armchair direction, respectively.

hydrogenation process as an endothermic reaction. The path connecting the H1 configuration to the Meta configuration has the lowest energy barrier, 2.26 eV (Fig. 6(d)). Table 3 reports all energy barriers for the explored paths from physisorbed to chemisorbed states for H_2 on phosphorene surface. The transition state (TS) is characterized by a broken H–H bond and by the formation of a new P–H bond (1.44 Å length), with a substantial distortion of the substrate. The results of barriers

Please cite this article as: Garara M et al., Phosphorene: A promising candidate for H_2 storage at room temperature, International Journal of Hydrogen Energy, https://doi.org/10.1016/j.ijhydene.2019.07.194

Table 2 – Migration energy barriers of H_2 on phosphorene from various initial to final sites.

Configuration		Migration direction	The activation energy (meV) (this work)	The activation energy (Graphene)
Initial state	Final state			
B′2	H1	Diagonal	2.5	≈14 meV
H1	T3	armchair	7.7	Arellano et al. [68]
H1	B′2	Diagonal	7.5	≈10 meV
T3	H1	armchair	1.4	Costanzo et al. [61]
B′2	B′2	armchair	14.0	
B′2	B′2	zigzag	0.3	

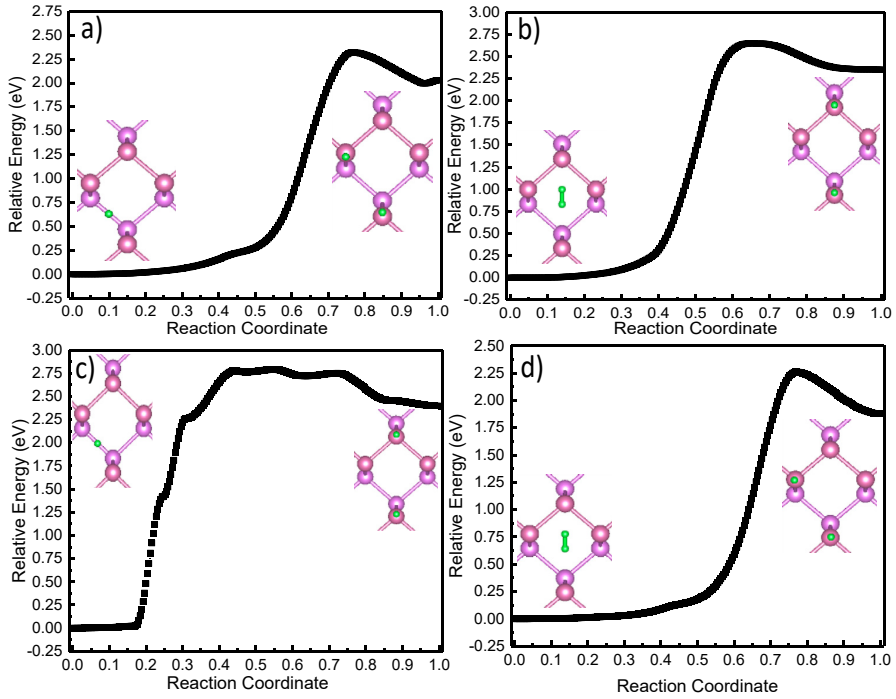

Fig. 6 – Chemisorption reaction path of H_2 on phosphorene, from the physisorbed state to the chemisorbed state: (a) Bridge2(B′2) to Top(meta), (b) Hollow(H1) to Top(para), (c) Bridge2(B′2) to Top(para) (d) Hollow(H1) to Top(meta).

Table 3 – Activation barriers for the H_2 Dissociation.

Configuration	The activation energy (eV) (this work)	The activation energy (eV) (Graphene)
B′2- > Top (meta)	2.32	2.68–3.86 Costanzo et al. [61]
B′2- > Top (para)	2.77	
H1- > Top (para)	2.64	
H1- > Top (meta)	2.26	
H3- > Top (para)	2.64	

for H_2 dissociation on the phosphorene surface are lowered compared with the case of graphene, which shows the remarkable effect of the substrate curvature in promoting hydrogen dissociation [80,81].

To get more inside, we perform adsorption calculations for the hydrogen atom of each phosphorene sites. Our results show that the decomposition of hydrogen molecule suggests a decomposition of phosphorene into weakly bonded one-dimensional 1D chains arranged in the zigzag direction (Fig. 7(b)). As we know phosphorus atoms have five valence electrons, each phosphorus atom becomes saturated by making a covalent σ-bond, two at the same plane while another is on a neighboring plane via 3p orbitals leaving a mono-electron pair oriented out-of-plane, orbitals giving rise to sp^3 hybridization. In the presence of hydrogen atom, the general mechanism of the bond formation between phosphorene and hydrogen atom redistribute, one σ-orbital form covalent bond with the hydrogen atom, two others keep covalent bonds with phosphorus atoms in plane and the last doubly occupied orbital forms alone pair pointing in the direction of the other phosphorus plane, which suggest an increase of distance between two plan of phosphorus which is

Please cite this article as: Garara M et al., Phosphorene: A promising candidate for H_2 storage at room temperature, International Journal of Hydrogen Energy, https://doi.org/10.1016/j.ijhydene.2019.07.194

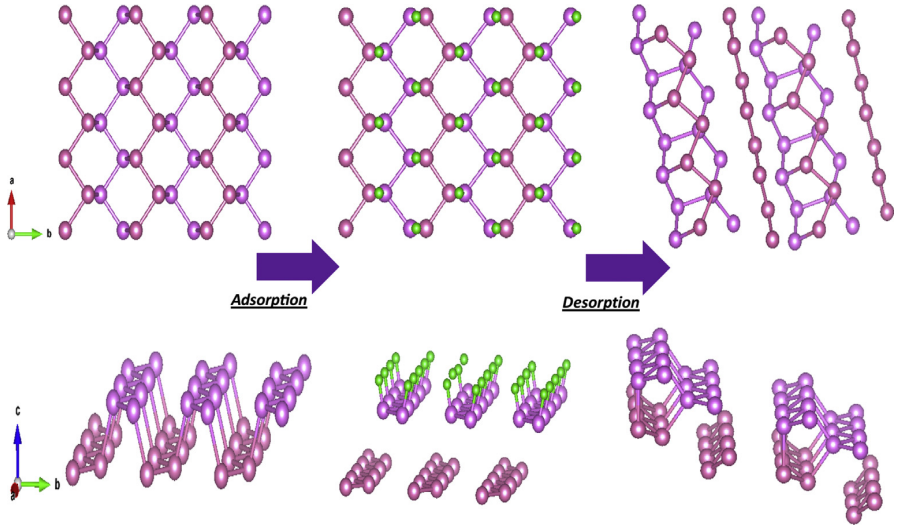

Fig. 7 – Optimized atomic structures of adsorption and desorption of hydrogen on single sides phosphorene.

significantly larger value of 3.54 Å (2.13 Å before the hydrogenation). To study the reversibility of hydrogen atom chemisorbed in phosphorene, we evaluate a calculation of hydrogen desorption (Fig. 7(c)). It can be seen from this figure the distortion of phosphorene structure during the hydrogen atom desorption. Thus, induce an across of the phosphorene chain after fully hydrogen desorbed. It is noticed that the chemisorption of hydrogen atom it is not likely reversible. However, the chemisorption of hydrogen atom in phosphorene does not seem to be directly observable from the adsorption of hydrogen molecule due to high energy barriers governed by molecular dissociation and atomic migration.

In order to understand the adsorption behaviors, hydrogen storage capacity and stability of substrate, we gradually increased the number of adsorbed H_2 molecules on both side of phosphorene layer. The different adsorption sites are also considered during such process (Fig. 8) and the adsorption energy per H_2 is calculated using the following term:

$$\overline{E_{ads}} = \frac{1}{n}\left(E_{syst} - E_{sub} - n.E_{H_2}\right) \quad (3)$$

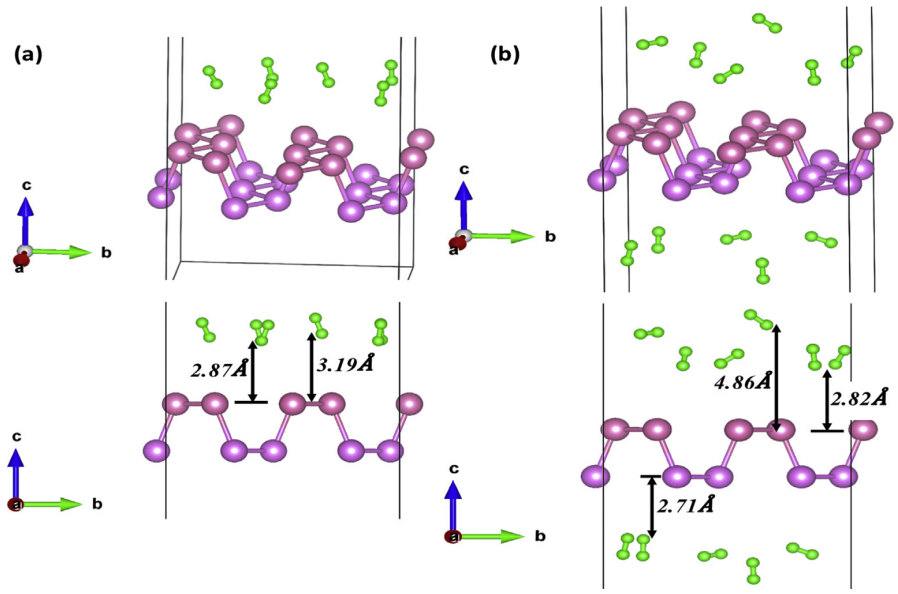

Fig. 8 – Optimized structures of phosphorene saturated with H_2 molecules on (a) one side and (b) both sides.

Please cite this article as: Garara M et al., Phosphorene: A promising candidate for H_2 storage at room temperature, International Journal of Hydrogen Energy, https://doi.org/10.1016/j.ijhydene.2019.07.194

Table 4 – Calculated adsorption energies of H_2 molecules (meV/H_2) on phosphorene, average height between H_2 and substrate (Å) and H–H bond length (Å).

Number of H_2	Adsorption energies per H_2 (meV)	Adsorbate height (Å)	H–H bond length (Å)
1	−292.4	2.98	0.7562
2	−307.3	2.98	0.7557
3	−300.8	2.98	0.7557
4	−298.2	2.98	0.7551–0.7556
5	−198.8	2.92–2.95	0.7484–0.7556
6	−268.2	2.87–3.19	0.7531–0.7548
7	−271.9	2.86–3.2	0.7534–0.7556
8	−275	2.86–3.2	0.7534–0.7562
9	−279.7	2.78–3.57	0.7537–0.7558
10	−280.9	2.78–3.57	0.7537–0.7558
11	−281.5	2.71–4.86	0.7539–0.7559

where E_{syst} and E_{sub} are the total minimized energies of substrate with and without H_2 respectively, and E_{H2} is the total energy of the H_2 molecule and n is the number of H_2 molecules adsorbed. Table 4 lists the adsorption energies per H_2 on the range distance of H_2 molecules from substrate for different number of adsorbed H_2 and as well as H–H bond length. It was also noted that the H_2 molecules do not move away from the substrate indicating adsorption to phosphorene layer.

From Fig. 8 and Table 4, by increasing of the number of H_2 in one or both sides, the hydrogen molecules adsorbed with non-uniform manner and the calculated adsorption energies per H_2 for the most stable configuration are in the range from −198.8 to −307.3 meV/H_2, which satisfies the requirement of effective hydrogen storage material specified by US-DOE (stable storage and release at near ambient conditions). It can be seen that all the relaxed H–H bond lengths are between 0.7484 and 0.7562 Å, good agreement compared with 0.75 Å of a free H_2 molecule, which indicate that all hydrogen remains in the molecular state. As a result, the saturate of the H_2 molecules adsorption is 11 and the maximum gravimetric density of hydrogen absorbed on phosphorene should be around 4.45 wt%.

Finally, due to the large dissociation energies, the phosphorene monolayer preferably adsorbs hydrogen molecules rather than dissociates hydrogen molecules, the H_2 molecules were adsorbed in a non-uniform manner and the distance to the H_2 molecules from the substrate increased due to the steric interaction between the adsorbed H_2 molecules.

Conclusions

Several adsorption sites and the orientation of hydrogen molecule relative to the phosphorene surface were explored. The most stable physisorbed state is in the bridge B' site, with a binding energy of −292 meV. This value, which is obtained using the DFT/vdW-DF2-C09x approach including the vdW interactions, is higher than obtained from graphene (−54 ~ −38 meV) and fulfills the requirement for appropriate hydrogen storage with a binding energy of −0.2 ~ −0.6 eV/H_2. The analysis of reaction pathways diffusion among physisorbed states shows that molecular hydrogen can easily diffuse on phosphorene at room temperature across sites separated by energy barriers of just a few meV. The situation is different when the hydrogen molecules approach the phosphorus surface and dissociate. In particular, we calculated the activation energy of dissociation from H_2 molecule on highly symmetric sites of phosphorene. The lowest dissociation barrier of 2.26 eV is that one that corresponds to the transition from the H_2 physisorbed state to the meta chemisorbed state. Other energy paths are characterized by higher activation barriers (~2.77 eV).

Acknowledgement

We would like to thank Mr. Ari PaavoSeitsonen from the chemistry department of the ENS, which provided us with the necessary On the Quantum Espresso code.

REFERENCES

[1] Schlapbach L, Züttel A. Hydrogen-storage materials for mobile applications. Nature 2001;414:353–8. https://doi.org/10.1038/35104634.
[2] He T, Pachfule P, Wu H, Xu Q, Chen P. Hydrogen carriers. Nat Rev Mater 2016;1:16059. https://doi.org/10.1038/natrevmats.2016.59.
[3] Schlapbach L. Technology: hydrogen-fuelled vehicles. Nature 2009;460:809–11. https://doi.org/10.1038/460809a.
[4] Satyapal S, Petrovic J, Read C, Thomas G, Ordaz G. The U.S. department of energy's national hydrogen storage project: progress towards meeting hydrogen-powered vehicle requirements. Catal Today 2007;120:246–56. https://doi.org/10.1016/j.cattod.2006.09.022.
[5] Partnership TF and F. Targets for onboard hydrogen storage systems for light duty vehicles. US Dep Energy 2009:1–22.
[6] Yang J, Sudik A, Wolverton C, Siegel DJ. High capacity hydrogenstorage materials: attributes for automotive applications and techniques for materials discovery. Chem Soc Rev 2010;39:656–75. https://doi.org/10.1039/B802882F.
[7] Yoon M, Yang S, Wang E, Zheng Z. Charged fullerenes as high-capacity hydrogen storage media. Nano Lett 2007;7:2578–83. https://doi.org/10.1021/nl070809a.
[8] Mohtadi R, Orimo S. The renaissance of hydrides as energy materials. Nat Rev Mater 2016;2:16091. https://doi.org/10.1038/natrevmats.2016.91.
[9] Darvish Ganji M, Hosseini-khah SM, Amini-tabar Z. Theoretical insight into hydrogen adsorption onto graphene: a first-principles B3LYP-D3 study. Phys Chem Chem Phys 2015;17:2504–11. https://doi.org/10.1039/C4CP04399E.
[10] Orimo S, Nakamori Y, Eliseo JR, Züttel A, Jensen CM. Complex hydrides for hydrogen storage. Chem Rev 2007;107:4111–32. https://doi.org/10.1021/cr0501846.
[11] Aguey-Zinsou K-F, Ares-Fernández J-R. Hydrogen in magnesium: new perspectives toward functional stores. Energy Environ Sci 2010;3:526. https://doi.org/10.1039/b921645f.
[12] Alapati SV, Karl Johnson J, Sholl DS. Using first principles calculations to identify new destabilized metal hydride reactions for reversible hydrogen storage. Phys Chem Chem Phys 2007;9:1438. https://doi.org/10.1039/b617927d.
[13] Ferrari AC, Bonaccorso F, Fal'ko V, Novoselov KS, Roche S, Bøggild P, et al. Science and technology roadmap for graphene, related two-dimensional crystals, and hybrid

Applied Physics A (2019)125:760
https://doi.org/10.1007/s00339-019-3052-4

Applied Physics A
Materials Science & Processing

Enhancing of hydrogen storage properties of perovskite-type $MgNiH_3$ by introducing cobalt dopant ($MgCo_xNi_{1-x}H_3$) using first-principle calculations

M. Abdellaoui[1] · M. Lakhal[1] · H. Benzidi[1] · M. Garara[1] · A. Benyoussef[2,3] · A. El Kenz[1] · O. Mounkachi[1] · M. Loulidi[1] · H. Ez-Zahraouy[1]

Received: 16 July 2019 / Accepted: 1 October 2019

Abstract
First-principle calculations have been performed to study the intermetallic alloys $MgCo_xNi_{1-x}$ and intermetallic hydrides $MgCo_xNi_{1-x}H_3$ using full-potential local orbital (FPLO). The electronic structure of Mg-hydride-based alloys has been elaborated to predict further modifications which destabilize the corresponding hydrides. In this paper, we have demonstrated that the insertion of Co element plays a crucial role in the stability of doped intermetallic hydrides ($MgCo_{0.50}Ni_{0.50}H_3$, $MgCo_{0.75}Ni_{0.25}H_3$ and $MgCo_{0.875}Ni_{0.125}H_3$), by enhancing the hydrogen storage capacities which becomes around 3.488 wt%, also the desorption temperature has improved significantly. Therefore, the mixture between Co and Ni plays an important role in the hydrogen uptake mechanism in the target intermetallic matrix.

1 Introduction

Hydrogen is considered a good energy carrier, thanks to its combustibility which generates about 3 times more energy than other fossil fuels. All these characteristics make hydrogen the key to the global energy revolution [1–5]. However, the problem of storage and transport of hydrogen safely and effectively prevents its wide uses. Magnesium hydride (MgH_2) is one of the most promising systems for storing solid hydrogen. Although, MgH_2 is a thermodynamically very stable compound, with a decomposition temperature of about 587 K under a hydrogen pressure of 2.3 bar [6]. Therefore, many attempts have been made to increase the rate of hydrogenation and to decrease the desorption temperature of hydrogen in MgH_2 while playing on several parameters such as the shape of the material, the size of the particle, the state of the surface, the thickness of the oxide layer, the presence of impurities, and the presence of precursors or additives [7–16]. In addition, Mg-based transition metal additives are easier to apply these attempts to improve the Mg–H and M–H bond [17–23].

To overcome the high decomposition temperature of Mg-based materials, many theoretical studies have been carried out using density functional theory (DFT) calculations. In this regard, an increasing number of studies have been proved the enhancement of desorption temperature when Mg is combined with several metallic additives [24-30]. More particularly, intermetallic hydrides MgCo–H and MgNi–H draw more intent through their hydrogen storage properties. Cadan et al. [31] revealed that the perovskite hybrid $MgCoH_3$ system is very stable with formation enthalpy of -73.80 kJ/mol H_2. In addition, it is reported that the analysis $MgNiH_3$ binding reveals a weak interatomic binding between Mg–H and Ni–H [32–34], and the same results have been reported by our group in the previous study of $MgCoH_3$, where the founded heat of formation value of $\Delta H = -73.32$ kJ/mol H_2 [32]. In addition, it has been shown that Mg–Co hydride has high stability [34–36], whereas it is lower in the case of Mg–Ni hydride [33]. Therefore, we expect that the mixture between these hydrides $MgNiH_3$ and $MgCoH_3$ gives rise to new ternary hydrides ($MgNi_xCo_{1-x}H_3$, $x = 0.50, 0.75, 0.875$) compounds with moderate stability

✉ M. Abdellaoui
bdellaoui@gmail.com

[1] Laboratory of Condensed Matter and Interdisciplinary Sciences (LaMCScI), Associated to CNRST (URAC 12), Physics Department, Faculty of Sciences, Mohammed V University, Rabat, Morocco

[2] Materials and Nanomaterials Centre, Moroccan Foundation for Advanced Science, Innovation and Research, MAScIR, Rabat, Morocco

[3] Hassan II Academy of Science and Technology, Rabat, Morocco

Published online: 14 October 2019

and rapid kinetics without significant loss of storage capacity of the compound [34].

It should be mention that the Mg–Co and Mg–Ni BCC intermetallic have been fabricated by the mechanical alloying (MA) method [37–43]. Moreover, the formation energies of magnesium-(Co,Ni) alloys employing, for example, a BCC and Perovskite structure such as $MgCoH_3$, $MgNiH_3$, and $MgCo_{0.50}Ni_{0.50}H_3$ hydrides have been done [33, 33]. Vegge et al. [32] have analyzed the properties of the perovskite structure $MgTMH_3$ (TM = 3*d* transition metals).

The aim of this paper is to investigate using DFT calculations the particular hydrogenation properties of intermetallic binary (MgCo, MgNi) and ternary ($MgNi_xCo_{1-x}$, $x = 0.50$, 0.75, 0.875) compounds. The stability of studied compounds is verified by computing the heats of formation and decomposition temperature. The obtained results are supported by the analysis of their electronic density of states (DOS). Herein, the computational method used to study our suggested compounds is described in the second section, while our obtained results are presented in Sect. 3. The conclusion is given in Sect. 4.

2 Computational method

In this paper, we used ab-initio calculations based on the all-electron full-potential local-orbital minimum-basis scheme FPLO9.00-34 [44, 45]. This has been performed to solve the Kohn–Sham equations using the scalar-relativistic scheme. The parameterization of the exchange–correlation energy has been done within the generalized gradient approximation GGA [46]. To ensure a high accuracy in our performed computations, we have used both self-consistent criterions of the energy and the density together with a precision of 10^{-8} Ha and 10^{-6} Ha^{-1} $Å^{-3}$, respectively. To accurate Brillouin zone integrations, a $12 \times 12 \times 12$ K-point mesh has been considered.

For MgCo and MgNi alloys, we use a simple body-centred cubic unit cell (*Pm3m* space group no. 221) [32–34] containing two atoms, i.e., a magnesium atom placed at the corner (0 0 0) and a Co or Ni atom in the centre (0.5 0.5 0.5) (see Fig. 1). Three additional hydrogen atoms are placed in octahedral sites at the face centres (0.5 0.5 0), (0.5 0 0.5), and (0 0.5 0.5), respectively, as shown in Fig. 1 (Perovskite structure [32, 34]). The lattice parameters have

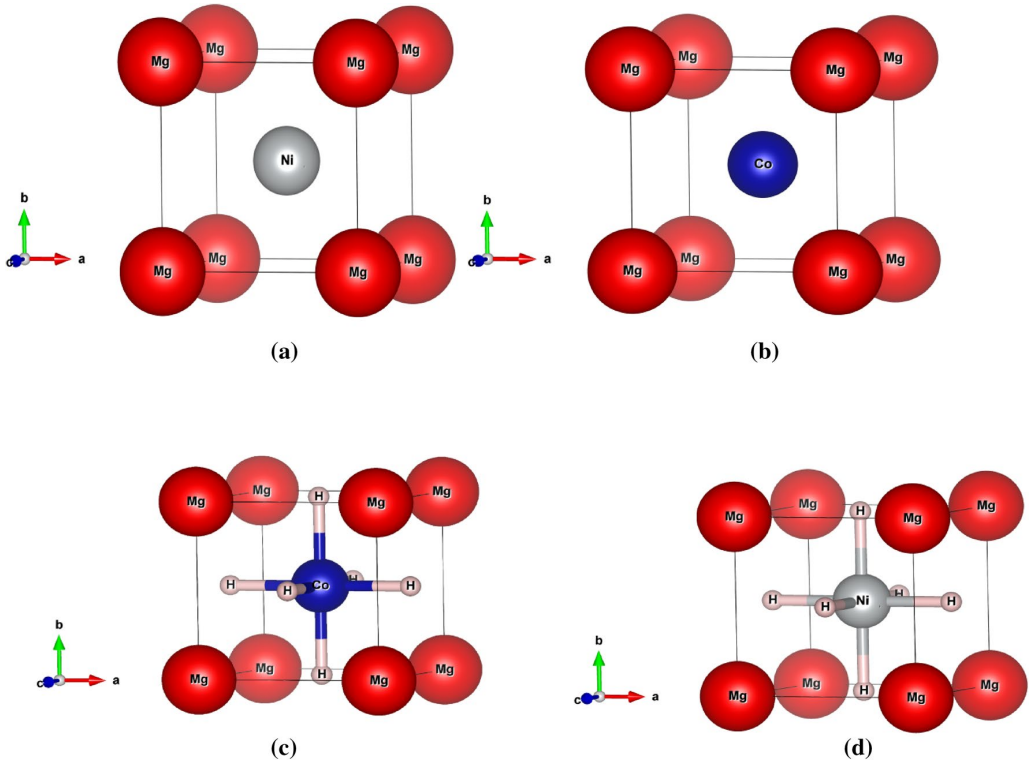

Fig. 1 Crystal structures of unit cell of MgCo, MgNi, $MgCoH_3$, $MgNiH_3$, and $MgCo_{0.50}Ni_{0.50}H_3$ hydrides in the Perovskite structure. **a** MgCo; **b** MgCo; **c** $MgCoH_3$; **d** $MgNiH_3$ (red-Mg atom, grey-Ni atom, blue-Co atom, white-H atom)

been optimized using the relaxation method for all systems MgCo, MgNi alloys, and their hydrides (see Table 1). The calculated equilibrium values agree well with the obtained results of other groups [32, 33].

To study the hydrogenation properties of $MgNi_{1-x}Co_xH_3$ ($x = 0.50, 0.75, 0.875$), the calculations have been carried out using a $2\times2\times2$ supercell, which allows us to reach such concentrations. This new system preserves the same crystal structure as intermetallics MgCo and MgNi (*Pm3m* space group no. 221) (Fig. 1), but the lattice parameter is modified by varying the concentration of the doped elements. Among the three dopants structures, the equation structure $MgNi_{0.50}Co_{0.50}H_3$ shown in Fig. 2 is selected.

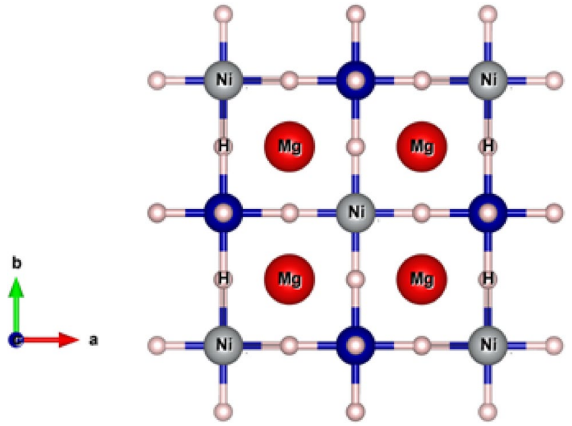

Fig. 2 Crystal structures of super cell of $MgCo_{0.50}Ni_{0.50}H_3$

3 Results and discussion

3.1 Crystal structure

The parameters were optimized using the relaxation method for the MgCo, MgNi systems, and their hydrides and the results are displayed in Table 1 and Fig. 3. The equilibrium values calculated are consistent with the obtained values in other studies [32, 33]. In Fig. 3, we plotted the total energy curves of the MgNi and MgCo alloys and their hydrides as a function of volume using the Murnaghan state equation [47]; based on this equation, the equilibrium parameters of the studied systems were extracted. It can be understood from the values presented in Table 1 that when hydrogen absorption in the intermetallic, a volume expansion ($\Delta V/V$) of 23.60% for $MgCoH_3$ and 26% for $MgNiH_3$ occurs. Constraints caused by the increase or decrease of the volume during hydrogenation and dehydrogenation lead to the decrepitation of the grains creating new surfaces liable to be corroded. Willems [48] proposes that hydride compounds with small volume variations should have a better lifetime. Therefore, the stability of the hydride system is inversely proportional to the volume expansion, i.e., the distance between the MgTM–H atoms is small while these bonds are stronger. It is found that the intermetallic MgCo is unstable and MgNi is stable according to several studies [32, 34], and the results have an effect on the properties of the intermetallic which will be studied in the following paragraph.

3.2 Hydrides stability: heat of formation

Before discussing intermetallic hydrides, we will study their formation energy and their stability. The heat of formation ΔH is the most important thermodynamic parameter used to identify and classify materials for solid-state hydrogen storage. This is due to the fact that it allows the determination of the stability of the systems (if $\Delta H < 0$ hydride is stable and vice versa), and also the desorption temperature of hydrogen. This value of ΔH could be defined as the difference between the sum of total energy of products and reactants [49]:

$$\Delta H = \sum E_{\text{tot}}(\text{products}) - \sum E_{\text{tot}}(\text{reactants}). \quad (1)$$

The reaction related to the formation of the hydride $MgTMH_3$ (TM = Ni and Co) reads as

$$MgTM + 3/2H_2 \rightarrow MgTMH_3. \quad (2)$$

Table 1 Relaxed parameters, equilibrium volumes (V), storage capacities and percentages $\Delta V/V$ (%) of the variation of the volume of the intermetallics to its hydride

Systems	Parameters (Å)	Symmetry group	Volume (Å^3)	Mass capacity (wt%)	Volumetric capacity ($gH_2\ l^{-1}$)	$\Delta V/V$ (%)
MgCo	3.026	*Pm3m* (221)	27.70	–	–	–
$MgCoH_3$	3.310	*P1*	36.26	3.488	133.73	23.6
MgNi	3.050	*Pm3m* (221)	28.37, 28.44 [33]	–	–	–
$MgNiH_3$	3.370	*P1*	38.27	3.478	130.01	26.0
$MgNi_{0.50}Co_{0.50}$	3.035	*Pm3m* (221)	27.95, 37.07 [33]	–	–	–
$MgNi_{0.50}Co_{0.50}H_3$	3.340	*P1*	37.25	3.488	133.73	24.9

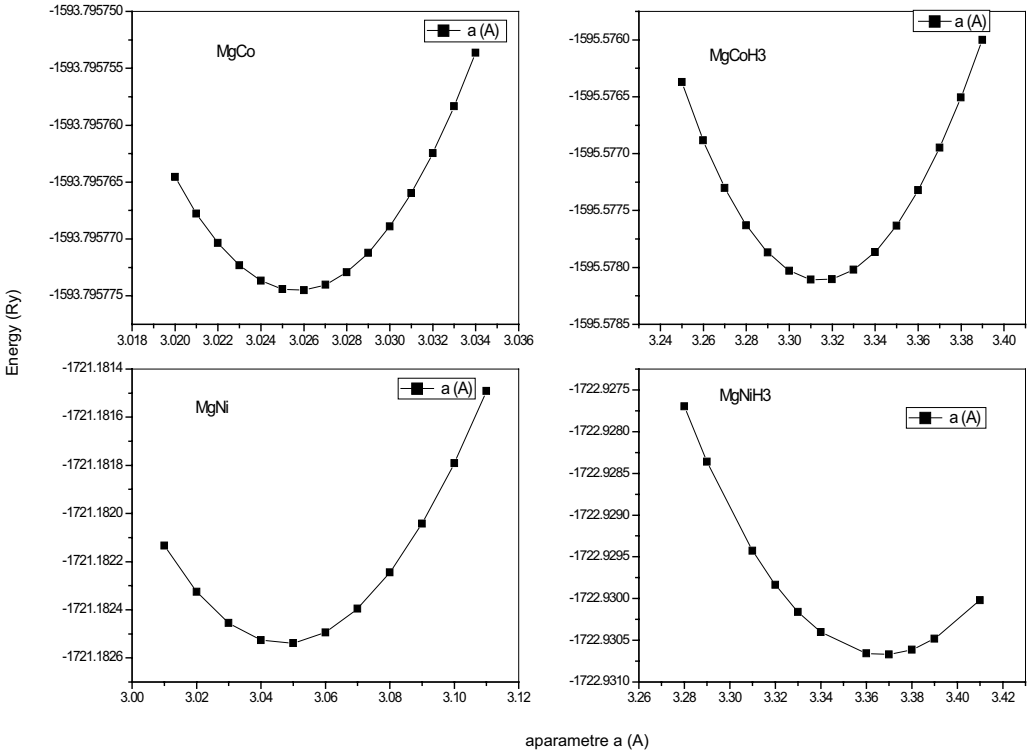

Fig. 3 Variation of the total energy according to the volume of the compounds of MgCo, MgNi, $MgCoH_3$, and $MgNiH_3$

To calculate the heat of formation of the reaction (2), we subtract the total energies of MgTM alloys and hydrogen molecule from its hydride $MgTMH_3$:

$$\Delta H = E_{\text{tot}}\left(\text{MgTMH}_3\right) - E_{\text{tot}}(\text{MgTM}) - 3/2E_{\text{tot}}\left(\text{H}_2\right). \quad (3)$$

The calculated energy of the H_2 molecule $E_{\text{tot}}(H_2) = -2.33$ Ry is close to -2.320 Ry found in [50].

The obtained heat formation of $MgNiH_3$, $\Delta H = -13.50$ kJ/mol H_2, is in good agreement with the measured values -8.68 kJ/mol $H_2 < \Delta H < -21.20$ kJ/mol H_2 of some Mg–Co–H systems, as given in [24, 31–34]. This value indicates that this system has a high thermodynamic stability, while $MgCoH_3$ is thermodynamically stable, since it presents a great enthalpy, which is -73.32 kJ/mol H_2 (Table 2); this value is similar as to the one found in the literature [31–34].

To stabilize $MgNiH_3$, we suggest making a mixture between $MgCoH_3$ and $MgNiH_3$ to reach a desirable heat of formation comprised between the ones of the two studied systems. For this purpose, it is worthy to study the influence of Co-doped $MgNiH_3$ on the stability of these hydrides.

The formation energies of $MgNiH_3$: Co for various doping Co concentrations are listed in Table 1. These energies are required to form the hydride phase using the following reaction:

$$\text{MgNi}_{1-x}\text{Co}_x + 3/2\text{H}_2 \rightarrow \text{MgNi}_{1-x}\text{Co}_x\text{H}_3. \quad (4)$$

Table 2 Heat formation, of MgCo, MgNi, $MgCoH_3$, $MgNiH_3$ and $MgCo_{0.5}Ni_{0.5}H_3$ and temperature of desorption and gravimetric capacity of $MgCo_{1-x}Ni_xH_3$ of $MgCoH_3$ and $MgNiH_3$ obtained from ab-initio calculations

Systems	Heat of formation (kJ mol^{-1} H_2)	Gravimetric capacity (wt%)	Desorption temperature (K)
$MgCoH_3$	−73.32, −73.80 [30], −62.72 [32]	3.483	560.97, 482.42
$MgNiH_3$	−13.50, −8.68 [32]	3.478	103.29, 66.80 [32]
$MgCo_{0.875}Ni_{0.125}H_3$	−67.35	3.479	515.30
$MgCo_{0.75}Ni_{0.25}H_3$	−60.36	3.481	461.82
$MgCo_{0.50}Ni_{0.50}H_3$	−45.92	3.488	351.33

As mentioned above, to investigate the influence of alloying elements on the stability of the $MgCoH_3$ hydrides, the enthalpies of formation of $MgNi_{1-x}Co_xH_3$ for different concentration ($x = 0.\ 05$, 0.75, and 0.875) are calculated according to the following expression (see Table 1):

$$\Delta H = E_{\text{tot}}\left(MgNi_{1-x}Co_xH_3\right) - E_{\text{tot}}\left(MgNi_{1-x}Co_x\right) - 3/2E_{\text{tot}}\left(H_2\right). \quad (5)$$

It follows that, the addition of an amount of Co, generally, reduces the stability, since the enthalpy decreases from − 13.50 kJ/mol H_2 for $MgNiH_3$ to − 45.92 kJ/mol H_2 for $MgCo_{0.5}Ni_{0.5}H_3$ and − 60.36 kJ/mol H_2 for $MgCo_{0.75}Ni_{0.25}H_3$. In addition, the stabilization effect on $MgNi_{1-x}Co_xH_3$ becomes important by increasing the concentration of Co, and consequently, the heat of formation decreases linearly.

3.3 Desorption temperature

The thermodynamic properties of the hydrides are described by the standard Gibbs energy:

$$\Delta G = \Delta H - T\Delta S, \quad (6)$$

where ΔH and ΔS are the enthalpy and the entropy change of the dehydrogenation reaction, respectively. For a complex hydride, when the material is being heated, the entropy factor slowly overcomes the enthalpy contribution. For a constant pressure, the standard Gibbs energy is equal to zero at the decomposition temperature. Thus, the temperature of dehydrogenation can be estimated using the following equation [30, 51]:

$$\Delta H = T\Delta S. \quad (7)$$

During the heating, the entropy change of solid materials is very small compared to the gas. This change in the entropy during the decomposition reaction is primarily due to H_2 evolution. At the standard pressure and temperature, for the most simple metal hydride, the entropy is taken equal to $\Delta S \approx \Delta S(H_2) = -130.7$ J/mol K, corresponding to the entropy due to a mole of a gas which transforms into a solid [52-54].

The calculation results show that $MgNiH_3$ has a low decomposition temperature equal to 103.29 K (see Table 2), which prevents its application for hydrogen storage.

The high amount of Co metal has a great effect in stabilization of the parent compound $MgNiH_3$ and leads to an increasing of the decomposition temperature from 103.29 to 515.30 K for $MgCo_{0.875}Ni_{0.125}H_3$, without reducing significantly its hydrogen capacity which is in of order 3.488 wt% (see Table 2).

3.4 Electronic structure

First, we recall that DFT calculations are performed to obtain the density of states (DOS) which is the main tool used to determine the chemical bonding characteristics of our systems without hydrogen and with hydrogen. Therefore, before being explained the state of change (binding, new hybridization, etc) in the hydrogenated system the system density of the without hydrogen system is first treated to determine the properties obtained during the hydrogenation.

The total density of states (DOS) and the partial density of states (PDOS) of MgCo and MgNi alloys are shown in Figs. 4 and 5, respectively. As the Fermi levels of the MgCo and MgNi alloys are filled by the density of states (DOS), both systems have a metallic character.

We know that the more the electronic states are towards the negative energies, the more the system is thermodynamically stable. From the figures, we noticed that most of the MgNi states are on the left of Fermi level, i.e., towards the lowest energies, so this system is more stable than MgCo than states around Fermi level.

The total density of states (DOS) and the partial density of states (PDOS) of $MgNiH_3$ and $MgCo_{0.5}Ni_{0.5}H_3$ are plotted in Figs. 6 and 7, respectively.

It follows from Fig. 6 that there are two parts in the valence band (VB). The first part is assorted with the band energy range from − 10.00 to − 5.0 eV which is called "lower VB" composed of strong hybridisation between H-*s*, Mg (*s*,*p*), and Co-3*d* states, and the second part with an energy ranging from − 4.0 to 0.0 eV called "high VB" originating almost from Mg (*s*,*p*) and Co-3*d* states. From Fig. 7, one can see that the VB for $MgCo_{0.5}Ni_{0.5}H_3$ is divided into three distinct regions: lower VB with the band energy range from − 10.00 to − 5.0 eV composed by H(1,2,3)-*s*, Mg (*s*,*p*) and 3*d* states of Co(1,2) and Ni(1,2); the second part with an energy range from − 4.0 to − 2.5 eV called "middle VB" originating from a weak hybridisation between Mg(*s*,*p*), Co1-3*d*, Co2-3*d* and Ni1-3*d*, Ni2-3*d* states; and the latest part is the "high VB" (from − 2.5 to 0 eV) originating almost from a strong hybridisation between Co-3*d* and Ni-3*d* states. Beyond the Fermi level, the DOS is dominated by the Mg(*s*,*p*) states.

One can see from Figs. 6 and 7 that the DOS of $MgCoH_3$-doped Ni at the Fermi level is lower than the one of $MgNiH_3$, which leads to a better stability of the doped component. Moreover, the analysis of the $MgNiH_3$ DOS reveals the occurrence of three bonds: a weak bond between Mg–Co, another very weak bonding between Mg–H and H–Ni that reduce the stability of this system. On the other hand, the DOS of $MgNiH_3$ doped Co exhibits, a very strong bonding between Co and Ni atoms, while the Co and H atoms form a very weak bond, since the hybridization between the orbital of Co

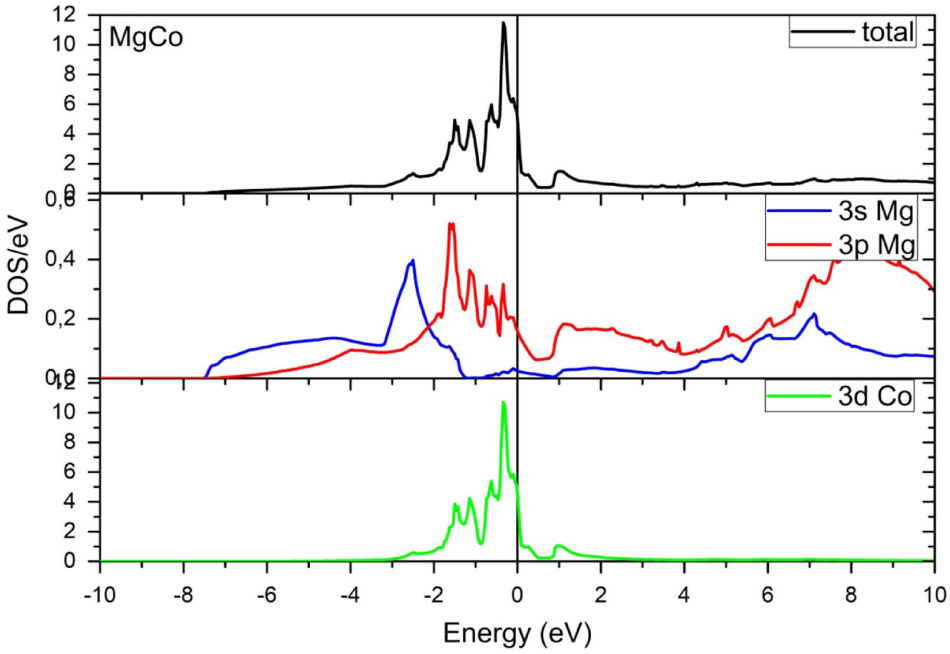

Fig. 4 Total and partial DOS of MgCo system

Fig. 5 Total and partial DOS of MgNi system

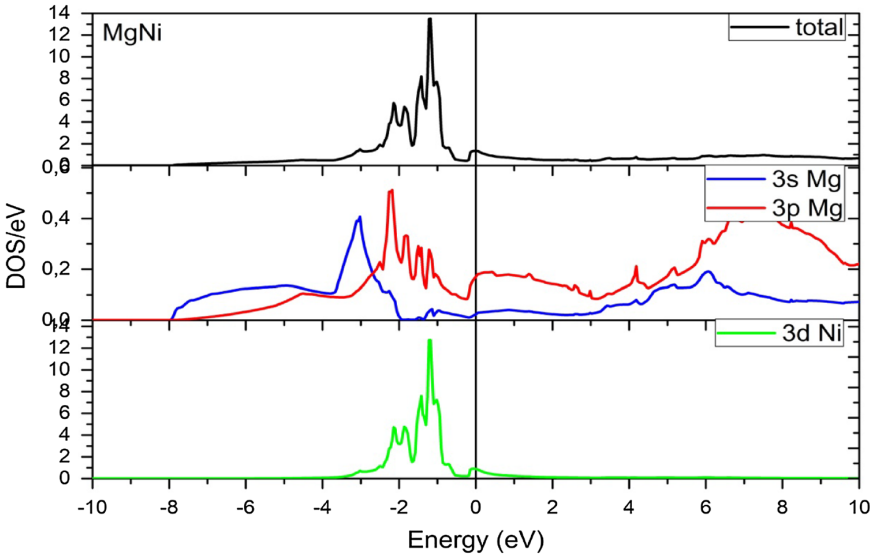

and H atoms is not relevant. Since, the strong hybridization between Co and Ni that reinforces the H–Ni bond Thus, the H atoms are trapped more low inside $MgNiH_3$ than $MgCo_{0.50}Ni_{0.50}H_3$ alloys. In other words, incorporation of a quantity of Co into intermetallic hydride can efficiently reduce the interactions between interstitial H atoms and MgNi host which leads to an improving of the system stability. In addition, experimental attempts of MgNi–H and MgCo–H mixture produced MgCoNi–H with moderate properties [55–57], and these results are quite similar to our work, which may explain the results reported in Sect. 3.2.

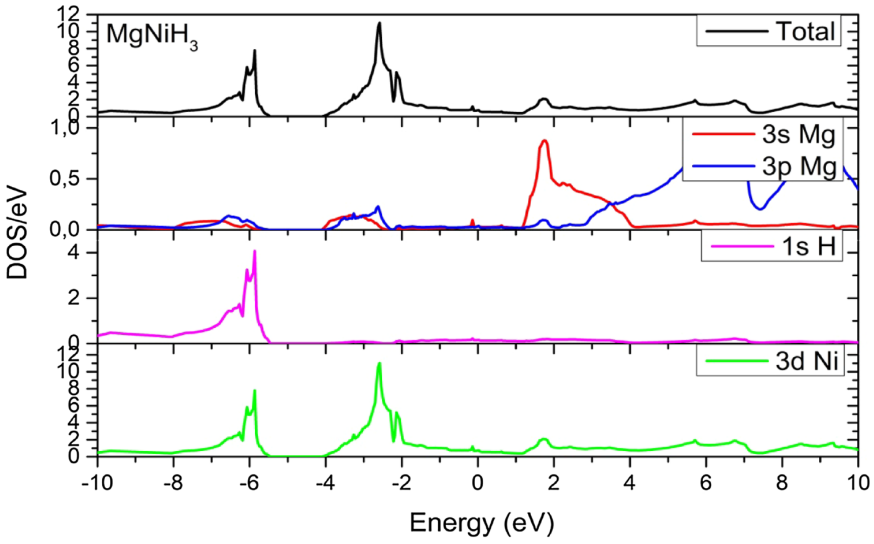

Fig. 6 Total and partial DOS of $MgNiH_3$ system

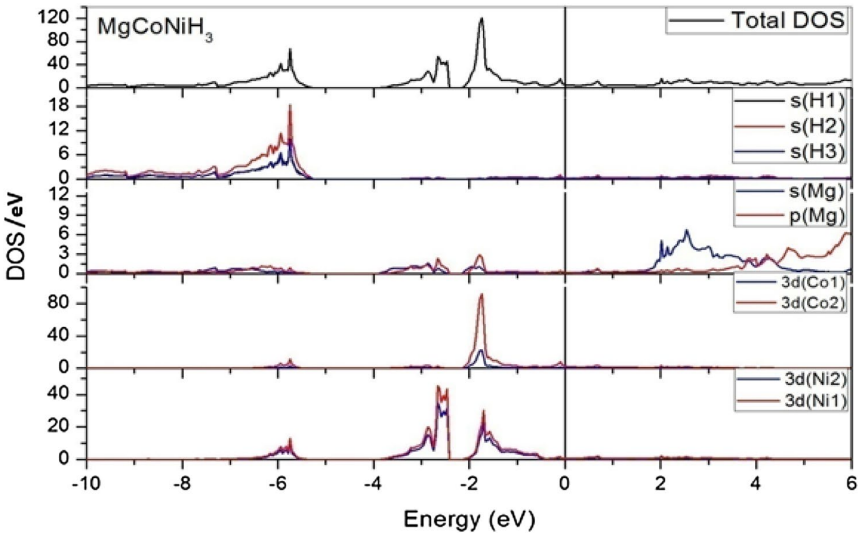

Fig. 7 Total and partial DOS of $MgCo_{0.50}Ni_{0.50}H_3$ system

4 Conclusion

In this paper, density functional theory (DFT) calculations have been used to study the hydrogen storage properties of hydrides intermetallic compounds with a cubic structure $MgCoH_3$, $MgNiH_3$, and $MgCo_xNi_{1-x}H_3$. More precisely, we have computed the formation enthalpy and decomposition temperature of the materials. These quantities are relevant for hydrides choice for hydrogen storage applications. Thus, by analyzing the heat of formation, the DOS and PDOS of both $MgNiH_3$ and $MgCo_{0.50}Ni_{0.5}H_3$, we have deduced that the insertion of Co element plays a crucial role in the stability of intermetallic hydride $MgCo_{0.5}Ni_{0.5}H_3$ leading to a decrease in the interactions between Co–H, Mg–H and consequently a decrease of the stability of the system, which is in agreement with the results obtained for formation energies (Table 2). The obtained value of the heat formation is $\Delta H = -45.92$ kJ mol^{-1} H_2. It approaches the desired value -40 kJ mol^{-1} H_2, which is a recommendation mentioned in reference [58].

Acknowledgements This work was supported by the CNRST in the framework of the national program Dev-RS/04. The authors acknowledge its financial support.

ARTICLE IN PRESS

INTERNATIONAL JOURNAL OF HYDROGEN ENERGY XXX (XXXX) XXX

Available online at www.sciencedirect.com

ScienceDirect

journal homepage: www.elsevier.com/locate/he

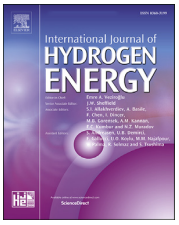

Improved thermodynamic properties of doped $LiBH_4$ for hydrogen storage: First-principal calculation

H. Benzidi [a,*], *M. Lakhal* [a], *M. Abdellaoui* [a], *M. Garara* [a], *A. Benyoussef* [b], *A. El kenz* [a], *M. Loulidi* [a], *M. Hamedoun* [b], *O. Mounkachi* [a,**]

[a] *Laboratory of Condensed Matter and Interdisciplinary Sciences (LaMCScI), Associated to CNRST (URAC 12), Physics Department, Faculty of Sciences, Mohammed V University, Rabat, Morocco*

[b] *Materials and Nanomaterials Center, MAScIR Foundation, Rabat Design Center Rue, Mohamed Al Jazouli Madinat Al Irfane, Rabat 10 100, Morocco*

ARTICLE INFO

Article history:
Received 27 February 2019
Received in revised form
6 April 2019
Accepted 23 April 2019
Available online xxx

Keywords:
First-principal calculations
Electronic properties
Complex hydride
Hydrogen-storage
Enthalpy
Kinetics

ABSTRACT

First-principles calculations have been performed on lithium borohydride $LiBH_4$ using the ultrasoft pseudopotential method, which is a potential candidate for hydrogen-storage materials due to its extremely large gravimetric capacity of 18 mass % hydrogen. We focus on an orthorhombic phase observed at ambient conditions and predict its fundamental properties; De-hydrogenation and electronic properties of doped $Li_{1+x}B_{1-x}H_4$ by Li (with $0 < x < 0.75$); to be used as a material for hydrogen-storage; are studied from density-functional theory based first-principles calculations. The results suggest that the substitution of B by Li decrease the desorption enthalpy of hydrogen from 75 kJ/mol.l to 40. Our calculation results show the function of Li in improving thermodynamics, which provides a favorable thermodynamic modification.

Introduction

As a new energy vector, hydrogen presents an attractive alternative fuel that can be produced from the electrolysis of water [1–3]. It is considered as a clean and renewable source of energy since it does not release greenhouse gas emissions [4,5]. In addition, hydrogen is considered as a good energy carrier, thanks to its combustion which generates about three times more energy than other fossil fuels [6]. All these qualities make hydrogen the key to the global energy revolution. However, the difficulties encountered in the storage and transportation of hydrogen without risk, efficiently and safely prevent its wide use and commercialization [7].

Among the available techniques for the storage of hydrogen, two forms are the most known: storage of gas under high pressure and storage of hydrogen in liquid form at low-temperature. Each of these methods has disadvantages

* *Corresponding author.*
** *Corresponding author.*
E-mail addresses: hind.benzidi@gmail.com (H. Benzidi), o.mounkachi@gmail.com (O. Mounkachi).
https://doi.org/10.1016/j.ijhydene.2019.04.241
0360-3199/

Please cite this article as: Benzidi H et al., Improved thermodynamic properties of doped $LiBH_4$ for hydrogen storage: First-principal calculation, International Journal of Hydrogen Energy, https://doi.org/10.1016/j.ijhydene.2019.04.241

which hinder their use, such as the safety problem that occurs when using high pressures (compression storage) and the energy cost necessary to cool the hydrogen (cryogenic storage). In recent decades, a new method of storing hydrogen in solid materials has emerged, enabling hydrogen atoms to be absorbed and stored in metallic matrixes such as metal hydrides, complex hydrides, intermetallic, Organic compounds and porous materials (activated carbons, carbon nanotubes and nanofibers and zeolites) [8–17].

The hydrogen-storage in complex and intermetallic hydrides are attracting considerable interest due to their high gravimetric capacities. However, the release of hydrogen in these materials requires a high temperature due to the chemical bonding of hydrogen in the interstitial sites of the host material for intermetallic compounds or covalent and ionic into the crystal structure of complex hydride. The magnesium hydride (MgH_2) one of the most studied intermetallic hydride. It presents 7.66% wt of H_2. It should be mentioned that dual-tuning effects of the thermodynamics and kinetics is one of the keys for hydrogen economy and hydrogen-storage materials issues. Thus, can be partially achieved by doping [18–21] or by reducing the particle size using a ball milling process [22–26].

The complex hydrides $LiBH_4$ has the highest capacities (18.3%wt of H_2) among other solid storing materials, the structure of lithium borohydride is a combination of the stable hydride LiH and a relatively unstable boron hydride which forms the complex hydride. Where, the hydrogenated complexes $[BH_4]^-$ ionically bind to the alkali-metal Li, this complex nature (ionic and covalent binding) of lithium borohydride is the reason for its complicated decomposition. Therefore, the release of hydrogen involves a several steps process under pressures of the order of 10 MPa and a very high desorption temperature [27–29].

$LiBH_4 \rightarrow LiH + B + 3/2H_2$ Reaction 1

$LiBH_4 \rightarrow Li + B + 2H_2$ Reaction 2

To avoid these difficulties, different techniques are adopted including, doping additives (metal halide [30], oxides [31], amides [32,33], reactive hydride composites [34,35], Nanoporous [36,37] are mixtures, by ball mill. For realizing a storage system of hydrogen several objectives are targeted: (i) increasing storage mass capacities, (ii) improving reversibility, (iii) carrying out cycling, (iv) improving kinetics of reaction, (vi) stabilizing the systems.

For that, various studies have been done to minimize the temperature desorption of $LiBH_4$, for example, Gennari et al. examined the composite mixtures of $6LiBH_4$ and RECl with RE = Ce, Gd and observed an amelioration in the decomposition temperature of $LiBH_4$ [38] Other researchers have worked on a mixture of $LiBH_4$ by Re=Er may decrease the decomposition temperature of about 373 K [39,40]. Widely of experimental work based on the enhance the sorption properties of $LiBH_4$ by nanoconfinement in porous materials [12,36,41–50]. Inside Nanoporous carbon or Nanoporous silica, faster dehydrogenation kinetics is reported for $LiBH_4$, accompanied by a decrease of the de-hydrogenation temperature by at least 100 °C [49]. It is relatively difficult to remove hydrogen from the surface of bulk crystals than from the surface of the clusters and nanowhiskers. This result is reported by Vajeeston P. et al. [51]. Since a chemical interaction between the products and an intermediate compound of the $LiBH_4$ reaction steps gives an improvement of the hydrogenation effect of the nanoconfined $LiBH_4$ [52]. AU et al. [53] recorded that metal halides $TiCl_3$, TiF_3, and ZnF_2 strongly ameliorate the desorption temperature via cation exchange interaction, a part of the halide doped $LiBH_4$. FANG et al. [54] remarked that TiF_3 indicate the predominant effect of $TiCl_3$ on the reversible de-hydrogenation of $LiBH_4$. In addition, metal oxides have been reported to be an effective method to reduce the hydrogen-storage performance of $LiBH_4$. In 2008, Yu et al. studied the effect of TiO_2 on $LiBH_4$ finding a clear influence on the thermodynamic properties of $LiBH_4$ especially the temperature, which decreases from 220 °C to 150 °C, due to the transfer of charge between B and Ti [55]. And also, Zuttel et al. noticed that TiO_2 have a decorative role in destabilizing LiBH4 with desorption of 9 %wt $LiBH_4$ [27]. The same effect is achieved with other oxidation, but with different variations or the stabilization changes as follows: $F_2O_3 > V_2O_5 > Nb_2O_5 > TiO_2 > SiO_2$ [56]. According to the study by Han et al. [57], the de-hydrogenation temperature was reduced to 230 °C, after grinding with MoS_2, which decreased by 80 °C relative to pure $LiBH_4$.

$LiBH_4$ is well known by the strong ionic bond between Li^+ cation and anion (BH_4^-). The removal of the charge transfer between the anion and the cation could considerably weaken the interactions of the ionic bonds in the complex BH_4, thus making the hydrogen more labile [58]. The B–H bond between H and B is easy to dissociate. To disrupt the B–H bond many efforts have been reported:

- Orimo et al. have proposed the substitution of the Li^+ cations by more electronegative elements, such as Mg, or Cu, Nb [59–61] and Al [62–64] is an effective mean of lowering the de-hydrogenation temperature of $LiBH_4$.
- Another decisive strategy is the anion substitution, which can stabilize the too unstable borohydrides or destabilize the too stable borohydrides [65,66]. It is reported that a significant improvement in the anion of $LiBH_4$ is an important result of the substitution of BH_4^- with Cl^-, F^-, Br^- and I^- anions in $LiBH_4$ [63,66–74].

By first-principles calculation methods, Gong XJ et. Al [66] proved that the migration barrier energy declines from 4.03 eV to 3.09 eV by calculating the diffusion pathway of H atom from one [BH_4] to the nearby [BH_4] on the clean and Mg-doped $LiBH_4$ (010) surfaces, respectively. This result shows that the H atoms easily diffuse on the Mg-doped $LiBH_4$ (010) surface rather than on the pure surface. In addition, the calculated average hydrogen desorption energies of Nb-doped LiBH4 (010) surface are found to be smaller than the pure $LiBH_4$ (010) [66]. All of this proves that enhancing the desorption properties of $LiBH_4$ can be effectively achieved through the doping strategy. However, even with the aid of these technologies, the dehydriding/rehydrating properties of $LiBH_4$ are still far below those required for practical application. This necessitates the development of a new method/technology to assess the potential of $LiBH_4$ for the hydrogen-storage application. From our previous work [75], the high stability of the

Please cite this article as: Benzidi H et al., Improved thermodynamic properties of doped $LiBH_4$ for hydrogen storage: First-principal calculation, International Journal of Hydrogen Energy, https://doi.org/10.1016/j.ijhydene.2019.04.241

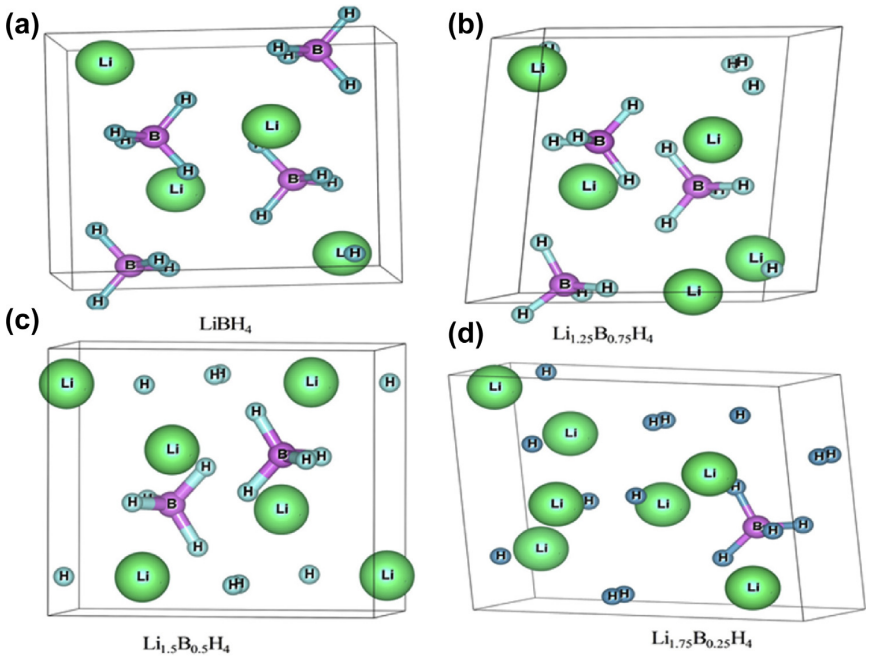

Fig. 1 – Crystal structures of (a) pure, (b) $Li_{1.25}B_{0.75}H_4$ (c) $Li_{1.5}B_{0.5}H_4$ (d) $Li_{1.75}B_{0.25}H_4$. Green, pink and blue balls represent respectively Li, B and H atoms. (For interpretation of the references to colour in this figure legend, the reader is referred to the Web version of this article)

system $LiBH_4$ is mainly due to the high hybridization between B and H atoms. For this reason, it was thought to have substituted the B by the light elements such as Lithium to reduce this hybridization and consequently reduce the energy of formation of the system.

In this study, we present a novel substitution approach to tune the problematic thermodynamic of $LiBH_4$. According to the first-principles calculation results, were used to investigate the effect of the substitution of boron by lithium inside $LiBH_4$ lattice. In addition, the vibrational and thermodynamic properties were investigated to explore the possibility of lowering the hydrogen desorption temperature and reversibility of substituted lithium borohydride structure.

Models and computational details

To study the decomposition reaction of doped $LiBH_4$, the cell of $Li_{1+x}B_{1-x}H_4$ (x = 0, 0.25, 0.5, 0.75) (see Fig. 1) was used to model the substitution of Li at B site in $LiBH_4$ bulk. The present calculations have been performed using the first-principles calculations based on a density-functional theory approach [76] the exchange and correlation energy corrections included through a generalized gradient approximation (PBE-GGA) [77], with plane wave pseudopotential method (PWSCF); as implemented in the Quantum Espresso code [78]. All pseudopotentials are constructed using the ultrasoft pseudopotential method [79], with a cutoff kinetic energy of 680 eV and the k-point grids for the Brillouin zone integration are sited to be 6 × 8 × 6, these values give good convergence of the total energy within 1 meV/atom. The atomic positions and the cell parameters, including the cell volume, are fully optimized by minimizing the Hellmann-Feynman forces and stresses without any symmetry constraint. All structures are considered to be fully relaxed when the Hellmann-Feynman forces on the atoms are smaller than 0.01 eV/Å.

The vibrational density of states (VDOS) was calculated using the software PHONOPY [80]. The phonon Eigenmodes are obtained by solving the eigenvalue problem for the

Table 1 – Lattice parameter, volume, formation enthalpy, gravimetric and volumetric capacity of $Li_{1+x}B_{1-x}H_4$ (x = 0, 0.25, 0.5, 0.75).

System	Parameters (Å)			Volume	Formation enthalpy (kJ/mol)	Gravimetric capacity (wt%)	Volumetric capacity (g H_2/l)
	a	b	c				
$LiBH_4$	7,05	4,33	6,74	205,75	−192.12	18,5	146,37
$Li_{1.25}B_{0.75}H_4$	6,50	4,32	7,18	200.88	−174.44	18,88	132,3
$Li_{1.5}B_{0.5}H_4$	7,54	4,03	6,67	203.1	−141.87	19,36	130,86
$Li_{1.75}B_{0.25}H_4$	7,93	3,93	6.65	206.59	−119.95	20,31	128,65

Please cite this article as: Benzidi H et al., Improved thermodynamic properties of doped $LiBH_4$ for hydrogen storage: First-principal calculation, International Journal of Hydrogen Energy, https://doi.org/10.1016/j.ijhydene.2019.04.241

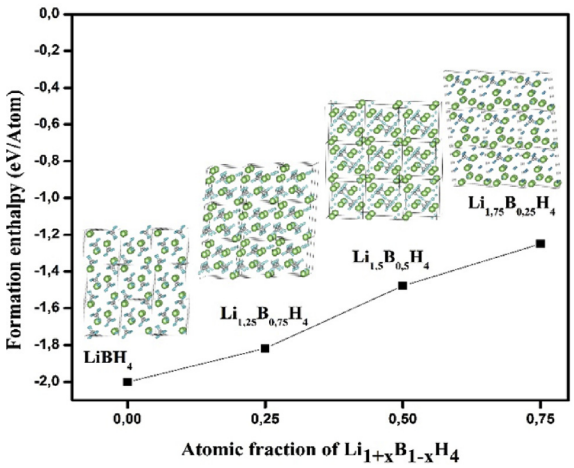

Fig. 2 – Formation enthalpies from the calculated static density-functional theory as function of atomic fraction of Li in $Li_{1+x}B_{1-x}H_4$.

dynamical matrix which is calculated by the force-constant using a finite displacement method based on the Parlinski-Li-Kawazoe method. The atomic displacement is set to be 0.02 Å. Several research groups have synthesized and characterized LiBH4, the reported X-ray diffraction data show that at the ambient condition the LiBH4 crystallizes in orthorhombic space group *Pnma* (62), and lattice parameters are a = 7.178 Å, b = 4.436 Å, and c = 6.803 Å [81]. At the first step, the experimental crystal structure was fully relaxed without any symmetry constraint of LiBH4 unit cell. Once the phonon spectrum is obtained, we can easily compute the temperature dependence of the vibrational specific, heat capacity Cv and the entropy S at constant-volume, as described below.

For calculations of lattice properties, the Helmholtz free energy is given by the equation below:

$$F = E + H_{vib} + TS_{vib} \quad (1)$$

Where E, H_{vib}, and S_{vib} are the internal energy of the crystal, harmonic phonon energy and entropy contributing to the lattice vibration.

The harmonic phonon energy is given by the equation below:

$$H_{vib}(T) = \sum_i \frac{1}{2}\hbar\omega_i + \hbar\omega_i\left[\exp\left(\frac{\hbar\omega_i}{K_\beta T}\right) - 1\right]^{-1} \quad (2)$$

Table 2 – Desorption enthalpy and temperature of $Li_{1+x}B_{1-x}H_4$ (x = 0, 0.25, 0.5, 0.75).

System	First reaction $LiBH_4 \rightarrow LiH + B + 3/2H_2$		Second reaction $LiBH_4 \rightarrow Li + B + 2H_2$	
	E_{des} (kJ/mol)	T_{des}(K)	E_{des} (kJ/mol)	T_{des}(K)
$LiBH_4$	75.75	658.75	96.06	835.31
$Li_{1.25}B_{0.75}H_4$	62.38	542.49	87.22	758.44
$Li_{1.5}B_{0.5}H_4$	61.46	534.48	70.93	616.81
$Li_{1.75}B_{0.25}H_4$	46.854	407.42	59.97	521.52

The entropy S and the heat capacity C_v at constant volume are given by the equations below:

$$S_{vib}(T) = k_\beta \sum_i \frac{\frac{\hbar\omega_i}{K_\beta T}}{\exp\left(\frac{\hbar\omega_i}{k_\beta T}\right) - 1} - \ln\left[1 - \exp\left(-\frac{\hbar\omega_i}{k_\beta T}\right)\right] \quad (3)$$

$$C_v = \left(\frac{\partial E}{\partial T}\right)_v = \sum_i k_\beta \left(\frac{\hbar\omega_i}{k_\beta T}\right)^2 \frac{\exp\left(\frac{\hbar\omega_i}{k_\beta T}\right)}{\left[\exp\left(\frac{\hbar\omega_i}{k_\beta T}\right) - 1\right]^2} \quad (4)$$

where ω is the phonon frequency and T is the temperature. k_B and $\hbar$ are the Boltzmann constant and the reduced Planck constant, respectively.

Results and discussion

Structural properties and formation enthalpies

In order to investigate the substitution of boron by lithium, the geometries of $Li_{1+x}B_{1-x}H_4$ (with x = 0.25, 0.5, 0.75) were fully relaxed. This substitution breaks the symmetry of $LiBH_4$ because of the different atomic radii of Li (1.52 Å), B (0.85 Å), which causes different lattice parameters and cell volumes for pure $LiBH_4$ and $LiBH_4$ substituted. Consequently, create changes on the periodicity of the crystal. As shown in Fig. 1. The relaxed lattice parameters and volume of all the systems are listed in Table 1. The possibility of the structure of $LiBH_4$ substituted by Li was evaluated by calculating the formation enthalpy of $LiBH_4$ and the related $Li_{1+x}B_{1-x}H_4$ (with x = 0.25, 0.5, 0.75). The formation enthalpies are calculated based on the equation:

$$Li_{1+x}B_{1-x}H_4 \rightarrow (1+x)Li + (1-x)B + 2H_2 \ (x = 0,\ 0.25,\ 0.5,\ 0.75)$$

Reaction 3

The formation enthalpy for each structure is determined with respect to the most stable structure of the pure elements. The calculated enthalpies are presented in Fig. 2, and reported in (kJ/mol) unit in Table 2. In all cases, the substitution of B by Li in the $LiBH_4$ lattice is an exothermic process. By virtue of,

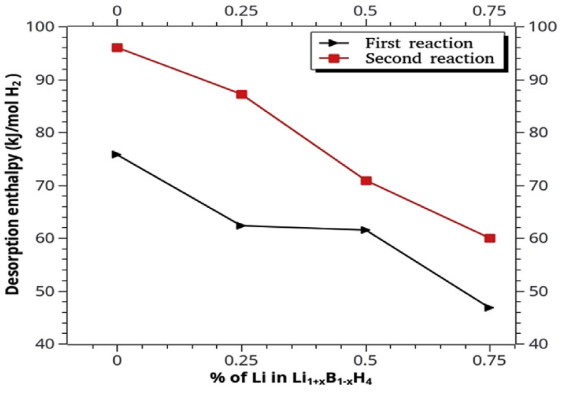

Fig. 3 – Desorption enthalpy and temperature as function of Li-substitution rate of $Li_{1+x}B_{1-x}H_4$ (x = 0, 0.25, 0.5, 0.75).

Please cite this article as: Benzidi H et al., Improved thermodynamic properties of doped $LiBH_4$ for hydrogen storage: First-principal calculation, International Journal of Hydrogen Energy, https://doi.org/10.1016/j.ijhydene.2019.04.241

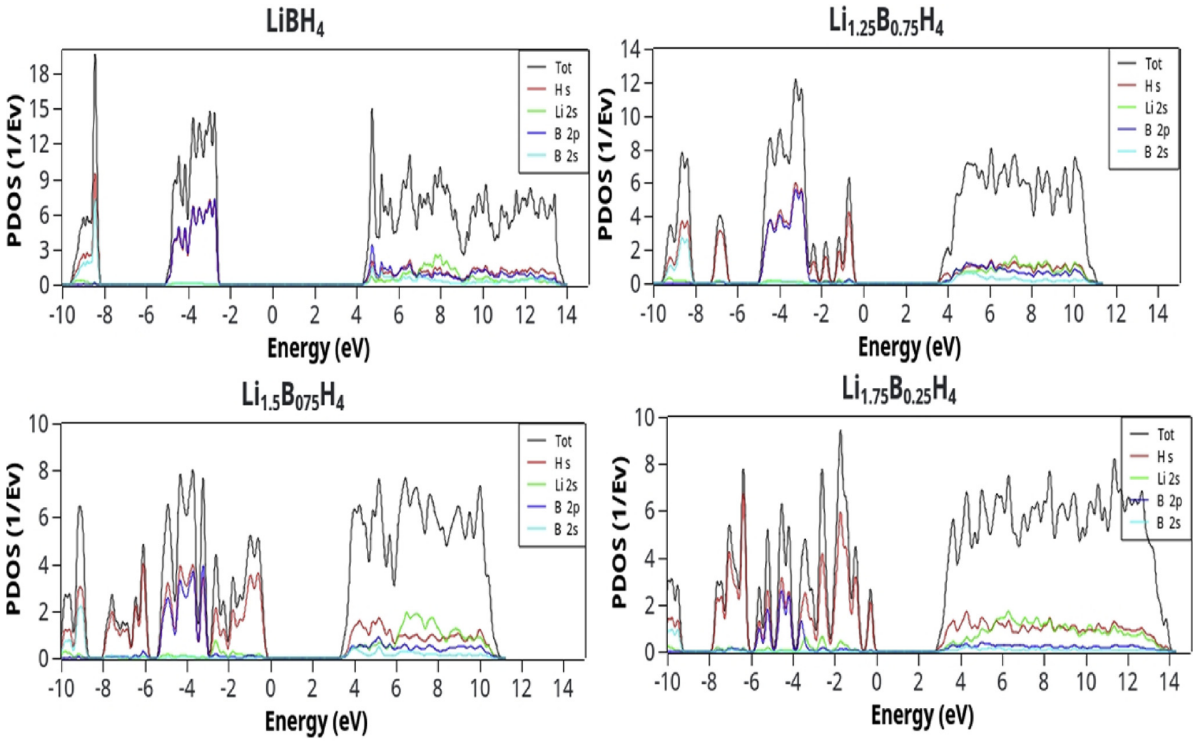

Fig. 4 – The calculated Total and partial DOS of $Li_{1+x}B_{1-x}H_4$ (x = 0, 0.25, 0.5, 0.75).

negative heats of formation, the complex hydride is thermodynamically stable with respect to the complete decomposition into its basic constituents (B, Li, and H_2).

De-hydrogenation properties

To further investigate the effects of the substitution on the de-hydrogenation behavior of $LiBH_4$. The desorption enthalpy E_{des}, which is the most important thermodynamic parameter, has been calculated and used to predict de-hydrogenation proprieties. As seen in Table 2. For pure $LiBH_4$, the computed desorption enthalpies for the first reaction (partial decomposition) is 75.7 kJ/mol H_2, which agrees well with the reported DFT calculation results [71,82,83]. Considering reversible hydrogen-storage as finding systems for which $30 \leq \Delta H \leq 60$ kJ/mol H_2 and that yield significant gravimetric quantities of H_2. In view of, the de-hydrogenation enthalpy ΔH is significantly less than 30 kJ/mol H_2, the material will not be easily reversible. However, for an ideal material for hydrogen-storage, the heat of formation ΔH should be around 40 kJ/mol (H_2) [84].

The temperature of de-hydrogenation can be reliably estimated by $\Delta H = T\Delta S$, where ΔH and ΔS are the enthalpy and entropy change of the de-hydrogenation reaction. The entropy changes estimate that $95 \leq \Delta S \leq 140$ JK-1 mol^{-1}. For almost all the intermetallic hydride the variation entropy reaction is $\Delta S = 130\,JK{-}1\ mol^{-1}$. H_2 corresponding to the change entropy of hydrogen gas to solid hydrogen. The stability of the hydride can be described and compared with the enthalpy of reaction only. For complex hydrides, the situation is a bit more complicated and entropy of the reaction appears to be lower and variable for different complex hydrides. Based on the theoretical calculation, it has estimated the value of ΔS about 115 J/K. mol H_2 [85]. The predicted decomposition temperature is 658.75 K for the first reaction (see Fig. 3) . This temperature is still too high for practical applications. According to the calculated desorption enthalpies listed in Table 2, The modified crystal structures after Li doping for the first equation is nearly reduced to 62.38, 61.46 and 46.85 kJ/mol H_2 with increasing the substitution level from x = 0.25 to 0.75.

Likewise, the de-hydrogenation temperature is reduced by 150 K of with about 20.31 wt% of hydrogen released at about 407.42 for $Li_{1.75}B_{0.25}H_4$. Therefore, the decomposition reaction following Eq. (1) is thermodynamically favorable than the process following Eq. (2). From a thermodynamic point of view. Generally, the stabilities of the reaction products are dramatically reduced with increasing the percentage of Li, our calculations show that substitution of B by Li in $LiBH_4$ structure result in a favorable modification of the thermodynamics that essentially constraints the potential of $LiBH_4$ for hydrogen-storage application.

Electronic structure

To understand and explain the improved performance of de-hydrogenation process during application of substitution

Please cite this article as: Benzidi H et al., Improved thermodynamic properties of doped $LiBH_4$ for hydrogen storage: First-principal calculation, International Journal of Hydrogen Energy, https://doi.org/10.1016/j.ijhydene.2019.04.241

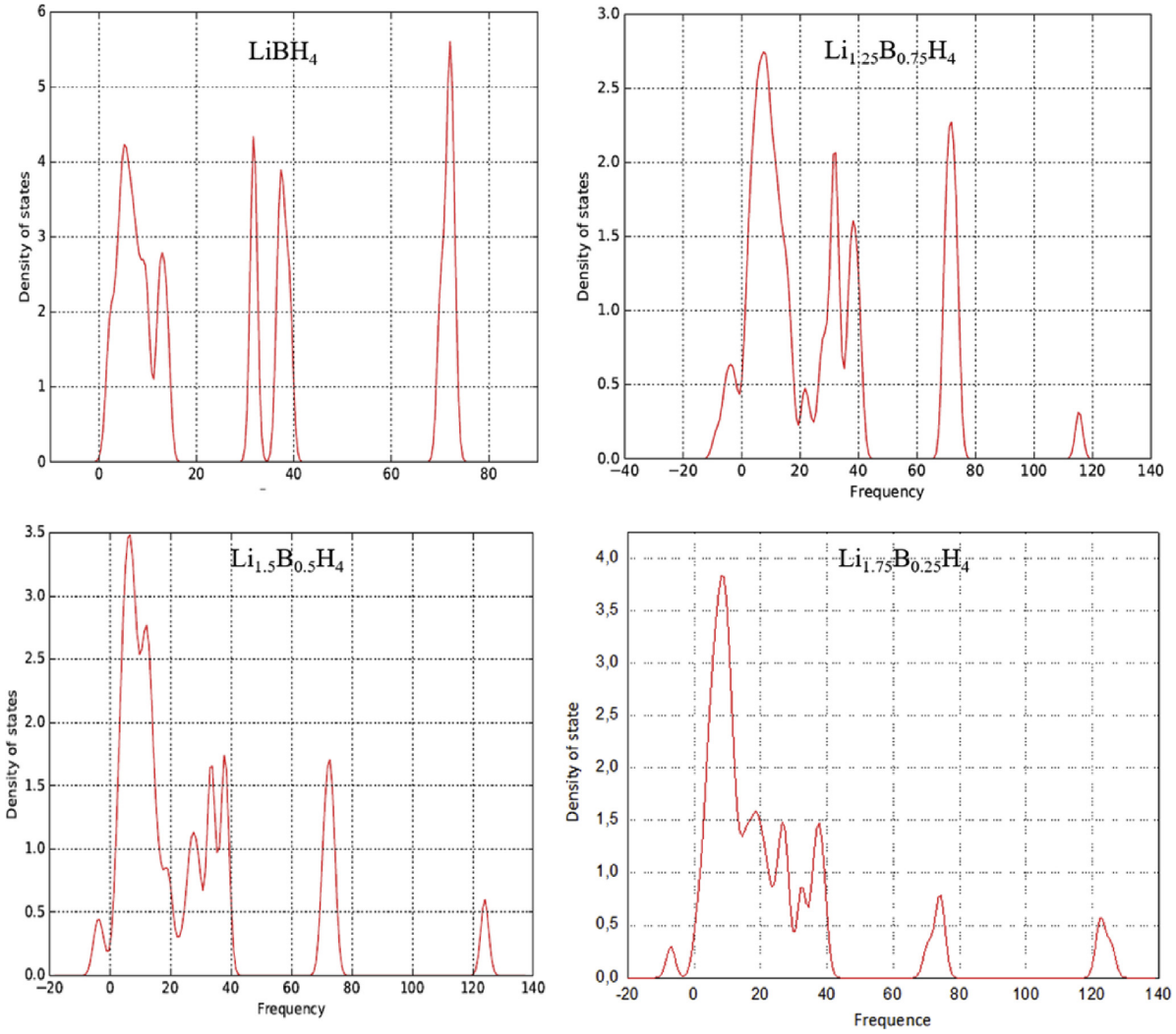

Fig. 5 – Phonon density of states of $Li_{1+x}B_{1-x}H_4$ (x = 0, 0.25, 0.5, 0.75).

with lithium, the density of states of pure and modified of $LiBH_4$ structure. This study will clarify the effect of the substitution with Lithium on the hydrogenation performance of this system.

Fig. 4 presents the total and partial densities of states for $Li_{1+x}B_{1-x}H_4$ with x varied from 0 to 0.75. In these figures, the Fermi level (E_F) is set to zero and used as a reference. The total density of state of pure shows an insulator behavior with the calculated energy gap of 6.79 eV. The gap energy value is a good agreement with the experimental and theoretical values [75,86–88]. The Valence band split into two regions: The region I (low-energy states) which composed of B-2s and H-1s orbitals and the region II (high-energy states) consist of B-2p and H-1s orbitals, which show a high hybridization. Boron atoms form covalent bonds with surrounding four H atoms. Because there is a little contribution of Li orbitals to the occupied states, Li atoms are thought to be ionized as Li^+ cations. As expected, after the substitution of boron by Li, the strong hybridization between BH begins to weaken by increasing the rate of substitution, and other states of individual hydrogen begin to appear, it can be explained that the covalent band between B and H has broken and other binding begins to appear to form hydrogen molecules in interstitial sites. This translates the release of the desorption enthalpy by adding the percentage of Li in the $LiBH_4$ structure. We should note also that the energy band gap decreases with increasing the percent of Li inside the $LiBH_4$ framework.

Lattice dynamic stability

To further study the lattice stability of $Li_{1+x}B_{1-x}H_4$ (x = 0, 0.25, 0.5, 0.75) compounds first-principles phonon calculations are carried out.

Please cite this article as: Benzidi H et al., Improved thermodynamic properties of doped $LiBH_4$ for hydrogen storage: First-principal calculation, International Journal of Hydrogen Energy, https://doi.org/10.1016/j.ijhydene.2019.04.241

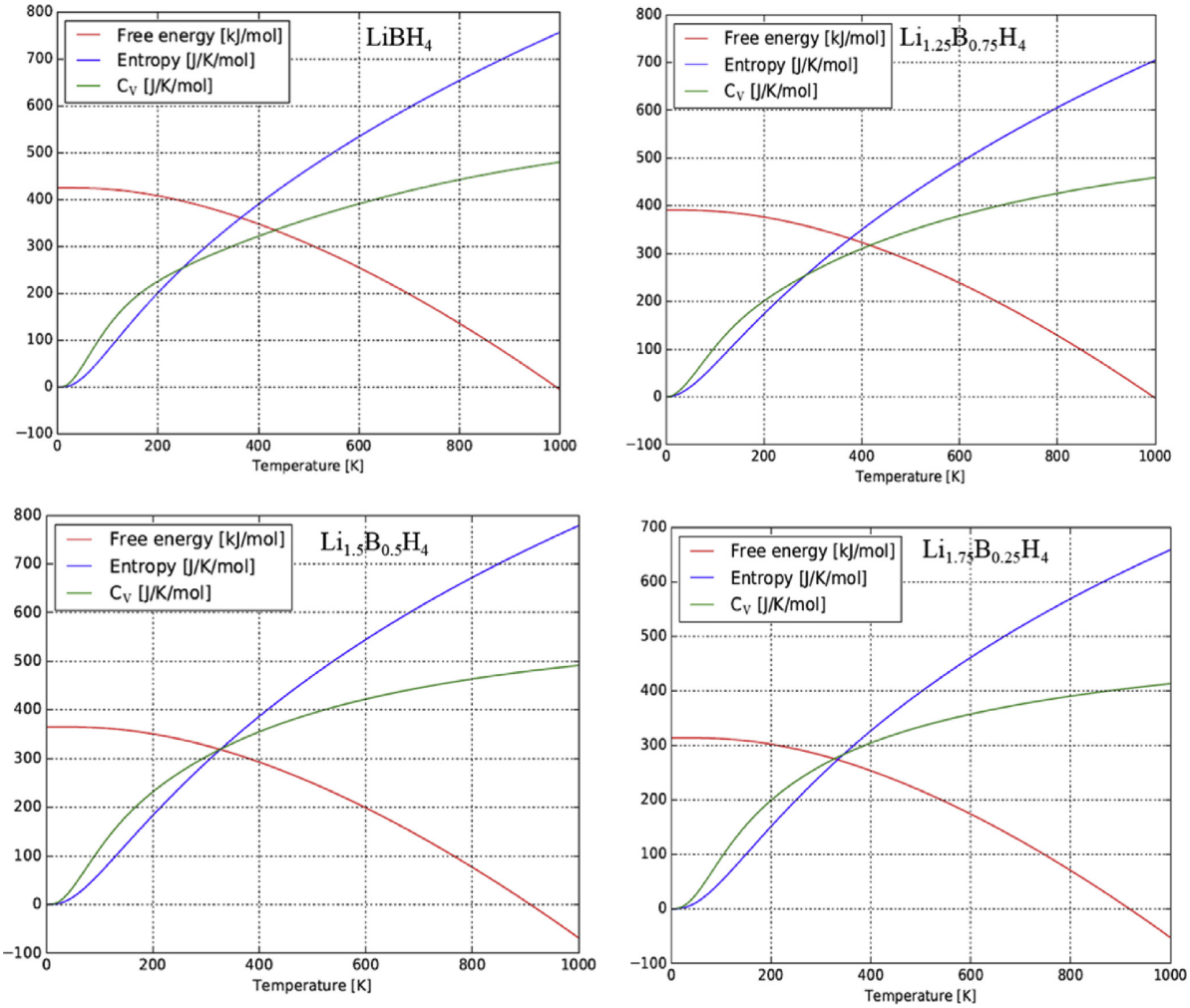

Fig. 6 – Temperature Helmholtz free energy F (V, T), vibrational entropy S, and heat capacity C_v of $Li_{1+x}B_{1-x}H_4$ (x = 0, 0.25, 0.5, 0.75).

According to harmonic approximation, this is possible when all the phonons have real and positive frequencies. Negative or imaginary frequencies of phonons indicate that crystal is dynamically unstable [80]. In our present study, from Fig. 5(a) any negative frequencies are not observed for the pure $LiBH_4$ compound. This means the compound is mechanically stable [89]. The phonon density of state shows three branches of optical phonons separated from the phonon branches of lower frequencies. The reason for the separation of these branches is from the lower mass H present in the compound. The peak in the lower energy region corresponds to the acoustic branches in the dispersion plot. The next separated higher energy peaks represent the coupled optical phonon branches. In the case of the modified $LiBH_4$ structure Fig. 5(b, c, d) a small phonon branches in the negative frequency range of −15 THz (negative frequencies are representative of imaginary frequencies. The vibration of the hydrogen is more independent than that of the complex bond of BH_4. Which explains the reduction of desorption enthalpies for modified $LiBH_4$ lattice. We believe applying external pressure can eliminate these imaginary phonons.

Lattice thermodynamic properties

Thermal properties such as Helmholtz free energy, entropy and constant-volume specific heat (C_V) as a function of temperature are computed using phonopy. It can be seen from Fig. 6 that the lattice heat capacity increases slowly with the temperature in the initial stage. The lattice heat capacity approaches almost linear when the temperature exceeds 400 K. Besides, with the increasing of Li-substitution concentration, the lattice heat capacities of the modified systems have small increases. Although Li-substitution has slight effects on the lattice heat capacity of $LiBH_4$, and the current framework can be useful to characterize complicated crystal structures of complex hydrides materials. Finally, the present framework is

Please cite this article as: Benzidi H et al., Improved thermodynamic properties of doped $LiBH_4$ for hydrogen storage: First-principal calculation, International Journal of Hydrogen Energy, https://doi.org/10.1016/j.ijhydene.2019.04.241

beneficial to optimize the material composition or to design a new modified crystal of $LiBH_4$, which could be applicable as solid-state hydrogen-storage materials.

Conclusions

To sum up, this study points towards the idea of the substitution of boron by lithium atom in the lithium borohydride $Li_{1+x}B_{1-x}H_4$ (x = 0, 0.25, 0.5, 0.75) framework. Firstly, the possibility of the fabrication of these systems was confirmed by the negative value of formation enthalpies and the weak soft modes in phonon dispersion of all the systems. Furthermore, the de-hydrogenation temperature is reduced to 521.52 K for fully released hydrogen for $Li_{1.75}B_{0.25}H_4$ system. The significantly enhanced hydrogen-storage properties of the $Li_{1+x}B_{1-x}H_4$ (x = 0, 0.25, 0.5, 0.75) systems are attributed to the decrease of the boron atoms in the lithium borohydride framework, which lead to a weaker hybridization between Boron and Hydrogen atoms, and subsequently high gravimetric capacities. Our theoretical calculations provide a novel approach for effectively tuning thermodynamics of $LiBH_4$, a leading candidate for high-capacity hydrogen-storage. Experimentally evidencing these theoretical predictions may pave a new way to pursue improved hydrogen-storage properties of $LiBH_4$ and other related complex hydrides.

REFERENCES

[1] de Valladares M-R. Mary-Rose de Valladares GMIHTCP (TCP). Global trends and outlook for hydrogen, ISBN 978-1-945951-07-7.
[2] Sprake D, Vagapov Y, Lupin S, Anuchin A. Housing estate energy storage feasibility for a 2050 scenario. In: Internet Technol Appl ITA 2017 – Proc 7th Int Conf 2017; 2017. p. 137–42. https://doi.org/10.1109/ITECHA.2017.8101925.
[3] Sørensen B, Spazzafumo G, Sørensen B, Spazzafumo G. Hydrogen. Hydrog Fuel Cells 2018:5–105. https://doi.org/10.1016/B978-0-08-100708-2.00002-3.
[4] Züttel A, Remhof A, Borgschulte A, Friedrichs O. Hydrogen: the future energy carrier. Philos Trans R Soc A Math Phys Eng Sci 2010;368:3329–42. https://doi.org/10.1098/rsta.2010.0113.
[5] IEA. Global energy & CO2 statuts report. ©OECD/IEA; 2017.
[6] Schlapbach L, Züttel A. Hydrogen-storage materials for mobile applications. Nature 2001;414:353–8. https://doi.org/10.1038/35104634.
[7] Dagdougui H, Sacile R, Bersani C, Ouammi A, Dagdougui H, Sacile R, et al. Hydrogen storage and distribution: implementation scenarios. Hydrog Infrastruct Energy Appl 2018:37–52. https://doi.org/10.1016/B978-0-12-812036-1.00004-4.
[8] Schlapbach L, Züttel A. Hydrogen-storage materials for mobile applications. Nature 2001;414:353–8. https://doi.org/10.1038/35104634. Co-Published with Macmillan Publishers Ltd, UK.
[9] Liu Y, Pan H. Hydrogen storage materials. New futur Dev Catal 2013:377–405. https://doi.org/10.1016/B978-0-444-53880-2.00018-1. Elsevier.
[10] Bellosta von Colbe J, Ares J-R, Barale J, Baricco M, Buckley C, Capurso G, et al. Application of hydrides in hydrogen storage and compression: achievements, outlook and perspectives. Int J Hydrogen Energy 2019:1–29. https://doi.org/10.1016/j.ijhydene.2019.01.104.
[11] Zhang L, Zheng J, Xiao X, Wang X, Huang X, Liu M, et al. A new strategy to remarkably improve the low-temperature reversible hydrogen desorption performances of LiBH4 by compositing with fluorographene. Int J Hydrogen Energy 2017;42:20046–55. https://doi.org/10.1016/J.IJHYDENE.2017.05.060.
[12] Gross Adam F, Vajo * John J, Van Atta Sky L, Olson GL. Enhanced hydrogen storage kinetics of LiBH4 in nanoporous carbon scaffolds. 2008. https://doi.org/10.1021/JP711066T.
[13] Hartman MR, Rush JJ, Udovic TJ, Bowman RC, Hwang SJ. Structure and vibrational dynamics of isotopically labeled lithium borohydride using neutron diffraction and spectroscopy. J Solid State Chem 2007;180:1298–305. https://doi.org/10.1016/j.jssc.2007.01.031.
[14] Shao J, Xiao X, Fan X, Zhang L, Li S, Ge H, et al. Low-temperature reversible hydrogen storage properties of LiBH $_4$: a synergetic effect of nanoconfinement and nanocatalysis. J Phys Chem C 2014;118:11252–60. https://doi.org/10.1021/jp503127m.
[15] Shao J, Xiao X, Fan X, Huang X, Zhai B, Li S, et al. Enhanced hydrogen storage capacity and reversibility of LiBH4 nanoconfined in the densified zeolite-templated carbon with high mechanical stability. Nanomater Energy 2015;15:244–55. https://doi.org/10.1016/J.NANOEN.2015.04.023.
[16] Suib SL, Liu Y, Pan H. Hydrogen storage materials. New Futur. Dev. Catal.; 2013. p. 377–405. https://doi.org/10.1016/B978-0-444-53880-2.00018-1. Chapter 13.
[17] Chen P. Hydrogen storage: liquid and chemical. Compr Renew Energy 2012:157–77. https://doi.org/10.1016/B978-0-08-087872-0.00414-5.
[18] Abdellaoui M, Lakhal M, Benzidi H, Mounkachi O, Benyoussef A, El Kenz A, et al. The hydrogen storage properties of Mg-intermetallic-hydrides by ab initio calculations and kinetic Monte Carlo simulations. Int J Hydrogen Energy 2018. https://doi.org/10.1016/J.IJHYDENE.2018.04.225.
[19] Abdellaoui M, Lakhal M, Bhihi M, El Khatabi M, Benyoussef A, El Kenz A, et al. First principle study of hydrogen storage in doubly substituted Mg based hydrides Mg5MH12 (M = B, Li) and Mg4BLiH12. Int J Hydrogen Energy 2016;41:20908–13. https://doi.org/10.1016/J.IJHYDENE.2016.04.122.
[20] Lakhal M, Bhihi M, Labrim H, Benyoussef A, Naji S, Belhaj A, et al. Kinetic Monte Carlo and density functional study of hydrogen diffusion in magnesium hydride MgH2. Int J Hydrogen Energy 2013;38:8350–6. https://doi.org/10.1016/J.IJHYDENE.2013.04.157.
[21] Lakhal M, Bhihi M, Benyoussef A, El Kenz A, Loulidi M, Naji S. The hydrogen ab/desorption kinetic properties of doped magnesium hydride MgH2 systems by first principles calculations and kinetic Monte Carlo simulations. Int J Hydrogen Energy 2015;40:6137–44. https://doi.org/10.1016/J.IJHYDENE.2015.02.137.
[22] Ouyang L, Cao Z, Wang H, Hu R, Zhu M. Application of dielectric barrier discharge plasma-assisted milling in energy storage materials – a review. J Alloy Comp 2017;691:422–35. https://doi.org/10.1016/J.JALLCOM.2016.08.179.
[23] Ouyang LZ, Cao ZJ, Wang H, Liu JW, Sun DL, Zhang QA, et al. Enhanced dehydriding thermodynamics and kinetics in Mg(In)–MgF2 composite directly synthesized by plasma milling. J Alloy Comp 2014;586:113–7. https://doi.org/10.1016/J.JALLCOM.2013.10.029.
[24] Ouyang LZ, Cao ZJ, Wang H, Liu JW, Sun DL, Zhang QA, et al. Dual-tuning effect of in on the thermodynamic and kinetic

Please cite this article as: Benzidi H et al., Improved thermodynamic properties of doped $LiBH_4$ for hydrogen storage: First-principal calculation, International Journal of Hydrogen Energy, https://doi.org/10.1016/j.ijhydene.2019.04.241

ARTICLE IN PRESS

INTERNATIONAL JOURNAL OF HYDROGEN ENERGY XXX (2018) 1–7

Available online at www.sciencedirect.com

ScienceDirect

journal homepage: www.elsevier.com/locate/he

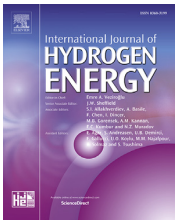

Vibrational and thermodynamic properties of $LiBH_4$ polymorphs from first-principles calculations

H. Benzidi [a], *M. Garara* [a], *M. Lakhal* [a], *M. Abdalaoui* [a], *A. Benyoussef* [b], *A. El kenz* [a], *M. Louilidi* [a], *M. Hamedoun* [b], *O. Mounkachi* [a,b,*]

[a] *Laboratoire de Matière Condensée et Sciences Interdisciplinaires (LaMCScI), B.P. 1014, Faculty of Science, Mohammed V University, Rabat, Morocco*

[b] *Materials and Nanomaterials Centre, Moroccan Foundation for Advanced Science, Innovation and Research, MAScIR, Rabat, Morocco*

ARTICLE INFO

Article history:
Received 17 July 2017
Received in revised form
6 February 2018
Accepted 7 February 2018
Available online xxx

Keywords:
First principles calculations
Hydrogen storage
$LiBH_4$
Enthalpy
Hydride
Phonon

ABSTRACT

The study of phonons describes the thermodynamic properties behavior of compounds with small atoms because phonons have an important influence on its properties. Lithium borohydride, $LiBH_4$, is one of the suitable materials for hydrogen storage solid state. Although the transformations of Lithium borohydride $LiBH_4$ were repeatedly studied by experiments and fundamental side, these transformations are still under discussion. In the present work, the mode vibrational analysis of orthorhombic and hexagonal $LiBH_4$ structures were considered with ab initio lattice-dynamics based on the quasi-harmonic approximation approach as implemented in Phonopy code. The results show that the orthorhombic structure is thermodynamically stable, while the hexagonal structure is unstable owing to the presence of negative mode frequency. The thermal expansion behavior and various thermodynamic properties stability like heat capacity, entropy and Helmholtz energy were also studied and the obtained results are in good agreement with experiments. This shows a deep connection between stability and strength and helps researchers to estimate accurately the thermodynamic performance of $LiBH_4$ materials.

Introduction

Lithium borohydride is known as a considerable potential candidate for solid hydrogen storage state, owing to its competence to store 18 wt% of hydrogen, which is substantially larger than the DOE roadmap value for 2015 [1]. Nevertheless, the phase transition mechanisms of $LiBH_4$ have not fully understood. Consequently, it is important to explain in detail the thermodynamic properties behavior of $LiBH_4$ according to temperature. Therefore, basic research studied the crystal structure of $LiBH_4$ at several temperatures and pressures and the complex phase transition scheme was analyzed [2,3]. At ambient conditions, lithium borohydride crystallized in the orthorhombic structure (Pnma, 62) and go through a first-order phase transition on heating at 381 K to a hexagonal high-temperature phase ($P6_3mc$, 186). At ambient temperature, a phase transition into a high-pressure phase (Ama2) is observed around 0.6 GPa and a second transition at

* *Corresponding author*. Laboratoire de Matière Condensée et Sciences Interdisciplinaires (LaMCScI), B.P. 1014, Faculty of Science, Mohammed V University, Rabat, Morocco.
E-mail addresses: o.mounkachi@mascir.com, o.mounkachi@gmail.com (O. Mounkachi).

https://doi.org/10.1016/j.ijhydene.2018.02.042
0360-3199/

Please cite this article in press as: Benzidi H, et al., Vibrational and thermodynamic properties of $LiBH_4$ polymorphs from first-principles calculations, International Journal of Hydrogen Energy (2018), https://doi.org/10.1016/j.ijhydene.2018.02.042

18 GPainduce to a cubic phase (Fm-3m) [4]. The melting of the compound appears at around 550 K. All reported experimental structural studies of $LiBH_4$ have mentioned a tragic increase in hydrogen thermal displacements by almost 2 orders of degree from 4 to 400 K. This was attributed to dynamical disorder in the hexagonal high-temperature phase [5,6]. Buchter et al. [7] reported that for the energies smaller than ~ 15 meV, the phonon density of states of $LiBH_4$ in the low-temperature phase depends quadratically on the phonon energy although for the high temperature phase a continuous dependency is examined, affirming a high lattice anharmonicity in the high-temperature phase. First-principles calculations were very acknowledged to augur structures properties of $LiBH_4$ polymorphs. Despite the fact that, most calculations were realized for the ground state at the zero temperature, a recent advance in computational technique enables us to determine the entire phonon dispersion of solids. Thus, can compute specific heats, vibrational entropy, furthermore many thermodynamic quantities according of temperature. The present study purpose of clarifying the origin of phase transition in $LiBH_4$ by first principles lattice dynamics calculations. Also, the thermodynamics properties of the $LiBH_4$ were be calculated in order to compare the phase transition temperature between orthorhombic and hexagonal structure. In section computational method, the details and methods to perform our calculation are given. Section result and discussion is devoted to the presentation, the discussion and the comparison of numerical results. In the last section, the conclusion is given.

Computational method

The first-principles calculations within the density functional theory (DFT) [8] were performed using the Quantum Espresso program [9]. The generalized gradient approximation (GGA) [11] in the form of the Perdew-Burke-Ernzerhof (PBE) functional [10] was used to solve the Kohn-Shame equation. The structures were optimized by a full relaxation of the ion positions as well as the volume of the unit cell, the electronic ground-state steps were allowed to converge to an accuracy of 10^{-8} Ry. During each of the electronic steps, a plane-wave energy cutoff of 50 Ry was used for all calculations. The Brillouin zones of the unit cells are represented by Monkhorst-Pack special k-point scheme with 8 x 10 x 8 for orthorhombic LiBH4 (o-$LiBH_4$) and 10 x 10 x 8 for hexagonal $LiBH_4$ (h-$LiBH_4$) grid meshes. Computational settings such as plane wave cutoff energy, the number of k-points, and convergence criteria were carefully chosen for high numerical accuracy. Once the converged structures for the both orthorhombic and hexagonal structure were obtained, in order to access the stability of materials, the vibrational density of states (VDOS) was calculated using the software PHONOPY [12]. The VDOS is evaluated using a finite displacement method based on the Parlinski-Li-Kawazoe method. Displacements of 0.02 Å were used for the calculation of the force constants in the displacement method [13]. A larger displacement was used to avoid possible numerical inaccuracies in the system. A complete force constant matrix was obtained, and the phonon frequencies (ω) were then calculated by diagonalization of the dynamical matrix, over the electronic density of states. The Helmholtz energy was thus obtained by combining them with the 0 K total energy calculated within (Plane-Wave Self-Consistent Field method).

Result and discussion

Crystalline structures and optimizations

Using first principles calculations, two $LiBH_4$ phases (o-$LiBH_4$ and h-$LiBH_4$) were built by using crystallographic data in Ref. [14], then, their cell parameters and atomic positions were optimized. As a result, the corresponding total energies as function of the unit cell volume are obtained and plotted in Fig. 1. The relaxed lattice constants and atom positions of $LiBH_4$ phases along with the experimental data are summarized in Table 1. The optimized lattice parameters of both structures are in good agreement with previous theoretical and experimental results [14–16].

Furthermore, the bond length between two different atoms is also calculated and the results are listed in Table 2. This

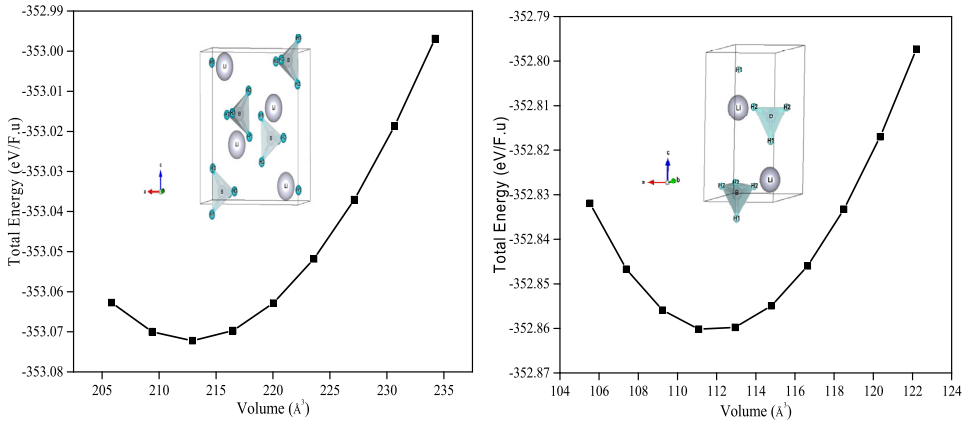

Fig. 1 – Total energy versus primitive unit cell volume of o-$LiBH_4$ (left) and h-$LiBH_4$ (right).

Please cite this article in press as: Benzidi H, et al., Vibrational and thermodynamic properties of $LiBH_4$ polymorphs from first-principles calculations, International Journal of Hydrogen Energy (2018), https://doi.org/10.1016/j.ijhydene.2018.02.042

Table 1 – Lattice parameters and positions for hexagonal and orthorhombic symmetries. Experimental results are included for comparison.

	Parameters			Positions						
		Calculated	Experimented [14]		Calculated			Experimented [14]		
o-$LiBH_4$				Li	0.1567	0.250	0.1015	0.157	0.250	0.1015
	a	7.2145	7.1785	B	0.3092	0.250	0.4275	0.304	0.250	0.4305
	b	4.3652	4.4368	H	0.8090	0.250	0.9275	0.900	0.250	0.9560
	c	6.6180	6.8032	H	0.4102	0.250	0.2719	0.404	0.250	0.2800
				H	0.2085	0.024	0.4270	0.172	0.054	0.4280
h-$LiBH_4$	a	4.1898	4.2763	Li	1/3	2/3	0.1107	1/3	2/3	0
	b	4.1898	4.2763	B	1/3	2/3	0.5362	1/3	2/3	0.5530
	c	7.3072	6.9484	H	1/3	2/3	0.3697	1/3	2/3	0.3700
				H	0.174	0.349	0.5927	0.172	0.344	0.6240

Table 2 – Interatomic distances (Å) of hydrogen and other neighboring atoms. Experimental results are included for comparison.

System	Interatomic distances (Å)							
	Calculated (at 0 K)				Experimented [7,17]			
	Li-H	B-H	H-H	Li-B	Li-H	B-H	H-H	Li-B
o-$LiBH_4$	1.9831	1.2234	1.9691	2.3408	1.980	1.25	1.80	2.475
	2.0516	1.2273	1.9934	2.5229	2.090	1.28	1.73	2.521
	2.0516	1.2289	2.0167	2.5237	2.150	1.04	2.13	2.542
	2.2499				2.289			
	2.3162				2.380			
h-$LiBH_4$	1.8924	1.2164	1.9919	2.4796	2.300	1.27	2.13	2.496
	2.0999	1.2219	2.1978	–	2.570	1.29	2.74	3.106
	2.0999		2.9138		2.629			
	2.9922				2.870			

result is in good agreement with recent theoretical results obtained by ab initio calculations [17] where the relative differences between the theoretical and experimental of the interatomic distances are essentially due to the larger difference of the temperature factors.

Phonon dispersion

Once the converged structures for each phase were obtained, the vibrational density of state (VDOS) are evaluated with a method utilizes a phonon calculation at 0 K to see if there are imaginary phonon modes, also called soft mode. The unit cell of orthorhombic (o-$LiBH_4$) structure holding four formula units have 72 modes, while the hexagonal (h-$LiBH_4$) structure holding two formula units have 36 modes. The Fig. 2 shows the density of states of phonons in both structures of $LiBH_4$ which is divided into three regions for o-LiBH4 (Fig. 2a) and four regions for h-LiBH4 hexagonal phase (Fig. 2b). Similar to the previous works [18,19], the present study shows that h-$LiBH_4$ ($P6_3mc$) phase (Fig. 2b) has a phonon with an imaginary frequency which indicates that the hexagonal structure is unstable. Or, the absence of any imaginary phonon frequencies in the entire Brillion zone of Fig. 2a confirms that o-LiBH4 (Pnma) structure is dynamically stable.

In the phonon PDOS (Fig. 3) for o- and h-$LiBH_4$, the region at low frequencies are composed of Li, B and H atoms states, by reason of the heavy weight of B and Li which is greater than hydrogen atoms and the vibration frequency of these atoms is visibly below than that of the hydrogen atom. While between 30 and 40 THz, two peaks are observed and composed of H atoms and a small fraction of states of B atoms. The apparent peaks at high frequencies are mostly composed of H states since its atomic mass is much lighter than those of the other atoms. The only noticeable difference between the orthorhombic phase (Fig. 3a) and hexagonal (Fig. 3b) is that the peak composed of H atoms appear at negative frequencies for h-$LiBH_4$.

In the phonon PDOS (Fig. 3) for o- and h-$LiBH_4$, the region at low frequencies are composed of Li, B and H atoms states, while between 30 and 40 THz, two peaks are observed and composed of H atoms and a small fraction of states of B atoms. The apparent peaks at high frequencies are mostly composed of H states since its atomic mass is much lighter than those of the other atoms. The only noticeable difference between the orthorhombic phase and hexagonal is that the peak composed of H atoms appear at negative frequencies for h-$LiBH_4$.

Thermodynamic properties

Based on the phonon frequencies, the thermodynamic functions of $LiBH_4$ phases can be obtained. The Helmholtz free energy could be written as:

$$F = E + H_{vib} + TS_{vib} \quad (1)$$

where, E, H_{vib} and $S_{vib\ are}$ the static electronic energy of the crystal, internal energy and entropy contributing to the lattice

Please cite this article in press as: Benzidi H, et al., Vibrational and thermodynamic properties of $LiBH_4$ polymorphs from first-principles calculations, International Journal of Hydrogen Energy (2018), https://doi.org/10.1016/j.ijhydene.2018.02.042

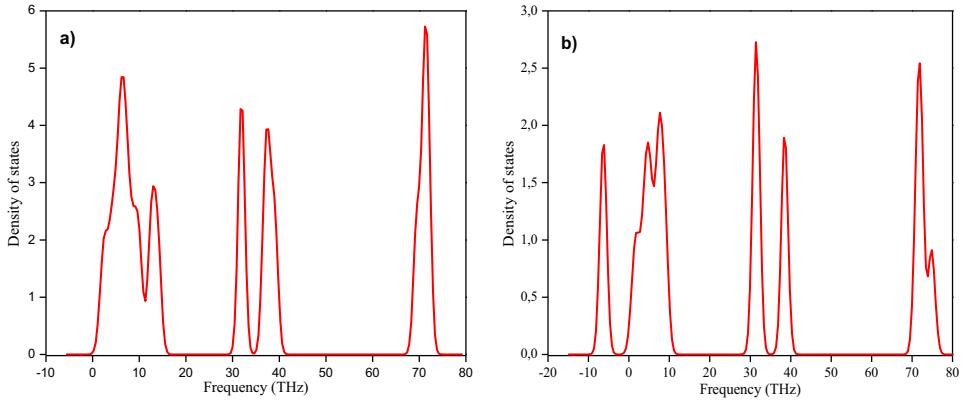

Fig. 2 – Phonon density of states of o-LiBH$_4$ (a) and h-LiBH$_4$ (b).

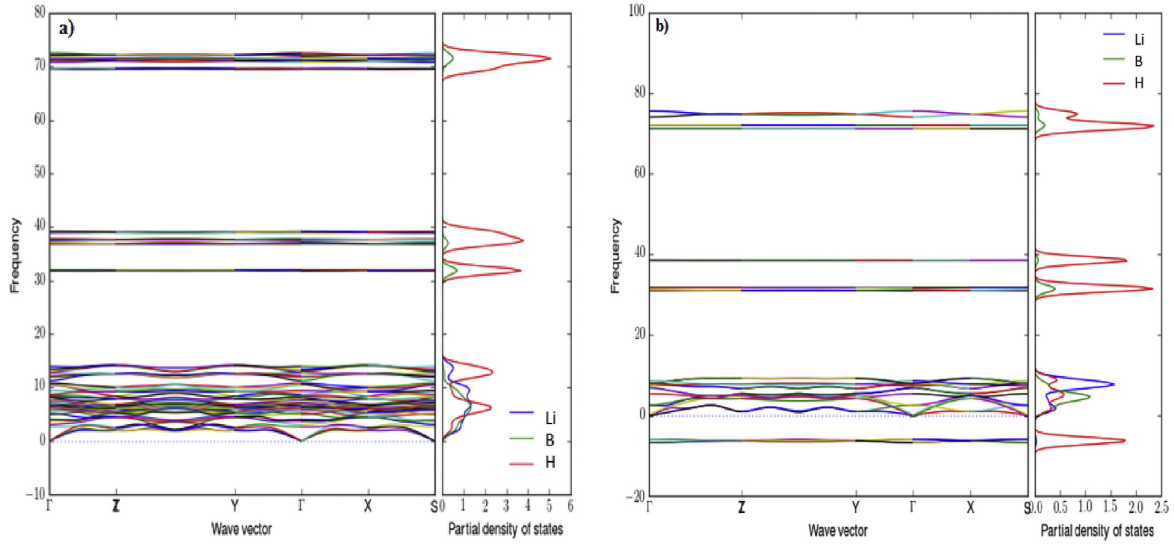

Fig. 3 – Phonon band structure and PDOS of o-LiBH$_4$ (a) and h-LiBH$_4$(b).

vibration. Within the harmonic approximation these contributions are given by:

$$H_{vib}(T) = \sum_i \frac{1}{2}\hbar\omega_i + \hbar\omega_i \left[\exp\left(\frac{\hbar\omega_i}{K_\beta T}\right) - 1\right]^{-1} \quad (2)$$

$$S_{vib}(T) = k_\beta \sum_i \frac{\frac{\hbar\omega_i}{K_\beta T}}{\exp\left(\frac{\hbar\omega_i}{k_\beta T}\right) - 1} - \ln\left[1 - \exp\left(-\frac{\hbar\omega_i}{k_\beta T}\right)\right] \quad (3)$$

where the sums run over vibrational frequencies, k_B is the Boltzmann factor and T is the absolute temperature. The zero-point energy ZPE can be recovered from equation (2) in the limit H_{vib} (T = 0); the Fig. 4 plots the calculated H_{vib} and S_{vib} of LiBH$_4$ phases as a function of temperature. Although having different structures, the H_{vib} and S_{vib} exhibit similar temperature dependencies for both structures. From Fig. 4a, it is noticed that the ZPE of h-LiBH$_4$ is about 7 kJ mol^{-1} lower than that of o-LiBH$_4$. Above 300 K, the internal energies H_{vib} increase almost linearly with temperature, tending to display k_BT behavior. Even more, at low temperature, the entropy S_{vib} of h-LiBH$_4$ is higher than that of o-LiBH$_4$, while increasing the temperature the o-LiBH$_4$ entropy becomes superior (see Fig. 4b).

The zero-point, enthalpy and entropic contributions to the free energy of the different phases are summarized in Table 3. As a further test of our computational methodology, there, our calculations results are compared to other values reported in the literature [20,22] and find good agreement.

The molar heat capacity has an importance in terms of energy, time and costs involved in changing temperatures of objects. Hence it is important as it will present a notion of how much energy will be appropriate to heat or cool an object of a given mass by a given supply. This will give information as to how long the heating or cooling process will take under a

Please cite this article in press as: Benzidi H, et al., Vibrational and thermodynamic properties of LiBH$_4$ polymorphs from first-principles calculations, International Journal of Hydrogen Energy (2018), https://doi.org/10.1016/j.ijhydene.2018.02.042

Table 3 – Comparison of vibrational enthalpy and entropy results with experimental data.

System	ZPE = H_{vib} (T = 0) (kJ mol^{-1})	ZPE other works [20,22]	$E_{vib} = H_{vib}-ZPE$	E_{vib} [20]	S_{vib} (T = 300K) (J mol^{-1} K^{-1})	S_{vib} [20]
o-$LiBH_4$	106.03	107.1106.5, 108.1	10.8 (300 K)	10.8	73.97	63.6
h-$LiBH_4$	99.9	–	21.2 (450 K)	–	75.57	–

given supply. The molar heat capacity at constant volume C_v and at constant pressure C_p are given by equations (4) and (5) and the results are presented in Fig. 5 and Table 4:

$$C_v = \left(\frac{\partial E}{\partial T}\right)_v = \sum_i k_\beta \left(\frac{\hbar\omega_i}{k_\beta T}\right)^2 \frac{\exp\left(\frac{\hbar\omega_i}{k_\beta T}\right)}{\left[\exp\left(\frac{\hbar\omega_i}{k_\beta T}\right)-1\right]^2} \quad (4)$$

$$C_p(T,p) = -T\frac{\partial^2 G(T,p)}{\partial T^2} = C_v(T,V(T,p)) + T\frac{\partial V(T,p)}{\partial T}\frac{\partial S(T,V)}{\partial V}\Big|_{V=V(T,p)} \quad (5)$$

At constant pressure, some of the heat goes into expanding the system, which does external work, and therefore leaves less energy available for raising the temperature. The heat capacity depends on the temperature, it increases with increasing temperature and this translates an accumulation of energy in the vibrational movement. Beyond room temperature, experimental values for the molar heat capacity of orthorhombic and hexagonal phases of $LiBH_4$ were realized by many authors. El Kharbachi et al. [23] deliberate the heat capacity from ambient temperature to approaching the melting point of the compound at 553 K using calorimetric measurements and found the following value C_p (285.6 K) = 76.6 ± 0.9 J K^{-1} mol^{-1}. At lower temperatures (i.e. 15–303 K), Hallett and Johnston [24] found the heat capacity of $LiBH_4$ by adiabatic calorimetry and proposed, for the standard molar heat capacity and entropy at 298.15 K, values of C_p (298.15 K) = 82.563 J K^{-1} mol^{-1} and S (298.15 K) = 75.860 ± 0.125 J K^{-1} mol^{-1}. Kim et al. [25] calculated by ab-initio methods the molar heat capacity for the hexagonal and orthorhombic phases from 0 to 1000 K. The agreement with the experimental data is limited, mainly at high temperatures. In fact, at room temperature, the value of Cp for the orthorhombic phase is around 10 J K^{-1} mol^{-1} lower than that obtained experimentally, while for the hexagonal phase at 450 K there is a difference about 23 J K^{-1} mol^{-1}. At constant volume, all the heat that goes into the system increases the temperature of the system and no external work is done. According to the phase diagram for $LiBH_4$ composition [3], at high temperature a coexistence of different phase (H_2 gas, LiH solid, B solid) can be observed between 450K and 850 K then the LiH decomposes and transforms to Li-liquid. A regular theory of heat capacity for liquids has not been accomplished and is still a rich area of research [27]. Thus, we find that we need more heat to raise the temperature of unit mass of the system over 1 K under constant pressure conditions, compared to the heat required to increment the temperature of the same unit mass of the system through 1K and under constant volume conditions.

The coefficient of thermal expansion (CTE) relates the change in volume of a material as a function of temperature change under constant pressure, and it is given by:

$$\alpha_v = \frac{1}{V}\left(\frac{\partial V}{\partial T}\right)_p \quad (6)$$

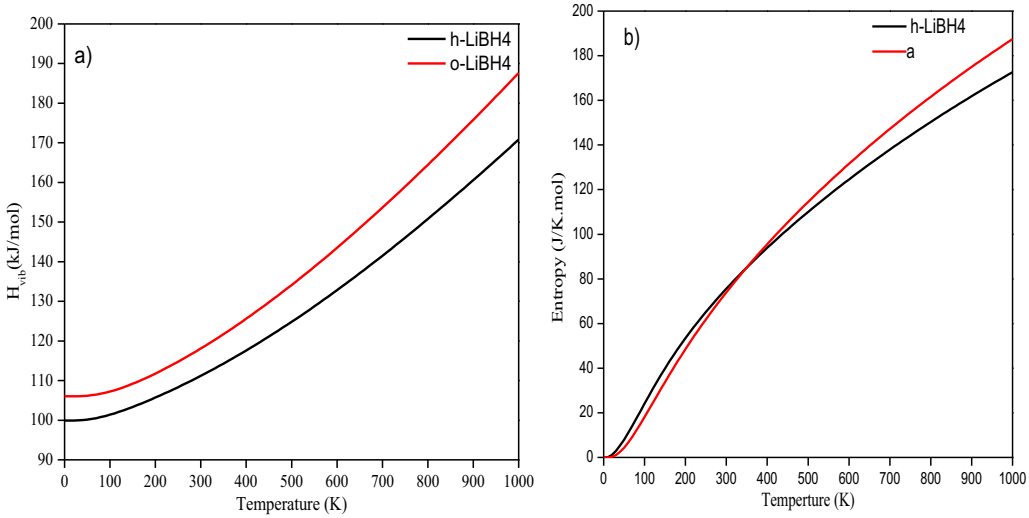

Fig. 4 – Vibrational enthalpy (a) and entropy (b) as function of temperature of both $LiBH_4$ structures.

Please cite this article in press as: Benzidi H, et al., Vibrational and thermodynamic properties of $LiBH_4$ polymorphs from first-principles calculations, International Journal of Hydrogen Energy (2018), https://doi.org/10.1016/j.ijhydene.2018.02.042

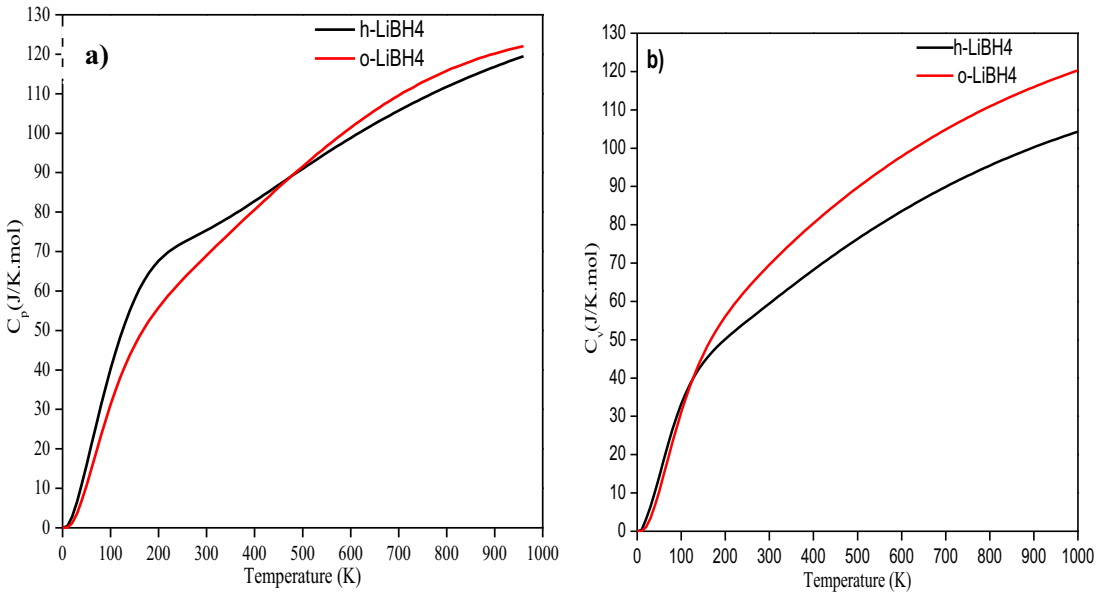

Fig. 5 – Calculated heat capacity as function of temperature of o-$LiBH_4$ and h-$LiBH_4$ at constant pressure (a) and constant volume (b).

Table 4 – Calculated heat capacity of o-$LiBH_4$ and h-$LiBH_4$ at constant pressure and constant volume compared with other calculated and experimental data.

System	C_p(J K^{-1} mol^{-1})	C_p other works	C_v(J K^{-1} mol^{-1})	C_v other works
o-$LiBH_4$	69.03 (300 K)	76.6 ± 0.9 (285.6 K) [23] 81.51 (298 K) [26]	59.45 (300 K)	–
h-$LiBH_4$	86.87 (450 K)	95.43 (450 K) [26]	85.23 (450 K)	–

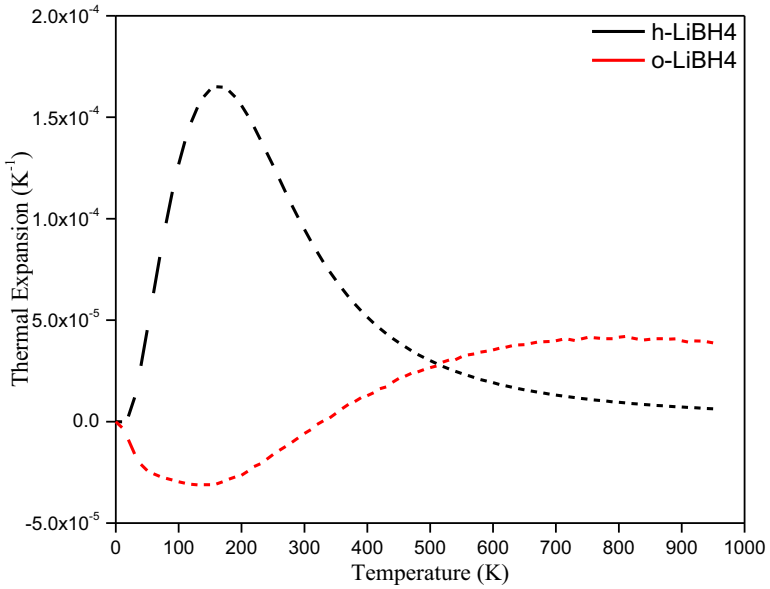

Fig. 6 – The coefficient of thermal expansion as function of temperature of o-$LiBH_4$ and h-$LiBH_4$.

Please cite this article in press as: Benzidi H, et al., Vibrational and thermodynamic properties of $LiBH_4$ polymorphs from first-principles calculations, International Journal of Hydrogen Energy (2018), https://doi.org/10.1016/j.ijhydene.2018.02.042

A negative value for CTE indicates a contraction on negative thermal expansion (NTE) while a positive value indicates a positive thermal expansion (PTE). From Fig. 6, it is found to be strongly dependent on temperature but remains negative for o-$LiBH_4$ (-2.5×10^{-5}) and positive for h-$LiBH_4$ ($1{,}6 \times 10^{-4}$) until to 500 K. Above 500 K for both phases are near ZTE.

Conclusion

First-principles DFT calculations combined with a quasi-harmonic approximation method were used to investigate phonon contribution of $LiBH_4$ polymorphs. The obtained optimized structural parameters of Pnma and P63mc structures are in good agreement with other results. Computed vibrational properties were used to illustrate thermodynamic properties of $LiBH_4$ phases (orthorhombic and hexagonal) like the vibrational enthalpy, entropy and the molar heat capacity etc. these properties are collected in order to compare other theoretical and experimental finding to our ab-initio calculation. Our obtained results are in good agreement with existing data. Thus, allowed us to understand some properties of a small atom like hydrogen which are not observable experimentally.

REFERENCES

[1] Satyapal S, Petrovic J, Read C, Thomas G, Ordaz G. The U.S. Department of Energy's National Hydrogen Storage Project: progress towards meeting hydrogen-powered vehicle requirements. Catal Today 2007. https://doi.org/10.1016/j.cattod.2006.09.022.

[2] Meisner GP, Scullin ML, Balogh MP, Pinkerton FE, Meyer MS. Hydrogen release from mixtures of lithium borohydride and lithium amide: a phase diagram study. J Phys Chem B 2006. https://doi.org/10.1021/jp056019b.

[3] Yan Y, Remhof A, Hwang S-J, Li H-W, Mauron P, Orimo S, et al. Pressure and temperature dependence of the decomposition pathway of LiBH4. Phys ChemChem Phys 2012. https://doi.org/10.1039/c2cp40131b.

[4] Dmitriev V, Filinchuk Y, Chernyshov D, Talyzin A, Ilewski A, Andersson O, et al. Pressure-temperature phase diagram of LiBH4: synchrotron X-ray diffraction experiments and theoretical analysis. Phys Rev B 2008. https://doi.org/10.1103/PhysRevB.77.174112.

[5] Gomes S, Hagemann H, Yvon K. Lithium boro-hydride LiBH4: II. Raman spectroscopy. J Alloys Compd 2002. https://doi.org/10.1016/S0925-8388(02)00668-0.

[6] Hagemann H, Gomes S, Renaudin G, Yvon K. Raman studies of reorientation motions of [BH4]- anionsin alkali borohydrides. J Alloys Compd 2004. https://doi.org/10.1016/S0925-8388(03)004687.

[7] Buchter F, Łodziana Z, Mauron P, Remhof A, Friedrichs O, Borgschulte A, et al. Dynamical properties and temperature induced molecular disordering of LiBH4 and LiBD4. Phys Rev B Condens Matter Mater Phys 2008. https://doi.org/10.1103/PhysRevB.78.094302.

[8] Kresse G, Furthmüller J, Efficient iterativeKresse G, Furthmüller J. Efficient iterative schemes for ab initio total-energy calculations using a plane-wave basis set. Phys Rev B 1996;54(16):11169–86. Retrieved from: http://link.aps.org/doi/10.1103/PhysRevB.54.1. Phys Rev B 1996.

[9] Giannozzi P, Baroni S, Bonini N, Calandra M, Car R, Cavazzoni C, et al. Quantum espresso: a modular and opensource software project for quantum simulations of materials. J Phys Condens Matter 2009;21:395502. https://doi.org/10.1088/0953-8984/21/39/395502.

[10] Perdew JP, Chevary JA, Vosko SH, Jackson KA, Pederson MR, Singh DJ, et al. Atoms, molecules, solids, and surfaces applications of the generalized gradient approximation for exchange and correlation (vol. 46, Pg 6671, 1992). Phys Rev B 1992. https://doi.org/10.1103/Physrevb.48.4978.2.

[11] Perdew JP, Burke K, Ernzerhof M. Generalized gradient approximation made simple. Phys Rev Lett 1996;77:3865e8. https://doi.org/10.1103/PhysRevLett.77.3865.

[12] Togo A, Tanaka I. First principles phonon calculations in materials science. Scr Mater 2015. https://doi.org/10.1016/j.scriptamat.2015.07.021.

[13] Parlinski K, Li Z, Kawazoe Y. First-principles determination of the soft mode in cubic ZrO2. Phys Rev Lett 1997. https://doi.org/10.1103/PhysRevLett.78.4063.

[14] Soulié JP, Renaudin G, Erný R, Yvon K. Lithium boro-hydride LiBH4: I. Crystal structure. J Alloys Compd 2002. https://doi.org/10.1016/S0925-8388(02)00521-2.

[15] Miwa K, Ohba N, Towata SI, Nakamori Y, Orimo SI. First-principles study on lithium borohydride LiBH4. Phys Rev B Condens Matter Mater Phys 2004. https://doi.org/10.1103/PhysRevB.69.245120.

[16] Zuttel A, Rentsch S, Fischer P, Wenger P, Sudan P, Mauron P, et al. Hydrogen storage properties of LiBH4. J Alloys Compd 2003:515–20. https://doi.org/10.1016/S0925-8388(02)01253–01257.

[17] Tekin A, Caputo R, Züttel A. First-principles determination of the ground-state structure of LiBH4. Phys Rev Lett 2010. https://doi.org/10.1103/PhysRevLett.104.215501.

[18] Miwa K, Ohba N, Towata S, Nakamori Y, Orimo S. First-principles study on copper substituted lithium borohydride, (Li 1-xCux)BH4. J Alloys Compd 2005. https://doi.org/10.1016/j.jallcom.2004.09.090.

[19] Gremaud R, Zttel A, Borgschulte A, Ramirez-Cuesta AJ, Refson K, Colognesi D. Origin of the large anharmonicity in the phonon modes of LiBH4. Chem Phys 2013. https://doi.org/10.1016/j.chemphys.2013.10.001.

[20] Siegel DJ, Wolverton C, Ozolins V. Reaction energetics and crystal structure of Li4BN3H10 from first principles. Phys Rev B 2007. https://doi.org/10.1103/Physrevb.75.014101. Artn 014101\nDoi.

[22] Łodziana Z, Vegge T. Structural stability of complex hydrides: LiBH_{4} revisited. Phys Rev Lett 2004;93:1–4. https://doi.org/10.1103/PhysRevLett.93.145501.

[23] El Kharbachi A, Pinatel E, Nuta I, Baricco M. A thermodynamic assessment of LiBH 4. Calphad Comput Coupling Phase Diagrams Thermochem 2012. https://doi.org/10.1016/j.calphad.2012.08.005.

[24] Zhang LJ, Di YY, Dou JM. Low-temperature heat capacities and thermodynamic properties of n-undecylammonium bromide monohydrate C11H28BrNO(s). Phase Transitions 2012. https://doi.org/10.1080/01411594.2012.660638.

[25] Kim KC, Allendorf MD, Stavila V, Sholl DS. Predicting impurity gases and phases during hydrogen evolution from complex metal hydrides using free energy minimization enabled by first-principles calculations. Phys ChemChem Phys 2010. https://doi.org/10.1039/c001657h.

[26] El Kharbachi A, Nuta I, Hodaj F, Baricco M. Above room temperature heat capacity and phase transition of lithiféum tetrahydroborate. Thermochim Acta 2011. https://doi.org/10.1016/j.tca.2011.02.043.

[27] Dehimi L, Benguerba Y, Virginie M, Hijazi H. Microkinetic modelling of methane dry reforming over Ni/Al2O3 catalyst. Int J Hydrogen Energy 2017. https://doi.org/10.1016/j.ijhydene.2017.05.231.

Please cite this article in press as: Benzidi H, et al., Vibrational and thermodynamic properties of $LiBH_4$ polymorphs from first-principles calculations, International Journal of Hydrogen Energy (2018), https://doi.org/10.1016/j.ijhydene.2018.02.042